Chemical Looping Combustion for carbon capture

Rosario Porrazzo

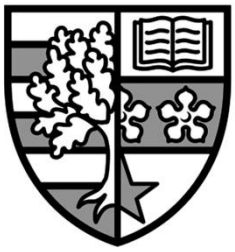

A thesis submitted for the degree of Doctor of Philosophy

Heriot-Watt University

Chemical Engineering

Institute of Mechanical, Process and Energy Engineering

School of Engineering and Physical Sciences

April 2016

Abstract

Among the well-known state-of-art technologies for CO_2 capture, Chemical Looping Combustion (CLC) stands out for its potential to capture with high efficiency the CO_2 from a fuel power plant for electricity generation. CLC involves combustion of carbonaceous fuel such as coal-derived syngas or natural gas via a red-ox chemical reaction with a solid oxygen carrier circulating between two fluidised beds, air and fuel reactor, working at different hydrodynamic regimes. Avoided NO_x emissions, high CO_2 capture efficiency, low CO_2 capture energy penalties and high plant thermal efficiency are the key concepts making worthy the investigation of the CLC technology.

The main issue about the CLC technology might concern the cost of the solid metal oxides and therefore the impact of the total solid inventory, solid make-up and lifetime of the solid particles on the cost of the electricity generated.

A natural gas fired power plant embedding a CLC unit is presented in this work. Macro scale models of fluidised beds (i.e. derived applying macroscopic equations) are developed and implemented in Aspen Plus software. Kinetic and hydrodynamic phenomena, as well as different operating conditions, are taken into account to evaluate their effect on the total solid inventory required to get full fuel conversion. Furthermore, a 2D micro scale model of the fuel reactor (i.e. derived applying partial differential equations), making use of a CFD code, is also developed. The results, in terms of the effect of the different kinetic and hydrodynamic conditions on the outlet gas conversion, are compared with the results using the macro-scale model implemented in Aspen Plus. Based on the micro scale (CFD) outcomes, the macro scale model is enhanced to capture the main physics influencing the performance of the fuel reactor. Thus, the improved macro scale model is embedded into different power plant configurations and mass and energy balances are solved simultaneously. Thermal efficiency evaluations for the different plant arrangements are carried out.

A detailed economic evaluation of the CLC power plant is undertaken by varying two relevant parameters: fuel price and lifetime of the solid particles. The effect of the aforementioned parameters on the Levelised Cost Of Electricity (LCOE) is investigated and the resulting outcomes are critically discussed.

Acknowledgements

Looking back at the past three years, I had the pleasure to meet people from all over the world and take the best from their experiences and knowledge. Therefore, I want to make use of this room to thank those who effectively influenced and supported my PhD journey.

Firstly, I would like to thank my first supervisor Raffaella Ocone with whom I shared more than just the same nationality. I thank her for giving me the opportunity to undertake this project, for letting me to share with her my ideas fairly, for helping me to overcome all the technical difficulties encountered, for supporting me in the darkest moments of my research and, above all, for her humanity.

I would like to thank my second supervisor Graeme White for all the technical support provided, for the extensive availability given and the precious advices.

I would like to thank my family who suffered with me during the low moments and enjoyed with me during the high moments. A special *thanks* goes to my parents who always believed that I could have made it.

Finally yet importantly, I would like to thank the people that made my journey lighter and happier with their friendship. Therefore, thanks to Alessandro, Aurora, Theo, Marica, Natalia, Francesca, Giuseppe, Daniele, Claudio, Claudia, Sean, Aimaro, Alice and all those who bore me in these years.

Declaration statement

ACADEMIC REGISTRY

Research Thesis Submission

Name*:*	Rosario Porrazzo		
School/PGI:	School of Engineering and Physical Sciences		
Version: *(i.e. First, Resubmission, Final)*	Final	Degree Sought (Award and Subject area)	**PhD** in Chemical Engineering

Declaration

In accordance with the appropriate regulations I hereby submit my thesis and I declare that:

1) the thesis embodies the results of my own work and has been composed by myself
2) where appropriate, I have made acknowledgement of the work of others and have made reference to work carried out in collaboration with other persons
3) the thesis is the correct version of the thesis for submission and is the same version as any electronic versions submitted*.
4) my thesis for the award referred to, deposited in the Heriot-Watt University Library, should be made available for loan or photocopying and be available via the Institutional Repository, subject to such conditions as the Librarian may require
5) I understand that as a student of the University I am required to abide by the Regulations of the University and to conform to its discipline.

* *Please note that it is the responsibility of the candidate to ensure that the correct version of the thesis is submitted.*

Signature of Candidate*:*		Date:	

Submission

Submitted By *(name in capitals):*	ROSARIO PORRAZZO
Signature of Individual Submitting:	
Date Submitted:	

For Completion in the Student Service Centre (SSC)

Received in the SSC by *(name in capitals):*			
Method of Submission *(Handed in to SSC; posted through internal/external mail):*			
E-thesis Submitted **(**mandatory for final theses)			
Signature:		Date:	

Contents

List of Publications

Publications in Reviewed Journals

Porrazzo R., G. White, R. Ocone (2014). Aspen Plus simulations of fluidised beds for chemical looping combustion. Fuel 136, 46-56.

Porrazzo R., G. White, R. Ocone (2016). Fuel reactor modelling for chemical looping combustion: From micro-scale to macro-scale. Fuel 175, 87-98.

Porrazzo R., G. White, R. Ocone (2016). Techno-economic investigation of a Chemical Looping Combustion-based power plant. Under review.

International Conferences

R. Porrazzo, G. White, R.Ocone, "Analysis of a Chemical Looping Combustion Power Plant Performances", ChemEngDayUK, Sheffield, April 2015

R. Porrazzo, G. White, R.Ocone, "Analysis of Chemical Looping Combustion for Power Plant Applications", AIChE Annual Meeting, Atlanta, US, November 2014

R. Porrazzo, G. White, R.Ocone, "Simulation of Chemical Looping Combustion power plant using Aspen Plus", ChemEngDayUK, Manchester, April 2014

R. Porrazzo, G. White, R. Ocone, "Chemical Looping Technology for Clean Energy Production: Integrating Aspen Plus and CFD", invited talk to the ACS Meeting, Dallas, US, March 2014

R. Porrazzo, G. White, R. Ocone, "Chemical Looping Simulations Using Aspen Plus", AIChE Annual Meeting, San Francisco, US, November 2013

R. Porrazzo, G. White, R.Ocone, "Chemical Looping Combustion Using Aspen Plus", 5th High Temperature Solid Looping Network Meeting, Cambridge, September 2013

R. Porrazzo, G. White, R.Ocone, "Aspen Plus Simulations of Circulating Fluidised Beds for Chemical Looping Combustion", Fluidisation XIV, The Netherlands, 2013

Academic Awards

2nd Year Postgraduate Research Prize 2014 award at Heriot-Watt University in recognition of my research performance during my second year of postgraduate study, October 2014

Poster competition award at the 36th Annual General Meeting of the International Fine Particle Research Institute (IFPRI), Jun 2014

Nomenclature

a	decay factor (-)
A_{AR}	riser superficial area (m^2)
A_b	bubble phase superficial area (m^2)
A_{FR}	fuel reactor superficial area (m^2)
A_{hex}	total heat transfer area (m^2)
A_o	area of the gas distributor per nozzle (m^2/number of nozzles)
A_V	area crossed by the gas flow-rate in the separator (m^2)
C_A	molar concentration of the A gas ($kmol/m^3$)
$CAPEX$	total capital investment ($)
C_b	gas bubble concentration ($kmol/m^3$)
C_c	solid concentration in the gas at the cyclone inlet (kg/m^3)
C_e	emulsion gas concentration ($kmol/m^3$)
CF_j	annual cash flow ($/year)
C_i	gas concentration of the i component ($kmol/m^3$)
C_{oj}	annual operating cost ($/year)
c_p	specific heat at constant pressure (kJ/(kgK))
CRF	recovery factor (year)
c_v	specific heat at constant volume (kJ/(kgK))
d_b	bubble diameter (m)
D_c	cyclone diameter (m)
$DCFR$	discount cash flow rate of return (%)
D_{FR}	fuel reactor diameter (m)
D_{gn}	diffusion coefficient of the n gas species (kg/(m s))
d_j	annual depreciation ($/year)
d_p	particle size (m)
D_{sn}	diffusion coefficient of the n solid species (kg/(m s))
D_{vessel}	diameter of the separator (m)
dX/dt	generic solid conversion rate (1/s)
dX_{red}/dt	solid reduction rate (1/s)
e	restitution coefficient (-)
E_a	activation energy (kJ/kmol)
E_c	solids emission rate in the cleaned gas at the cyclone outlet (kg/s)
e_w	wall restitution coefficient (-)

F_{air}	inlet mass air flow-rate (kg/s)
F_{fuel}	inlet mass fuel flow-rate (kg/s)
$F_{j\ in}$	inlet molar solid flow-rate of the *j* component (kmol/s)
$F_{j\ out}$	outlet molar solid flow-rate of the *j* component (kmol/s)
F_{O2}	oxygen mass flow-rate (kg/s)
F_s	total solid circulating mass flow-rate (kg/s)
F_{sb}	inlet solid mass flow-rate in the bubble phase (kg/s)
F_{sm}	inlet solid mass flow-rate in the emulsion phase (kg/s)
g	gravity acceleration (m/s^2)
g_o	radial distribution function (-)
GP_j	annual gross profit ($/year)
G_s	solid circulating mass flow-rate per area unit ($kg/(m^2\ s)$)
h	generic fuel reactor height (m)
H_1	inlet enthalpy at the steam turbine (kJ/kg)
H_{2s}	isentropic outlet enthalpy at the steam turbine (kJ/kg)
H_c	height of the cyclone (m)
H_{FR}	fuel reactor exit (m)
i	interest rate (%)
i'	annual rate of inflation (%)
k	generic kinetic coefficient (m/s)
K_{bc}	mass transfer coefficient between bubble and cloud (1/s)
K_{be}	overall mass transfer coefficient between bubble and emulsion (1/s)
K_{ce}	mass transfer coefficient between cloud and emulsion (1/s)
k_i	kinetic coefficient of the *i* component ($kmol^{(1-n)}m^{(3n-3)}/s$)
k_o	pre-exponential factor ($mol^{(1-n)}m^{(3n-2)}/s$)
$k_{o,p}$	apparent pre-exponential factor ($mol^{(1-n)}m^{(3n-2)}/(s\ atm^q)$)
$LCOE$	levelised cost of electricity ($/kWh)
L_f	height of a fluidised bubbling bed (m)
LHV	lower heating value (MJ/kg)
L_m	height of a fixed bed (m)
LT_{MO}	lifetime of solid particles (h)
L_{vessel}	length of the separator (m)
M	molar flow-rate (kmol/s)
m_{ar}	minimum acceptable rate of return (%)
m_{in}	inlet mass gas flow-rate at the turbines and compressors (kg/s)

M_{ox}	molar mass of the fully oxidised carrier (kg/kmol)
M_{red}	molar mass of the fully reduced carrier (kg/kmol)
MW_{CH4}	methane molecular weight (kg/kmol)
MW_i	molecular weight of the *i* specie (kg/kmol)
MW_{O2}	oxygen molecular weight (kg/kmol)
n	order of reaction (-)
n_{stages}	number of stages (-)
N_B	number of moles of the B solid reactant (kmol)
NP_j	annual net profit ($/year)
NPW	net present worth (-)
$OPEX$	annual operating costs ($/year)
P	pressure (atm)
P_{eff}	power at turbines, pumps and compressors (kW)
P_{fuel}	fuel power (MW)
P_g	gas pressure (Pa)
POT	capacity factor (h/year)
P_{rj}	annual product rate (kWh/year)
P_s	solid pressure (Pa)
q	pressure effect exponent (-)
Q_{air}	volumetric air flow-rate (m^3/s)
Q_b	bubble volumetric gas flow-rate (m^3/s)
Q_e	emulsion volumetric gas flow-rate (m^3/s)
Q_{fuel}	inlet volumetric fuel flow-rate (m^3/s)
Q_{hex}	heat duty at the heat transfer units (kW)
Q_L	volumetric liquid flow-rate in the separator (m^3/s)
Q_{oc}	cyclone overflow volumetric gas flow-rate (m^3/s)
$Q_{p,in}$	inlet volumetric flow-rate at the pumps (m^3/s)
Q_V	volumetric gas flow-rate in the separator (m^3/s)
R	external radius of the particle (m)
r	generic reaction rate ($kmol/(m^3\ s)$)
$R^{'}$	universal gas constant (kJ/(kmol*°K)
r_c	core radius (m)
r_g	grain radius size (m)
r_{gn}	reaction rate of the n gas specie ($kg/(m^3 s)$)
$r_{i\ Aspen}$	Aspen Plus reaction rate ($kmol/(m^3 s)$)

$r_{i\,CFD}$	CFD reaction rate (kmol/(m^{3}s))
R_o	oxygen transport capacity (-)
r_{sn}	reaction rate of the n solid specie (kg/(m^3 s)
S_j	annual revenue ($/year)
st	stoichiometric coefficients ratio (-)
T	temperature (°C)
TCI	total capital investment ($)
U_{air}	air superficial velocity (m/s)
U_b	gas bubbles velocity (m/s)
U_{br}	single bubble velocity (m/s)
U_e	gas emulsion velocity (m/s)
U_{hex}	overall heat transfer coefficient (kW/(m^{2}K))
U_L	settling velocity of the liquid droplets in the separator (m/s)
U_{mf}	minimum fluidisation gas velocity (m/s)
U_o	inlet superficial gas velocity (m/s)
U_t	terminal solid particles velocity (m/s)
U_V	gas velocity in the separator (m/s)
V_b	bubble phase volume (m^3)
V_{CSTR}	CSTR volume (m^3)
V_e	emulsion phase volume (m^3)
V_L	volume occupied by the liquid in the separator (m^3)
V_{PFR}	PFR volume (m^3)
V_{tot}	reactor total volume (m^3)
W_{bed}	solid inventory in a generic bed reactor (kg)
W_{bedAR}	solid inventory in the air reactor (kg)
W_{bedFR}	solid inventory in the fuel reactor (kg)
W_{bedTOT}	total solid inventory into the beds (kg)
W_L	liquid mass flow-rate in the separator (kg/s)
W_{net}	net electricity produced (kW)
W_V	gas mass flow-rate in the separator (kg/s)
X_B	average conversion of the B solid reactant (-)
X_{CH4}	methane gas conversion (-)
X_j	average solid conversion of the *j* component (-)
x_{MeO}	active metal oxide content (-)
X_{MO_exit}	metal oxide conversion at the riser exit (-)

Y_{gn}	mass fraction of the n gas specie (-)
Y_{Ni}	nickel mass fraction (-)
Y_{NiO}	nickel oxide mass fraction (-)
Y_{sn}	mass fraction of the n solid specie (-)
z	height either of the freeboard in the fuel reactor or of the riser (m)
Z_{NiO}	metal oxide volumetric fraction (-)
β	coefficient for the interphase force between gas and solid (kg/(m^{3}s))
β_c	compression ratio (-)
δ	diffusivity coefficient (m^2/s)
ΔX_{fuel}	change in fuel conversion (-)
ΔX_{solid}	change in solid conversion (-)
ε_b	gas volume fraction in the bubble phase (-)
ε_e	gas volume fraction in the emulsion phase (-)
ε_f	gas volume fraction in bubbling conditions (-)
ε_g	gas volume fraction in a fluidised bed (-)
ε_m	gas volume fraction in a fixed bed (-)
ε_{mf}	gas void at minimum fluidisation conditions (-)
ε_s	solid volume fraction in a fluidised bed (-)
ε_s^*	solid volume fraction at the exit of a fluidised bed (-)
ε_{sd}	solid volume fraction of the dense phase in the riser and in the fuel reactor (-)
ζ	gas-solid contact efficiency in the freeboard (-)
η_c	cyclone overall separation efficiency (-)
η_{CO2}	CO_2 capture efficiency (%)
η_{eff}	pump efficiency (-)
η_{is}	isentropic efficiency (-)
η_{th}	net power efficiency (%)
ξ	gas phase expansion factor (-)
ρ_{air}	air density (kg/m^3)
ρ_{CH4}	methane density (kg/m^3)
ρ_g	gas density (kg/m^3)
ρ_L	liquid density in the separator (kg/m^3)
ρ_{Ni}	nickel density (kg/m^3)
ρ_{NiO}	nickel oxide density (kg/m^3)
ρ_s	solid particles density (kg/m^3)
ρ_V	gas density in the separator (kg/m^3)

σ	volumetric fraction of the bubble phase (-)
τ_{eff}	effective residence time in the separator (s)
τ_g	gas stress tensor (Pa)
$\tau_{hold\text{-}up}$	liquid residence time in the separator (s)
τ_{req}	required residence time in the separator (s)
τ_s	solid stress tensor (Pa)
Φ	angle of internal friction (-)
φ	fractional income tax rate (-)
Θ	granular temperature (m^2/s^2)
Υ	energy dissipation rate ($kg/(s^3 m)$)
γ_{red}	yield in CO_2 (-)
$\overrightarrow{U_g}$	gas phase velocity vector (m/s)
$\overrightarrow{U_s}$	solid phase velocity vector (m/s)
μ_s^P	frictional viscosity (kg/(m s))
μ_s^v	solid shear viscosity (kg/(m s))
λ_s^v	solid bulk viscosity (kg/(m s))
μ_g	gas viscosity (kg/(m s))

Chapter 1

Introduction

The dynamic Earth's energy balance between the incoming energy from the sun and its release back to space is responsible for the change in the Earth's temperature. Greenhouse gas concentration, sun's energy and reflectivity of Earth's atmosphere and surface can cause changes in the above-mentioned energy balance. Greenhouse gases (GHGs) are constituents of the atmosphere that absorb the infrared radiation (heat) reflected from the Earth's surface and trap the heat in the atmosphere, slowing or preventing its loss to space. This process is known as the greenhouse effect (IPCC, 2008). Therefore, GHGs greatly affect the Earth's temperature; without them the planet's average temperature would be about –18 °C (Jacob, 1999). The primary GHGs in the atmosphere include water vapour (H_2O), carbon dioxide (CO_2), methane (CH_4), nitrous oxide (N_2O) and ozone (O_3). All of them have an associated Global Warming Potential (GWP) as a measure of the capacity of the gases to trap heat in the atmosphere. For instance, CO_2 has a GWP equal to 1 (reference gas) whereas CH_4 has 25 for 100-year time horizon (IPCC, 2007).

Since the beginning of the Industrial Revolution (1750), human activities have contributed extensively to the increase in the concentration of GHGs. In particular, between 1970 and 2004, global emissions of CH_4, CO_2, N_2O and halocarbons increased by 70%, from 28.7 to 49 Gt of CO_2-equivalent per year (IPCC, 2007). Under ongoing greenhouse gas emissions, available Earth System Models have estimated an increase in the average planet's temperature that would affect drastically ecosystems on Earth and the livelihoods of over 3 billion people worldwide (Mora et al., 2013). If no effort is made to reduce GHG emissions, an increase in the average planet temperature up to between 3.7 and 4.8 °C above the pre-industrial level is expected by 2100, corresponding to more than 1000 ppm of greenhouse gas concentration in the atmosphere (IPCC, 2014).

In order to minimise the risks connected with climate change, the international community has agreed (see "Copenhagen agreement" (www.eur-lex.europa.ue)), in 2009, to limit the temperature rise to 2 °C above pre-industrial levels (1.4 °C above the present level), corresponding to 450 ppm of GHG concentration in the atmosphere

(Lazarusand Kartha, 2009). The latter has resulted in a decisive act, undertaken by most of the countries (192 parties), that targets the reduction of the GHG emissions in the next three decades, in accordance with the "Kyoto protocol" guidelines. From a local point of view, the UK (and similarly EU) responded to the "Kyoto protocol" requests enacting, in 2008, the Climate Change Act. The latter set an 80% cut of the UK GHG emissions by 2050 (based on the GHG emissions level in 1990) leading to 156 $MtCO_2$-eq of allowed emissions per year, with exported manufacturing not included (see Fig. 1.1). Furthermore, to encourage progress to meet the final goal, the UK Committee on Climate Change (CCC) set four "Carbon Budgets", each lasting five years, working as short-term targets (Committee on Climate Change, 2014). Practically, the progressive reduction in the worldwide GHG emissions can be achieved by tackling the main anthropogenic sources of CO_2 emissions, as explained in the following section.

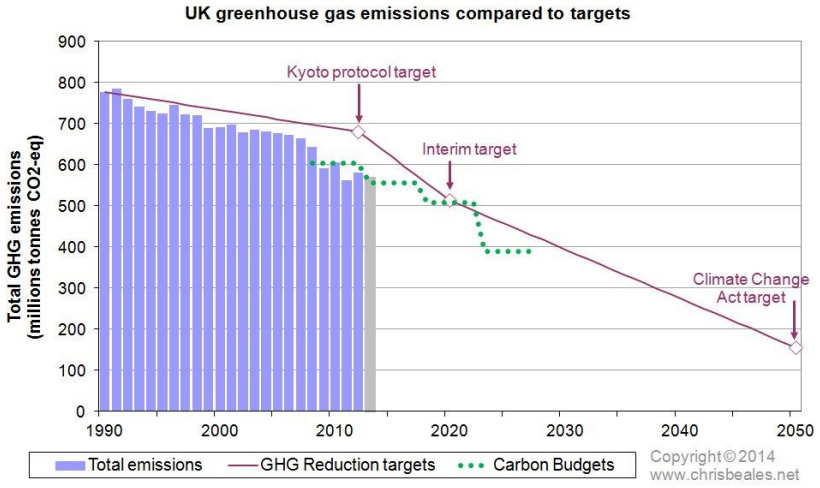

Fig. 1.1 UK greenhouse gas emissions compared to targets (www.chrisbeales.net)

In this scenario, the carbon credit market has arisen. By definition, a carbon credit is "*a generic term to assign a value to a reduction or offset of greenhouse gas emissions usually equivalent to one tonne of carbon dioxide equivalent (CO2-e)*" (EPAV, 2008). Based on the Kyoto protocol, a carbon credit is a permission representing the right to emit one tonne of CO_2 or a mass of any other GHG with a tCO2-e equivalent to one tonne of CO_2. All the countries that present GHG emissions higher than the threshold allowed must reduce their emissions. All the countries that have not reached yet the maximum threshold allowed (mainly the developing countries) can sell their rights to emit (i.e. carbon credits) to the other countries fostering the investments from the rich

countries in new technologies for the GHG reductions in the developing countries. More information about carbon credits are reported by Miller et al. (2009).

1.1 Carbon Dioxide global emissions and need for CCS

CO_2 is the most important anthropogenic GHG since it represents the largest anthropogenic GHG emission (77% of the total GHG emissions in 2004) (see Fig. 1.2). Moreover, its contribution to the greenhouse effect (20%) is the second biggest after water vapour based on the gas characteristics and abundance in atmosphere (Schmidt et al., 2010).

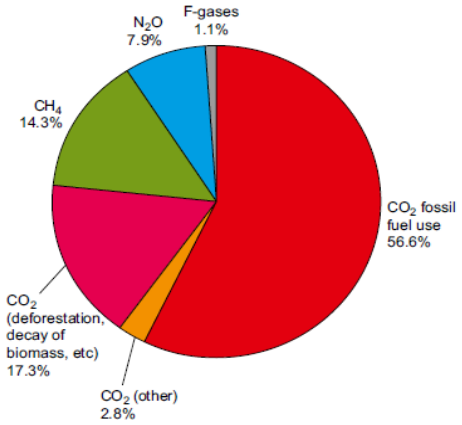

Fig. 1.2 Global anthropogenic GHG emissions in 2004 (IPCC, 2007)

Since pre-industrial times (1750) the CO_2 concentration in the atmosphere has increased by 43% from 278 to 400 parts per million (ppm) in 2015 and 25% of its increase has occurred just in the last 50 years (NOAA/ESRL, 2015). Although natural sources of CO_2 emissions are more than 20 times greater than those coming from human activities (the present carbon cycle – Climate Change, 2010), they are perfectly balanced by natural sinks. Thus, the abrupt increase in CO_2 emissions is strongly related to the anthropogenic activities, such as burning of fossil fuel, deforestation, use of CFCs in refrigeration systems and fertilizers in agriculture. For instance, fossil fuel accounts for about 75% of current anthropogenic CO_2 emissions (IPCC, 2005). Within the range of human activities, the industrial sector accounts for most CO_2 emissions (Fig. 1.3); specifically, power stations are the largest contributor of anthropogenic CO_2 emissions; indeed, 29% of CO_2 emissions are linked to power generation (Fig. 1.4).

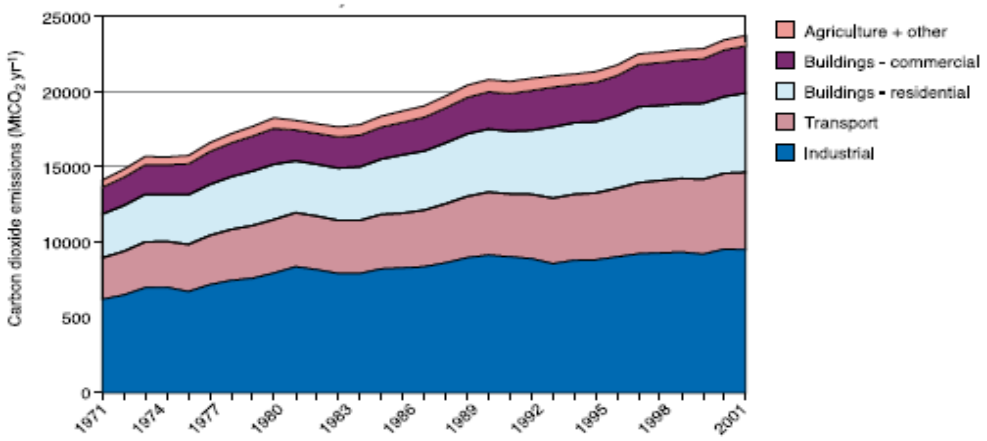

Fig. 1.3 World CO_2 emissions by source from 1971 to 2001 (IEA, 2003)

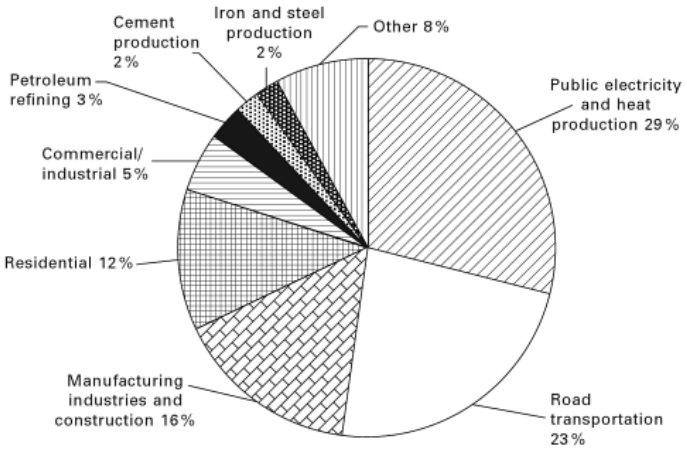

Fig. 1.4 EU-15 CO_2 emissions by source for 2006 (EIA, 2008)

Fossil fuels are the dominant form of energy utilised in the world with a value higher than 80% of the total energy sources (Figs. 1.5 - 1.6) and represent the main source of electricity generation (Fig. 1.7). This aspect, in conjunction with the increase in electricity demand (70% higher than the current demand by 2035 (WEO, 2012)), leads to a strong dependence between CO_2 emissions rate, electricity generation and, consequently, between CO_2 emissions rate and type of fossil fuel.

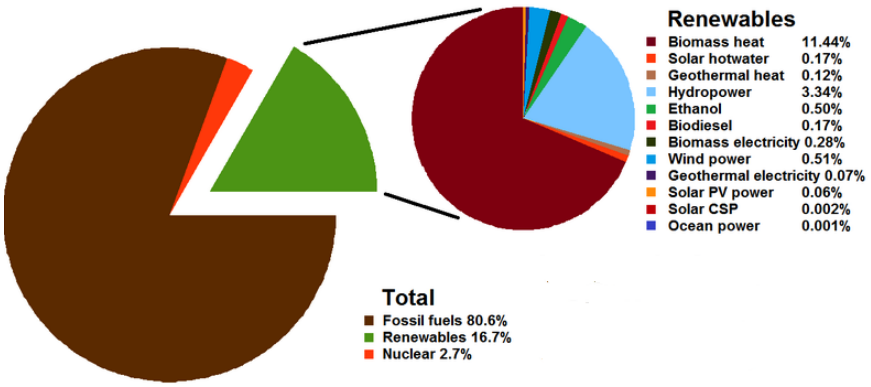

Fig. 1.5 Total world energy consumption by source (Renewable Energy Policy Network for the 21st Century, 2010)

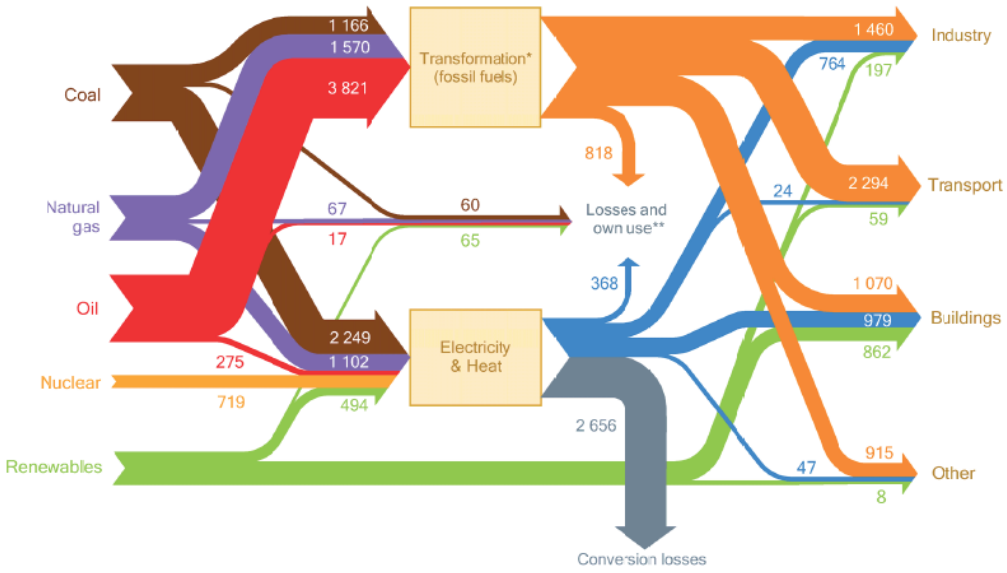

Fig. 1.6 The global energy system (Million tonne of oil equivalent, Mtoeq) (WEO, 2012)

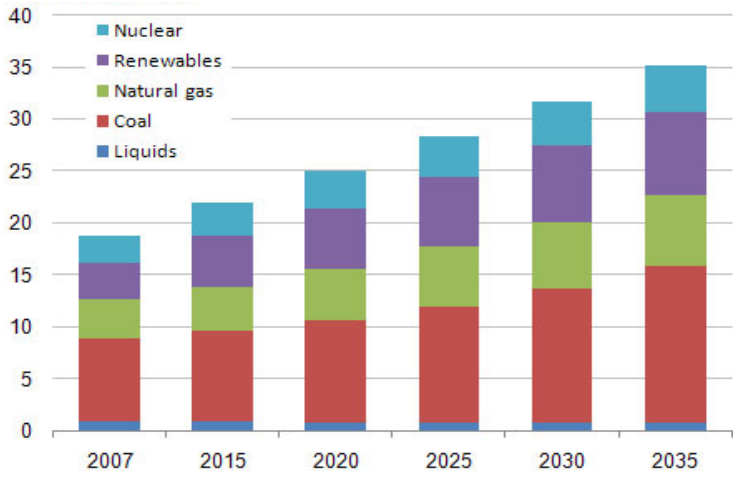

Fig. 1.7 World electricity generation by fuel type (trillion kWh) (EIA, 2014)

Since not all sources of CO_2 emissions are readily reduced (i.e. aviation and shipping) and the power sector represents one of the major CO_2 emission sources, the latter was the most stressed sector, in the recent years, subject to solutions for mitigating climate change to be applied.

Different options for CO_2 emissions reduction are listed in the IPCC report (2005). The improvement of the efficiency of energy conversion via high efficiency turbines, combined cycles concepts as well as integrated heating and cooling systems for electricity generation, gives a reduction in fossil fuel consumption; however, enhancements cannot be sufficient, and some of them are not economically feasible, to target deep reductions in CO_2 emissions (IPCC, 2005).

Another solution involves the switch to nuclear power and renewable energy. In the field of renewable energy, there is a variety of near-zero-carbon energy sources potentially available: solar, wind, hydro, biomass, geothermal and tidal power. Many of them face constraints related to intermittency of supply, cost, land use and other environmental impacts depending on the location and policy of the different countries (IPCC, 2005). Different issues concern nuclear power plants: safety, long-term storage of nuclear wastes and public opposition.

As Fig. 1.7 shows, the projections for 2035 point out the central role of fossil fuel, in particular coal and natural gas, for electricity generation. Coal is the dominant fuel in the power sector (Fig. 1.6) and it will be the largest source of fuel for electricity generation for the future (WEO, 2012). The switch from coal-fired plants to modern Natural Gas Combined Cycle (NGCC) power plants would lead to a significant reduction in CO_2 emissions as a result of the lower carbon content of natural gas compared to, e.g., bituminous coal (117 vs. 205.7 CO_2 emitted per million Btu of energy for natural gas and coal respectively (EIA, 2014)) as well as the higher efficiency of the NGCC power plant (IPCC, 2014). The latter aspect is mainly due to the application of two thermodynamic cycles (Brayton and Hirn cycle) to recover the heat of combustion for electricity production. Nevertheless, the worldwide average higher price of natural gas, compared to the coal's one, as well as the geographic restrictions of lower carbon fuel availability, set the coal as the primary source for electricity generation also in the early future.

In a scenario that highlights how no single technology could provide all of the emissions reductions required, a fundamental role, in the abatement of the CO_2 emissions from fossil fuel power plant, is played by carbon capture and storage (CCS), which is expected to account for the 20% of electricity generation from low-carbon technologies by 2035 (WEO, 2012). The other 80% will be covered by nuclear and renewable technologies.

CCS refers to the concept of capturing CO_2 streams at high pressure from large (>0.1 $MtCO_2$ yr^{-1}) stationary point sources such as fossil fuel power plant, refineries and cement plants, transporting it to a storage location, injecting the compressed CO_2 into a suitable deep geologic structure (IPCC, 2014) to assure its isolation from the atmosphere. CCS technology can be applied to CO_2 streams coming from the combustion of fossil fuel, as in power plants, or from the preparation of fossil fuel, as in natural gas processing; it can also be applied in industrial processes, such as the production of hydrogen, ammonia, cement, iron and steel (IPCC, 2005). Table 1.1 lists the candidate gas streams from an emission source that can be ascribed to a capture process.

Table 1.1 Properties of candidate gas streams that can be ascribed to a capture process (IPCC, 2005)

Source	CO_2 concentration % vol (dry)	Pressure of gas stream MPa[a]	CO_2 partial pressure MPa
CO_2 from fuel combustion			
• Power station flue gas:			
Natural gas fired boilers	7 - 10	0.1	0.007 - 0.010
Gas turbines	3 - 4	0.1	0.003 - 0.004
Oil fired boilers	11 - 13	0.1	0.011 - 0.013
Coal fired boilers	12 - 14	0.1	0.012 - 0.014
IGCC[b]: after combustion	12 - 14	0.1	0.012 - 0.014
• Oil refinery and petrochemical plant fired heaters	8	0.1	0.008
CO_2 from chemical transformations + fuel combustion			
• Blast furnace gas:			
Before combustion[c]	20	0.2 - 0.3	0.040 - 0.060
After combustion	27	0.1	0.027
• Cement kiln off-gas	14 - 33	0.1	0.014 - 0.033
CO_2 from chemical transformations before combustion			
• IGCC: synthesis gas after gasification	8 - 20	2 - 7	0.16 - 1.4

[a] 0.1 MPa = 1 bar.
[b] IGCC: Integrated gasification combined cycle.
[c] Blast furnace gas also contains significant amounts of carbon monoxide that could be converted to CO_2 using the so-called shift reaction.

Since the CO_2 emissions from fossil fuel in the power sector account for more than 80% of the $MtCO_2$ yr^{-1} emitted from industrial activities worldwide (≈ 10000 $MtCO_2$ yr^{-1} over ≈ 13000 $MtCO_2$ yr^{-1}) (IPCC, 2005), the next sections will focus on the different

existing fossil fuel power plants for electricity generation and the role of CCS in this specific sector, which would allow fossil fuels to be used with limited CO_2 emissions.

1.2 Electricity generation from power plants without CCS technologies

The main existing fossil energy power plants can be categorised as follows: Pulverised Coal (PC), Integrated Gasification Combined Cycle (IGCC), and Natural Gas Combined Cycle (NGCC). The first two power systems burn coal differently to generate electricity whereas the latter power system burns natural gas for the same purpose.

In 2007, a full report was released by the National Energy Technology Laboratory (NETL) aimed to highlight the main differences among the above-mentioned power plants in terms of thermal efficiency, plant investment cost, levelised cost of the electricity generated and amount of CO_2 emitted. The main features of the aforementioned analysis are summarised as follows.

The NGCC power plant exhibits the highest thermal efficiency (≈ 50.8% based on HHV) compared to the PC (between 36.8% and 39.1% depending on the operating mode) and the IGCC (between 38.2% and 41.1% depending on the type of gasifier). The remarkable difference between NGCC and PC is due to the application in the NGCC of two thermodynamic cycles (gas and steam cycle) to recover the heat of combustion. Indeed, PC power plants employ just one steam cycle that suffers of limited inlet steam turbine temperature (maximum 560 °C) affecting negatively the thermal efficiency of the plant. On the other hand, IGCC power plants employ both gas and steam cycle, as in the case of NGCC plants, but they experience a reduced thermal efficiency compared to NGCC due to the energy consumption of the Air Separation Unit (ASU) for oxygen production at 95% of purity.

The NGCC also presents the lowest total plant investment cost (≈ 554 $/kW updated at 2007) compared to the PC (≈ 1562 $/kW updated at 2007) and the IGCC (≈ 1841 $/kW updated at 2007). The noticeable difference between the NGCC and the two coal-based power plants can be roughly explained considering that more unit operations have to be employed for the purification of the flue gases coming from the coal combustion due to the substantial amount of unwanted sub-products (mainly SO_2, NO_x, Hg).

The Levelised Cost of the Electricity (*LCOE*) generated is the most important parameter to evaluate different power plant performances since it represents the price at which the electricity generated has to be sold to break even over the lifetime of the plant, as discussed later in the manuscript. Since *LCOE* accounts for the investment cost, operating cost, capital charge factor and more importantly for the fuel cost, its value is subject to the plant location and the fuel market. Nevertheless, it is possible to generally accept that at average fuel price (coal price equal to 1.8 $/MMBtu and natural gas price equal to 6.75 $/MMBtu updated at 2007), the NGCC and PC power plant without CO_2 capture systems exhibit the lowest *LCOE* compared to that from the IGCC system. The scenario changes when a CO_2 capture section is added, as explained later. However, the sensitivity of the *LCOE* to the fuel price for the NGCC is much higher than in the other cases, around 78% in the no CO_2 capture case. The latter feature, in conjunction with the average low price of coal, its abundance and wide geographic distribution (Emun et al., 2010), points out how PC and IGCC systems, regardless their high investment cost, are definitely efficient solutions to generate electricity.

In terms of CO_2 emissions, NGCC emits 55% less CO_2 than PC and 46% less than IGCC per unit of gross output (DOE/NETL, 2007) due to the lower carbon intensity of natural gas relative to coal.

Overall, it is not possible to state which technology is the best to be adopted since fuel price market, accessibility to the raw material, location and national policy play a crucial role in the choice of the most suited technology to be employed.

The next section describes the general concepts behind the three fuel-based power plant technologies without carbon capture section; the impact of CCS in reducing the CO_2 emissions will be discussed consequently.

1.2.1 IGCC power plant

Fig. 1.8 shows the main unit blocks of an IGCC power plant without CO_2 capture section.

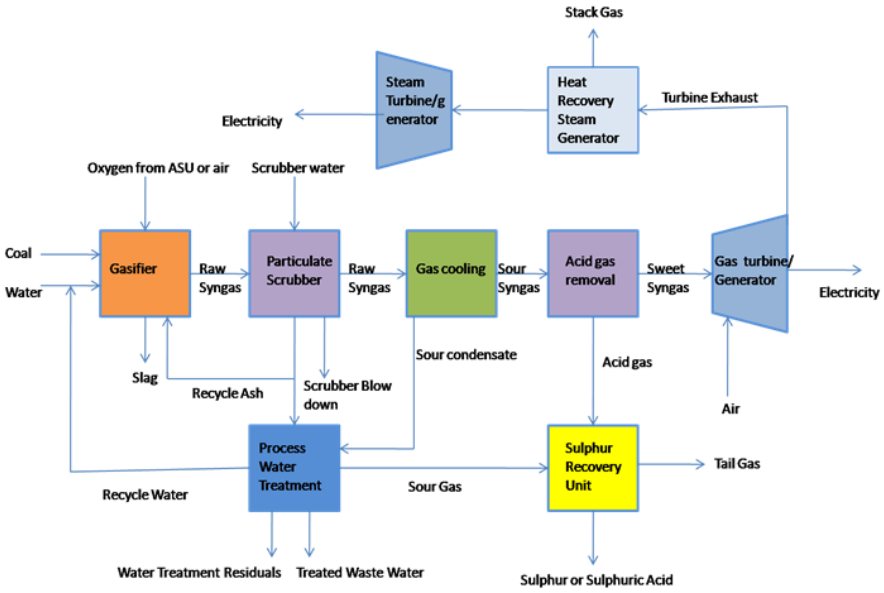

Fig. 1.8 IGCC power plant with no CO_2 capture (www.aerosols.wustl.edu)

Coal, either dry or slurry, is fed under pressure to a gasifier through lock hoppers. In the gasifier, coal turns into syn-gas in the presence of oxygen at 95% purity, steam injection and recycling of a small amount of syn-gas. The operating pressure is between 3 and 7.1 MPa and the temperature in the gasifier rises up to 1340-1400 ˚C to remove the ash as a low viscosity liquid: the coal mineral matter melts to form a slag. The oxygen is supplied by an air separation unit (ASU). The most used gasifiers available on the market are the GEE slurry feed gasifier, the Shell dry feed gasifier and the ConocoPhillips (CoP) gasifier.

If the GEE gasifier is employed, the flue gases are quenched with water; then, the saturated gas is cooled and either condensed water or water-soluble impurities are removed (Davison, 2007). The gas is passed through a COS hydrolysis reactor to convert COS in CO_2 and H_2S via alumina-based catalyst. The product gas is cooled prior to entering the mercury removal process and the acid gas removal (AGR). The AGR unit consists of an absorber and a stripper to regenerate the acid-rich solvent usually by application of heat. The regenerated solution is cooled and recycled to the top of the absorber (DOE/NETL, 2007). Different solvent can be applied: chemical absorption with MEA or MDEA (usually when low or moderate H_2S partial pressure levels are present) and physical absorption with dimethyl ether of polyethylene glycol (Selexol process) or methanol (Rectisol) at high selectivity for H_2S. The removed sulphur compounds are converted to elementary sulphur in a Claus plant. In the latter

case, H_2S reacts with oxygen leading to liquid S through two steps of reaction with SO_2 as intermediate product. The sweet syn-gas is burned, under dilution with nitrogen to lower the flame temperature in the combustor for NO_x emissions control, in a gas turbine to produce electricity. The heat in the hot gases is recovered in a heat recovery steam generator (HRSG) unit to produce additional steam to drive a steam turbine in a combined-cycle power block for additional electricity production.

In the Shell gasifier plant, the flue gases are quenched with recycle flue gases and cooled in a heat recovery boiler; then, they are fed to a dry particulate removal unit, scrubbed with water, reheated, and sent to an COS hydrolysis reactor first and an AGR unit at a later stage (Davison, 2007). The sweet flue gases drive a gas turbine combined cycle.

In terms of thermal efficiency, the Shell IGCC plant has a higher thermal efficiency than the GEE IGCC plant (43.1% vs 38% according to Davison (2007)), mainly because of a higher coal conversion efficiency and the adoption of the heat recovery boiler instead of the water quench to cool the flue gases (Davison, 2007). The CO_2 emissions from an IGCC power plant without CO_2 capture range between 630 and 660 kg/MWh (DOE/NETL, 2007) depending on the gasification technology; 85–90% of CO_2 capture is required to meet the new environmental targets, as explained later on.

1.2.2 PC power plant

A pulverized coal-fired power plant generates thermal energy, and therefore electricity, by burning pulverised coal that is blown into a boiler. Coal is ground to the size of a fine grain, mixed with air and burned. The boiler operates at pressures slightly lower than atmospheric to avoid flue gases losses into the atmosphere. The flue gases exiting the furnace react with ammonia in a selective catalytic reactor to convert NO_x into N_2 and H_2O to target the NO_x emissions constraints. The flue gases pass through a filter for particulate removal and then to the flue gas desulfurization (FGD) unit for SO_2 removal. In the latter unit, flue gases react with limestone slurry, via chemical absorption, to produce gypsum and clean gas (mainly CO_2, N_2, H_2O), ready to be discharged to the atmosphere. The heat from the coal combustion drives the production of steam for electricity generation. There are two different steam generator operating modes: subcritical and supercritical.

In the supercritical mode, the steam conditions are above the critical one (usually 24.1 MPa/593°C/593˚C, (DOE/NETL, 2007)). Having higher inlet steam turbine pressure and temperature, the supercritical mode guarantees higher thermal efficiency than the subcritical one; furthermore, the immediate change in phase from liquid to steam under supercritical conditions results in less fuel use, to target the same net power output, and thus less CO_2 emissions in the "no CO_2 capture" scenario.

The choice of subcritical cycles rather than supercritical ones has been mainly due to relatively low fuel costs. Indeed, since the fuel price does not represent a large fraction of total LCOE, the lower thermal efficiency of the subcritical plants is still compensated by the lower total capital investment. At higher fuel cost the subcritical plants cannot compete with the supercritical solution since the latter offers more favourable *LCOE* as well as lower CO_2 emissions (due to the higher thermal efficiency and thus the lower amount of fuel burned). The CO_2 emissions are around 807 kg/MWh for the subcritical case and 762 kg/MWh for the supercritical case in a no CO_2 capture scenario (DOE/NETL, 2007).

1.2.3 NGCC power plant

In a NGCC power plant, natural gas is burned with pressurised air in a combustion chamber. The flue gas exits at temperature higher than 1200 °C (sometimes 1400 ˚C) and it expands in a gas turbine for electricity generation. The extra heat from the hot gas is recovered in a Heat Recovery Steam Generator (HRSG) to generate the steam to drive the steam cycle. The flue gas exiting the HRSG passes to the plant stack. The exit gas is manly CO_2, N_2 and un-reacted O_2. The NO_x emissions are reduced using a SCR reactor inside the HRSG to convert ammonia and NO_x into N_2 and H_2O.

As mentioned in Section 1.2, the CO_2 emissions (355 kg/MWh according to DOE/NETL, (2007)), are lower than those coming from coal power plants due to the lower carbon intensity of gas relative to coal, the higher heat content of natural gas and the higher thermal efficiency of the NGCC compared to coal power plants (DOE/NETL, 2007).

1.3 Carbon capture systems

CCS involves technologies aimed to collect, concentrate, transport and store CO_2 streams. Those processes are able to reduce CO_2 emissions, mainly from stationary sources, leading to a remarkable contribution to the abatement of the greenhouse gas pollutions. Capturing CO_2 directly from small and mobile sources in the transportation and residential building sectors is foreseen to be more expensive and difficult than from large point sources. The opportunity to capture CO_2 from ambient air (Lackner, 2003) is at an early stage of research because the CO_2 concentration in air is about 400 ppm, meaning much lower than in flue gas.

Focusing on the large exhaust stacks from power plants, CCS technologies could reduce CO_2 emissions by approximately 80-90% kWh^{-1} (85-95% capture efficiency) compared to plants without CCS (IPCC, 2005). Obviously, the reduction of the CO_2 emissions has a cost. Indeed, the energy required to capture CO_2 streams lowers the overall thermal efficiency of the power plants, leading to an increase in fuel requirement to target the same electricity production as in the case without CO_2 capture process applied. For this reason, the minimisation of the CO_2 energy losses together with the technological improvement to augment the efficiency of the new power plants represents a "must" to be followed.

Two main parameters, such as the *LCOE* generated and the cost of CO_2 avoided, (explained later), describe the impact of CCS technologies on existing or new power plant and they are useful for comparing various CO_2 capture strategies.

There are three basic concepts for capturing CO_2 from use of fossil fuels and/or biomass power plant (Fig. 1.9):

- Post-combustion carbon capture
- Pre-combustion carbon capture
- Oxy-fuel combustion carbon capture

Other industrial processes (Fig. 1.9), such as purification of natural gas and production of hydrogen-containing syngas for the synthesis of ammonia, synthetic liquid fuel and alcohols as well as steel and cement production, and fermentation processes for drink and food production, apply one of these three capture concepts (IPCC, 2005).

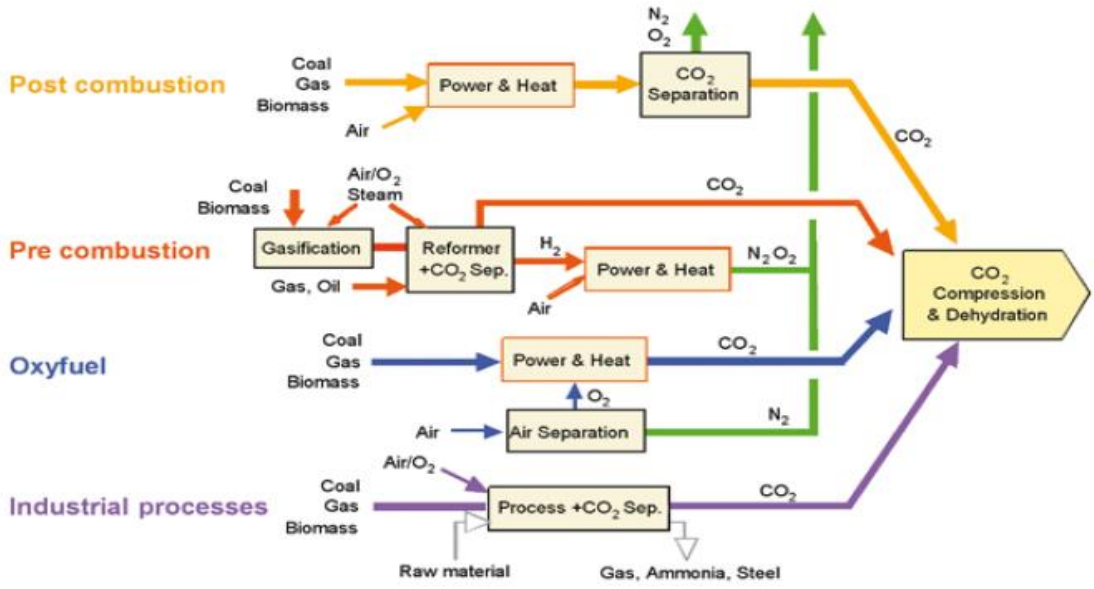

Fig. 1.9 Overview of carbon capture systems (IPCC, 2005)

1.3.1 Post-combustion carbon capture

Post-combustion carbon capture processes refer to systems that separate CO_2 streams from flue gases produced by combustion of biomass and fossil fuel with air. The flue gases, before being released to the atmosphere, are processed by a unit operation, which separates the CO_2 usually by means of contact with chemical liquid solvent such as monoethanolamine (MEA). Flue gases are usually at atmospheric pressure with a CO_2 content ranging from 3% by volume for NGCC power plant to roughly 15% by volume for PC power plant. Thus, the resulting low CO_2 partial pressure makes the utilisation of a chemical absorption unit more efficient in capturing CO_2 and economically more favourable than a physical absorption unit. The CO_2 streams, after being captured, are compressed for either storage or their use in Enhanced Oil Recovery (EOR) systems.

1.3.2 Pre-combustion carbon capture

Pre-combustion carbon capture processes involve the reaction of primary fuel with air or oxygen and steam to produce mainly a mixture of CO and H_2 (syngas). If the primary fuel reacts just with steam the process is called “steam reforming”; if the primary fuel reacts with oxygen the process is called either “partial oxidation” in the case of liquid/gaseous fuels or “gasification” in the case of solid fuels. Existing technologies, employing a pre-combustion carbon capture approach, are: steam methane reforming, partial oxidation of gas and light hydrocarbons, auto-thermal reforming of gas, and gasification of biomass or coal. The latter case refers to IGCC power plants where coal

is gasified in the presence of oxygen at high purity with a syngas stream as product (see Section 1.2.1). Subsequently, the CO, from the syngas mixture, is converted to CO_2 in a catalytic reactor, called "shift reactor", which produces, in parallel, additional hydrogen. The resulting CO_2/H_2 mixture at high total pressure (typically 2-7 MPa) and high CO_2 content (typically 15%-60% by volume) (IPCC, 2005) can be processed usually by either a chemical or a physical absorption unit. After capturing the CO_2, the H_2 stream is combusted to generate power.

1.3.3 Oxy-fuel combustion carbon capture

Oxy-fuel combustion carbon capture processes use oxygen instead of air for combustion of the primary fuel, resulting in a flue gas that is mainly H_2O and CO_2. Oxygen is conventionally produced by a cryogenic Air Separation Unit (ASU) since it is economically considered the best solution for large applications (Wilkinson et al., 2003), although adsorption using multi-bed pressure swing units or polymeric membranes can be also employed. To moderate the flame temperature in the combustion chamber, CO_2 and/or H_2O is recycled to the combustor (Takami et al., 2009). The H_2O stream can be then removed by stages of inter-cooling compression. Thus, the resulting nearly pure CO_2 stream is ready to be transported in a dense supercritical phase and stored.

1.4 Carbon capture technologies

The aforementioned carbon capture approaches apply many of the known technologies for gas separation integrated into the basic methods for CO_2 capture purposes. Fig. 1.10 exhibits the main separation processes applicable for CO_2 capture. Those processes can be gathered into three main separation concepts: separation with solvents/sorbents (that includes chemical/physical absorption and adsorption operations), separation with membranes and cryogenic distillation.

Depending on the carbon capture system involved, and thus on the properties of the flue gas mixture to be processed, the most economically favourable separation process is employed. Therefore, the CO_2 capture systems shown in Fig. 1.9 can be cross-referenced with the separation options of Fig. 1.10 resulting in a capture toolbox. Table 1.2 summarises the leading commercial options. An insight of alternative separation options is given later. More details on the emerging carbon capture options are described in the IPCC report (2005).

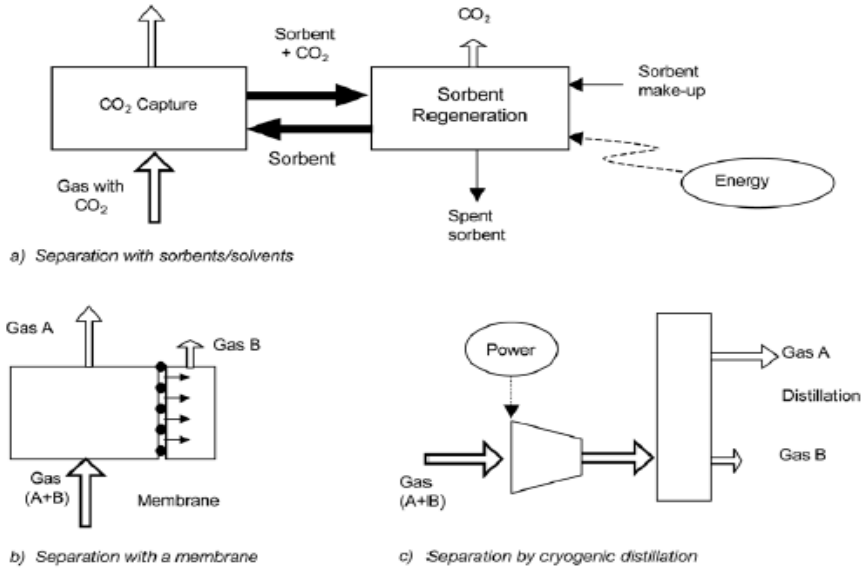

Fig. 1.10 General schemes of the main separation methods applicable for CO_2 capture (IPCC, 2005)

Table 1.2 Carbon capture toolbox for leading commercial options

	Post combustion capture	**Pre-combustion capture**	**Oxy-fuel combustion capture**
	CO_2/N_2	CO_2/H_2	O_2/N_2
Leading capture technology	Chemical absorption	Physical absorption	Cryogenic distillation

1.4.1 Chemical absorption

Chemical absorption processes represent the preferred solution for post-combustion CO_2 capture (Hendriks, 1994; Riemer and Ormerod, 1995) since they guarantee high CO_2 capture efficiency as well as selectivity, and above all they have reached a mature commercial stage of operation. Chemical absorption processes integrated in a post-combustion capture configuration employ an aqueous alkaline solvent, usually MEA, to chemically react with an acid or sour gas in a fashion shown in Fig. 1.11.

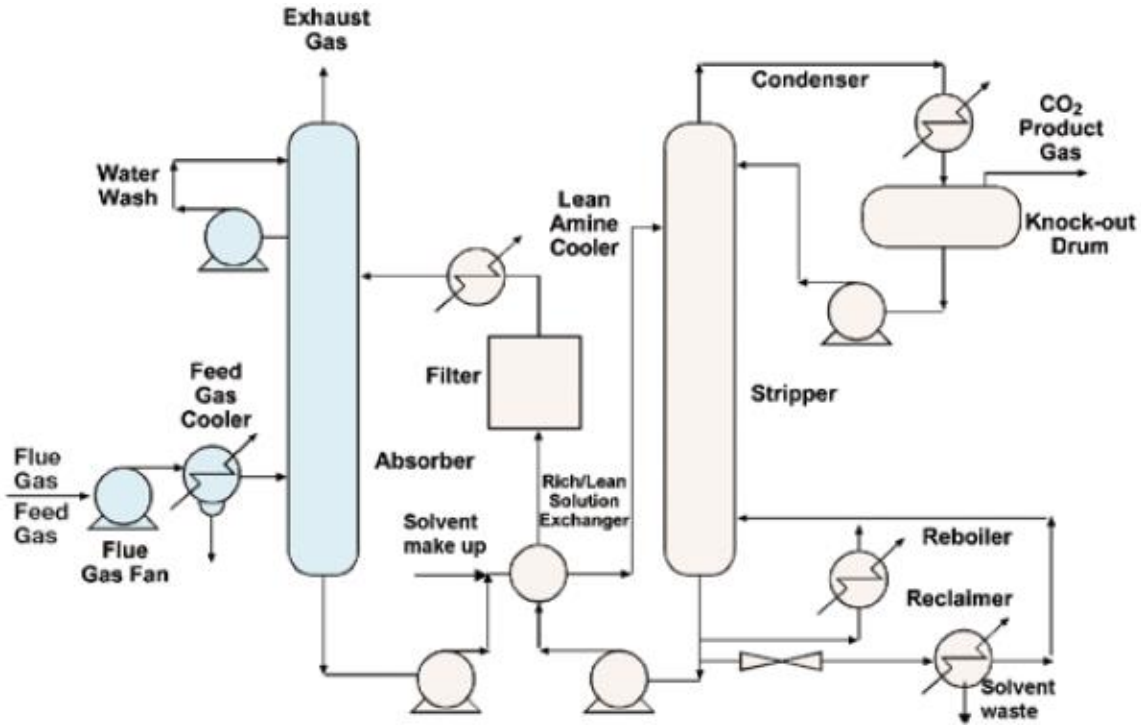

Fig. 1.11 Chemical absorption system for CO_2 recovery from the flue gas (IPCC, 2005)

In a PC power plant either under subcritical or supercritical condition the CO_2 capture unit is placed after the flue gas desulfurization (FGD) unit, before the stack gas is discharged into the atmosphere. In a NGCC power plant the CO_2 capture unit is placed after the HRSG, before the plant stack.

In both power plants, the flue gas, entering the CO_2 capture unit, is cooled and brought into contact with the solvent in the absorption column. CO_2 reacts with the solvent at temperatures between 40 and 60 ˚C. Before leaving the absorber, the flue gas is washed with water to balance water in the system and to remove any solvent vapour or solvent droplets carried over. The chemical reaction occurring reduces greatly the CO_2 concentration in the exit gas down to low values that depend also on the height of the absorption column. The CO_2-rich solution is then pumped to the top of a stripper via a heat exchanger to be regenerated. The stripper operates at higher temperatures than the absorber (typically 100-140 ˚C) and at pressures slightly higher than the atmospheric one. Heat is supplied to the reboiler to sustain the regeneration conditions meaning the removal of the chemically bound CO_2 and the steam production which works as a stripping gas. Then, steam is recovered in the condenser while liberating the CO_2 and heating the down-coming solution. The CO_2-lean solution leaves the reboiler and enters the cross heat exchanger where it is cooled down to the absorber temperature level.

The key features influencing the technical and economic operation of a CO_2 chemical absorption system are: the flue gas flow rate, the CO_2 content in the flue gas and its removal, the solvent flow rate, the energy and cooling requirements. A key factor of post-combustion CO_2 capture processes based on absorption is the high energy requirement to regenerate the solvent, to produce steam used for stripping and finally to compress the CO_2 for transport and storage. Thus, modifications of the low pressure section of the steam cycle are needed to integrate the absorption process with an existing power plant, since a fraction of steam will be extracted upstream of the low pressure steam turbine for the reboiler duty and hence will be not be usable for power production (Mimura et al., 1997; Nsakala et al., 2001). For a PC power plant, low pressure steam (typically between 0.9-1.2 MPa) will be extracted before the last expansion stage of the steam turbine whereas for a NGCC power plant, low pressure steam will be extracted from the last stage in the HRSG. The energy penalties due to the reboiler duty are around 3.52 MJ_{th}/kg_{CO2} at 90% CO_2 capture if the aforementioned conventional absorption unit is applied (DOE, 2007).

To reduce the energy consumption for solvent regeneration, different novel solvents have been investigated (Chakma, 1995; Mimura et al., 1999; Zheng et al., 2003) as well as new process designs have been proposed (Leites et al., 2003; Ahn et al., 2013). For instance, Ahn et al. (2013) proposed multiple modifications of the amine process integrated in a sub-critical PC power plant that lead to a decrease of the duty at the reboiler up to 2.22 MJ_{th}/kg_{CO2} due to a 37% reduction of the steam fraction required at the reboiler.

Chemical absorption can be also applied in a pre-combustion system to remove CO_2 from syngas at partial pressure below 1.5 MPa (Astarita et al., 1983). The chemical solvent removes CO_2 from the shifted syngas via a reversible chemical reaction. MEA, MDEA and Sulfinol are the chemical solvents widely used for the removal of CO_2 from shifted syngas in pre-combustion carbon capture processes (IPCC, 2005).

1.4.2 Physical absorption

There are over 30 Acid Gas Removal (AGR) processes based on physical absorption in commercial use throughout the oil, chemical and natural gas industries (DOE/NETL, 2007). Physical solvent processes are mostly suitable to gas streams at high CO_2 partial pressure and/or a high total pressure. They are often used to remove the CO_2 from the

CO_2/H_2 mixture coming from the shift reaction in pre-combustion CO_2 capture processes. Table 1.3 exhibits the main physical solvent processes.

Table 1.3 Common solvent used in pre-combustion capture processes (IPCC, 2005)

Solvent name	Type	Chemical name	Vendors
Rectisol	Physical	Methanol	Lurgi and Linde, Germany Lotepro Corporation, USA
Purisol	Physical	N-methyl-2-pyrolidone (NMP)	Lurgi, Germany
Selexol	Physical	Dimethyl ethers of polyethylene glycol (DMPEG)	Union Carbide, USA
Benfield	Chemical	Potassium carbonate	UOP
MEA	Chemical	Monoethanolamine	Various
MDEA	Chemical	Methyldiethylamine	BASF and others
Sulfinol	Chemical	Tetrahydrothiophene 1,1-dioxide (Sulfolane), an alkaloamine and water	Shell

Physical solvent absorbers operate at lower temperatures than in the case of chemical solvents. The absorption step occurs at high pressure and nearly ambient temperature whereas the regeneration of the solvent occurs by release of pressure at which CO_2 evolves from the solvent; deeper regeneration needs the solvent to be stripped by heating. This process has low energy requirements since the energy for pressurising the liquid solvent is the only needed. It was estimated that physical solvents become increasingly economical and preferable to amine-based solvents, as the partial pressure of the gas stream to be treated increases (DOE/NETL, 2007).

The use of high sulphur fossil fuels in a pre-combustion capture process results in syngas with high content of H_2S to be removed. CO_2 and H_2S can be removed together if the transport and storage of a CO_2/H_2S mixture is possible. Sulphinol solvent was developed to achieve higher solubility of acidic components compared to amine solvents. Sulphinol is composed of diisopropanolamine (30-45%) or methyl diethanolamine (MDEA), sulfolane (tetrahydrothiophene dioxide) (40-60%), and water (5-15%). Its acid gas loading is significantly higher than that of pure chemical solvents and the energy penalty for its regeneration is lower. It has the advantage over purely physical solvents that strict product specifications can be met more easily. The Sulphinol process is widely applied for selective absorption of H_2S and carbonyl sulphide (COS), while co-absorbing only part of the carbon dioxide (CO_2).

If pure CO_2 is needed, then a selective process using physical solvents, often Rectisol or Selexol, is required. The CO_2 removal via physical absorption in IGCC power plants

requires some modifications of the plant configuration shown in Fig. 1.8. Indeed, in the case with CO_2 capture, the gasifier product must be turned to hydrogen-rich syngas. The CO is converted to H_2 and CO_2 through a reaction with water over a bed of catalyst ("water shift reaction"). The catalyst also serves to hydrolyse COS thus removing the need for a separate COS hydrolyse reactor. After the mercury removal unit, the untreated gas stream enters a two stages absorption unit (typically two-stage Selexol process). The raw syngas enters the first of two absorbers where H_2S is preferentially removed using CO_2-laden solvent from the CO_2 absorber. The gas exits the H_2S absorber and it is sent to the CO_2 absorber where CO_2 is removed using first flash regenerated, chilled solvent followed by thermally regenerated solvent added at the top of the absorber. The treated gas, exiting the CO_2 absorber, is sent to the combustion turbine. The CO_2-laden solvent, exiting the CO_2 absorber, is split into three streams: a portion is sent to the H_2S absorber, a portion is sent to a re-absorber and the rest is sent to a series of flash drums for regeneration. The pure CO_2 stream is obtained from the three flash drums, and after flash regeneration the semi-lean solvent is chilled and returned to the CO_2 absorber. The rich solvent exiting the H_2S absorber must be stripped in a column with reboiler to remove the high H_2S content gas. The acid gas from the stripper is sent to the Claus plant for liquid sulphur production. The lean solvent exiting the stripper is chilled before returning to the top of the CO_2 absorber.

Overall, the three main product streams from the physical absorption unit are: clean syngas to the combustion section, the acid gas feed to the Claus plant and the CO_2-rich stream to compression, transport and storage.

1.4.3 Adsorption

Adsorption process is an emerging technology in the field of post-combustion carbon capture. Activated carbons or molecular sieves are employed to adsorb CO_2; desorption step occurs by pressure swing operation (PSA) or temperature swing operation (TSA). PSA operations are preferred (Ishibashi et al., 1999; Yokoyama, 2003) since TSA operations require long cycle times to heat up the solid bed during sorbent regeneration. The main feature of PSA is the application of a decrease in pressure and/or the purge by a gas to clean the bed. In addition to the adsorption and desorption steps, a single PSA cycle includes other steps, such as co- and counter-current pressurisation, pressure equalisation and co- and counter-current depressurisation.

Adsorption technology has not yet reached a commercial stage for CO_2 recovery from flue gas although specific energy consumptions in the range 1.6-2 MJ_{th}/kg_{CO2} make this technology a good potential alternative to the amine process. A drawback of all adsorptive methods is the need to treat the gaseous feed before entering the adsorber; this aspect limits the attractiveness of PSA and TSA compared to amine processes. The development of a new generation of materials that would efficiently adsorb CO_2 will improve the competitiveness of adsorptive separation in a flue gas application (IPCC, 2005).

PSA could be also applied to pre-combustion systems for the purification of syngas especially when high purity H_2 is required. However, the process does not selectively separate CO_2 from other waste gases and so further upgrading to obtain a pure CO_2 stream to be stored is needed. Simultaneous H_2 and CO_2 separation is possible by using an additional PSA unit to remove the CO_2 before the H_2 separation step, such as the Air Products Gemini Process (Sircar, 1979).

1.4.4 Membranes

Membrane processes are applied commercially for CO_2 removal from natural gas at high pressure and at high CO_2 concentration (IPCC, 2005). In a post-combustion carbon capture system, the low CO_2 partial pressure difference provides a low driving force for gas separation. Thus, the CO_2 removal employing polymeric membranes leads to either higher reduction in the plant thermal efficiency or lower maximum percentage of CO_2 removed compared to amine process (Feron, 1994; Van der Sluijs et al., 1992; Herzog et al., 1991).

To make the membrane separation process attractive, the membrane selectivity must be improved. The selectivity of the membrane to different gases depends on the properties of the material, although the gas flow through the membrane is usually driven by the pressure difference across the membrane. Recently, hybrid membrane – absorbent/solvent system are under investigation. These systems are being developed for flue gas CO_2 recovery. Membrane/solvent systems use membranes to supply high surface area to volume ratio for mass exchange between a solvent and a gas stream. This results in a membrane contactor system where the membrane acts as a gas permeable barrier between a liquid and a gaseous phase. In the case of porous membranes, gaseous components diffuse through the pores and are absorbed by the liquid; in the case of non-

porous membranes, they dissolve in the membrane and diffuse via the membrane. The solvent mainly determines the selectivity of the partition. Absorption in the liquid phase is controlled either by physical partition or by a chemical reaction. Recent development works applicable to both CO_2/H_2 and CO_2/N_2 separations have focused on membranes containing amines (Teramoto et al., 1996), potassium carbonate polymer gel (Okabe et al., 2003) and dendrimer (Kovvali and Sirkan, 2001).

For pre-combustion carbon capture application, membrane reactors for CO_2 capture have been emerged (IPCC, 2005). An IGCC system can be configured with a water gas shift membrane reactor (WGSMR) instead of a physical absorption unit. This unit can be followed by an oxygen transport membrane (OTM) to utilise the remaining combustible in the gas coming from the retentate side of WGSMR (Rezvani et al., 2009). The WGSMR combines reaction and separation of H_2 in a single stage and CO_2 is produced without the need for additional separation unit. The syngas reacts in the retentate side of the perm-selective membrane (typical membrane materials: palladium/silver alloy, silica, carbon, alumina) via a catalytic reaction with iron and chromium oxides. A CO_2-rich stream at relative high pressure is produced with additional H_2 production. The generated H_2 permeates through the hydrogen selective membrane and a steam flow from the HRSG is applied to sweep the H_2 from the permeate side to the gas turbine. The CO_2-rich stream contains small fraction of combustibles that can be combusted in an oxygen selective membrane composed of ionic and mixed-conducting ceramic oxides. CO_2 and H_2O are produced from the reaction of the combustibles with oxygen (Rezvani et al., 2009). The CO_2/H_2O mixture is cooled to separate H_2O and, then, CO_2 is compressed for the transport through the pipeline.

Membrane reactors could achieve more than 90% CO_2 recovery (Rezvani et al., 2009). The commercialisation of WGSMR for CO_2 capture relies strictly on the properties of the materials used to fabricate the membranes. High perm-selectivity, chemical and thermal stability, mechanical strength to work at high temperature and pressure as well as low costs are the requirements to make the membrane technology attractive for CO_2 capture purposes.

1.4.5 Cryogenic distillation

Cryogenic distillation is currently applied commercially on large scale to air separation. Oxygen is separated from air and used in a range of CO_2 capture system, such as oxy-fuel combustion and pre-combustion capture. The gas stream is made liquid after a series of compression, cooling and expansion steps. This system can be also used to separate CO_2 from other components of a gas stream. In particular, it is the applied technology in food and beverage industries since a very high CO_2 purity (>99.9%) is required (ISBT, 2006).

1.4.6 Calcium Looping (CaL)

Calcium looping (CaL) represents an alternative to the chemical absorption solution with MEA for CO_2 capture in a post-combustion power plant (Shimizu et al., 1999). The system is composed of two fluidised bed reactors, i.e. carbonator and calciner, with solid sorbent circulating between them. The flue gas from the boiler at high CO_2 content (3-30% by volume) enters the carbonator where a reaction with CaO occurs. The exothermic reaction occurs at 650-700 °C producing $CaCO_3$ and exhausted gas at low CO_2 content. $CaCO_3$ is recycled to the calciner to regenerate CaO and release a pure CO_2 stream. The latter reaction is endothermic and it occurs at 900-950 °C. The carbonator cannot supply the required heat at the calciner since it works at lower temperature. Thus, the heat at the calciner is supplied directly by in-situ oxy-fired combustion of fuel (e.g. coal) with oxygen coming from the ASU. The CO_2 outlet stream from the calciner is suitable for final purification and compression.

The high-grade heat in the carbonator at relative high temperature (> 600 °C) can be recovered from the CO_2-free exhausted gas and from the heat of reaction via steam cycles. The latter feature represents the main advantage of this technology compared to the MEA solution. Indeed, the waste heat from the MEA unit is at temperature around 150 °C and consequently it can generate much less extra electricity through a steam cycle. Dean et al. (2011) reported 6-8% of energy penalties for CO_2 capture in a post-combustion power plant with CaL solution applied. The application of the MEA technology would lead to 9-12% of energy penalties (Dean et al., 2011).

The drawback of the CaL technology concerns the fast deactivation of the sorbent during the reactive cycles and thus, spent CaO needs to be replaced often with fresh limestone (Dean et al., 2011).

However, the spent CaO can be used as a raw material in the cement industry to reduce the CO_2 emissions from cement plants resulting from the calcination of limestone in the pre-calciner and the kiln (Dean et al., 2011; Ozcan et al., 2013).

1.4.7 Chemical looping

Similar to CaL technology, the Chemical looping employs a system of reactors with solid material circulating between them. Chemical looping is a new technology involving combustion of carbonaceous fuel such as coal-derived syngas or natural gas via heterogeneous chemical reaction with an oxygen carrier exchanged between two fluidised beds. An oxidation reaction between air and reduced metal particles takes place in the air reactor; the oxidised particles are conveyed in a fuel reactor to combust the fuel. CO_2 and H_2O, as products of the reduction reaction, are separated by condensation allowing the free-water CO_2 flux to be transported and stored. The fact that the combustion takes place in two reactors is due to the CO_2 not being diluted with N_2, but almost pure after separation from water, without the need for any extra demand and costly additional equipment for CO_2 separation (IPCC, 2007). The technology can be either integrated in an IGCC system for CO_2 capture from a syngas stream or applied as a primary reactor for firing natural gas or solid fuel. The Chemical looping technology will be discussed in detail in Section 1.6.

1.5 Cost of CO_2 capture

Power plants including CO_2 capture systems require significant amounts of energy for their operation leading to a reduction of their net plant efficiency. The latter, together with the extra costs from the installation of the CO_2 capture units, leads to an increase in the cost of the electricity generated. Published estimates of CO_2 capture costs vary widely, due to different assumptions regarding technical factors related to plant design and operation (e.g. fuel properties, net efficiency, plant size and load factor), as well as financial and economic factors such as interest rates, plant lifetime and fuel cost (IPCC, 2005, 2014). A number of works have addressed this issue and classified the main sources of cost difference and variability (Simbeck, 1999; Herzog, 1999; Rubin and Rao, 2003). Thus, the generally-accepted measures of CO_2 capture costs, suitable for

evaluating and comparing different plant arrangements, are: *LCOE* generated, the cost of CO_2 avoided and the cost of CO_2 captured or removed.

By definition, the *LCOE*, expressed in \$/kWh, represents the price at which electricity must be generated from a specific source to break even over the lifetime of the project. It is defined as follows (see also Chapter 5):

$$LCOE = \frac{TCI+\sum_{j=1}^{N}[(C_{oj}+d_j)(1+DCFR)^{-j}(1-\varphi)]-\sum_{j=1}^{N}[d_j(1+DCFR)^{-j}]}{\sum_{j=1}^{N}[P_{rj}(1+DCFR)^{-j}(1-\varphi)]} \quad (1.1)$$

where *TCI* is the total capital investment, C_{oj} is the annual operating cost, d_j is the annual depreciation, *DCFR* is the discounted cash flow rate of return, φ is the income tax rate, P_{rj} is the annual product rate expressed in kWh/year and *N* is the plant lifetime. Simplified formulae for *LCOE* not counting for the tax rate and the annual depreciation can be applied. Overall, the *LCOE* is one of the most important parameters to evaluate the advantages of applying a specific CO_2 capture technology to a reference system. Indeed, it is crucial to minimise the obvious increase in the electricity cost compared to a plant reference case without CO_2 capture, which produces the same amount of primary product (electricity). *LCOE* accounts for most of the main features involved in an economic evaluation of a project: total capital cost (which represents the total expenditure required to design, purchase and install the system of interest), fixed and variables costs associated with plant operation and maintenance, effective rate of interest used to amortise the capital cost, unit fuel cost, capacity factor of the plant (meaning the total hours of plant production per year), lifetime of the plant. Usually the *LCOE* includes the cost of compressing CO_2 (typically to about 11-14 MPa) but it does not include CO_2 transport and storage costs.

Another widely used measure for the cost of CO_2 capture is the *cost of CO_2 avoided*, expressed in \$/tCO_2 and defined as follows (IPCC, 2005):

$$Cost\ of\ CO_2\ avoided = \frac{[LCOE_{capture}-LCOE_{ref}]}{[(CO_2\ kWh^{-1})_{ref}-(CO_2\ kWh^{-1})_{capture}]} \quad (1.2)$$

The cost of CO_2 avoided represents the average cost of reducing atmospheric CO_2 emissions by one unit while providing the same amount of electricity as a reference

plant without carbon capture unit applied (IPCC, 2005). CO_2 kWh^{-1} is the CO_2 mass emission rate per kWh generated based on the net plant capacity for each case. The subscripts "capture" and "ref" refer to the plant with and without carbon capture unit, respectively.

Furthermore, the cost of CO_2 captured is defined as follows (IPCC, 2005):

$$Cost\ of\ CO_2\ captured = \frac{[LCOE_{capture} - LCOE_{ref}]}{(CO_2\ kWh^{-1})_{capture}} \quad (1.3)$$

The cost of CO_2 capture represents the economic viability of a CO_2 capture system given a market price for CO_2 as an industrial commodity (IPCC, 2005).

As mentioned in Section 1.2, the NETL (2007) published a report in which the three main power plant concepts PC, IGCC and NGCC were compared with and without CO_2 capture section using the leading commercial options for carbon capture: physical absorption unit with Selexol solvent for IGCC power plants, chemical absorption unit with amine solvent for PC and NGCC power plants. Figs. 1.12 - 1.13 exhibit the trend of net thermal efficiency and *LCOE* for the different plant cases under specific assumptions (DOE/NETL, 2007).

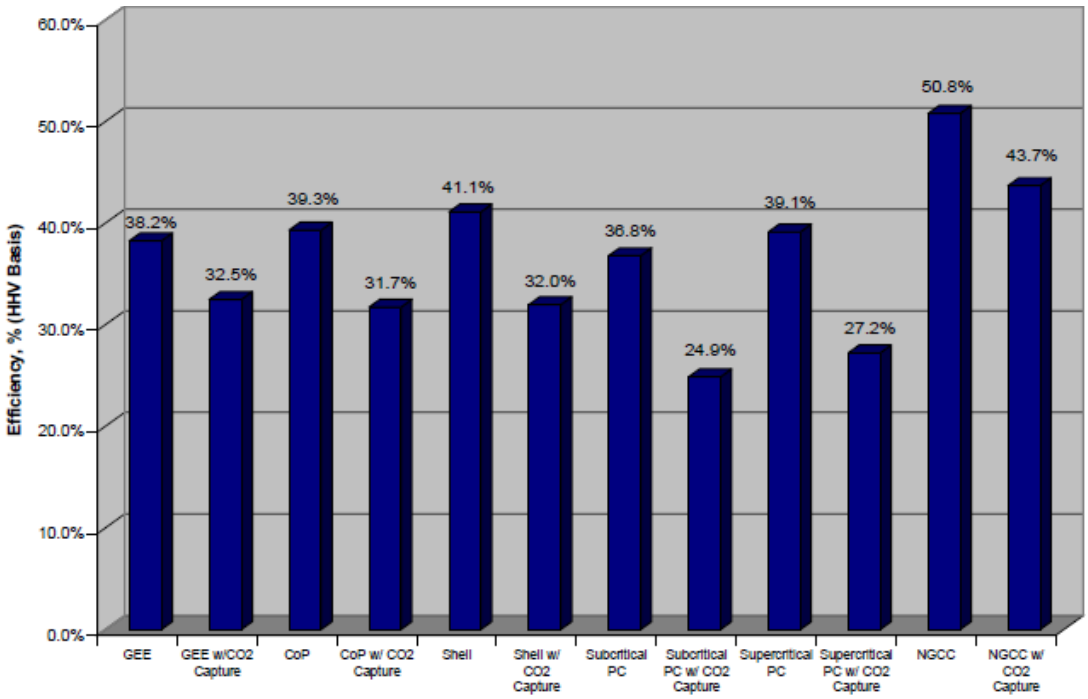

Fig. 1.12 Net plant efficiency based on HHV values (DOE/NETL, 2007)

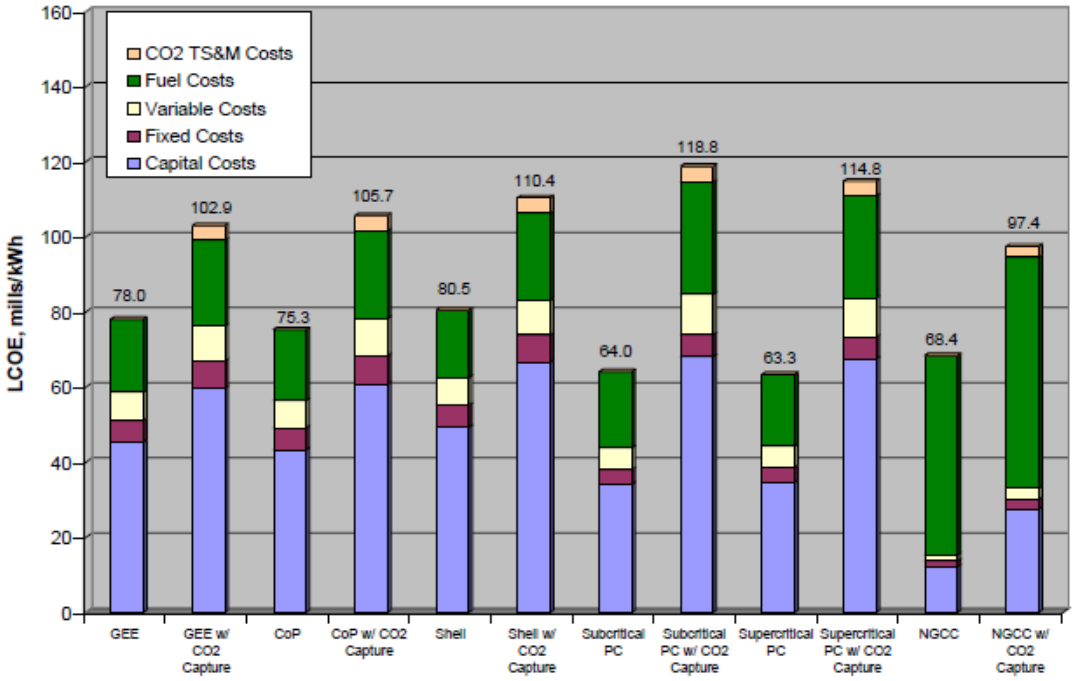

Fig. 1.13 LCOE by cost component (DOE/NETL, 2007)

Although the results from the NETL analysis are not updated, it is possible to make general considerations that are valid regardless of the year performed and the assumptions taken into account. NGCC power plant has the highest energy efficiency either with or without CO_2 capture included. The decrease in efficiency for NGCC plants with post-combustion capture via an amine process is around 7% (Fig. 1.12). This result has been confirmed by several additional contributions (Rubin et al., 2007; Davison, 2007; Wolf et al., 2005; Mores et al., 2014). The cost of electricity for NGCC with CO_2 capture tends to be lower than in the case of IGCC and PC power plants since the total capital requirement is always lower due to the lower complexity of the plant and, thus, the less units required (IPCC, 2005; DOE/NETL, 2007; Rubin et al., 2007; Davison et al., 2007).

However, since the coal price is lower than natural gas price, in the case of high natural gas price, NGCC plants might have higher electricity production costs than coal-based plants, either with or without capture. This aspect points out how the best economic solution between a coal-fired power plant and a natural gas-fired power plant depends significantly on the market price of the feedstock.

IGCC and PC power plants can be compared on the same feedstock basis. IGCC without capture exhibits higher thermal efficiency than PC subcritical power plants

regardless the gasifier applied (GEE, CoP or Shell gasifier). PC based on supercritical steam cycle without CO_2 capture exhibit efficiency comparable with the IGCC configurations (DOE/NETL, 2007; Rubin et al., 2007; Davison, 2007). The addition of the amine CO_2 capture unit to the PC power plant leads to a greater reduction in efficiency than the Selexol CO_2 capture unit in the IGCC. This aspect is mainly due to the more energy requirements for the solvent regeneration in a chemical absorption process than a physical one. So, IGCC power plant with CO_2 capture tends to be more efficient than the PC configuration (IPCC, 2005; DOE/NETL, 2007; Rubin et al., 2007).

With respect to the *LCOE*, the PC cases show lower electricity cost than IGCC cases without CO_2 capture and higher with CO_2 capture. The *LCOE* trend follows the total plant capital cost trend that is much more affected by the addition of a chemical absorption CO_2 capture system in PC power plants than a physical absorption CO_2 capture system in IGCC power plants (DOE/NETL, 2007; Rubin et al., 2007; Hoffmann and Szklo, 2011).

The CO_2 emissions from IGCC power plants are less than PC power plants either without or with CO_2 capture at the same CO_2 capture efficiency (usually chosen equal to 90%). The cost of CO_2 avoided is less for IGCC than PC power plants since the IGCC CO_2 removal is reached prior to combustion and at elevated pressure using physical absorption (IPCC, 2005; DOE/NETL, 2007; Rubin et al., 2007).

The above considerations are based on the existing commercial technologies applied to pre- and post- combustion. Emerging technologies for CO_2 capture, such as IGCC with membrane CO_2 capture separation unit (Rezvani et al., 2009) or oxy-combustion PC configurations (Kanniche et al., 2010), might change the economic and environmental comparison among IGCC, PC and NGCC power plants, depending on their influence in the minimisation of the carbon capture energy penalties, increase in the power plant thermal efficiency and therefore reduction in the cost of electricity.

1.6 Chemical Looping Combustion (CLC) technology

Among the well-known state-of-art technologies for CO_2 capture, Chemical Looping Combustion (CLC) stands out for its potential to capture efficiently the CO_2 from a power plant. Being aware that every CO_2 capture technology has strengths and

weaknesses depending either on its nature and field of applicability or its degree of development, CLC exhibits actual potential advantages compared to other CO_2 capture systems.

Traditional separation units involve large energy loss and, thus, additional costs for the electricity generated. Indeed, major drawbacks with MEA and other solvents are the equipment corrosion in presence of O_2 and the energy intensive solvent regeneration (Abu-Zhara et al., 2007; Singh et al., 2003). Furthermore, the presence of common flue gas contaminants such as NO_x, SO_x have a negative impact on solvent-based process performance. For instance, SO_2 and NO_x react with MEA to form a stable (no-regenerable) salt, which reduces the absorption capacity of the solvent leading to high costly fresh solvent make-up (Rao and Rubin, 2002). Adsorption processes based on the selective adsorption of CO_2 on a solid adsorbent require also energy intensive adsorbent regeneration. Membrane separations have the disadvantages of low gas throughputs requiring multistage operations or stream recycling (Herzog et al., 1999). ASU units for air separation involve additional energy penalties.

For the above reasons, current efforts cover not only improvements to the state-of-the-art technologies, but also development and commercialisation of several innovative concepts, such as CLC (Fig. 1.14).

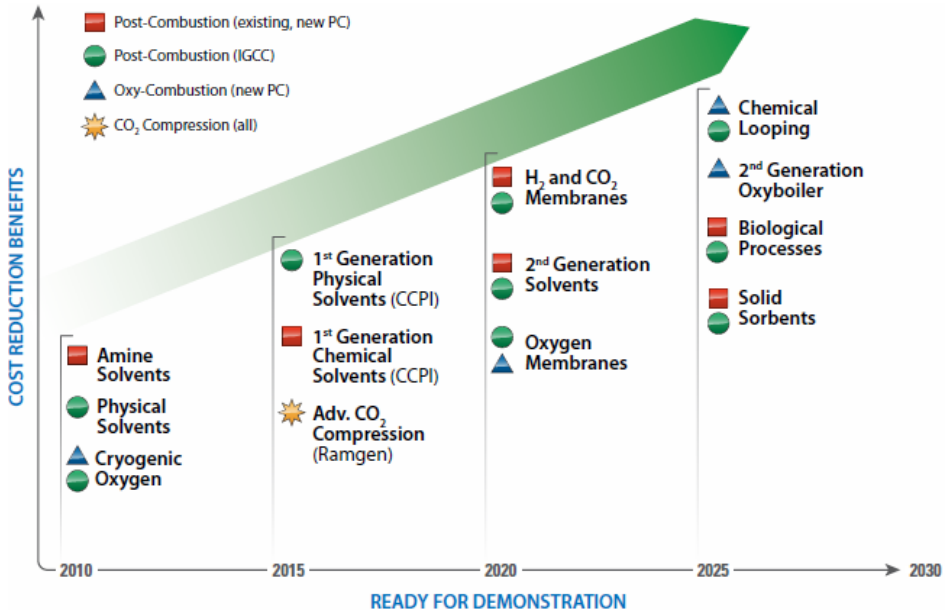

Fig. 1.14 CO_2 capture technology development (DOE/NETL, 2011)

Chemical looping combustion (CLC) is considered to be both pre-combustion capture and oxy-combustion capture since the carbon in the fuel is separated prior to the combustion, and the fuel is converted by an oxygen carrier rather than by air. CLC is potentially the technology best suited for efficient, low cost and low energy capture of CO_2 from flue gases (Ritcher and Knoche, 1983; Ishida et al., 1987; Wolf et al., 2005; Kerr at el., 2005).

As mentioned in Section 1.4.6, CLC may operate, in principle, with a variety of fuel types, including carbonaceous fuel such as coal-derived syngas or natural gas via heterogeneous chemical reaction with an oxygen carrier exchanged between two fluidised beds.

A well-tested CLC reaction system (Adanez et al., 2006; Lyngfelt et al., 2001; Mattisson and Lyngfelt, 2001a, 2001b) is composed of two interconnected fluidised beds working in different hydrodynamic regimes. In the "fuel reactor", the incoming fuel reacts with solid metal oxide particles to produce CO_2, H_2O and reduced metal oxide solid particles; the latter in their reduced state enter the "air reactor" or "riser" where they are regenerated through an oxidation reaction with air (Fig. 1.15). A system of cyclones drives the separation between the depleted air leaving the air reactor and the oxidised oxygen carrier entering the fuel reactor. A well-known setup comprises a riser working in the fast fluidisation regime and a fuel reactor working in the bubbling hydrodynamic conditions (Lyngfelt et al., 2001; Mattisson et al., 2011; Ryu et al., 2004).

A generalised description of the overall reaction in the fuel reactor can be expressed as follows:

$$(2n + m)M_yO_x + C_nH_{2m} \rightarrow (2n + m)M_yO_{x-1} + mH_2O + nCO_2 \quad (1.4)$$

The reduced metal oxide M_yO_{x-1} is then transported to the air reactor where it is re-oxidised to M_yO_x:

$$MyO_{x-1} + 1/2\ O_2(\text{air}) \rightarrow M_yO_x + (\text{air} : N_2 + \text{unreacted } O_2) \quad (1.5)$$

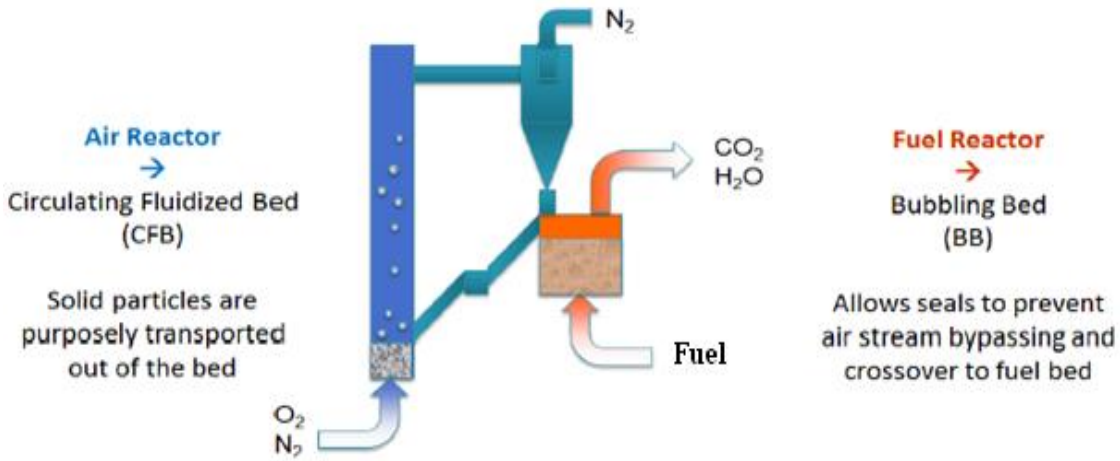

Fig. 1.15 CLC scheme

Air is never mixed with the fuel thereby avoiding NO_x emissions (Ishida and Jin, 1996) and producing a stream of CO_2 and H_2O vapour; the latter can be then easily separated from the CO_2 through condensation. The gas stream leaving the air reactor contains nitrogen and un-reacted oxygen. These gases can be released to the atmosphere with minimal negative environmental impact. In addition, the hot air leaving the combustor is used to drive a steam turbine/gas turbine combined cycle system for electricity generation.

Whereas the reduction reaction of the metal oxide is often endothermic, the oxidation reaction of the metal oxide is exothermic. The heats of reaction depend on the fuel type and on the metal oxide used as oxygen carrier (see Table 1.4). The overall generation of heat equals the heat of combustion. Depending on the metal oxide utilised, the thermal energy released in the oxidation reactor is usually larger than the energy required by direct combustion of the fuel (Fan, 2010; Hatanaka et al., 1997). In addition, the heat absorbed in the reduction reactor is at low temperature and heat is released at high temperature in the oxidation reactor. These features imply that the combustion system can be highly efficiency (Hatanaka et al., 1997). The free-of-water CO_2, obtained after condensation of the water vapour, can be captured or/and used for other applications.

1.6.1 Oxygen carrier employed in CLC

Transitional metal oxides, such as nickel, copper, iron, cobalt and manganese, are adequate oxygen carrier candidates for CLC applications given their favourable reductive/oxidative thermodynamics that means almost full fuel conversion to CO_2

(Mattisson and Lyngfelt, 2001a, 2001b; Jerndal et al., 2006). Oxygen carrier particles should also have (Lyngfelt et al., 2001; Fan, 2010; Hossain and De Lasa, 2008):

- Good oxygen-carrying capacity, defined by the amount of transferable oxygen in the particle during the looping operation; it depends on the property of the metal oxide and the percentage of inert support into the particle; a higher oxygen capacity reduces the circulating rate of solids between the reactors.
- High oxidation and reduction activity, which determines smaller reactor to be used to achieve the same gas conversion.
- Good long-term recyclability and stability under repeated oxidation/reduction, which reduces fresh particle make up rate; this property can be improved by the use of suitable inert support (e.g. Al_2O_3, TiO_2, SiO_2) mixed with the metal oxide;
- Good mechanical strength and resilience to agglomeration, which depends on the inert support added to the reacting metal;
- Suitable heat capacity, so that the particle can serve as a heat transfer medium avoiding the use of heat exchangers to control the heat effects in the reactors; this property depends on the inert support material within the particle;
- Suitable particle size, density and pore structure, which determine the fluidisability of the oxygen carrier and the overall reaction rate; According to the literature, oxygen carriers with particle sizes ranging from 0.08 to 2 mm are suitable for CLC.

Other important factors for a successful oxygen carrier are its cost, its environmental impact, resistance to contaminant and inhibition of coke formation.

Table 1.4 exhibits the reduction and oxidation reactions of the main candidates as oxygen carriers for CLC purposes, with syngas/methane and oxygen, respectively. The reactions shown in Table 1.4 proceed in one-step reaction but different steps of reaction might occur. For instance, CuO can be partially reduced to Cu_2O releasing gaseous oxygen to react with the fuel.

Table 1.4 Reactions of the oxygen carrier used in CLC, oxygen transport capacity of the materials, R_o, and combustion heat (Abad et al., 2007)

		R_o	ΔH_c^0 (kJ/mol)
CuO/Cu		0.20	
	$CH_4 + 4\,CuO \longleftrightarrow 4\,Cu + CO_2 + 2\,H_2O$		−178.0
	$H_2 + CuO \longleftrightarrow Cu + H_2O$		−85.8
	$CO + CuO \longleftrightarrow Cu + CO$		−126.9
	$O_2 + 2\,Cu \longleftrightarrow 2\,CuO$		−312.1
Fe_2O_3/Fe_3O_4		0.03	
	$CH_4 + 12\,Fe_2O_3 \longleftrightarrow 8\,Fe_3O_4 + CO_2 + 2\,H_2O$		141.6
	$H_2 + 3\,Fe_2O_3 \longleftrightarrow 2\,Fe_3O_4 + H_2O$		−5.8
	$CO + 3\,Fe_2O_3 \longleftrightarrow 2\,Fe_3O_4 + CO_2$		−47.0
	$O_2 + 4\,Fe_3O_4 \longleftrightarrow 6\,Fe_2O_3$		−471.9
NiO/Ni		0.21	
	$CH_4 + 4\,NiO \longleftrightarrow 4\,Ni + CO_2 + 2\,H_2O$		156.5
	$H_2 + NiO \longleftrightarrow Ni + H_2O$		−2.1
	$CO + NiO \longleftrightarrow Ni + CO_2$		−43.3
	$O_2 + 2\,Ni \longleftrightarrow 2\,NiO$		−479.4

In addition to the main reactions shown in Table 1.4, undesirable reactions, such as shift reaction (Eq. 1.6), methanation reaction (Eq. 1.7) and coke formation via pyrolysis (Eq. 1.8) and/or Boudouard reaction (Eq. 1.9), can also occur, as listed below:

$$CO + H_2O \rightarrow H_2 + CO_2 \quad (1.6)$$

$$CO + 3H_2 \rightarrow H_2O + CH_4 \quad (1.7)$$

$$CH_4 \rightarrow 2H_2 + C \quad (1.8)$$

$$2CO \rightarrow C + CO_2 \quad (1.9)$$

These secondary reactions are catalysed by the reduced state of the metal. They can be avoided by choosing the right range of temperature, pressure and oxygen added ratio. The latter is defined as the actual amount of O added with the metal oxide over the stoichiometric amount needed to achieve full conversion to H_2O and CO_2 (Mattisson et al., 2006; Jerndal et al., 2006).

Carbon formation, via pyrolysis and/or Boudouard reaction, is negligible in the absence of a catalyst. However, transition metals such as Ni and Fe can catalyse these reactions. Thus, if the latter transitional metals are applied as oxygen carrier, operating conditions that avoid coke formation have to be selected. For instance, Ryu et al. (2003) reported for Ni-based oxygen carrier an operating temperature higher than 900 ˚C to avoid coke formation during the reduction stages. Jerndal et al. (2006) agreed with the previous

findings and, in addition, pointed out the need to operate with an oxygen added ratio higher than 0.25.

An important parameter is the oxygen transport capacity, R_o, (Lyngfelt et al., 2001):

$$R_0 = \frac{M_{ox} - M_{red}}{M_{ox}} \tag{1.10}$$

In Eq. 1.10, M_{ox} and M_{red} are the molar mass of the fully oxidised and reduced carrier, respectively. R_o is the mass fraction of oxygen that can be applied in the oxygen transfer. Higher R_o values lead to less solid needing to be circulated between the two reactors to get full fuel conversion since higher amounts of oxygen per unit mass of solid are transferred to react with the fuel. The latter aspect will benefit the kinetics since it will be possible to keep low the solid conversion inside the reactors and consequently high the reaction rate. The latter aspect will be explained in Chapter 4. Hossain and De Lasa (2008) listed R_o for various metal oxides expressing them in moles of oxygen per mole of metal (Table 1.5).

Table 1.5 R_o for various metal oxides (Hossain and De Lasa, 2008)

Metal oxide	Moles of O_2/mole metal
NiO/Ni	0.5
CuO/Cu	0.5
Cu_2O/Cu	0.25
Fe_2O_3/Fe_3O_4	0.083
Mn_2O_3/MnO	0.25
Mn_3O_4/MnO	0.17
Co_3O_4/Co	0.67
CoO/Co	0.5

Not all the metal oxides listed in Table 1.5 are suitable candidates as oxygen carrier for CLC applications. Indeed, e.g. Mn_3O_4/MnO, Mn_2O_3/MnO metal/metal oxides pairs show a low oxygen carrying capacity and they decompose at low temperature. On the other hand, Co_3O_4/Co exhibits the highest oxygen carrying capacity but it is subjected to decomposition into CoO at low temperature. The metal oxides that meet all the requirements previously mentioned are those shown in Table 1.4: NiO/Ni, Fe_2O_3/Fe_3O_4, CuO/Cu.

Fe_2O_3/Fe_3O_4 and CuO/Cu have the main advantage at being abundant in the earth and cheap. Nevertheless, some restrictions concern those metal oxides: e.g. the CuO/Cu

oxygen carrier has a relatively low melting point (1085 ˚C); thus, to avoid agglomeration of circulating particles, the CuO/Cu oxygen carrier has a limited operating temperature leading to restrictions in terms of thermal power efficiency (Wolf et al., 2005). Also the pure hematite, if not supported, exhibits a relatively low maximum feasible temperature close to 1000 ˚C (Copeland et al., 2002). On the other hand, NiO/Ni exhibits high oxygen carrying capacity, and also high reactivity, melting point and thermal stability leading to high kinetic rates and potential use of high temperature to increase the gas turbine performances in a CLC power plant (Villa et al., 2003).

To increase the reactivity, fluidisability and durability of the metal oxides, different inert supports have been employed: TiO_2, ZrO_2, Al_2O_3, SiO_2, YSZ and bentonite. The drawback of adding an inert support is the decrease of the oxygen transport capacity since it becomes a function of the active metal oxide content x_{MeO}:

$$R_o' = R_o x_{MeO} \tag{1.11}$$

1.6.1.1 Ni-based oxygen carrier

Nickel-based oxygen carrier has been the most studied metal oxide for its high oxygen carrying capacity and favourable thermodynamics. Among all the inert supports, Al_2O_3 has been the most investigated since it exhibits high thermal stability and fluidisability (Ishida and Jin, 1997; Jin et al., 1999; Mattisson et al., 2003; Son and Kim, 2006; Garcia-Labiano et al., 2006). A drawback of using NiO/Ni supported with Al_2O_3 is the formation of a small amount of $NiAl_2O_4$ that does not participate in the redox reactions; thus, the active metal content in the oxygen carrier decreases.

Based on the previous considerations, several authors have used $NiAl_2O_4$ as an inert support instead of Al_2O_3 (Mattisson et al., 2011; Ryu et al., 2003; Cho et al., 2004). They found that $Ni/NiAl_2O_4$ presents high thermal stability (up to 1200 ˚C), high reactivity with methane and syngas, no agglomeration and almost absence of carbon formation under different operating conditions. A negative feature is that $Ni/NiAl_2O_4$ oxygen carrier requires more nickel than Ni/Al_2O_3.

Nickel supported on bentonite shows lower performances at higher temperature compared to the aforementioned oxygen carrier supports due to its limited thermal stability (Ryu et al., 2001, 2003; Son and Kim, 2006). The use of TiO_2 inert support exhibits a high tendency for coke formation (Ishida et al., 1998; Jin et al., 1999; Adanez et al., 2004). Thus, despite some limitations, Al_2O_3 as inert support for nickel is considered the most promising option for large scale CLC applications (Hossain and De Lasa, 2008).

The main issue with the use of Ni-based oxygen carrier concerns its cost and environmental impact. Thus, several efforts have been carried out to improve the performance of Fe-based oxygen carriers and make it competitive (Mattisson et al., 2001; Ryden et al., 2008; Galinsky et al., 2013).

1.6.1.2 Fe-based oxygen carrier

Fe-based oxygen carriers are cheaper than Ni-based oxygen carriers and they do not present any environmental issues. They usually exhibit lower oxidation and reduction rates with methane and syngas compared to Ni-based oxygen carrier regardless of the inert support used (Mattisson et al., 2001; Adanez et al., 2004; Fan and Li, 2010). In addition, they exhibit low oxygen carrying capacity since only the transformation from Fe_2O_3 to Fe_3O_4 in the reducer can be taken into account. In fact, although Fe-based carriers have different oxidation states (Fe_2O_3-Fe_3O_4-FeO-Fe), only the first transformation from hematite to magnetite can lead to almost complete CO_2 formation; furthermore, it is the dominant chemical transformation since it is the fastest step of reaction compared to the transformations to FeO and Fe. Further reduction to FeO would determine a decrease in CO_2 purity due to the increase in CO and H_2 concentrations (Copeland et al., 2001; Kronberger et al., 2005b).

Different inert supports have been investigated to improve the hematite reactivity and avoid agglomeration. In particular, Al_2O_3 is one of the most suited supports since it increases the Fe-based oxygen carrier reduction rate (Abad et al., 2007; Adanez et al., 2004; Mattisson et al., 2001, 2004; Son and Kim, 2006). As in the case of Ni-based oxygen carriers, hematite reacts with Al_2O_3 giving an inert compound, $FeAl_2O_4$, that causes loss of particle reactivity (Mattisson et al., 2004). High interactions metal oxide–inert support were detected also when TiO_2 is used as support with high reduction in oxygen carrying capacity (Ishida et al., 1998; Adanez et al., 2004; Mattisson et al.,

2004; Son and Kim, 2006). $MgAl_2O_4$ has also been used as a support to avoid aluminate formation (Mattisson et al., 2004; Zafar et al., 2006). Unfortunately high particle agglomeration was observed at elevated temperatures. Ishida et al. (1998) proposed YSZ as inert support. Although, no interactions between the hematite and the support were detected, the reduction rate of this oxygen carrier was quite slower than the one supported on Al_2O_3.

Since the key limitation of Fe-based oxygen carriers is the lower reactivity compared to the Ni-based oxygen carriers regardless of support used (Kang et al., 2010; Adanez et al., 2004; Lyngfelt et al., 2008; Mattisson et al., 2001), efforts have been made out to find a suitable support to enhance the reactivity of the iron-based oxygen carriers. Galinsky et al. (2013) reported a Fe-based oxygen carrier mixed with an ionic-electronic conductive (MIEC) support such as $La_{0.8}Sr_{0.2}FeO_{3-x}$ (LSF) that exhibits more than an order of magnitude higher reactivity to H_2, CO and CH_4 when compared to TiO_2-, Al_2O_3- and YSZ-supported oxygen carrier. Indeed, the LSF support facilitates the conduction of electrons and O^{2-} allowing for easy O^{2-} transport and accessibility through the iron oxide. Furthermore, the LSF-supported oxygen carrier shows high resistance toward coking formation and secondary reactions; therefore, it can be considered as a suitable material for application in chemical looping processes.

1.6.1.3 Cu-based oxygen carrier

Cu-based oxygen carrier exhibits many advantages, such as the cost that is the one of the lowest for the metals that can be used in CLC and a reduction reaction that is exothermic eliminating the need of energy supply in the fuel reactor (see Table 1.4). The drawback is related to its tendency to decompose at temperatures above 900 ˚C (Jerndal et al., 2006; Mattisson et al., 2003). Thus, the application of Cu-based oxygen carriers in CLC imposes restrictions to the fluidised beds operating temperature, leading to reductions of the plant thermal efficiency.

Al_2O_3, SiO_2 and TiO_2 have been the most frequently used supports (Adanez et al., 2004; de Diego et al., 2004; Mattisson et al., 2003; Zafar et al., 2006). Al_2O_3 as inert support seems to lead to reduction in reactivity under several reduction-oxidation cycles and defluidisation of the bed. Cu-based metal oxides prepared with SiO_2 suffer from CuO

decomposition to Cu_2O and very low reactivity. TiO_2 as a Cu support has a high tendency to form $CuTiO_4$ inert compound, leading to a large drop in reactivity.

Table 1.6 summarises the main advantages and disadvantages of the most suitable oxygen carriers for CLC applications.

Table 1.6 Main advantages/disadvantages of Ni-, Fe-, Cu-oxygen carriers

	Ni- oxygen carrier	**Fe - oxygen carrier**	**Cu- oxygen carrier**
Advantages	high oxygen capacity, high melting point, high heat of exothermic reaction, high kinetics	cheap, high heat of exothermic reaction, no environmental issues, abundant in earth	cheap, no environmental issues, high oxygen capacity, exothermic reduction reaction
Disadvantages	expensive, environmental issues	low kinetics, low oxygen capacity	low melting point

1.6.2 CLC applications

The first use of chemical looping was proposed to increase the exergetic efficiency of the combustion process reducing its thermodynamic irreversibility. Indeed, the direct combustion of fuel exhibits irreversibility due to the process itself and further losses due to the decrease of the outlet products temperature to match the inlet turbine temperature requirements (i.e. adiabatic flame temperature is much higher than the maximum allowed turbine temperature). In chemical looping, the split of the combustion process in two steps (i.e. reduction and oxidation) characterised by two different working temperatures, which are lower than the adiabatic flame temperature, leads to no exergy loss in the transfer from the reactor to the turbine. Thus, the total exergetic efficiency of the combustion process results improved. More thermodynamic details are given by Ishida et al. (1987) and Dennis (2009).

Modern applications of chemical looping strategy are prompted by the need to minimise the energy penalties in the chemical energy conversion systems tackling the target of the reduction in CO_2 emissions (Fan, 2010).

As previously mentioned in Section 1.6, both gaseous and solid fuel can be applied in a CLC scheme. Gaseous fuels are easier to convert than solid fuel. Nevertheless, the direct-solid fuel chemical looping systems are attractive because of the potential economic impact. Certainly, several additional issues, compared to the gaseous fuel utilisation, have to be tackled, such as ash removal, tar conversion, solid fuel conversion and in situ oxygen carrier interaction with gaseous pollutants.

CLC schemes can be either applied as primary reactor for firing natural gas (or solid fuel) or integrated in a IGCC power plant as a CO_2 capture unit either for electricity production or electricity and hydrogen co-production (Syngas Chemical Looping (SCL)). A brief description of the possible CLC applications is given in the next sections.

1.6.2.1 IGCC integrated with CLC technology

Fig. 1.16 shows a schematic diagram of a CLC unit integrated in an IGCC power plant. In Section 1.4.2, an IGCC power plant with CO_2 capture equipped with a water gas shift reactor and dual-stage Selexol unit was briefly described. The application of a CLC unit performs various functions avoiding the need of a two step operation: water gas shift reaction to increase the CO_2 content in the gas stream and separation unit for CO_2 capture. However, a hot gas cleanup unit is needed to remove most of the sulphur in the raw syngas before it enters the CLC unit. The syngas, entering the reducer is converted to CO_2 and H_2O via heterogeneous gas-solid reaction with a metal oxide. Then, the reduced metal oxide reacts with air in the combustor to be regenerated. CO_2 is separated from H_2O via cooling and captured. The hot spent air from the combustor runs through an expander for power generation and an HRSG to recover the heat needed to drive a steam cycle.

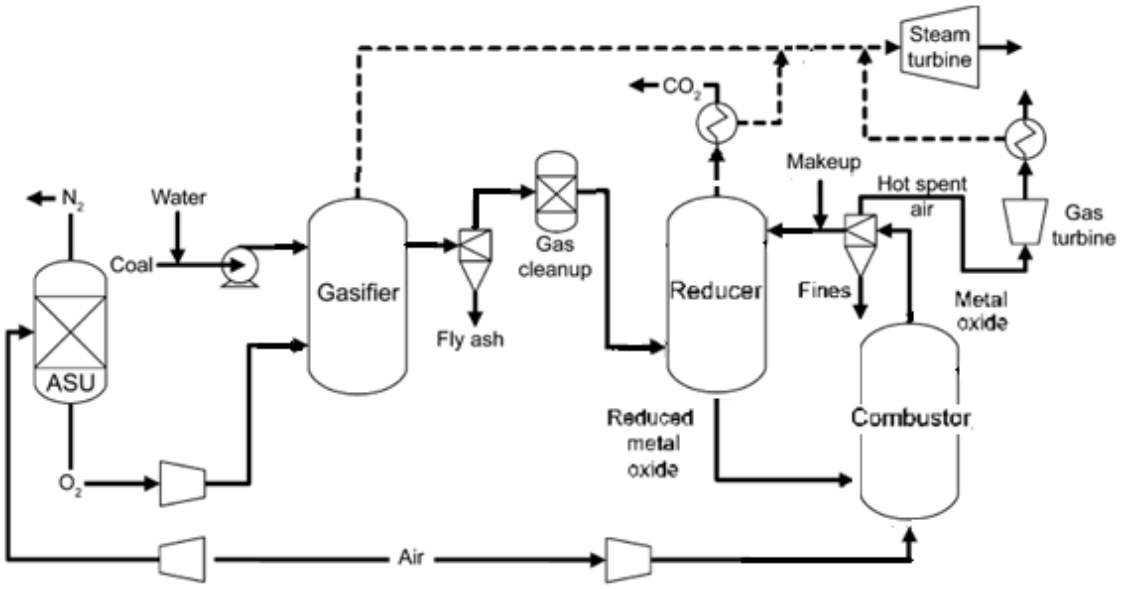

Fig. 1.16 Schematic diagram of CLC process (--- steam) (Fan, 2010)

In this configuration, Ni-based oxygen carrier is preferred, having more favourable kinetics and thermodynamics compared to Cu- and Fe-based oxygen carriers. The main issue of this process concerns the presence of sulphur that may be present even after the gas cleanup unit; indeed, depending on the coal composition, if the sulphur concentration is too high, formation of i.e. NiS and Ni_3S_2 may arise leading to high oxygen carrier losses and agglomeration.

Rezvani et al. (2009) reported a comparison of different CO_2 capture strategies integrated in IGCC power plants: Dual-stage Selexol process, selective membranes and CLC unit. The analysis exhibits a power plant thermal efficiency equal to 35.6 % if equipped with physical absorption unit, 36.4% if equipped with selective membranes and 35.2% if equipped with CLC unit. A novel dual-stage CLC unit could achieve 36.6% in thermal efficiency. Since the CLC unit shows the highest investment cost compared to the other capture technologies, the resulting cost of electricity generated using a CLC approach is the highest whereas the membrane approach seems to lead to the lowest price for the electricity to be sold (Rezvani et al., 2009). This result is not surprising since the purchased cost of a CLC unit is believed to be very high, around 16 million of dollars for a volume of 180 m^3 (Klara, 2007).

The latter aspect, together with the already high investment cost of a IGCC power plant, might result in an uncompetitive cost of electricity generated, when CLC is applied,

compared to other CO_2 capture solutions. In fact, it is believed that CLC process can exploit its full potential when used as a primary reactor in a power generation plant (Rezvani et al., 2009).

1.6.2.2 IGCC with Syngas Chemical Looping (SCL) process

The traditional IGCC configuration for hydrogen coproduction is similar to the carbon-constrained IGCC process, which employs a dual-stage Selexol unit to remove both H_2S and CO_2 (see Section 1.4.2). The major difference lies in the usage of the H_2-rich stream after the acid gas removal (AGR) process. Indeed, the treated syngas from the AGR unit is split into two streams. One streams flows to the gas turbine and the other flows to a pressure swing adsorption unit (PSA) for hydrogen production at 99.99+ vol% purity (Luberti et al., 2014). The high-purity hydrogen is used as an end product, while the tail gas from the PSA unit is recompressed before being combusted in a combined cycle system to generate electricity. On the other hand, the Syngas Chemical Looping (SCL) process offers an alternative way to coproduce hydrogen and electricity, as shown in Fig. 1.17.

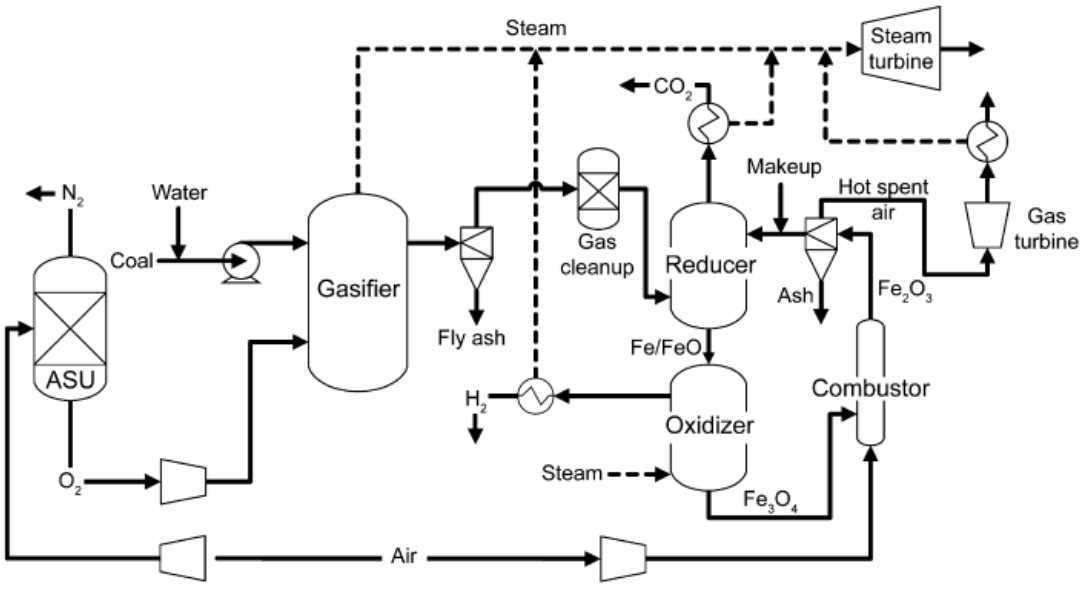

Fig. 1.17 Schematic diagram of SCL process for hydrogen coproduction (--- steam) (Fan and Li, 2010)

The main difference between the SCL process and the traditional coal-to-hydrogen process is related to the way H_2 is generated. Indeed, the SCL process carries out various functions replacing the water gas shift reactor, the CO_2 separation unit and the PSA unit for H_2 purification.

In the reducer, the syngas is converted completely into CO_2 and H_2O via reaction at 750-900 ˚C and 30 atm with Fe_2O_3. The steam in the product stream is condensed, resulting in a concentrated, high pressure CO_2 stream ready to be transported and stored. The reaction in the reducer can be either endothermic or exothermic depending on the syngas composition, particle reduction rate and reaction temperature. The metal oxide particles, reduced to a mixture of Fe and FeO, enter the oxidiser operating at 500-750 ˚C. In the oxidiser, they react with steam producing a mixture of H_2 and unconverted steam readily separable via condensation. The heat released from the reaction is used in the same reactor to heat the feed water/steam. The resulting Fe_3O_4 particles, from the oxidation reaction, are regenerated in the entrained flow combustor where an exothermic reaction with air produces Fe_2O_3 particles and hot spent air. The regenerated oxygen carrier is conveyed to the reducer inlet to close the chemical looping whereas the hot spent air drives a gas/steam turbine combined cycle system for electricity generation.

In contrast to the CLC processes, where nickel oxides offer better performances, the desired particles for SCL application are Fe/FeO since Ni has a low steam-to-hydrogen conversion rate and poor reaction kinetics (Fan, 2010). As reported by Fan and Li (2010), the four oxidation states of the iron carrier are the key feature of the SCL process. Indeed, from a thermodynamic point of view, iron at higher oxidation states (Fe_2O_3/Fe_3O_4) leads to higher equilibrium values of CO_2 and H_2O concentrations and it is the desirable feedstock for the reducer to obtain high syngas conversions (Fe_2O_3/Fe_3O_4 is the stable transformation under high ratio P_{CO2}/P_{CO} and low ratio P_{H2}/P_{H2O}). Conversely, iron at lower oxidation states (FeO/Fe) leads to higher equilibrium value of H_2 and CO concentrations and it is the desirable feedstock for the oxidiser to obtain high steam conversions (FeO/Fe is the stable transformation under high ratio P_{H2}/P_{H2O} and low ratio P_{CO2}/P_{CO}).

In this scenario, a fluidised bed mode for the reducer and the oxidiser is not the best option to apply since it is not practically possible to achieve high solid reduction conversions meaning low iron state of oxidation. Indeed, in a fluidised bed reactor significant mixing for the gas and the solid phases occurs. Thus, in the reducer, high concentrations of CO_2 from the syngas conversion will dilute the syngas feedstock leading to low solid conversion in the form of Fe_3O_4.

Since a mixture of FeO/Fe is also desired as a product, to be applied in the oxidiser consequently, a counter current moving bed arrangement is the preferred option. A counter current moving bed has the minimal axial mixing of the solid and gas phases; thus, fresh syngas at high H_2 and CO concentrations will react with iron at lower oxidation states (FeO/Fe) whereas the partially converted syngas at low H_2 and CO concentrations will react with the fresh iron at higher oxidation states (Fe_2O_3/Fe_3O_4). The overall result is a gas product mixture of CO_2 and H_2O and a solid mixture of FeO/Fe entering consequently the oxidiser.

In the same way, a counter current moving bed arrangement in the oxidiser will lead to steam at high concentration in the bottom of the bed reacting with iron at higher oxidation states (Fe_2O_3/Fe_3O_4) and steam at low concentration in the top of the bed meeting iron at lower oxidation states (FeO/Fe). This arrangement will produce high H_2 concentrations at the top exit of the oxidiser as well as a mixture of Fe_2O_3/Fe_3O_4 solid particles at the bottom exit to be further oxidised in the combustor with air to complete the chemical looping.

Fan (2010) reported an energy efficiency for the SCL process equal to 66.5% (based on HHV), which is about 4% higher than the output from a traditional coal-to-hydrogen process. However, since no economic analysis of both processes was carried out, it is not possible to make an actual estimation of the potential positive effect of the SCL process application on the cost of the electricity and H_2 sold.

1.6.2.3 Coal-Direct Chemical Looping (CDCL) process

In principle, the chemical looping concepts can be applied to the direct combustion of coal either for electricity production or for hydrogen and electricity coproduction, as shown in Fig. 1.18. The concepts applied reflect those behind the SCL process. In the scheme of Fig. 1.18, Fe_2O_3 particles similar to those used in SCL enter the reducer together with fine coal powder. By employing suitable gas-solid contact patterns, coal is gasified to a CO/H_2 mixture. The reductive gas will convert Fe_2O_3 particles to FeO/Fe producing a concentrated CO_2 and H_2O fuel gas stream. Then, the reactions in the oxidiser and the combustor occur in the same fashion examined in the SCL process (see Section 1.6.2.2).

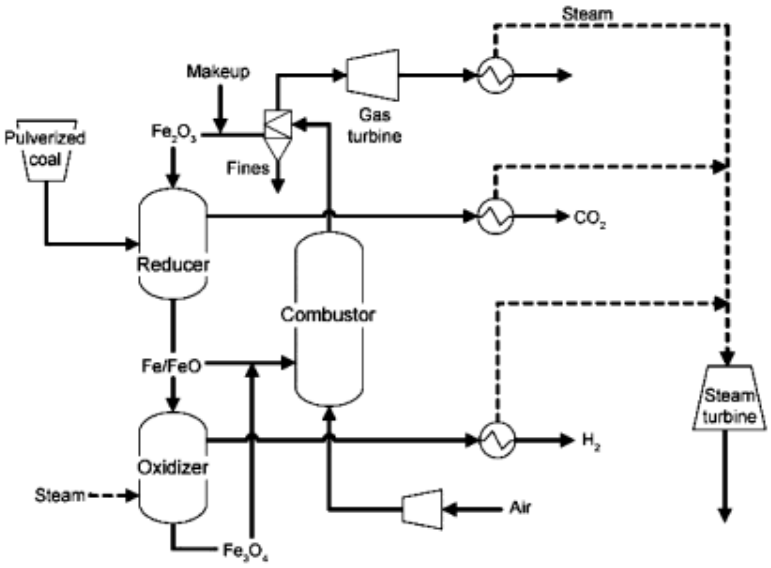

Fig. 1.18 Schematic diagram of CDCL process for electricity and hydrogen co-production (--- steam) (Fan and Li, 2010)

It is worth noticing that when only electricity generation is required, either in the SCL or CDCL process, all the reduced particles from the reducer can by-pass the oxidiser and be introduced directly to the combustor avoiding the H_2 production step. If the latter is the case, a reducer in a fluidised bed mode employing more reactive particles such as Ni-based particles is a solution that has to be considered, particularly in the SCL process. Indeed, in the CDCL process, even if NiO reacts faster with H_2 or CO compared to Fe_2O_3, the reaction rate between coal char and oxygen carrier is controlled by char gasification (Scott et al., 2006) that is the limiting step of reaction. Thus, the reactivity advantage of using NiO with syngas rather than Fe_2O_3 is lost when coal is directly combusted.

In the CDCL process, the reducer is the most crucial unit. Fan and Li (2010) suggest a counter current gas-solid moving bed configuration where Fe_2O_3 is introduced at the top of the bed whereas coal powders are fed in the middle of the bed dividing it into two zones: upper and lower. In the upper zone, coal devolatilisation, metal oxide reduction and CO_2/H_2O production occur. Coal volatiles move upward from the middle of the reactor, along with other gases such as CO, H_2O, CO_2 and H_2, encountering the fresh metal oxide particles. The counter current interaction between the oxygen carrier and the coal volatiles ensures the potential complete conversion to CO_2 and H_2O. In the lower zone, char gasification and further metal oxide reduction producing CO_2 and H_2O

occur. The descending coal char, from the middle of the reactor, reacts with an up-flow of CO_2 and H_2O formed at the bottom of the reactor via metal oxide reduction reaction, and thus is consequently gasified. A portion of CO_2 recycled at the bottom of the reducer can be used to improve the char conversion. The coal ash exits, together with the FeO/Fe particles, from the bottom of the reducer and they can be separated from the Fe_2O_3 particles at the exit of the combustor, in a cyclone, based on the particle size difference.

Fan (2010) reported a simulation of the CDCL process under simplified assumption for the reaction system using the commercial software Aspen Plus. The results show that in theory the CDCL process for electricity and hydrogen co-production might achieve efficiency close to 79% based on HHV (72% coming from hydrogen and 7% from electricity generation). This results 20% higher than the traditional coal-to-hydrogen process. However, due to the complexity of the phenomena involved in the direct combustion of coal, the current solid fuel CLC systems on sub-pilot scale lead to lower fuel conversion efficiency as well as lower CO_2 capture efficiency than the gaseous fuel CLC system (Fan and Li, 2010). Thus, further research on the metal oxides particles, improvements of the contact between oxygen carrier and coal char/volatile, ash separation and efficient design of the reducer reactor together with an appropriate heat integration strategy is needed to develop valuable and competitive solid fuel CLC systems.

In this respect, e.g. if the solid fuel is not completely burned in the reducer, it will enter in the combustor, along with the oxygen carrier, leading to CO_2 in the off-gas to be emitted in the atmosphere. Since the separation of unburned fuel from the oxygen carrier is a key feature in the development of a CLC strategy with solid fuel, several researchers proposed various operating strategies to overcome the issue (Cao and Pan, 2006; Leion et al., 2007; Berguerand and Lyngfelt, 2008). For instance, Dennis and Scott (2010) proposed the application of several fluidised beds operating in a fashion common for fixed beds under continuous operation to carry out *in situ* gasification and combustion of solid fuel in the form of lignite. Each reactor is subjected to three operation periods. In the first period, solid fuel is introduced in a bed of oxygen carrier, fluidised by steam or CO_2. Coal devolatisation and gasification take place. Thus, volatile matter and produced syngas react with the oxygen carrier to form CO_2 and H_2O. In the second period, the coal feed is stopped and the remaining char completes the

gasification process. In the third period, the bed is fluidised by air to regenerate the oxygen carrier. The small ash particles are elutriated from the bed. Since the coal gasification reaction is highly endothermic, a Cu-based oxygen carrier is considered a good choice in this configuration; indeed, its reduction reaction is sufficiently exothermic to balance the gasification reaction (Dennis and Scott, 2010). Further investigations on this promising approach are still ongoing.

1.6.2.4 CLC with natural gas as feedstock

Section 1.4.1 briefly described how chemical absorption with MEA is the traditional technology to capture CO_2, in a post-combustion fashion, from a natural gas fired power plant. The high reduction in the thermal efficiency of the plant when the chemical absorption unit is integrated and the resulting increase in the cost of electricity generated (Rao and Rubin, 2002; Davison, 2007) have driven the need to find alternatives to capture CO_2 from an NGCC power plant. Kvamsdal et al. (2007) reported eight different concepts for CO_2 capture applied to an NGCC to be compared either with the MEA solution (see Section 1.4.1) or the NGCC without CO_2 capture section (see Section 1.2.3). The eight concepts reported by Kvamsdal et al. (2007) are briefly described as follows:

1) *Oxy-fuel Combined Cycle*: the reaction in the combustion chamber occurs between natural gas and oxygen from ASU unit instead of air; so, CO_2 and H_2O readily separable via condensation are the only products of reaction. 90% of CO_2 is recycled to the combustor to moderate the turbine inlet temperature.

2) *Water cycle (WC)*: instead of recycling CO_2, water is the re-circulating working fluid to the combustor, where natural gas and oxygen react at high pressure (Bolland et al., 2005).

3) *Graz cycle*: this solution is a combination of the oxy-fuel and water cycle concepts. Either a fraction of CO_2 or steam is recycled to the combustor chamber for the purposes previously discussed (Jericha et al., 2003).

4) *Advanced zero emission power plant (AZEP)*: in this configuration air instead of oxygen is fed to the plant. A mixed conductive membrane (MCM) reactor replaces the combustion chamber allowing the separation of oxygen from air, the resulting reaction

between natural gas and pure oxygen with CO_2 and H_2O as only products, the transfer of combustion heat to the oxygen depleted air to be used in the air turbine. The drawback of this concept is a turbine inlet temperature lower than that applied in the previous configurations due to the limited membrane material resistance at high temperature (Griffin et al., 2004).

5) *Solid Oxide Fuel Cell (SOFC) integrated with a Gas Turbine (GT)*: in this configuration the SOFC unit replaces the combustion chamber allowing the natural gas to react with pure oxygen at the anode producing a stream of CO_2 and H_2O. Oxygen depleted air from the cathode is fed to the gas turbine (Maurstad et al., 2004).

6) *Pre-combustion with an auto-thermal reformer (ATR)*: in this scheme heavy hydrocarbons in the natural gas are converted to methane and hydrogen in a pre-reformer unit. Then, an ATR unit (with the addition of air) and two shift reactors in series produce a mixture of CO_2, H_2, H_2O and N_2. Water is separated through condensation, CO_2 is separated by an absorption unit and the remaining mixture of H_2 and N_2 is burned with air in a combustion chamber (Kvamsdal et al., 2002).

7) *Pre-combustion with a hydrogen membrane reactor (MSR-H_2)*: in this scheme the ATR and the two shift reactors are replaced with a membrane reactor of the methane-steam reformer type with a hydrogen separating membrane. Thus, hydrogen and water, from one side of the membrane, run to the combustor to react with air whereas CO_2 and H_2O, from the other side of the membrane, are cooled and the resulting water stream is separated (Jordal et al., 2004).

8) *CLC process*: in this configuration the CLC unit replaces the combustion chamber of the gas turbine. The process works in a way previously explained in Section 1.6: natural gas reacts in the reducer with metal oxide particles producing a CO_2/H_2O stream whereas air reacts with the reduced metal oxide particles in an air reactor for solid regeneration purposes.

Fig. 1.19 shows the comparison in terms of plant thermal efficiency among the aforementioned concepts as reported by Kvamsdal et al. (2007).

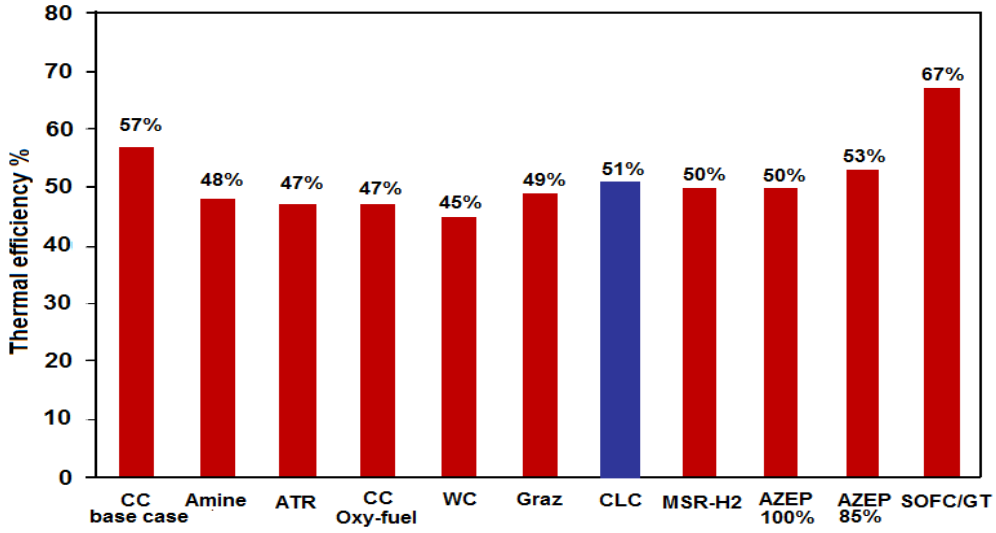

Fig. 1.19 Thermal efficiency of natural gas fired plant with different CO_2 capture technologies (Kvamsdal et al., 2007)

Although each CO_2 capture technology exhibits energy penalties compared to the case without CO_2 capture, CLC seems to be the best option under the assumptions made. Indeed compared to the CLC approach, the amine solution exhibits higher energy penalties (mainly due to the regeneration of the solvent in the stripper since part of the low pressure steam is withdrawn from the steam cycle to be used in the stripper boiler). The oxy-fuel, WC and Graz cycle exhibits also higher energy penalties (mainly due to the cryogenic production of oxygen). ATR, MSR-H_2 and AZEP at 100% CO_2 capture efficiency show lower thermal efficiencies. AZEP at 85% CO_2 capture efficiency shows higher thermal efficiency but the CO_2 capture efficiency is not satisfactory (CO_2 capture efficiency equal to or higher than 90% are usually required); the SOFT/GT solution is not mature, to date, for large scale applications. Overall, the application of a CLC unit for CO_2 capture to an NGCC power plant seems to be a viable and better efficient solution that will be further investigated later on.

1.6.2.5 Novel applications of chemical looping processes

Ryden and Lyngfelt (2006) were the first to study a CLC scheme integrated with steam methane reforming (CLR). The main target of a CLR process is the production of syngas. In the CLR scheme, the air reactor works in the same way of a traditional CLC loop whereas the reducer exhibits different features. In fact, in the reducer the feed (mainly methane and steam) has to react with catalytic particles to produce a syngas stream; then, a water shift reactor converts the syngas to hydrogen and CO_2 and finally, a PSA unit separates the pure hydrogen stream. Due to optimum heat integration, this

arrangement has the potential to lead to higher hydrogen yield (up to 5% more) than the conventional steam methane reforming process (Fan and Li, 2010; Ryden and Lyngfelt, 2006).

Different metal oxides have been under investigation for the methane partial oxidation such as Ni-based oxygen carriers (Ortiz et al., 2012, Proll et al., 2010), $La_xSr_{1-x}FeO_3$ perovskite oxygen carriers (Ryden et al., 2008) and $Fe_2O_3@La_xSr_{1-x}FeO_3$ core-shell oxygen carriers (Shafiefarhood et al., 2014) with the latter reporting the highest reactivity and selectivity towards syngas (Shafiefarhood et al., 2014).

Another potential application of the CLC concept concerns the integration of a chemical looping reducer with a direct solid fuel cell for electricity generation. A fuel cell, able to process solid, oxidises the reduced metal oxide particles producing electricity; the oxidised particles are recycled back to the reducer to react with the fuel to generate a CO_2/H_2O stream as a product. The preliminary estimations of the thermal efficiency of the process look highly promising although several issues need to be tackled (Fan and Li, 2010).

1.6.3 CLC operational experience

Since 2000, research in CLC has been steadily increasing. Over 700 oxygen carriers have been tested by thermogravimetry or in laboratory fluidised bed, different reactor designs have been proposed (Lyngfelt et al., 2001; Kronberger et al., 2005a; de Diego et al., 2007; Kolbitsch et al., 2009a, 2009b, 2010) and thermodynamic efficiency estimations have been carried out (Ishida et al., 1987; Wolf et al., 2005; Kvamsdal et al., 2007; Naqvi et al., 2007). Significant developments towards industrial demonstration with gaseous fuel have been achieved, with the groups at the Instituto de Carboquimica (CSIC), Spain, and at Chalmers University, Sweden, being in the forefront of these advance. The Korea Institute of Energy Research (KIER) and the Vienna University of Technology (VUT) have been also giving great contributions for the enhancement of the CLC technology.

Section 1.6 reported a feasible setup for a CLC unit composed of a fuel reactor at bubbling hydrodynamic conditions, a riser at fast fluidisation conditions and a system of cyclones for gas-solid separation. However, various reaction systems of different design

and size have been tested to find out the most suitable configuration for the future scaling up of the CLC technology (Lyngfelt et al., 2011). In this respect, some recent CLC operational experience is briefly summarised.

Lyngfelt and Thunman (2004) presented results from a 10 kW CLC prototype unit. The unit was composed of a bubbling fuel reactor and a circulating air reactor with two loop seals separating the two reactors and a cyclone. Ni-based oxygen carrier was used, leading to 99.5% conversion of natural gas without carbon deposition detected, no decrease in particle reactivity, low loss of fines (0.002%/h after 100 h operation) and nearly 100% CO_2 capture achieved.

Also Ryu et al. (2004) reported results from a 50 kW combustor working with CH_4 as fuel; under a reaction system arrangement similar to the previous one, 98% of fuel conversion using nickel oxide particles was detected during 3.5 h operation.

Son and Kim (2006) tested a CLC unit composed of an air and fuel reactor both in bubbling bed configuration in the form of concentric tubes with the air reactor placed inside the fuel reactor and an external riser for particles recycling; mixed oxide carriers of NiO-Fe_2O_3/Bentonite were investigated.

CLC applied to solid fuel in a form of bituminous and pet coke was demonstrated for the first time by Berguerand and Lyngfelt (2009). The system presented an air reactor working in fast fluidisation regime and a fuel reactor, under bubbling conditions, which exhibits some differences in its design compared to the one used for gaseous fuel. Indeed, the reducer is divided into three chambers: low velocity chamber for fuel devolatilisation, high velocity chamber for solids recirculation and a carbon stripper chamber to recover the unconverted fuel from the metal oxides particles to be transferred to the air reactor (Fan and Li, 2010). Solid fuel is fed on the top of the fuel reactor and ilmenite oxygen carrier particles were used to convert the fuel. The solid fuel conversion detected was between 50% and 80% for bituminous coal and around 70% for pet coke. CO_2 concentration in the fuel reactor off-gas ranged from 70% to 80%. High value of unconverted char, fuel volatiles leaving the system unconverted and CO_2 detection in the air reactor off-gas represent the main issues that still have to be tackled in the development of an efficient CLC system for solid fuel conversion.

Adanez et al. (2009, 2010) published results performed in a 500 W CLC unit using natural gas as a feedstock and Ni- and Cu-based oxygen carriers. Fuel and air reactor in bubbling regime with the latter equipped with a narrow upper section for the particles entrainment are the main features of this configuration.

Vienna University of Technology proposed a different fuel reactor operating mode at turbulent conditions. A 140 kW dual circulating fluidised bed system fed with natural gas or syngas using either nickel or ilmenite oxides was successfully operated (Kolbitsch et al., 2009a, 2009b, 2010; Proll et al., 2010). The air and fuel reactor are both circulating with the latter having a return flow for the particles and a direct fluidised connection at the bottom with the air reactor that allows for the particles moving back to the air reactor. The choice to operate with a fuel reactor at turbulent regime seems to lead to several advantages compared to the bubbling bed solution in terms of: increase in the gas-solid contact over the whole length of the fuel reactor due to avoided gas by-pass through the bubble phase, resulting decrease in solid inventory to achieve full gas conversion. The drawback is related to the more complex reactor design. The overall results show a fuel conversion up to 95% for methane and 99% for syngas when NiO particles were used.

Ryu et al. (2010) presented a new 50 kW CLC unit operating with nickel oxide particles supported with bentonite. Air and fuel reactor are both bubbling beds with internal risers into which the solid particles are transferred through holes. The gas, flowing in each riser, carries the particles up to the reactor outlet where a cyclone allows for the gas-solid separation. The particles then fall down in a downcomer immersed in the fluidised beds. From processing methane, 99.2% CO_2 and 0.8% CO was achieved at the exit from the fuel reactor.

Overall, being aware that scale effects could alter the CLC performances (e.g. CO_2 capture efficiency drops from 99+% in 10 kW scale CLC unit to 97% in 120 kW scale CLC unit (Fan, (2010)), the results from the different groups suggest that CLC technology is ready to be scaled up to 1 or 10 MW size in the case of gaseous fuel. On the other hand, it needs more research into fuel reactor design in the case of solid fuels (Lyngfelt et al., 2011).

1.6.4 CLC key features

In Section 1.6.1, an overview of the oxygen carriers for CLC and their characteristics was discussed. Their performance is fundamental for the feasibility of the CLC process; indeed the analysis of the particles reactive properties from Thermo Gravimetric Analysis (TGA) test and/or lab scale fluidised bed reactors helps in understanding the optimal design and operation of a future CLC system application at large scale. For this reason, as mentioned in Section 1.6.3, over 700 metal oxides have been tested and even more will probably be examined in the future. Furthermore, several other parameters play an important role in achieving the desired output from a CLC process, such as solid inventories, solid circulation rate between the reactors, gas-solid contact mode, gas velocity, solid hold-up, heat and mass transfer and solid degree of conversion. Lyngfelt et al. (2001) reported an understandable link between the oxygen carrier properties and the CLC design parameters as shown in Fig. 1.20.

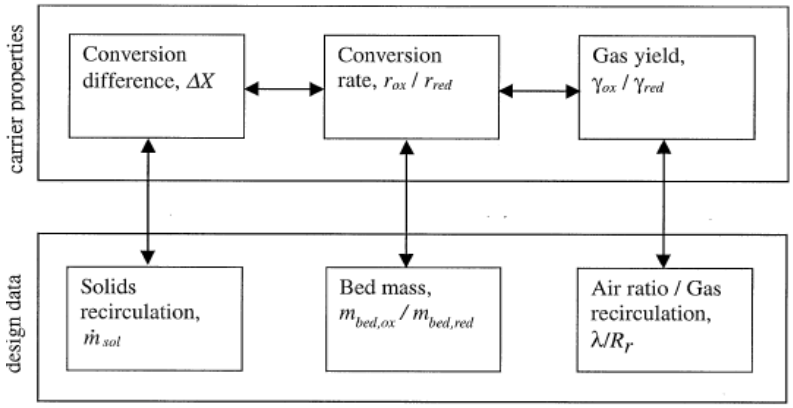

Fig. 1.20 Basic relations between carrier reactivity and design data (Lyngfelt et al., 2001)

From Fig. 1.20, it is noticeable that the oxygen carrier conversion rate for both oxidation and reduction reactions is linked to the difference in solid conversion that, in its turn, affects the solid circulation flow-rate between the reactors. These three variables influence the total solid inventory needed to achieve a desired gas yield. In particular, an inverse proportionality between conversion rate and bed mass as well as solid conversion difference and solid circulating flow-rate exists and it will be discussed later. The gas yield in the oxidiser is linked to the reaction rate and the oxygen in excess that could be fed whereas the gas yield in the reducer is linked to the reduction rate and the gas recirculation, if the latter is applied.

Also Kronberger et al. (2005a) reported a comprehensive design procedure for CLC process (Fig. 1.21) based on schematic interconnected blocks. The CLC process is divided into five schematic blocks: design specifications, reaction kinetics, hydrodynamics, design criteria and further design specifications. The procedure considers the flow rates of fuel and oxygen carrier, the oxygen capacity of the carrier and the kinetics and hydrodynamics in both the air and fuel reactors. The interconnection between these five blocks is considered to optimise the whole CLC process.

In addition, Wolf (2004) pointed out in a similar way the essential factors of an efficient CLC system: adequate solid circulation between the fuel and air reactors as well as satisfactory contact time between the fuel/air and the solid oxygen carrier to achieve complete fuel combustion, high temperature and high pressure operation to maximise the overall efficiency of the power generation.

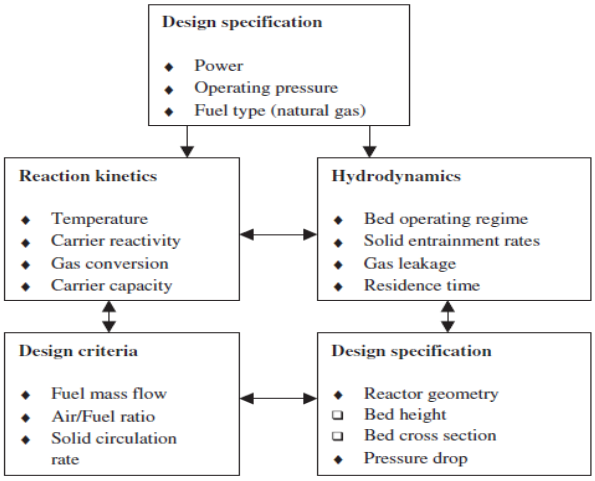

Fig. 1.21 Design procedure of a CLC system (Kronberger et al., 2005a)

In respect of the concepts aforementioned, a modelling approach is extremely important to predict the effect of the operating conditions, kinetic and hydrodynamic phenomena involved in the CLC process on the gas yield as well as the solid inventory required to achieve full fuel conversion. Furthermore, adequate models can also estimate the influence of the reactors performance on the thermal efficiency of the power plants in which the CLC units are embedded.

Overall, since all these factors contribute to the cost of electricity generated from a power plant, an appropriate modelling strategy will allow a comparison between

different CO_2 capture solutions. Furthermore, it will address the choice of the best option aimed either to minimise the CO_2 emissions into the atmosphere or to reduce the obvious raise in the cost of the electricity due to the implementation of the CO_2 capture units.

1.6.5 CLC modelling with natural gas as feedstock: state of the art in the literature

As previously discussed, CLC is a promising technology for CO_2 capture that can be applied with gaseous and/or solid fuel either as a primary reactor or embedded e.g. in an IGCC power plant as a CO_2 capture unit. The choice of using a CLC unit e.g. in a IGCC power plant as a separation unit, either for electricity or hydrogen and electricity production, does not seem to be the best option to exploit fully its potential. Indeed, the main issue that slows down a wide commercialisation of an IGCC power plant concerns with the high cost of investment of an IGCC power plant. The latter is more expensive than a PC power plant with no CO_2 capture section employed whereas a difference trend was estimated if a CO_2 capture section based on the traditional carbon capture technologies is applied (DOE/NETL, 2007). However, since a CLC unit exhibits a high cost of investment (Klara, 2007), the high cost of the gasifier together with the CLC unit cost would lead to a plant cost investment so high that the application of a CLC separation unit would not be justified even if a high thermal efficiency could be achieved (Rezvani et al., 2009).

On the other hand, a CLC unit as a primary reactor to burn directly gaseous or solid fuel is a very attractive solution. As pointed out by Lyngfelt (2011), reactor design issues need to be sorted out when a solid fuel is directly burned in the fuel reactor of a CLC unit. Conversely, a CLC unit as primary reactor to burn natural gas is considered ready to be commercialised. In this respect, a modelling approach of an NGCC power plant with CLC applied is very useful to understand under which conditions this technology exhibits an actual advantage compared to the traditional carbon capture technologies such as chemical absorption with MEA.

Several works on the modelling of the CLC technology fed with natural gas (or simply pure methane) have been reported in the literature and the most relevant to the objectives and the novelty of this thesis are presented as follows.

Abad et al. (2007) reported a mathematical model to estimate the total solid inventory in a CLC unit for different oxygen carriers (Ni-, Cu- and Fe-based carriers) reacting with methane. The main outcomes of their work are related to the optimisation of either the solid circulating flow-rate or the metal oxide conversion at the riser exit to minimise the total solid inventory in the reaction system. Higher circulating solid flow-rates leads to lower average solid conversion and thus higher kinetic rates and lower amount of bed material needed to achieve full gas conversion. The model proposed assumes riser and fuel reactor with perfect mixing of solid and under the same hydrodynamic conditions: gas plug flow in the beds and no resistance to the gas exchange between the bubble and the emulsion phase in the fuel reactor. Since the effect of gas by-pass and the mass transfer limitations in the fuel reactor as well as the decrease in the solid volume fraction in the riser are not taken into account, the values of the minimum solid inventory reported are very low (from 40 to 133 kg/MW at atmospheric pressure if Ni- and Cu-based carriers are used). The results obtained are in agreement with the data reported by Lyngfelt (2011) that states how under predicted values of solid inventory to achieve full gas conversion are estimated if only kinetic aspects are considered. Indeed, values of solid inventory that range from 100 to 500 kg/MW, depending on the solid carrier and operating conditions, are expected if the actual hydrodynamics is taken into account.

Abad et al. (2010) reported a full mathematical model written in FORTRAN of a bubbling bed fuel reactor based on the two phase theory (Davidson et al., 1963). The reaction occurred between methane and Cu-based oxygen carrier. The fuel reactor modelled was not connected to an air reactor model and was not embedded into an NGCC power plant simulation. Therefore the effect of the optimal conditions applied to the fuel reactor on the riser cannot be estimated; moreover, the influence of the operating conditions of the reactor on the thermal efficiency of the power plant cannot be evaluated.

Computational fluid dynamics (CFD) simulations of gaseous fuel combustion in CLC unit (Jung and Gamwo, 2008; Kruggel-Emden et al., 2010, 2011; Mahalatkar et al., 2011; Shuai et al., 2011a, 2011b) have been employed to understand at the particle level how the kinetics and the hydrodynamics influence the motion of the solid particles into a fluidised bed, the gas-solid contact efficiency and therefore the outlet fuel conversion. The disadvantages of this micro level approach are related to the computational cost, the

long runs of simulation and in particular, the small domain that can be processed (few or most commonly just one unit processed).

Focusing on the whole NGCC power plant, Wolf et al. (2005) and Naqvi et al. (2004, 2007) carried out a plant thermal efficiency evaluation employing a CLC unit as a primary reactor. The main outcomes of their work can be summarised as follows: the temperature of the spent air at the riser exit to drive a gas turbine has the most important impact on the thermal efficiency of the power plant since a drop in temperature of 200 ˚C (from 1200 ˚C to 1000 ˚C) results in an efficiency decrease by about 4% points; an operating pressure of the CLC system ranges from 10 to 20 atm is considered optimal to maximise the plant efficiency; an overall thermal efficiency by about 52-53% with only 2-3% efficiency drop compared to the case with no capture was estimated; the overall thermal efficiency reported is higher than the one from an NGCC with MEA post-combustion carbon capture applied. The analysis of the plant thermal efficiency was based on simplified assumptions for the reaction system using a code written in FORTRAN; in fact, no kinetics and hydrodynamics were implemented. In this way the size of the two reactors cannot be calculated precisely and an economic analysis of the power plant cannot be carried out with a good degree of accuracy.

Kvamsdal et al. (2007) reported an overall thermal efficiency at about 51% for an NGCC power plant integrated with CLC (see Section 1.6.2.4); the reactors were modelled under simplified assumptions from the work presented by Naqvi et al. (2004).

Hassan and Shamim (2012) simulated in Aspen Plus software an NGCC power plant employing CLC technology; employing a Gibbs reactor model for both fuel and air reactor they reported a plant thermal efficiency at about 50% with energy penalties of about 2%. Unfortunately, the use of a Gibbs reactor model does not allow estimation of the size of the reactors and thus an economic analysis of the process.

Focusing on the economics, Petrakopoulou et al. (2010, 2011) carried out an economic analysis of a NGCC power plant based on the CLC technology assuming the CLC unit size based on an analogy with a fluidised bed biomass gasifier under simplified considerations.

Overall, research linking the kinetic and hydrodynamic phenomena of CLC to the cost of electricity generated is not available in the literature but isolated parts of whole topic have been investigated, as reported above. The linking among sections is crucial in making comparisons between CLC and different carbon capture technologies since the reaction system largely influences the *LCOE* that represents the parameter that really matters. Indeed, the main issue for the feasibility of the CLC technology might concern the amount of the solid material needed to get full fuel conversion and the associated costs (Abad et al., 2007). The total solid inventory affects the sizes of the fluidised beds and thus the capital cost of the CLC power plant. Furthermore, the price of the metal oxide particles, together with their lifetime would be partly responsible for the extra operating cost due to the solid make-up. Thus, a modelling strategy that links reactor models counting for kinetic and hydrodynamic phenomena to power plant configurations for overall thermal efficiency estimations and consequently leads to an economic analysis of the whole process is considered essential.

1.7 Objectives of the work

The objective of the work is the modelling of the CLC unit by means of software potentially able to link the physics of the reaction unit to the cost of the electricity generated. This work makes use of Aspen Plus, simulation software largely used in industry for whole plant modelling, given its ability to simulate a variety of steady-state processes ranging from single unit operations to complex processes involving many units. The use of this kind of software sets some limitations in terms of accuracy in modelling the complex phenomena taking place in reactors such as fluidised beds. On the other hand, it offers the possibility of integrating a reaction system into power plant configurations and evaluate the influence of the reaction conditions on the plant efficiency in terms of either thermal output or economic impact. Therefore, one of the aims of this work concerns the improvement of the capability of the software. The latter is achieved using additional subroutines in FORTRAN and Excel, to implement and link in only one package all the information needed for a full evaluation of the CLC technology applied to a NGCC power plant, from the reaction aspects to the cost of the electricity generated.

Overall, the aims of this thesis can be summarised as follows:

- Development of our own model in Aspen Plus for the CLC reaction system composed of the fuel reactor working in bubbling bed regime and the air reactor working at fast fluidisation conditions;
- Implementation of the kinetic and hydrodynamic phenomena to mimic the behaviour of the fluidised beds at macro-scale level;
- Improvement of the macro-scale model built in Aspen Plus through comparisons with a micro-scale model coming from computational fluid dynamic (CFD) simulations;
- Integration of the reactor models in different NGCC power plant configurations with mass and energy balances solved simultaneously at the conditions specified by each plant arrangement;
- Analysis of the optimum operating conditions for the CLC unit to minimise the total solid inventory into the beds, so reducing the plant costs;
- Estimation of the thermal efficiency of the different plant configurations;
- Development of our own economic model for the economic evaluation of the NGCC-CLC power plant with particular attention to the effect of the fuel price and the lifetime of the solid particles on the *LCOE*.

Finally, a general approach to compare the CLC technology with the well-known state-of-art technologies for CO_2 capture is suggested.

1.8 Outline of the thesis

The present thesis is organised in six chapters with their own introduction.

Chapter 1 reviews the main sources of CO_2 emissions, explains the need to reduce them and points out the effectiveness of applying a CCS strategy. Furthermore, a general overview of the existing power plants for electricity production and their integration with different carbon capture strategies is presented; in addition, particular attention is given to the Chemical Looping Combustion (CLC) technology for carbon capture. The main features of the CLC technology as well as its applicability and operational experience are reported. Finally, the motive and the objectives of the thesis are manifested in detail.

Chapter 2 focuses on the modelling of the fuel reactor at bubbling bed conditions. A preliminary fluidised bed model is developed and implemented in Aspen Plus to

account for gas by-pass and mass transfer limitations. Kinetics and hydrodynamics are implemented using subroutines in FORTRAN and Excel.

Chapter 3 reports a strategy to improve the macro-scale bubbling bed model built in Aspen Plus. A 2D computational fluid dynamics (CFD) analysis of the fuel reactor is carried out in an open source code called MFIX. The results, in terms of the effect of the different kinetic and hydrodynamic conditions on the outlet gas conversion, are compared with the results coming from the macro-scale model implemented in Aspen Plus. Based on the micro-scale (CFD) outcomes, the macro-scale model is enhanced to capture the main physics influencing the performance of the fuel reactor.

Chapter 4 describes the integration of the improved fuel reactor model into a NGCC power plant. An air reactor model for fast fluidisation conditions is developed to complete the modelling of the CLC unit. The CLC unit is embedded into three power plant configurations. The analysis of the main variables affecting the total solid inventory into the beds is carried out; mass and energy balances are solved simultaneously for the reaction system; optimum operating conditions for the CLC unit aimed to minimise the total solid inventory are applied and the overall plant thermal efficiency as well as CO_2 capture efficiency is estimated.

Chapter 5 reports an economic analysis for the plant configuration that exhibits the highest thermal efficiency. An economic model is developed in Excel code in a way that is easy to link with the process simulation run in Aspen Plus. Plant investment costs, operating costs and the *LCOE* are estimated. The influence of the fuel price and the lifetime of the solid particles on the *LCOE* are highlighted. A comparison between the CLC technology and a post–combustion capture strategy with MEA is carried out and more in general a method to compare the CLC technology with other carbon capture solutions is proposed.

Chapter 6 summarises the results of the previous chapters and it suggests the future work to be undertaken.

Chapter 2

Preliminary Fuel Reactor model in Aspen Plus

When a variety of information on the CLC process is needed, process simulators such as Aspen Plus, Aspen Hysys, PRO/MAX, PRO/II can be applied. These packages are largely used for whole plant modelling given their ability to simulate a variety of steady-state processes ranging from single unit operation to complex processes involving many units. Such codes work with different standard blocks that represent the main unit operations in the simulated process (e.g. PFR and CSTR reactors, absorbers, distillation columns, etc.). Mass and heat balances are executed within the blocks. Inlet and outlet mass and heat streams link the blocks to each other. In this way, thermal efficiency estimation and cost analysis can be readily undertaken for the whole process.

When an attempt is made to simulate CLC processes with one of the process packages, fluidised beds would need to be represented, and these are not described specifically in any of the above packages. Nevertheless, a comprehensive representation of the process cannot neglect the complex hydrodynamics and kinetics in the reactors. A way to solve this issue has been proposed by Jafari et al. (2004) who employed a number of basic blocks (e.g. ideal reactors, usually PFRs and CSTRs) combined in a fashion that could simulate the real hydrodynamics and/or kinetics. Indeed, single CSTR or PFR reactors would take into account only the kinetics of the reactive system but not the hydrodynamics; conversely, combinations of CSTRs and PFRs and additional employed subroutines may be able to model both the kinetics and hydrodynamics inside the fluidised beds. Following this strategy, fluidised beds have been implemented in Aspen Plus for a number of process set-ups (e.g. Sarvar-Amini et al. (2007) modelled a fluidised bed membrane reactor; Sotudeh-Gharebaagh et al. (1998) and Liu et al. (2012) modelled a fluidised bed for coal combustion; Sohi et al. (2012) modelled a fluidised bed for gas natural combustion).

To the best of my knowledge, in Aspen Plus fluidised beds for CLC have been modelled exclusively by using a Gibbs reactor which is based on the minimisation of the Gibbs free energy (Fan, 2010; Li et al., 2009). The Gibbs reactor has the advantage that stoichiometric equations are not needed. Equilibrium final conditions are determined from the Gibbs free energy and the heat of reaction is calculated

automatically. Processes that come close to equilibrium may be modelled using this technique. The drawback of this approach lies on the overestimation of the conversions of the species inside the reactor since effects such as gas by-pass and mass transfer and/or kinetic limitations, for instance, are neglected. Those effects are of importance in determining the real gas conversion. Additionally, if ideal conditions are assumed i.e. the Gibbs reactor is employed, the reactor size cannot be estimated. Thus, the solid inventory inside the reactor to get full gas conversion cannot be calculated and its impact on the economics results unpredicted.

In this chapter, a model is proposed for the fuel reactor of the CLC unit, working in bubbling bed conditions, in a fashion that accounts for the mass transfer limitations affecting the gas conversion inside the reactor. Additionally, a heterogeneous, non-catalytic reaction is incorporated in the model, to take into account the kinetics of reaction (shrinking-core model).

2.1 Reduction reaction system under investigation

In this work, pure methane as representative of natural gas feedstock and NiO/Ni oxygen carrier (supported with Al_2O_3) were chosen as fuel and solid reactant, respectively. The choice of NiO as oxygen carrier is related to its higher oxygen carrier capacity, higher melting point and heat of exothermic reaction compared to the other carriers. These aspects lead to higher kinetic rate; indeed, either the fuel or the air reactor can work at higher reaction temperatures and higher amount of heat would be conveyed from the riser to the fuel reactor using a lower solid circulating flow-rate. Furthermore, being aware that a Ni-based oxygen carrier might present environmental issues, its reduction reaction with methane has been also selected because of the large amount of kinetic data available from the literature useful to implement and validate the model proposed. However, various metal oxide particles could be employed in this work, once their kinetics are known.

Eq. 2.1 shows the main reduction reaction employed:

$$CH_4 + 4NiO \longrightarrow CO_2 + 2H_2O + 4Ni \qquad (2.1)$$

Various studies have been carried out to characterise the reduction behaviour of metal oxides and different gases have been considered including CO, H_2, CH_4 (Ishida et al., 1996; Ryu et al., 2001; Mattisson et al., 2001). Many authors have used kinetic models, based on shrinking core and nucleation and nuclei growth model, to represent the chemical kinetics of the metal oxides (Hossain and de Lasa, 2008). The best fit with experimental data is achieved with one of these two models depending on the gas reactant, the metal oxides considered and its preparation method.

As reported by several authors (Garcia-Labiano et al., 2005; Mattisson et al., 2011), a kinetic expression based on the shrinking core model fits reasonably the experimental data for the reduction of NiO with methane. The model assumes that the reaction happens on the surface separating the unreacted solid from the reacted shell. The initial reaction surface corresponds to the initial external surface of the solid. The thickness of the reacted shell increases with time, determining the shrinking core of un-reacted solid (Ryu et al., 2001; Levenspiel, 1972). Additionally, even if the heterogeneous gas-solid reaction proceeds via three steps (namely, external mass transfer, internal diffusion and chemical reaction (Levenspiel, 1972)), the reduction of NiO particles, having diameters as small as hundreds of microns, with methane seems to be controlled by the chemical reaction step.

Ruy et al. (2001) demonstrate that the reduction rate for NiO/Ni particles supported by bentonite is controlled by the chemical reaction. Garcia-Labiano et al. (2005, 2006) studied the CLC kinetics and the variations in the structure of the oxygen carrier were considered together with various geometries; the changing grain size model was utilised. Small particles (30–70 μm) were selected to minimise mass transfer limitations. The overall result was that the shrinking core model with the reaction being the controlling step describes well the experimental data.

Overall, since the oxygen carrier particles used in CLC have small diameter and high internal porosity, the shrinking core model with the reaction being the controlling step can be considered a good model to be applied. Consistently, the kinetic parameters for the reduction reaction to applied in our work (see Table 2.1) are taken from the work of Abad et al. (2007). They derived them using the Shrinking Core Model (SCM) for spherical grain size geometry, meaning that it was assumed that the particle was

composed of spherical grains of NiO reacting according to the SCM under chemical reaction control in the grain surface.

NiO particles are (60% - 40%) Al_2O_3 supported but only 40% of their mass content is active. The particle density, ρ_s, is equal to 3446 kg/m^3. The kinetic constant k for the reduction reaction follows the Arrhenius law. In addition, Abad et al. (2007) provided the kinetic parameters for the oxidation reaction between the air and reduced metal oxide particles, as shown in Table 2.1.

Table 2.1 Kinetic parameters for the reduction and the oxidation of NiO (Abad et al., 2007)

	Reduction reaction	**Oxidation reaction**	
particle size d_p	2.00x10^{-4}	2.00x10^{-4}	m
grain radius size r_g	6.90x10^{-7}	5.80x10^{-7}	m
kinetic coefficient k_o	0.71	1.80x10^{-3}	mol$^{(1-n)}$m$^{(3n-2)}$/s
activation energy E_a	78000	7000	kJ/kmol
order of reaction n	0.8	0.2	
pressure effect q	0	0.46	

The parameters in Table 2.1 can be applied to calculate the Thiele modulus, *mL* (Eq. 2.2), and verify that the chemical reaction is the controlling step of reaction, as stated by the authors. The Thiele modulus comes from a mathematical derivation applied to catalytic porous solid particles (Levenspiel, 1972) but it provides a general indication on the controlling step of reaction also in the case of non-catalytic gas-solid reactions with porous solid structure.

$$mL = \frac{R}{3}\sqrt{\frac{k_o e^{-\frac{E_a}{R^I T}} S \rho_s}{\delta}} \tag{2.2}$$

Eq. 2.2 is derived under the assumption of first order kinetics. In Eq. 2.2, R is the external radius of the particle, S is the specific surface area, equal to 0.8 m^2/g (Abad et al., 2007), and δ is the methane coefficient of diffusivity, assumed equal to 2*10^{-4} m^2/s for a rough calculation (typical diffusivity coefficient value of methane in gases at 950 °C). The resulting Thiele modulus, *mL*, is equal to 0.06. From the literature (Levenspiel, 1972), Thiele modulus values lower than 0.5 guarantee that the internal diffusion

resistance inside the pores is negligible. Thus, the assumption of chemical reaction as the controlling step of the reduction reaction can be considered reasonable.

Beside the main reduction reaction of methane with NiO producing CO_2 and H_2O, secondary reactions that lead to CO and H_2 production were found (Iliuta et al., 2010; Linderholm et al., 2008; Ortiz et al., 2012). Indeed, the nickel oxide in its reduced state catalyses the steam methane reforming reaction and the water-gas shift reaction. H_2O produced from the main reaction can react again with methane to produce catalytically CO and H_2; CO can either react catalytically with H_2O to produce CO_2 and additional H_2 or react with NiO to produce CO_2; the H_2 produced can react again with NiO for H_2O formation. The combination of catalytic and no catalytic reactions leads, if the equilibrium conditions are reached, to almost 100% in methane conversion with selectivity in CO_2 that ranges from 98.5% to 99.5% depending on the temperature conditions. Overall, the yield in CO_2, defined as the mole fraction of carbon dioxide in the carbon-containing products (see Eq. 2.3), is less than 100%.

$$\gamma_{red} = \frac{P_{CO2\ out}}{P_{CH4\ out}+P_{CO\ out}+P_{CO2\ out}} \tag{2.3}$$

In Eq. 2.3, P_i is the partial pressure of the *i* gaseous species. Linderholm et al. (2008) carried out experiments with a 10 kW CLC prototype using a fuel reactor in bubbling conditions. They reported a CO_2 molar fraction at the exit of the reactor around 99% in a range of temperature 800-1000 ˚C with a small percentage of CO and H_2 detected, close to the equilibrium conditions: around 1% for H_2 and less than 1% for CO detected after condensation of H_2O. In 2001, Mattisson and Lyngfelt determined the equilibrium conditions for different metal oxides, including NiO, while reacting with methane. They used the method of the minimisation of Gibbs free energy considering pure methane that reacts in a range 700-1200 ˚C and 1 bar and including in the calculation all the possible gaseous species that could be produced: CO_2, H_2O, CO, H_2 and O_2. They found a yield in CO_2 that was temperature-dependent and always above 97% for the NiO oxygen carrier in the range of temperature applied. Jerndal et al. (2006) reported an analysis similar to the previous one leading to a yield in CO_2 equal to 98.83% at 1000 °C with almost 100% of methane conversion.

In this work, the same analysis was performed in Aspen Plus using a Gibbs reactor to confirm the thermodynamic constrictions of the reactive system. Methane and a stoichiometric amount of NiO enter a Gibbs reactor at atmospheric pressure and constant temperature. CO_2, H_2O, CO, H_2 and O_2 are considered as potential products of the reaction and thus, they are implemented in our simulation. The results are displayed in Table 2.2.

Table 2.2 Analysis of the equilibrium conditions at P = 1 atm using a Gibbs reactor

Temperature		1200 ˚C	1100 ˚C	950 ˚C
	in (kmol/s)	out (kmol/s)	out (kmol/s)	out (kmol/s)
CH_4	0.125	$6x10^{-16}$	$2x10^{-15}$	$2x10^{-14}$
CO_2	0	0.1231	0.1233	0.1237
H_2O	0	0.2480	0.2480	0.2480
CO	0	0.0016	0.0013	0.0010
H_2	0	0.0013	0.0013	0.0013
O_2	0	0	0	0
CH_4 conversion %	-	99.99	99.99	99.99
CO_2 selectivity %	-	98.73	98.90	99.23
CO_2 yield %	-	98.73	98.92	99.23
CO %	-	0.42	0.36	0.26
H_2 %	-	0.34	0.35	0.35

My analysis shows that, at equilibrium, the methane conversion is around 99.99% while the selectivity and consequently the yield in CO_2 is around 99% with very small percentage of CO and H_2 at the reactor exit. Based on all the previous considerations, we assumed to neglect the secondary reactions that lead to CO and H_2 production and to implement only the main reduction reaction in the fuel reactor (see Eq. 2.1) applying the kinetic parameters reported by Abad et al. (2007). The reason for the latter is also linked to the fact that not all the kinetic parameters were found in the literature to implement either all the reactions occurring in the fuel reactor or the oxidation reaction occurring in the riser. Indeed, to be consistent, the kinetic parameters for the oxidation reaction, which will be applied at a later stage for the air reactor modelling, are taken from the same work.

However, in the case of the oxidation reaction, the activation energy, equal to 7 kJ/mol, is very low compared to the values reported in the literature, raising the doubt that the chemical reaction is not the controlling step of the reaction as stated by Abad et al. (2007). Kofstad (1957) reported an activation energy around 170 kJ/mol in a range 700-

1050 °C; Fueki and Wagner (1965) reported activation energy values of the same magnitude in a range 900-1400 °C; Karmhag and Niklasson (1999) reported an activation energy around 140 kJ/mol in a range 200-700 °C. Ruy et al. (2001) described how the nickel oxidation reaction is product-layer diffusion control due to the resistance that the oxygen encounters in penetrating the compact NiO layer whose thickness increases with time. The latter finding is supported by the fact that the kinetic rates in Abad et al.'s (2007) work drop as the total pressure increases. Usually the increase in the total pressure has a negative effect on the molecular diffusivity leading to the conclusion that the internal mass transfer affects the kinetics. In Abad et al.'s (2007) work, the negative effect of the pressure on the kinetics is taken into account assuming an apparent pre-exponential kinetic coefficient that is inversely proportional to the total pressure (see also Section 4.2) while keeping the SCM under chemical reaction control. It is likely that the authors found the values of activation energy, pre-exponential kinetic coefficient and order of the reaction that better fit their kinetic model although the latter might not be the right representation of the actual mechanism, which likely involves the internal transport resistances.

However, further investigation of the actual kinetic mechanism of oxidation is beyond the purpose of this work; thus, as aforementioned, to be consistent, the kinetic parameters and assumptions for the oxidation reaction provided by Abad et al. (2007) are kept and applied at a later stage for the air reactor modelling.

2.1.1 Kinetic expression implemented in Aspen Plus

The reduction and the oxidation rate of the oxygen carrier in the field of CLC are usually expressed in percentage of solid conversion over time ([=] %/min) calculated through the weight loss percentage of the solid sample over the time from TGA experiments. Aspen Plus software does not accept a kinetic expression in %/min unit and thus, some manipulations of the kinetic expression (see Eqs. 2.4-2.12) are needed to express the kinetic rate in an acceptable form for the software. Indeed, in Aspen Plus the reaction volume considered in the mass and energy balances is often the occupied gas volume and the kinetic rate is mainly expressed in kmol/(m^3s) of gas-volume.

Thus, a suitable kinetic expression for both the reduction and the oxidation reaction of Ni-based carrier applying the shrinking core model is derived from the theory reported

by Levenspiel (1972). If the chemical reaction is the controlling step, the amount of reacting moles is proportional to the available surface of the unreacted core and the kinetic rate for a single solid particle is expressed as follows:

$$-\frac{1}{4\pi r_c^2}\frac{dN_B}{dt} = bkC_A \tag{2.4}$$

where N_B is the number of moles of the B solid reactant, C_A is the molar concentration of the A gas ([=] kmol/m^3), r_c is the average particle radius at the reaction surface, b is the stoichiometric coefficient of the reaction and k is the kinetic coefficient expressed in m/s. According to the shrinking core model:

$$r_C = R(1 - X_B)^{\frac{1}{3}} \tag{2.5}$$

where X_B is the average conversion of the B solid reactant and R is the external radius of the particle.

Thus:

$$-\frac{dN_B}{dt} = bkC_A 4\pi R^2 (1 - X_B)^{2/3} \tag{2.6}$$

If we refer, as a reaction volume, to the occupied gas volume expressed as a fraction of the total volume of the reactor, we obtain:

$$-\frac{1}{V_{reaction}}\frac{dN_B}{dt} = \frac{bkC_A 4\pi R^2 (1-X_B)^{2/3}}{V_{tot}\varepsilon_g} \tag{2.7}$$

where V_{tot} is the volume of the reactor and ε_g is the gas volume fraction. In our reactive system n_p spherical particles are present, defined as follows:

$$n_p = \frac{V_{tot}\varepsilon_s}{\frac{4}{3}\pi R^3} \tag{2.8}$$

where ε_s is the solid volume fraction. Hence, the global kinetic rate expressed in kmol/(m^{3}s) of gas volume is the result of the product between the kinetic rate for a

single solid particle (Eq. 2.7) multiplied by the number of solid particles (Eq. 2.8), as follows:

$$r = \frac{3bkC_A\varepsilon_s(1-X_B)^{2/3}}{R\varepsilon_g} \tag{2.9}$$

The kinetic expression implemented in Aspen Plus applying the order of reaction reported by Abad et al. (2007) is finally expressed as follows (Porrazzo et al., 2014):

$$r_{i\ Aspen} = \frac{k_i\varepsilon_s C_i^n(1-X_j)^{\frac{2}{3}}}{\varepsilon_g} \tag{2.10}$$

and

$$k_i = \frac{3k_o e^{-\frac{E_a}{R'T}}}{r_g} \tag{2.11}$$

where *i* is referred to CH_4 for the reduction and O_2 for the oxidation reaction, *n* is equal to 0.8 for the reduction and 0.2 for the oxidation reaction; *j* is referred to NiO for the reduction and Ni for the oxidation reaction.
Hence, the kinetic rate is a function of the solid fraction inside the reactor, ε_s, the gas concentration, C_i, and the metal oxide conversion, X_j. The kinetic expression is divided by the gas void ε_g because the reference volume of reaction is the volume occupied by the gas phase.

Different ways to express the solid conversion are reported in the literature (Jung and Gamwo, 2008; Kruggel-Emdem et al., 2011; Lyngfelt et al., 2001; Mahalatkar et al., 2011). In the present work, the solid conversion is a function of the molar solid flow-rate (Eq. 2.12), F_j, since it is only suitable way to carry out a steady state simulation in Aspen Plus.

$$X_j = 1 - \frac{F_{j\,out}}{F_{j\,in}} \tag{2.12}$$

2.2 Bubbling bed hydrodynamics

In fluidised bed reactors, the hydrodynamics play an important role in achieving the desired gas conversion. Lyngfelt (2011) pointed out how neglecting the mass transfer resistances and the imperfect gas-solid contact efficiency in the fluidised beds leads to wrong results in terms of total solid inventory needed in the CLC system. Indeed, considering just the kinetic phenomena, only 10-20 kg/MW of solid material might be sufficient to achieve full gas conversion when NiO is used as an oxygen carrier, depending on the operating conditions.

In the bubbling bed fuel reactor, bubble growth determines gas by-pass along the bed and thus most of the gas is subtracted to the contact with the solid particles. As a result of this phenomenon, a decrease in the efficiency of the gas-solid reaction occurs and a larger amount of solid inventory is necessary to achieve the desired gas yield; the latter aspect affects greatly the economics of the process.

Kunii and Levenspiel (1990) proposed various strategies to model the actual behaviour of the fluidised bed depending on the class of particles involved. All these models recall the two phase theory introduced by Davidson et al. (1964). According to this theory, at the macroscopic scale, a bubbling bed can be ideally thought as made of two phases: a so called "emulsion phase" characterised by good mixing of gas and solid particles and a so called "bubble phase" at low content of solid acting as gas by-pass along the bed. Furthermore, the excess of gas to keep the minimum fluidisation condition in the emulsion phase is transferred to the bubble phase. Based on this theory, Kunii and Levenspiel (1990) proposed three different models:

1) For fine solid particles and bubble velocity $U_b >> U_e$ (with U_e being the gas velocity in the emulsion phase), an up-flow of gas in the bubble phase along the bed and perfect mixing of gas and solid in the emulsion phase are assumed; gas mass transfer occurs between the two phases along the bed height;
2) For intermediate solid particles and $U_e < U_b < 5 * U_e$, up-flow of gas in both phases along the bed height is assumed and gas mass transfer occurs between them;
3) For large particles and $U_b < U_e$, only one phase with up-flow of gas and solid along the bed is assumed with occasional shortcut through the bubbles.

The two phase model points out the importance of the gas mass transfer between the bubble phase and the emulsion phase. As previously mentioned, several authors

proposed combinations of CSTRs and PFRs to mimic the real behaviour of a fluidised bed in Aspen Plus (Eslami et al., 2012; Jafari et al., 2004; Porrazzo et al., 2014; Sarvar-Amini et al., 2007). Given the initial conditions assumed, the case studied in this work reflects Kunii and Levenspiel model 1. Consequently, a conceptual modelling initially proposed by Jafari et al. (2004) for first order catalytic reaction in fluidised beds is applied for CLC purposes, as described below.

2.2.1 Hydrodynamics implemented in Aspen Plus

The fluidised bed model implemented in Aspen Plus assumes that the emulsion phase is at minimum fluidisation conditions; the excess of gas with respect to U_{mf} is transferred to the bubble phase since for Geldart class B particles, which reflect our case, the minimum bubbling velocity, U_{mb}, is equal to the minimum fluidisation velocity (Kunii and Levenspiel, 1991). Isothermal conditions within the bed are assumed and the radial mass solid gradient is neglected.

Fig. 2.1 shows the fluidised bed model implemented in Aspen Plus. The bubble phase is modelled with a plug flow reactor (PFR) and the emulsion phase is modelled with a perfect mixing reactor (CSTR). The whole bed is axially divided into several stages of the same length/height; each stage is composed of a PFR to mimic the up-flow of gas through the bubble phase and a CSTR to mimic the perfect mixing between gas and solid. Mass transfer between the two reactors (PFR and CSTR) representing each stage occurs at their respective exit streams and the values of the molar gas flow-rates (M_{CH4}, M_{CO2} and M_{H2O}) at the beginning of the following stage are updated.

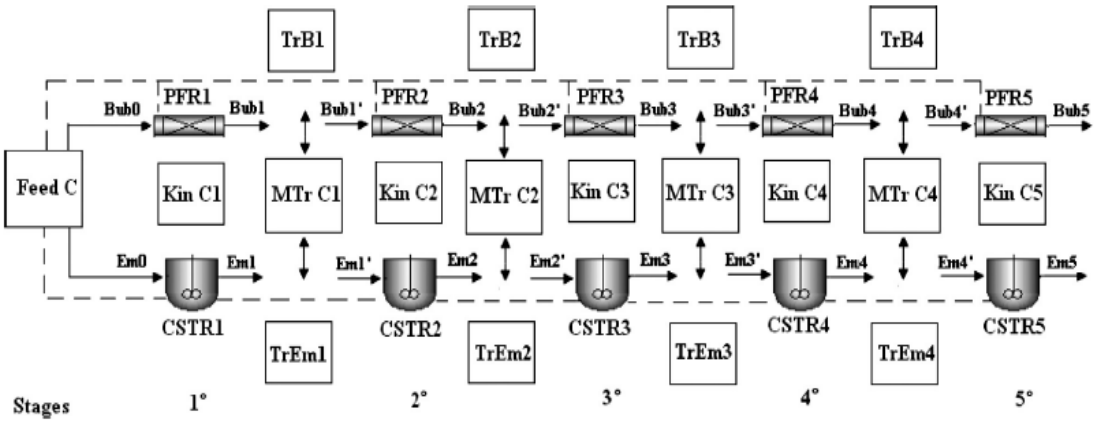

Fig. 2.1 Aspen Plus fuel reactor: bubbling bed region

The first block of the model is called "Feed C". This block is a user-defined calculator block that allows for implementing the initial conditions of the system. It can be written in FORTRAN or connected with Excel spreadsheets. In our case, the initial conditions are inserted in Excel spreadsheets appropriately linked with the flow sheet in Aspen Plus. Table 2.3 shows the equations applied to implement the initial conditions in the order that they have been used.

Table 2.3 Initial conditions implemented in Aspen Plus

Inlet mass methane flow-rate:	$F_{fuel} = \frac{P_{fuel}}{LHV}$
Inlet volumetric methane flow-rate:	$Q_{fuel} = \frac{F_{fuel}}{\rho_{CH4}}$
Fuel reactor superficial area:	$A_{FR} = \frac{Q_{fuel}}{U_o}$
Height of a fixed bed:	$L_m = \frac{W_{bedFR}}{\rho_s A_{FR}(1-\varepsilon_m)}$
Height of fluidised bed:	$L_f = \frac{L_m(1-\varepsilon_m)}{(1-\varepsilon_f)}$
Total volume:	$V_{tot} = L_f A_{FR}$
Bubble phase volume:	$V_b = V_{tot}\sigma$
Emulsion phase volume:	$V_e = V_{tot}(1-\sigma)$
PRF volume:	$V_{PFR} = V_b \varepsilon_b$
CSTR volume:	$V_{CSTR} = V_e \varepsilon_e$
PRF volume at *i* stage:	$V_{PFR(i)} = \frac{V_{PFR}}{n_{stages}}$
CSTR volume at *i* stage:	$V_{CSTR(i)} = \frac{V_{CSTR}}{n_{stages}}$

After choosing a fuel power, P_{fuel}, the inlet mass flow-rate is calculated; the gas density is derived from the ideal gas law and consequently the inlet volumetric gas feed flow-rate is calculated. The inlet superficial gas velocity, U_o, is chosen to guarantee the bubbling conditions inside the bed, meaning a value between the minimum fluidisation velocity, U_{mf}, and the terminal velocity of the isolated particles, U_t (Kunii and Levenspiel, 1991). Thus, the total fuel reactor superficial area, A_{FR}, is derived. The total

volume of the bed is a function of the solid inventory inside the bed, W_{bedFR}. Indeed, from the mass balance of the bed solids, the height of a fixed bed is first calculated and then, the height of the fluidised bed, L_f, as well as the corresponding total volume is derived. Afterwards, the volumes of the bubble and the emulsion phases are calculated, given the volumetric fraction of the bubbles in the bed, σ; finally, the total volume of the two reactors, PFR and CSTR, are derived, given the average bed void in the bubble and emulsion phase, ε_b and ε_e, respectively. If n_{stages} is the number of stages in the system, the volumes of the two reactors, PFR and CSTR, must be divided by n_{stages} to obtain the volume of each sub-reactor in each stage.

In the "Feed C" calculator block, U_{mf} and U_t are also derived to set an appropriate value of U_o to guarantee the bubbling conditions ($U_{mf} < U_o < U_t$). U_{mf} depends on both the physical property of the gas, since it is a function of the gas density ρ_g and viscosity μ_g, and the physical property of the solid, since it is a function of the average particles diameter d_p and solid density ρ_s.

Kunii and Levenspiel (1991) defined the Galileo number, *Ga*, as follows:

$$G_a = \frac{d_P^3 \, \rho_g \, (\rho_s - \rho_g) \, g}{{\mu_g}^2} \tag{2.13}$$

Reynolds number at minimum fluidization velocity Re_{mf} is a function of *Ga*:

$$Re_{mf} = [(33.7)^2 + 0.0408Ga]^{0.5} - 33.7 \tag{2.14}$$

Thus, U_{mf} is finally calculated:

$$U_{mf} = \frac{Re_{mf} \, \mu_g}{d_p \, \rho_g} \tag{2.15}$$

U_t is calculated solving the following equations (Kunii and Levenspiel, 1991):

$$d_P^* = d_P \left[\frac{\rho_g (\rho_s - \rho_g) g}{{\mu_g}^2}\right]^{0.33} \tag{2.16}$$

$$U_t^* = \left[\frac{18}{\left(d_P^*\right)^2} + \frac{0.591}{\left(d_P^*\right)^{0.5}}\right]^{-1} \tag{2.17}$$

$$U_t = U_t^* \left[\frac{\mu_g(\rho_s - \rho_g)g}{\rho_g^2}\right]^{0.33} \tag{2.18}$$

Furthermore, in the "Feed C" calculator block, a split of the inlet volumetric flow-rate to enter the two phases, bubble and emulsion, has to be accomplished. The difference U_o-U_{mf} is the term the drives the split. The approach proposed by Johnson et al. (1991) and applied also by Adanez et al. (2003) is taken into account. In 1991, Johnson et al. reported an expression of the volumetric bubble fraction independent of the height of the bed. Combining the two-phase theory with the dependence of the bubble velocity, U_b, from the bubble diameter and applying the Darton correlation for the bubble size (Darton et al., 1977), they first defined a function f_2 as follows:

$$f_2 = \frac{(0.26 + 0.7\mathrm{e}^{-3300\mathrm{d_p}})}{(0.15 + (U_o - U_{mf}))^{0.33}} \tag{2.19}$$

and, after some manipulations, they expressed consequently the volumetric fraction of the bubble phase in the following way:

$$\sigma = \frac{1}{\left(1 + \frac{1.3\left(U_o - U_{mf}\right)^{-0.8}}{f_2}\right)} \tag{2.20}$$

σ is the volumetric fraction of the bubble phase in the whole bed and its value is independent of the height in the bed. Given σ, the rise bubble velocity, U_b, is calculated from the gas mass balance as follows:

$$U_b = \frac{U_o - (1-\sigma)U_{mf}}{\sigma} \tag{2.21}$$

Then, given σ and U_b, the inlet volumetric gas flow-rate, Q_{fuel}, is split into two streams, Q_b and Q_e;

$$Q_{fuel} = Q_b + Q_e \tag{2.22}$$

$$Q_b = U_b \, A_{FR} \, \sigma \tag{2.23}$$

$$Q_e = U_{mf} \, A_{FR} \, (1 - \sigma) \tag{2.24}$$

U_b is calculated applying Eq. 2.21 to preserve the gas mass balance during the split of the gas inlet flow-rate into the two sub-streams: the bubble volumetric gas flow-rate, Q_b, entering the first PFR reactor and the emulsion volumetric gas flow-rate, Q_e, entering the first CSTR reactor. Further considerations on the volumetric bubble fraction, σ, are made after some manipulations of Eq. 2.21 as follows:

$$\sigma = \frac{U_o - U_{mf}}{U_b - U_{mf}} \tag{2.25}$$

Eq. 2.25 is in accordance with the expression derived from the K-L two-phase model introduced by Kunii and Levenspiel (1991). The latter recalls the two-phase theory introduced by Davidson et al. (1963) but it shows some modified equations compared to the original two-phase model. For instance, in the simple two-phase model, σ is calculated as follows:

$$\sigma = \frac{U_o - U_{mf}}{U_b} \tag{2.26}$$

The numerical difference between Eq. 2.25 and 2.26 is negligible especially under fast bubbles condition, which reflects the present case (see Table 2.5). Furthermore, the definition of σ according to the K-L model allows for the conservation of the gas mass balance (Eqs. 2.21-2.24) during the split of the inlet gas flow-rate to feed the bubble and the emulsion phase. For the latter reasons Eq. 2.21 is kept to calculate U_b.
Given σ, it is possible to calculate also the fluidised bed void, ε_f, and thus the height of the fluidised bed, L_f ; indeed, the latter is a function of ε_f (see Table 2.3), defined as follows (Kunii and Levenspiel, 1991):

$$\varepsilon_f = \sigma \, \varepsilon_b + (1 - \sigma) \, \varepsilon_e \tag{2.27}$$

where ε_e is the void fraction in the emulsion phase equal to the void fraction at minimum fluidization conditions and ε_b is the void fraction in the bubble phase. ε_b is usually assumed to be one; however, since it was found experimentally a fraction of

solid also in the bubble phase in a range from 0.2% to 1% (Kunii and Levenspiel, 1991), we assume ε_b not equal to one and we split also the inlet solid mass flow-rate, F_s, as follows:

$$F_{sb} = F_s\ \sigma\ (1 - \varepsilon_b) \tag{2.28}$$

$$F_{sm} = F_s - F_{sb} \tag{2.29}$$

where F_{sb} and F_{sm} are the inlet solid mass flow-rate entering the bubble phase and the emulsion phase, respectively. All the previous equations are implemented in the Feed C block and the values of Q_b and Q_e, F_{sb} and F_{sm} as well as the volumes of the reactors at the first stage of reaction are transferred from the Excel spreadsheets to the Aspen environment to run the simulation. Starting from the first stage of reaction, in each sub-reactors the mass balances shown in Table 2.4 are solved.

Table 2.4 Mass balances for each component in each sub-reactor of the bubbling bed model

Bubble phase:

$$M_{CH4b(i-1)} - M_{CH4bi} - A_b\ \varepsilon_b\ \int_{z_{i-1}}^{z_i} r_{CH4bi} dz = 0$$

$$M_{NiOb(i-1)} - M_{NiObi} - 4\ A_b\ \varepsilon_b\ \int_{z_{i-1}}^{z_i} r_{CH4bi} dz = 0$$

$$M_{CO2b(i-1)} - M_{CO2bi} + A_b\ \varepsilon_b\ \int_{z_{i-1}}^{z_i} r_{CH4bi} dz = 0$$

$$M_{H2Ob(i-1)} - M_{H2Obi} + 2\ A_b\ \varepsilon_b\ \int_{z_{i-1}}^{z_i} r_{CH4bi} dz = 0$$

$$M_{Nib(i-1)} - M_{Nibi} + 4 * A_b\ \varepsilon_b\ \int_{z_{i-1}}^{z_i} r_{CH4bi} dz = 0$$

Emulsion phase:

$$M_{CH4e(i-1)} - M_{CH4ei} - r_{CH4ei}\ V_{CSTRi} = 0$$

$$M_{NiOe(i-1)} - M_{NiOei} - 4\ r_{CH4ei}\ V_{CSTRi} = 0$$

$$M_{CO2e(i-1)} - M_{CO2ei} + r_{CH4ei}\ V_{CSTRi} = 0$$

$$M_{H2Oe(i-1)} - M_{H2Oei} + 2\ r_{CH4ei}\ V_{CSTRi} = 0$$

$$M_{Nie(i-1)} - M_{Niei} + 4\ r_{CH4ei}\ V_{CSTRi} = 0$$

In Table 2.4, M is the molar flow-rate for each component in each phase and r_{CH4} is the methane kinetic rate. As previously mentioned, in Aspen Plus environment the kinetic rate must be expressed in kmol/(m^{3}s) in the form of Eq. 2.30:

$$r_{CH4} = k_{CH4}{}' \, C_{CH4}^{n} \tag{2.30}$$

where $k_{CH4}{}'$ is the methane kinetic coefficient expressed in kmol$^{(1-n)}$m$^{(3n-3)}$/s. Combining Eq. 2.30 with Eqs. 2.10, 2.11, 2.12, we can express $k_{CH4}{}'$ as follows:

$$k_{CH4}{}' = \frac{3\, k_o\, e^{-\frac{E_a}{R'T}}}{r_g} \, \frac{\varepsilon_s}{\varepsilon_g} \left(\frac{F_{NiO\ out}}{F_{NiO\ in}}\right)^{2/3} \tag{2.31}$$

$k_{CH4}{}'$ is a "tear variable" since its value depends on an outlet stream (in this case $F_{NiO\ out}$); thus, applying an initial guess for $F_{NiO\ out}$, an internal loop in each sub-reactor needs to be run to solve the mass balances and get the convergence of the system. For this reason, a number of calculator blocks called "kin Ci" (see Fig. 2.1), as many as the sub-reactors modelling the fluidised bed, are applied. In each *kin Ci* block, a FORTRAN statement is written to implement Eq. 2.31 and the Wegstein convergence solver (Gupta, 1995) is used for solving the mass balance on the streams from and to the sub-reactors in each stage.

At the exit of the first stage of reaction, the gas mass transfer between the bubble and the emulsion phase (i.e. the two sub-reactors) occurs. Specifically, the calculator block *MTr Ci* (in Excel spreadsheet) is used to modify the outlet molar gas flow-rate from each sub-reactor by solving the mass transfer term between bubble and emulsion phase. Transfer block functions (i.e. *TrBi* and *TrEmi* –see Fig. 2.1), insure that the streams between stages verify mass continuity for each component. In this way, the gas molar flow-rate along the bed is always redistributed between bubble and emulsion phase. At the end of the first stage and, more generally, at the end of each stage, the superficial gas velocity, U_o, the bubble volume fraction, σ, the fluidised bed void, ε_f, and thus, the volumes of the two sub-reactors, are updated in the *Mtr Ci* block to be used in the next stage. The variables aforementioned need to be updated at the beginning of each stage since the increase in number of moles, which is produced as a consequence of the gas conversion, determines an increase in the superficial gas velocity and so a change in σ,

ε_f, and in the volumes of the sub-reactors. All these variables influence the mass transfer term between the two phases and thus the updated inlet gas molar flow-rates (M_{CH4}, M_{CO2} and M_{H2O}) to the next stages (Eqs. 2.32 and 2.33):

$$M_{b(i+1)} = M_{bi} - K_{be}\,(C_{bi} - C_{ei})\,V_{bi} \tag{2.32}$$

$$M_{e(i+1)} = M_{ei} + K_{be}\,(C_{bi} - C_{ei})\,V_{ei}\,(\frac{\sigma}{1-\sigma}) \tag{2.33}$$

where K_{be} is the overall mass transfer coefficient between bubble and emulsion phase ([=] 1/s) and C_b and C_e are the gas concentrations in the bubble and emulsion phase, respectively. Eqs. 2.32 and 2.33 are applied to all the gas species: CH_4, CO_2 and H_2O. K_{be} is calculated using the Eqs. 2.34 - 2.36, as follows:

$$K_{bc} = 4.5\left(\frac{U_e}{d_b}\right) + 5.85(\frac{\delta^{0.5}\,g^{0.25}}{d_b{}^{\frac{5}{4}}}) \tag{2.34}$$

$$K_{ce} = 6.77(\frac{\delta\,\varepsilon_{mf}\,0.711(g\,d_b)^{0.5}}{d_b^3})^{0.5} \tag{2.35}$$

$$\frac{1}{K_{be}} = \frac{1}{K_{ce}} + \frac{1}{K_{bc}} \tag{2.36}$$

where K_{bc} is the mass transfer coefficient between bubble and cloud whereas K_{ce} is the mass transfer coefficient between cloud and emulsion. Indeed, in a real system, a bubble may be also surrounded by what is called cloud. This phenomenon, which occurs mainly when the bubble velocity is higher than the emulsion velocity, is related to the gas that from the emulsion penetrates the bubble at its bottom and leaves it at the top; then, it returns at the base of the bubble. The region around the bubble penetrated by the gas recirculation is called cloud. In the system the cloud is considered as a part of the bubble phase but its presence is counted as a resistance to the mass transfer between the two phases, bubble and emulsion. K_{bc} is composed of two terms: the first term is assumed to represent the convection contribution as a result of bubble through-flow whereas the second term arises from the diffusion across a limited thin layer where the mass transfer takes place. In Eq. 2.34, U_e is the gas velocity in the emulsion phase, expressed as U_{mf}/ε_{mf}, d_b is the bubble diameter and δ is the coefficient of gas diffusivity.

The expression for K_{ce} was derived from the Higbie penetration model. Usually, K_{ce} provides the major resistance to the mass transfer even if both resistances are of the same order of magnitude; thus, in modelling these transfer processes, it is recommended to account for both resistances (Kunii and Levenspiel, 1991). Explanations about the expressions for the mass transfer terms are well discussed by Kunii and Levenspiel (1991) as well as by Makkawi and Ocone (2009).

Overall, the updated inlet gas molar flow-rates, at the exit of the first stage, enter the second stage of reaction and the same steps previously explained are carried out for the n_{stages} of reaction. The sequence to solve correctly all the blocks of calculation composing the bubbling bed is the following: Feed C, CSTR1, PFR1, Kin C1, TrEm1, TrB1, Mtr C1, CSTRn, PFRn, Kin Cn, TrEmn, TrBn, Mtr Cn, for n_{stages} number of stages.

In a fluidised bed, the bubble diameter changes with the height of the bed and its value might greatly influence the mass transfer coefficient and thus the final gas conversion. In the case of Geldart A solid particles, the bubbles grow fast up to their equilibrium size above the gas distributor and stay roughly at that size due to the equilibrium between splitting and coalescence. Thus, it might be reasonable to assume a constant bubble diameter along the bed height. For Geldart B solid particles, which reflects the present case, the bubbles grow constantly with the height of the bed and thus, the bubble diameter is a function of the bed height.

Being aware of the latter, the first attempt to model in Aspen Plus a fluidised bed should be as simple as possible to introduce a minimum number of variables in the model. Therefore, the bubble diameter, $d_{b,}$ is initially assumed to be constant along the bed height.

From a gas conversion point of view, the latter assumption is expected to lead to reasonable results in the case of slow kinetics (Kunii and Levenspiel, 1991). On the other hand, under fast kinetic conditions, as in the case of CLC processes, this assumption might overestimate the solid inventory needed to achieve the desired gas conversion due to underrated mass transfer, especially at the bottom of the bed.

Therefore, further investigations are required and the initial fluidised bed model proposed can be considered only as the starting point of this work.

2.3 Initial conditions and preliminary results

Since the bubbling model involves a large numbers of blocks, either reactors or calculator blocks, preliminary simulations are needed mainly to determine a minimum but satisfying number of stages.

Table 2.5 summarises the parameters used in our simulations and the main variables derived applying the equations reported in Section 2.2.

Table 2.5 List of the main parameters used for the simulation of the bubbling bed

Parameter	Value	Units	Parameter	Value	Units
P_{fuel}	10	MW	A_{FR}	3.48	m^2
LHV	50	MJ/kg	d_b	0.11	m
P	1	atm	F_s	75	kg/s
T	950	°C	X_{MO_exit}	0.9	-
U_{mf}	0.036	m/s	$\varepsilon_{mf} = \varepsilon_e$	0.5	-
U_t	2.54	m/s	ε_b	0.9	-
$U_o = 10U_{mf}$	0.36	m/s	ε_m	0.45	-

The modelled bubbling reactor has a fuel power of 10 MW corresponding to 0.2 kg/s of inlet methane mass flow-rate. The simulation is carried out at atmospheric pressure and at constant temperature equal to 950 °C. The latter value is chosen since it is in the optimal range of temperature for methane – nickel oxide reaction to achieve full gas conversion (Hossain and de Lasa, 2008; Lyngfelt and Thunman, 2005; Mattisson and Lyngfelt, 2001a) and it is the value employed by Abad et al. (2007) to derive the SCM parameters for the kinetic rate. The inlet superficial gas velocity, U_o, is chosen to be 10 times the minimum fluidization velocity. Indeed, given the inlet volumetric gas flow-rate, lower values of U_o would give cross sectional area of the reactor too large and of difficult design, especially if the CLC unit is supposed to be embedded in power plants of medium/large size (e.g. 500 MW of gross plant power). Under P_{fuel} equal to 10 MW and U_o equal to $10U_{mf}$, the reaction diameter, D_{FR}, is 2.11 m. The parameters applied guarantee that the bubbling regime is preserved and thus, no transition from bubbling to slugging regime is expected to occur. Indeed, the three conditions required to have a

slugging regime in terms of minimum bed height, superficial gas velocity and maximum stable bubble size are not satisfied (Constantineau et al., 2007).

The void fraction at minimum fluidization conditions, ε_{mf}, equal to 0.5, as well as the void fraction of a fixed bed, ε_m, equal to 0.45, are typical values assumed (Kunii and Levenspiel, 1991). The void fraction in the bubble phase, $\varepsilon_{b,}$ is assumed to be 0.9 to take into account the small fraction of solids that might be present in the bubbles.

The circulating solid mass flow-rate, F_s, is chosen equal to 75 kg/s (i.e. about 8 times higher than the stoichiometric ratio of oxygen carrier to fuel). The influence of F_s on the total solid inventory in the bed and its optimal values to minimise it, will be investigated in Chapter 4. However, F_s values higher than the stoichiometric one are usually applied in a CLC system to keep fast kinetics inside the bed and lower the solid inventory, as explained later. The metal oxide conversion at the fuel reactor inlet (or at the riser exit), X_{MO_exit}, equal to 0.9, means that at the riser not all the nickel is regenerated but a small fraction is still present and it enters the fuel reactor. The latter condition is considered realistic to minimise, once again, the total inventory in the CLC unit, as further explained later.

As mentioned in Section 2.2, the initial model assumes a constant bubble diameter and the value applied is equal to 11 cm. Lyngfelt et al. (2011) reported all the results coming from different CLC units at pilot scale. In summary it is shown that the range of solid inventory expected to lead to almost full gas conversion is in a range 100 – 600 kg/MW depending on the conditions applied (our operating conditions reflect the common conditions applied). Thus, we decided to use an average value of the bubble diameter considering the aforementioned solid inventory range of operability and applying the Darton correlation (Eq. 2.37):

$$d_b = 0.54(U_o - U_{mf})^{0.4}(h + 4\sqrt{A_o})^{0.8} g^{-0.2} \tag{2.37}$$

In Eq. 2.37, h is the height of the bed whereas A_o is the area of the gas distributor per nozzle. Since the gas distributor is not modelled in our analysis, in the absence of available data on the distributor characteristics, a value for A_o equal to zero is assumed, as suggested by Darton et al. (1977), Shen et al. (2004) and Busciglio et al. (2007).

2.3.1 Determination of the number of stages

The effect of the number of stages on the final gas conversion varies depending on the hydrodynamic and kinetic variables, i.e. on the ratio between the inlet superficial gas velocity U_o and the inlet superficial gas velocity at minimum fluidisation condition U_{mf} and the ratio between the kinetic coefficient k and the mass transfer coefficient K_{be}.

When $U_o >> U_{mf}$, since it is assumed that the bubble phase takes the excess of gas, with respect to the emulsion phase, the volumetric fraction of the bubble phase, σ, is high; in this case, if the number of stages increases, the mass transfer between the two phases also increases and so the conversion (more gas available for the reaction). When $U_o \approx U_{mf}$, the volumetric bubble fraction σ is low compared to the emulsion volumetric fraction, and the amount of gas that by-passes the emulsion phase is small; in this case, the presence of the bubbles is less relevant and the mass transfer between the two phases is low. In this situation, the number of stages affects slightly the gas conversion.

When $k >> K_{be,}$ the mass transfer between the two phases is the controlling step and most of the unreacted gas remains in the bubble phase while the gas in the emulsion phase is quickly consumed; an increase in the number of stages allows a large amount of fresh gas coming from the bubbles to react with the solid particles. When $k << K_{be}$ the kinetic term becomes the controlling step and a large amount of unreacted gas is present in the emulsion phase. In the latter case, the gas conversion is slightly affected by the mass transfer and by the number of stages: the effect of the by-pass of gas in the bubble phase is not very relevant since the gas in the emulsion phase is not largely consumed (Porrazzo et al., 2014).

Aiming to select a correct number of stages that can cover a large range of operating conditions, we decided to vary some variables in our system. Keeping constant U_o at the value reported in Table 2.5 and setting a solid inventory W_{FR} equal to 3000 kg (i.e. 300 kg/MW), we studied first how the gas conversion changes, varying the number of stage, moving from very low kinetic rates to very high kinetic rates (the latter are typical of CLC operations), as shown in Fig. 2.2.

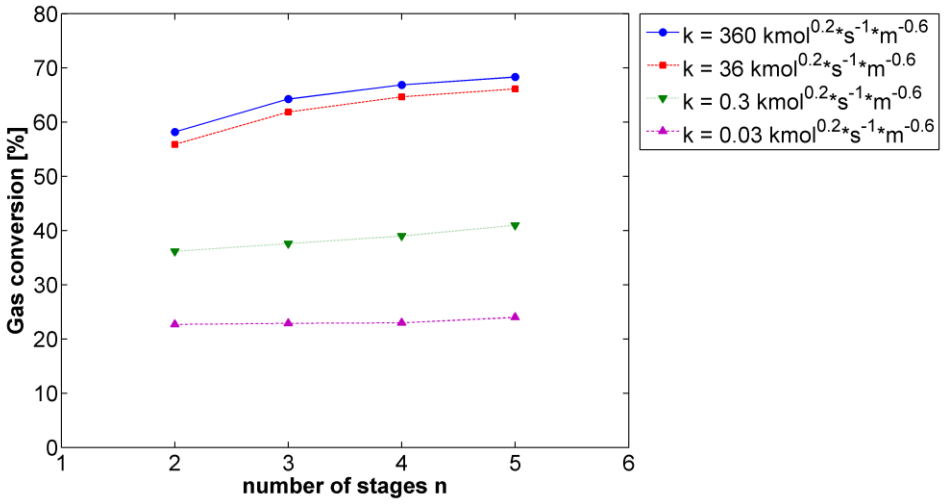

Fig. 2.2 Gas conversion vs. number of stages n at different kinetic constant *k*

The ratio between the mass transfer coefficient K_{be} and the kinetic constant *k* is varied with K_{be} kept constant. As mentioned previously, a *k* value lower than K_{be} (under the conditions applied, K_{be} is equal to 1.24 1/s) implies that the kinetics is the controlling step and therefore the contribution of gas by-pass to the overall gas conversion is lower. In this case, the overall gas conversion is not affected greatly by the number of stages, therefore the system can be modelled with a fewer stages. Conversely, a higher value of *k* implies the mass transfer to be the controlling step: consequently, a good gas redistribution between the bubble and the emulsion phase is more relevant. In this case, the variation of the overall gas conversion with the number of stages is larger than that obtained in the case of kinetic control.

After 5 stages, the system reaches a plateau and therefore the multi-stage model can assume 5 stages as the maximum number of stages. To further evaluate a suitable number of stages to apply, the size of the reactor is varied, as shown in Fig. 2.3. The kinetic constant applied comes from the parameters reported by Abad et al. (2007) and presented in Section 2.1.

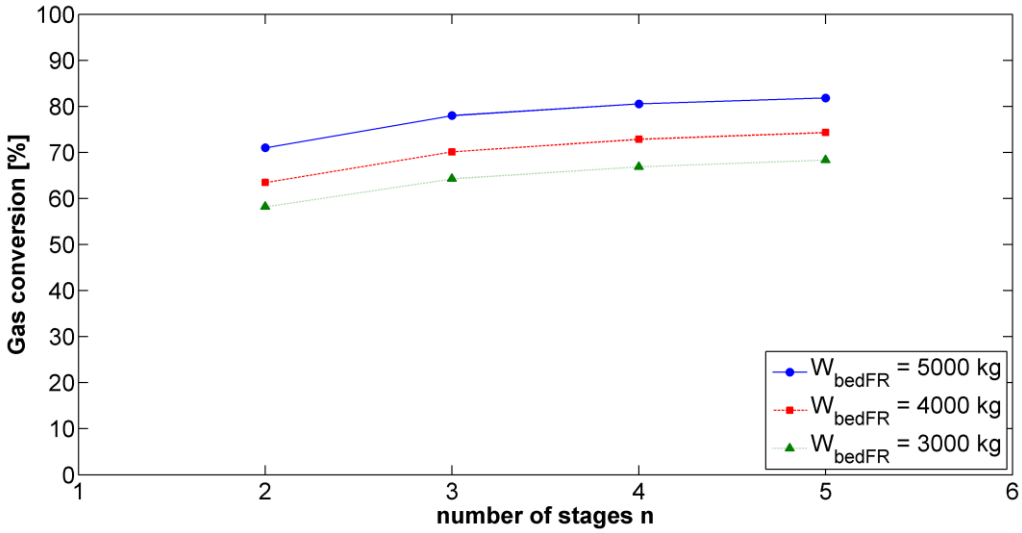

Fig. 2.3 Methane conversion vs. number of stages n at different W_{bedFR}

An increase in the solid inventory determines an increase in the gas conversion at constant number of stages. The gas conversion, at fixed initial conditions and solid inventory, must reach a plateau for physical reasons. 5 stages are considered, once again, to be the correct number to adopt for the next analysis since the plateau is reached in all the range of solid inventory taken into account. Keeping constant at 5 the number of stages, Fig. 2.4 shows the first preliminary result coming from the bubbling multi-stage model in terms of gas conversion while varying the solid inventory inside the bed.

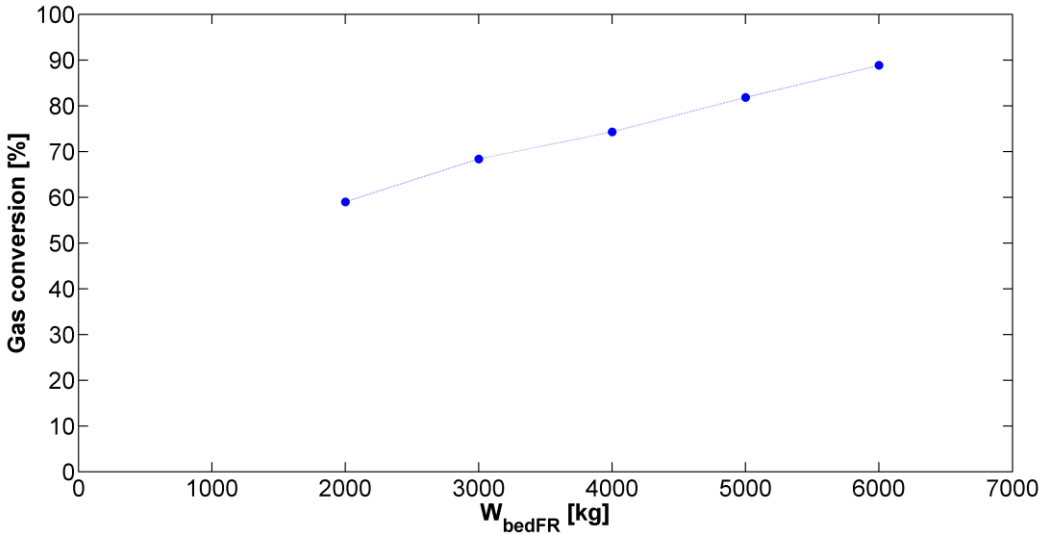

Fig. 2.4 Methane conversion vs. W_{bedFR}

The gas conversion increases while increasing the solid inventory inside the bed, as physically expected, but its strong linear dependency is greatly due to the assumption of constant bubble diameter along the bed leading to a constant mass transfer coefficient across the bed length. This aspect might underestimate the mass transfer and thus the gas conversion at the bottom of the bed as well as overestimate the gas conversion at the top of the bed leading to inaccurate results. Thus, further investigations and relative improvements of the model as well as the study of the gas conversion profile inside the bed are required. For this reason, a CFD analysis is undertaken as presented in the next chapter.

2.4 Alternative bubbling bed modelling approach

In Sections 2.2 - 2.3 a bubbling bed model was proposed and analysed. This model is based on an initial split between the bubble and the emulsion phase that is dependent on the gas exceeding the minimum fluidisation velocity (i.e. U_o-U_{mf}). The bubble volumetric fraction, σ, is first calculated (see Eq. 2.20) to derive later U_b (see Eq. 2.21) and drive the initial split (see Eqs. 2.22 - 2.24). The formula to calculate σ is independent from the bed height accounting for an average value of σ inside the bed as reported by Johnson et al. (1991). Furthermore, this model assumes a constant bubble diameter, d_b, along the bed height, which might not be representative of our CLC system. To compensate, one approach is to use information from CFD, as indicated early; alternatively, we can apply different bubbling bed models similar to those reported by Abad et al. (2010) or Jafari et al. (2004) and among them the bubbling bed model reported by Porrazzo et al. (2014) is described below. The model is based on a different sequence than that explained in Section 2.2.1 to determine the initial split of the two phases and the new equations employed are those reported by Kunii and Levenspiel (1991).

Firstly, the rise velocity of the bubble at minimum fluidization condition, U_{br}, is calculated according to the Eq. 2.38:

$$U_{br} = 0.711(g\ d_b)^{0.5} \tag{2.38}$$

Later, the rise velocity of the bubbles, U_b, at conditions different from U_{mf} is derived as follows:

$$U_b = U_o - U_e + U_{br} \tag{2.39}$$

Thus the bubble volumetric fraction, σ, is obtained following the gas mass balance:

$$\sigma = \frac{U_o - U_e}{U_b - U_e} \tag{2.40}$$

Eq. 2.40 follows the K-L two-phase model introduced by Kunii and Levenspiel (1991) as explained in Section 2.2.1.
Given U_b and σ, the inlet flow rate at superficial gas velocity U_o is split into the two terms linked to the bubble and emulsion phase (see also Eqs. 2.22 - 2.24):

$$U_o = (1 - \sigma)\, U_e + \sigma\, U_b \tag{2.41}$$

Apart from the different approach to initially split the inlet volumetric flow-rate, the model applies the same relations described previously in Section 2.2 and 2.3, following the same logical sequence: mass transfer between the two phases according to Eqs. 2.32 - 2.33 at the end of each stage of reaction, superficial gas velocity, bubble volumetric fraction, fluidised bed void and volumes of the sub-reactors updated at the end of each stage to account for the increase in the number of moles.

Unfortunately, the applicability of this model is limited to specific conditions (e.g. Porrazzo et al. (2014) applied this model under constant bubble diameter along the bed height). Indeed, the introduction of a formula that accounts for the change in the bubble diameter along the bed height (see Eq. 2.37) leads to numerical issues when an initial split of the two phases is attempted. Under the assumption of area of the gas distributor per nozzle, A_o, equal to zero, Eq. 2.37 produces a zero value for d_b at the bottom of the bed; the latter leads to a bubble volumetric fraction, σ, higher than the unity (see Eqs. 2.38 - 2.40), resulting in an unfeasible initial phases' split. Therefore, it is possible to conclude that this model can be applied under two specific cases: constant bubble diameter (Porrazzo et al., 2014) or variable bubble diameter when A_o is not longer zero.

In the analysis of the CLC reactor, the knowledge of the gas distributor is missing and hence A_o is equal to zero. However, we wish to introduce a variable bubble diameter term to take into account the nature of the solid particles (i.e. Geldart B), the

dependence of the reaction on the gas-solid interaction and the overall conversion of the fuel. Thus, the approach taken is based on that presented in Section 2.2.1 but informed by CFD modelling as described in the next chapter.

Chapter 3

CFD analysis and improvement of the bubbling bed model in Aspen Plus

In this chapter, it is applied a Computational Fluid Dynamics (CFD) analysis to gain a better understanding of the phenomena involved in a bubbling fluidised bed aimed to improve the macro-scale model implemented in Aspen Plus and derive eventually information about the cost of electricity generated from a CLC power plant.

CFD accounts for both numerical techniques and physical models aimed at the computer simulation of fluid flows and their associated phenomena such as mass and heat transfer. Three fundamental principles such as the mass conservation, the momentum conservation and the energy conservation dictate the fluid flow and they are usually expressed in the form of Partial Differential Equations (PDEs). CFD allows for solving the system of PDEs applying specific boundary conditions to obtain a numerical description of the flow field of interest. The PDEs (or transport equations) to be solved are known as the Navier-Stokes equations and their solution, within the computational space domain, requires the manipulation of millions of numbers; thus, improvements in CFD are related to improvements in computer hardware concerning the execution speed and memory storage.

There are several advantages in undertaking a CFD analysis of a system of interest: time in design and development is significantly reduced, unlimited level of detail of results, studying of hazardous conditions and flow conditions difficult to reproduce in experimental model tests. In this respect, CFD simulations for chemical looping combustion purposes have been employed (Deng et al., 2008, 2009; Jung and Gamwo, 2008; Kruggel-Emden et al., 2010, 2011; Mahalatkar et al., 2011; Shuai et al., 2011a, 2011b) to understand at the particle level how the kinetics and the hydrodynamics influence the motion of the solid particles into a fluidised bed, the gas-solid contact efficiency and therefore the outlet fuel conversion. The disadvantages of the CFD approach are related to the computational cost, the long runs of simulation and in particular the small domain that can be processed (few or most commonly just one unit processed).

This work aims to model the fuel reactor of the CLC system using a CFD approach (called micro scale approach) to achieve a better understanding of the kinetic and hydrodynamic phenomena involved. The results from the micro scale approach are analysed and compared to those coming from the macro scale approach using Aspen Plus model. The latter are improved to increase the accuracy of the macro scale model making it useful for thermal efficiency and economic evaluations of a fully integrated CLC power plant (see Chapters 4 and 5).

3.1 Set of PDEs employed

The bubbling bed fuel reactor model in MFIX environment is implemented in a 2D fashion and it is based on the Eulerian – Eulerian approach. Gas and solid phases are considered as continuum phases in the domain under investigation. A continuum phase is characterised by properties such as density, temperature, pressure and velocity that change with continuity in each volume of the matter taken into account; thus, no matter how small the computational volume is since its mathematical limit is reached over a scale that remains large compared to the molecular dimensions (Armstrong scale). The Eulerian – Eulerian approach sets up the equations governing the dynamics of a "fluid particle" (defined as a geometrical point in a mathematical continuum of numbers), either gas or solid, using coordinates fixed in space and it provides the spatial distribution of all the desired flow quantities at each instant during the motion. Another approach commonly applied, called Lagrangian approach, uses coordinates that move with the particle and it describes the dynamical history of a selected fluid element.

In a 2D model the continuity and momentum equations are solved in two directions (x and y) for both phases, with mass and momentum exchanged between them. The solid phase is characterised by uniform spherical particles of constant mean density and diameter (see Chapter 2). No energy equation is solved to reduce the computational cost. Indeed, being aware that the reduction reaction is substantially endothermic (about +150 kJ/mol), the drop in temperature under few seconds of simulation is negligible. The latter statement is supported by Shuai et al. (2011b) who reported a drop in temperature of just 4 degree (from 950 K to 946 K) for the same reactive system and few seconds of simulation.

All the equations described below come from the well known theory embedded in the MFIX code (Syamlal et al., 1993).

3.1.1 Continuity and species transport equations

Gas phase:

$$\frac{\partial}{\partial t}\left(\varepsilon_g \rho_g\right) + \nabla \cdot \left(\varepsilon_g \rho_g \overrightarrow{U_g}\right) = \sum_{n=1}^{N_g} r_{gn} \tag{3.1}$$

Solid phase:

$$\frac{\partial}{\partial t}\left(\varepsilon_s \rho_s\right) + \nabla \cdot \left(\varepsilon_s \rho_s \overrightarrow{U_s}\right) = \sum_{n=1}^{N_s} r_{sn} \tag{3.2}$$

Gas species:

$$\frac{\partial}{\partial t}\left(\varepsilon_g \rho_g Y_{gn}\right) + \nabla \cdot \left(\varepsilon_g \rho_g \overrightarrow{U_g} Y_{gn}\right) = \nabla \cdot \left(D_{gn} \nabla Y_{gn}\right) + r_{gn} \tag{3.3}$$

Solid species:

$$\frac{\partial}{\partial t}\left(\varepsilon_s \rho_s Y_{sn}\right) + \nabla \cdot \left(\varepsilon_s \rho_s \overrightarrow{U_s} Y_{sn}\right) = \nabla \cdot \left(D_{sn} \nabla Y_{sn}\right) + r_{sn} \tag{3.4}$$

The continuity equation is the result of a local mass balance. It states that the increase or decrease of the bulk density of a phase in a finite volume is equal to the net mass flow-rate entering the control volume divided by the same volume. Indeed, the first term on the left in Eqs. 3.1 and 3.2 represents the rate of mass accumulation per unit volume whereas the second term represents the net rate of convective mass flux. The term on the right hand side represents the inter-phase mass transfer because of chemical reaction. In Eqs. 3.3 and 3.4 an extra term on the right accounting for the diffusion flux of the *n* species in each phase is also present.

Since in each finite volume more than one phase is present, new field variables called volume fractions for the two phases, ε_g and ε_s, are introduced. The volume fractions are continuous functions of space and time. In each finite volume of the computational domain, the sum of the gas and solid volume fractions must be unity. The sum of the reaction rates of all the species in each phase represents the mass transfer term

exchanged between the two phases and their combined sum must be zero; the sum of the mass fractions of all the species at each phase must be unity. The gas density is calculated by the ideal gas law.

3.1.2 Momentum equations

The momentum equations refer in their simplest form to the Navier-Stokes equations (constant density and viscosity) that can be derived from the Newton's second law of motion. They state that the momentum accumulation term is equal to the net momentum flow-rate entering the control volume plus all the forces acting on it: gravity force, pressure forces and viscous forces. In the case of chemical reactions and two or more phases interacting between each other, additional terms have to be taken into account.
Gas phase:

$$\frac{\partial}{\partial t}\left(\varepsilon_g \rho_g \vec{U_g}\right) + \nabla \cdot (\varepsilon_g \rho_g \vec{U_g} \vec{U_g}) = -\varepsilon_g \nabla P_g + \nabla \cdot \tau_g + \varepsilon_g \rho_g \vec{g} - \beta(\vec{U_g} - \vec{U_s}) + \sum_{n=1}^{N_g} r_{gn} * (\xi_o \vec{U_s} + (1 - \xi_o) \vec{U_g})$$

$$\xi_o = \begin{cases} 1 \; if \; \sum_{n=1}^{N_g} r_{gn} < 0 \\ 0 \; if \; \sum_{n=1}^{N_g} r_{gn} > 0 \end{cases} \tag{3.5}$$

Solid phase:

$$\frac{\partial}{\partial t}\left(\varepsilon_s \rho_s \vec{U_s}\right) + \nabla \cdot (\varepsilon_s \rho_s \vec{U_s} \vec{U_s}) = -\varepsilon_s \nabla P_g + \nabla \cdot \tau_s + \varepsilon_s \rho_s \vec{g} + \beta(\vec{U_g} - \vec{U_s}) + \sum_{n=1}^{N_s} r_{sn} * (\xi_o \vec{U_s} + (1 - \xi_o) \vec{U_g})$$

$$\xi_o = \begin{cases} 1 \; if \; \sum_{n=1}^{N_s} r_{sn} > 0 \\ 0 \; if \; \sum_{n=1}^{N_s} r_{sn} < 0 \end{cases} \tag{3.6}$$

In Eqs. 3.5 and 3.6 the first term on the left represents the net rate of momentum increase whereas the second term represents the net rate of momentum transfer by convection. Following the order of appearance, the terms on the right represent: pressure forces, shear forces, gravity forces, drag force between the two phases caused by their difference in velocities, momentum transfer due to mass transfer related to the chemical reaction in each phase.

3.1.3 Gas phase shear tensor

The gas phase shear tensor is expressed as follows:

$$\tau_g = 2\varepsilon_g \mu_g \overline{\overline{D_g}} - \frac{2}{3}\varepsilon_g \mu_g tr\left(\overline{\overline{D_g}}\right)\bar{\bar{I}} \tag{3.7}$$

where

$$\overline{\overline{D_g}} = \frac{1}{2}\left[\nabla \vec{v_g} + (\nabla \vec{v_g})^T\right] \tag{3.8}$$

In the present work the gas viscosity, μ_g, is assumed to be constant (Newtonian fluid). Eqs. 3.7 and 3.8 state that the shear tensor is proportional to the strain rate through two constants: gas viscosity related to the linear strain and λ=-2/3μ_g related to the volumetric strain.

3.1.4 Solid phase stress tensor

The MFIX code takes into account two different flow regimes for the solid phase: plastic and viscous flow. In the plastic regime the stresses arise because of Coulomb friction between grains in enduring contact (Jenkins and Cowin, 1979). In the viscous regime the stresses arise because of collisional momentum transfer. Through a switch function based on the minimum fluidisation void, ε_g^*, the solid stress tensor is physically dependent on the particle-particle friction at conditions closed to packed bed state and on particle-particle collisions at low particle concentrations (Eq. 3.9).

$$\tau_s = \begin{cases} -P_s^P \bar{\bar{I}} + \tau_s^P & \varepsilon_g \leq \varepsilon_g^* \\ -P_s^v \bar{\bar{I}} + \tau_s^v & \varepsilon_g > \varepsilon_g^* \end{cases} \tag{3.9}$$

The plastic regime is described by the Schaeffer frictional stress model (Schaeffer, 1987):

$$P_s^P = \varepsilon_s 10^{25}\left(\varepsilon_g^* - \varepsilon_g\right)^{10} \tag{3.10}$$

$$\tau_s^P = 2\mu_s^P \overline{\overline{D_s}} \tag{3.11}$$

where $\overline{\overline{D_s}}$ is the strain rate tensor defined as:

$$\overline{\overline{D_s}} = \frac{1}{2}\left[\nabla \vec{v_s} + (\nabla \vec{v_s})^T\right] \tag{3.12}$$

The frictional viscosity is given by:

$$\mu_s^P = \frac{P^* \sin \Phi}{2\sqrt{I_{2D}}} \tag{3.13}$$

where Φ is the angle of internal friction and I_{2D} is defined as:

$$I_{2D} = \frac{1}{6}[(D_{s11} - D_{s22})^2 + (D_{s22} - D_{s33})^2 + (D_{s33} - D_{s11})^2] + D_{s12}^2 + D_{s23}^2 + D_{s31}^2 \tag{3.14}$$

where D_s is the strain rate tensor in directions 1, 2 and 3. The viscous regime is defined by the granular kinetic theory (Chepurniy, 1984; Gidaspow, 1994) that describes the particle – particle interactions as binary collisions, resembling those between molecules in the gas kinetic theory. The granular temperature Θ is introduced to account for the energy fluctuating velocity C of the particles ($\Theta = < C^2 > /3$) that dissipates as heat because of inelastic collisions between spherical particles. Θ is not the particle thermodynamic temperature since the latter is a measure of the kinetic energy of molecular vibrations within the particle. Based on the granular kinetic theory, the terms constituting the stress tensor are defined below.

Solid kinetic pressure:

$$P_s^v = K_1 \varepsilon_s^2 \Theta \tag{3.15}$$

with

$$K_1 = 2(1 + e)\rho_s g_o \tag{3.16}$$

P_s^v represents the solid phase normal forces due to particle collisions. The model for the solids pressure is questionable, since the kinetic part of the solid pressure is not included (Gidaspow and Huilin, 1998).

Solid granular stress:

$$\tau_s^v = \lambda_s^v tr\left(\overline{\overline{D_s}}\right)\bar{\bar{I}} + 2\mu_s^v \overline{\overline{D_s}} \tag{3.17}$$

The solid bulk viscosity, λ_s^v, gives a measure of the resistance of a fluid again compression and it is defined as follows:

$$\lambda_s^v = K_2 \varepsilon_s \sqrt{\Theta} \tag{3.18}$$

The solid shear viscosity, μ_s^v, represents the tangential forces due to particle collisions and it is defined as follows:

$$\mu_s^v = K_3 \varepsilon_s \sqrt{\Theta} \tag{3.19}$$

with

$$K_2 = \frac{4 d_P \rho_s (1+e) \varepsilon_s g_o}{3\sqrt{\pi}} - {}^2/_3 K_3 \tag{3.20}$$

and

$$K_3 = \frac{d_P \rho_s}{2} \left\{ \frac{\sqrt{\pi}}{3(3-e)} [1 + 0.4(1+e)(3e-1)\varepsilon_s g_o] + \frac{8 \varepsilon_s g_o (1+e)}{5\sqrt{\pi}} \right\} \tag{3.21}$$

The radial distribution function g_o, as a statistical measure of the probability of inter-particle contact (Carnahan and Starling, 1969), is defined as:

$$g_o = \frac{1}{\varepsilon_g} + 1.5 \varepsilon_s \left(\frac{1}{\varepsilon_g}\right)^2 + 0.5 \varepsilon_s^2 \left(\frac{1}{\varepsilon_g}\right)^3 \tag{3.22}$$

The function g_o allows a tight control of the solids volume fraction so that the maximum packing is not exceeded and more accurate flow characteristics can be achieved. As shown in Eqs. 3.15 - 3.22, in addition to the granular temperature, the granular kinetic theory introduces the coefficient of restitution for particle – particle interaction, *e* (ranging from 0 to 1), to account for the non – ideal behaviour or inelasticity of the solids.

3.1.5 Conservation of granular energy

The granular temperature Θ is obtained from an algebraic expression (Eq. 3.24), because of a simplified granular energy equation (Eq. 3.23) where convection and

diffusion contributions to the granular flow are neglected and it is assumed that Θ is dissipated locally:

$$\left(P\bar{\bar{I}} + \tau_s\right) : \nabla \vec{v_s} - \Upsilon = 0 \tag{3.23}$$

In Eq. 3.23 the generation term balances the dissipation term Υ due to inelastic collisions. The granular temperature is, finally, defined as follows:

$$\Theta = \left\{ \frac{-K_1 \varepsilon_s tr(\overline{\overline{D_s}}) + \sqrt{K_1^2 tr^2(\overline{\overline{D_s}})\varepsilon_s^2 + 4K_4\varepsilon_s\left[K_2 tr^2(\overline{\overline{D_s}}) + 2K_3 tr(\overline{\overline{D_s}})^2\right]}}{2\varepsilon_s K_4} \right\}^2 \tag{3.24}$$

with

$$K_4 = \frac{2(1-e^2)\rho_s g_o}{d_P\sqrt{\pi}} \tag{3.25}$$

Overall, Θ is introduced to define and solve the solid pressure, P_s, the solid viscosity, μ_s, and thus the solid stress tensor, τ_s (see Section 3.2.4).

3.1.6 Drag force model

The drag force, as part of the momentum transfer between the gas and the solid phase, is based on correlations for the terminal velocity in fluidised beds as reported by Syamlal et al. (1993):

$$\beta = \frac{3\mu_g \varepsilon_s \varepsilon_g}{4V_{rm} d_p^2}\left(0.63\sqrt{\frac{Re_s}{V_{rm}}} + 4.8\right)^2 \tag{3.26}$$

The terminal velocity correlation V_{rm} is expressed as:

$$V_{rm} = 0.5\left(A - 0.06Re_s + \sqrt{(0.0036Re_s^2) + 0.12Re_s(2B - A) + A^2}\right) \tag{3.27}$$

with

$$A = \varepsilon_g^{4.14} \tag{3.28}$$

and

$$B = \begin{cases} 0.8\varepsilon_g^{1.28} & \varepsilon_g \leq 0.85 \\ \varepsilon_g^{2.65} & \varepsilon_g > 0.85 \end{cases} \quad (3.29)$$

The Reynolds number of the solid phase is given by:

$$Re_s = \frac{\rho_g d_P |U_g - U_s|}{\mu_g} \quad (3.30)$$

However, different ways to express the drag force coefficient β are available in MFIX and thus different drag models can be applied (Syamlal et al., 1993).

3.1.7 Additional considerations on the PDEs

The equations shown in the previous sections describe the behaviour of a multi-phase gas-solid flow and in general they can be applied either under laminar or turbulent conditions. In order to solve the flow equations by any numerical method, the computational domain has to be spatially discretised in cells (and grid points) that need to be smaller than the smallest significant structures to be resolved. Furthermore, the simulation has to be conducted by using a time step small enough to resolve the time dependent behaviour of the various quantities.

In the case of laminar flow, the spatial-temporal discretisation does not exhibit high computational costs since the significant flow structures, which determine the cells size, have the same order of magnitude of the physical structures of the domain. Furthermore, laminar cases are at steady state conditions, unless the boundary conditions are time-dependent, leading to an additional computational simplification.

In the case of turbulent flow, the flow field varies in a non-periodic way with time and lacks spatial symmetries. The spatial structures in the flow field called “eddies” cover a wide range of scales, from the scale of the physical domain down to that of the “dissipative eddies”, in which the kinetic energy of the eddy motion is dissipated into heat by viscous effects. The latter scale is called “Kolmogorov scale”.

The Kolmogorov scale refers to the homonymous theory widely used to explain the turbulence. According to this theory, an energy cascade process is present in all turbulent flows, involving a transfer of turbulent kinetic energy, k_t, from larger to smaller eddies. In the smallest eddies, the dissipation of kinetic energy to heat occurs due to molecular viscosity. An energy spectrum of turbulent flow shows that about 80% of the energy, coming from pressure gradient or mechanical agitation, is present in the large eddies and 90% of the energy is dissipated below the so called Kolmogorov scale. Kolmogorov's universal equilibrium theory states that the net rate of change of small scale eddies is smaller than the rate at which energy is dissipated and this aspect guarantees that eddies do not disappear and the turbulence is kept. Since the small-scale motion occurs on a short time scale, it can be assumed that it is independent of the relatively slow dynamics of the large eddies and of the mean flow; therefore, the Kolmogorov scale is only a function of the energy supplied (or dissipated) and viscosity.

Following the relationships reported by Landau and Lifshitz (1959), all the previous considerations lead to expressions for the Kolmogorov length and time scale that are useful to estimate the number of grid points and time steps necessary for a correct Direct Numerical Simulation (DNS) of the transport equations. Indeed, the cells size has to be smaller than the Kolmogorov length scale to capture the turbulent phenomena and, as a consequence, the time step will be extremely small (see Courant criterion (Courant et al., 1967)). Overall, the minimum number of grid points characterising the domain, N_p, is demonstrated to be a function of $Re^{9/4}$ whereas the overall number of time step, N_t, to be a function of $Re^{7/8}$. The latter means that, under turbulent conditions (i.e. very high Re number), N_p and N_t are so high that there is not any computer having the capability to solve directly the set of equations describing the fluid flow.

For this reason, turbulent models are applied: Large Eddy Simulation (LES) and Reynolds averaging (RANS). In the first approach, each field variable is decomposed into two parts: the first, which accounts for the large scale phenomena, is filtered over the space and it is called *resolved component* whereas the second is called *unresolved fluctuation* and it accounts for the small scale phenomena. The second approach follows the first but the filter is temporal; thus, the first term is the average of the variable over the time whereas the second term accounts for the temporal fluctuations.

Focusing on the second approach, when the decomposed variables are introduced in the Navier-Stokes equations, six extra fluctuating terms called Reynolds stresses appear (products of the turbulent fluctuating components) and they need to be modelled. The Reynolds stresses can be solved either one by one applying the Reynolds Stress Model (meaning six extra PDEs) or modelled through the gradient-diffusion models (e.g. k_t - ε model, (Launder and Spalding, (1974)). In the latter case, the Boussinesq's theory is introduced: it is assumed that the Reynolds (or turbulence) stresses act like the viscous stresses and thus, they are directly proportional to the mean velocity gradient through the turbulent viscosity, μ_t. This quantity is a function of the turbulent kinetic energy, k_t, and the dissipation energy rate, ε, through the Prandtl – Kolmogorov equation. From this point, different sub-models can be applied depending on how k and ε are derived (i.e. algebraically or through PDEs). The well known k_t-ε model is based on two PDEs for k and ε in a form similar to the transport equations (e.g. see Eq. 3.5). In the case of multi-phase flow, the PDEs for k_t and ε, applied to each phase, exhibit a term based on a drag force coefficient to account for the turbulent interaction between the phases. In the case of gas – solid multi-phase flow with the granular model applied, the turbulent interaction term between the gas and the solid phase is a function of both k_t and Θ. Indeed, k_t and ε model the turbulence of the continuous phase (i.e. the gas) to calculate the turbulence viscosity μ_t whereas the granular temperature models the turbulence of the dispersed phase (i.e. the solid) to calculate the solid pressure and the solid viscosity.

Gas – solid motion in a bubbling fluidised bed is not clear if it belongs or not to the category of turbulent phenomena. Being aware of the latter, if simulations in this work were in 3D fashion, the implementation of any turbulence model (e.g. $k_t - \varepsilon$ model) to capture the physics of the turbulence would be necessary. Since our simulations run in a 2D fashion, none of the turbulence models is implemented and all the flow quantities refer to mean values (not instantaneous values). The reason behind the choice recalls the inherent three dimensional nature of turbulence meaning that applying turbulence models in a 2D simulation might lead to nonphysical results. The latter statement is supported by Teaters (2012) who studied the gas-solid motion in a 2D fluidised bed under bubbling condition with and without $k_t - \varepsilon$ turbulence model applied. The outcome of her analysis showed the nonphysical bed hydrodynamics and difficulties in finding any real discernible flow features when the turbulence model is applied.

3.1.8 Numerical methodology

The set of PDEs describing the flow field cannot be solved analytically due to the non-linear partial differential equations; thus, numerical methods are adopted and among them the most applied approach is the finite volume method, which is the one used in the MFIX code.

In order to apply this method, the computational domain is divided in a number of cells and the model equations have to be integrated over each cell volume. Moreover, when dealing with unsteady flows, the integration is also required over a small time step. Then, a discretisation method is applied to transform the integrated equations into a set of algebraic equations to be solved with an iterative procedure. In each cell the continuity and momentum equations of each phase are solved simultaneously. The scalar variables such as void fraction and pressure are positioned at the cell centre whereas the vector variables (velocities) at the cell faces of scalar control volumes (staggered grid arrangement). So, scalar and vector quantities refer to different control volumes (e.g. momentum equations are solved in the staggered volumes where the cell faces contain the scalar nodes). The staggered grid approach is used to reduce numerical instabilities, unrealistic behaviour of the discretised momentum equations (especially in the case of spatially oscillating pressure) and furthermore it generates velocities at exactly the positions where they are required for the scalar transport computations (Versteeg and Malalasekera, 1995).

The algorithm applied to solve the set of partial differential equations (PDEs) is an extension of the Semi-Implicit Method for Pressure Linked Equations (SIMPLE) algorithm (Patankar, 1980) introduced for the solution of pressure-velocity coupled PDEs (Syamlal, 1998a). So, two modifications have been introduced to improve the stability of the code and speed up the calculations. The first modification uses a solid volume fraction correction equation (instead of a solid pressure correction equation typical of the standard SIMPLE algorithm) that includes the effect of the solids pressure to help facilitate convergence for both loosely and densely packed regions (Syamlal, 1998a; Deza et al, 2009). The second modification uses a variable time step to improve convergence and execution speeds (the range selected in our simulations is between 10^{-4} and 10^{-8} s).

Discretisation of time derivatives are first-order differencing scheme whereas the convection terms of PDEs are discretised using a second upwind order called Superbee to improve the numerical accuracy and the bubble shape resolution (rounded bubbles instead of unphysical pointed bubbles) with affordable grid refinements (Syamlal, 1998b). Furthermore, the application of a second upwind order method avoids the so-called "false diffusion" issues (Versteeg and Malalasekera, 1995).

3.1.9 Initial and boundary conditions

The PDEs applied in the simulation are parabolic equations (i.e. Navier-Stokes equations applied to unsteady viscous flows). The solution of these types of equations requires initial conditions of all the field variables in the entire computational domain as well as boundary conditions at $t > 0$. In our system the field variables involved are: void fraction, gas pressure, gas and solid velocities in two directions (X and Y), gas and solid species mass fractions. These variables are initialised in the entire computational domain (i.e. bubbling bed and freeboard region) as shown in Appendix A. In particular, the solids velocity is set to zero, and the gas velocity is given some uniform unidirectional value equal to the inlet fluidising gas velocity divided by void fraction to yield the interstitial gas velocity (Syamlal et al., 1993).

No-slip boundary condition for the gas phase (i.e. gas velocities set to zero at the walls) and the free-slip condition for the solid phase (i.e. solid velocity gradients set to zero at the walls) are applied at the walls (see Appendix A); these boundary conditions are imposed with the help of fictitious boundary cells. At the inlet section of the bed the Dirichlet boundary condition is applied (with constant inlet mass flux) useful for compressible fluid to prescribe mass flow rate at inlet; Dirichlet boundary condition consists in imposing the values of the variables in a section. At the outlet section of the bed the Neumann boundary condition is assumed (with constant outlet pressure). The Neumann boundary condition consists in imposing the values of the derivates (i.e. gradients) of the field variables (set to zero in the flow direction) except for the pressure, which is specified.

Given the assumed conditions, a 2D reactor is filled up with solid particles in a packed bed manner at time equal zero. At the beginning of the simulations, nitrogen flows uniformly from the bottom to the top of the bed fluidising the solid particles. After 2

seconds of simulation, the feed is switched from nitrogen to methane and the simulation runs until approximately constant values of flue gas concentrations are achieved (pseudo stationary condition). Nitrogen is used at time equal zero (with no reaction occurring) to help the convergence at the beginning of the simulation. The initial conditions are shown in Table 3.1 and they were chosen to make reasonable comparisons with the macro model implemented in Aspen Plus (see Table 2.5).

Table 3.1 Initial operating conditions in CFD model

P_{fuel}	10^{-2}	MW
T	950	°C
P	1	atm
D_{FR}	0.35	m
H_{FR}	0.98	m
U_o	0.36	m/s
d_p	2.00E-04	m
ρ_s	3446	kg/m^3
Al_2O_3 content	60%	
NiO content	36%	
Ni content	4%	
L_m	0.45	m
ε_m	0.45	
E	0.92	
e_w	0.99	
Φ	30°	
grid size dx*dy (cmxcm)	0.7x0.7	cmxcm

The size of the reactor has to be decreased compared to the system implemented in Aspen Plus to reduce the computational costs (see Table 2.5). The hydrodynamic conditions simulated in Aspen Plus are kept to guarantee a right comparison between micro and macro model. Thus, the reactor is scaled to a fuel power of 10 kW just reducing the area to 34.8 cm^2 that means 300 g/kW of solid inventory in the bed given a fixed bed length, $L_{m,}$ equal to 0.45 m. Since the simulation runs in a 2D fashion the thickness of the reactor is unitary and so the area corresponds to the reactor diameter, D. As reported by Mahalaktar et al. (2011), the fuel reactor can be simulated over the time in decoupling it from the air reactor for the following reasons:

- The amount of solid material inside the bed is high compared to the reacting gas flow-rate, implying that the metal oxide conversion does not appreciably change during the simulation time (of the order of few seconds);
- Few seconds of simulation are enough to reach pseudo stationary conditions at roughly constant metal oxide conversion; consequently, such the solid flow-rate is not needed to be simulated for replacing the converted metal oxide particles.

In the MFIX environment, the initial NiO mass fraction (i.e. 36%) is chosen equal to the NiO mass fraction in the inlet solid flow-rate simulated in Aspen Plus (X_{MO_exit} is assumed to be 0.9). This assumption does not influence greatly the comparisons between the micro model (CFD) and the macro model (Aspen Plus) since in the either CFD or Aspen simulations this value is almost constant, so its influence on the kinetic rate is the same. Indeed, in CFD the metal oxide conversion does not appreciably change during the simulation time due to few seconds of simulation; in Aspen instead, the metal oxide conversion changes slightly, regardless the degree of gas conversion, since the solid flow-rate applied for models comparison is 8 times higher than the stoichiometric one (F_s = 75 kg/s).

The particle – particle coefficient of restitution, e, is assumed 0.92 whereas the wall – particle coefficient of restitution, e_w, is assumed 0.99. The coefficient of restitution accounts for how much kinetic energy remains in the particle after a collision compared to its value before the collision. The angle of internal friction between particles, Φ, as a measure of the frictional force within the particles and eventually of the flowing characteristics of the particles, is assumed equal to 30°. All the CFD simulations were run in a computational domain divided into 7000 cells (see Table 3.1). In preliminary simulations a grid independence test was carried out increasing the number of cells up to 28000. No appreciable effects on the flow behaviour and main variables such as void fraction and velocities profiles as well as the outlet gas concentration, which represents the main variable of interest, were found.

3.1.10 Kinetics implemented in MFIX

The kinetic rate, in the form of Eq. 2.9, must be modified in its solid conversion term because no solid flow-rate circulates through the fuel reactor. Different expressions are reported in the literature to define the average solid conversion X_j. Jung and Gamwo (2008) substituted the solid conversion term with the averaged oxygen molar fraction

into the solid particles. Mahalatkar et al. (2011) derived an expression for *Xj* from the definition of actual mass of oxygen divided by the mass of oxygen when fully oxidised. Kruggel-Emden et al. (2011) derived an expression for *Xj* from the definition suggested by Levenspiel (1972) of ratio radial position of the reaction front over the external radius of the particle. Kruggel-Emden et al. (2011) showed how the latter definition fits much better the experimental results compared to the others. Thus, we defined the solid conversion term as the volumetric fraction of reacted metal oxide into the solid particles:

$$\left(1 - X_j\right) = \frac{{r_c}^3}{R^3} = Z_{NiO} = \frac{Y_{NiO}}{Y_{NiO} + \frac{\rho_{NiO}}{\rho_{Ni}} Y_{Ni}} \tag{3.31}$$

where Z_{NiO} is the volumetric fraction of NiO and Y_{NiO} and Y_{Ni} are the mass fraction of NiO and Ni respectively. Y_{NiO} and Y_{Ni} have an upper limit equal to 0.4 since the solid material used has a maximum active NiO content of 40% (see Section 2.1). The kinetic rate is finally expressed as:

$$r_{i\,CFD} = k_i \varepsilon_S C_i^n \left(\frac{Y_{NiO}}{Y_{NiO} + \frac{\rho_{NiO}}{\rho_{Ni}} Y_{Ni}}\right)^{\frac{2}{3}} \tag{3.32}$$

Compared to Eq. 2.9, the kinetic rate does not include the gas void fraction because the reference reaction volume is the total volume of the computational cell. The kinetic reaction in the form of Eq. 3.32 is specified in the file *usr_rate.f* (see Appendix A) with the gas concentration expressed as follows:

$$C_i = \frac{\rho_g Y_{gi}}{MW_i} \tag{3.33}$$

where Y_{gi} is the mass gas fraction and MW_i is the molecular weight of the *i* component (i.e. methane for the fuel reactor). In the *mfix.dat* file the stoichiometry of the reaction (see Eq. 2.1) is specified by providing species aliases and chemical equations to recall the *usr_rate.f* file; in addition the thermodynamic data of all the species involved are copied and pasted in the *mfix.dat* file from the MFIX database (see Appendix A).

The comparison between the steady state case implemented in Aspen Plus and the "pseudo stationary" case implemented in MFIX under the same operating conditions was run for two different case studies called "high" and "low" kinetics. High kinetics refers to the value of k_i obtained from the data reported by Abad et al. (2007) and shown in Table 2.1 whereas low kinetics refers to a fictitious low value of k_i equal to 0.1 $kmol^{(1-n)}m^{(3n-3)}/s$. The different kinetics (with two orders of magnitude difference) affect largely the hydrodynamics of the system allowing for a better understanding and comparison between the macro scale model (Aspen Plus) and the micro scale model (CFD).

3.2 Hydrodynamic analysis

As previously mentioned, low and high kinetics were implemented to study their effect on the hydrodynamics and the outlet gas concentrations. In the simulations, the inlet superficial gas velocity, U_o, and the solid inventory, expressed by the initial bed height, L_m, were the main variables that were varied to study the behaviour of the system. U_o was changed from 10 to 36 cm/s whereas L_m was changed from 20 to 45 cm. High kinetic simulations were run for 10 seconds whereas low kinetic simulations were run for 15 seconds since longer times were needed to achieve pseudo stationary condition in terms of gas outlet concentrations (Figs. 3.1-3.4). X coordinate referred to the reactor radial direction whereas Y coordinate referred to the reactor axial direction.

A pure nitrogen flow-rate was fed up to t = 2 seconds. Nitrogen was used at time equal zero (with no reaction occurring) to help the convergence at the beginning of the simulation. For t > 2 seconds, the feed flow-rate was switched from pure nitrogen to methane (Figs. 3.1-3.4) and the heterogeneous reaction with NiO occurred. In Figs. 3.1-3.4, the delay in the methane mass fraction detection after t > 2 seconds was due to the time that the methane feed flow-rate needed to cross the whole fluidised bed and it increased as the inlet gas velocity was decreased (Figs. 3.2, 3.4). The plots were noisy due to the bubbling regime characterised by a non-periodic gas motion across the reactor. Jung and Gamwo (2008) reported the same behaviour. The simulations need to run for a time that allows all nitrogen to be removed from the reactor. Thus, pseudo stationary conditions were assumed to be reached after 13 seconds for the low kinetic case (Figs. 3.1 – 3.2) and after 8 seconds for the high kinetic case (Figs. 3.3 – 3.4). Therefore, all the variables of interest will be averaged over time in a range 13 – 15 and 8 - 10 seconds for the low and the high kinetic case, respectively.

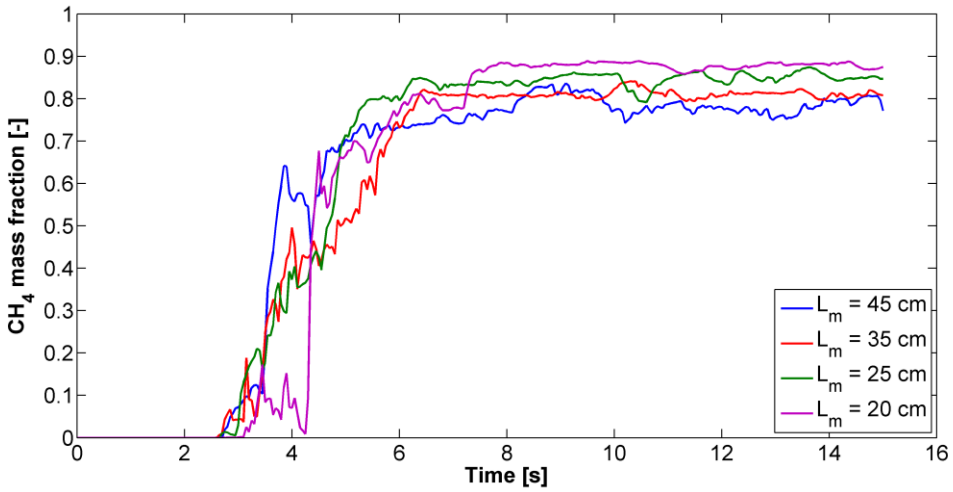

Fig. 3.1 CH_4 mass fraction averaged on X axis at the bed exit vs. time at U_o = 36 cm/s (low kinetics case)

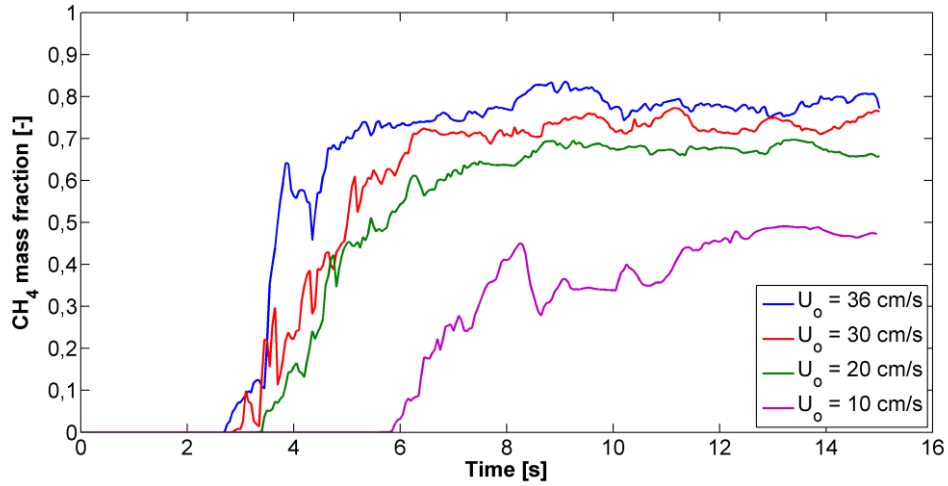

Fig. 3.2 CH_4 mass fraction averaged on X axis at the bed exit vs. time at L_m = 45 cm (low kinetics case)

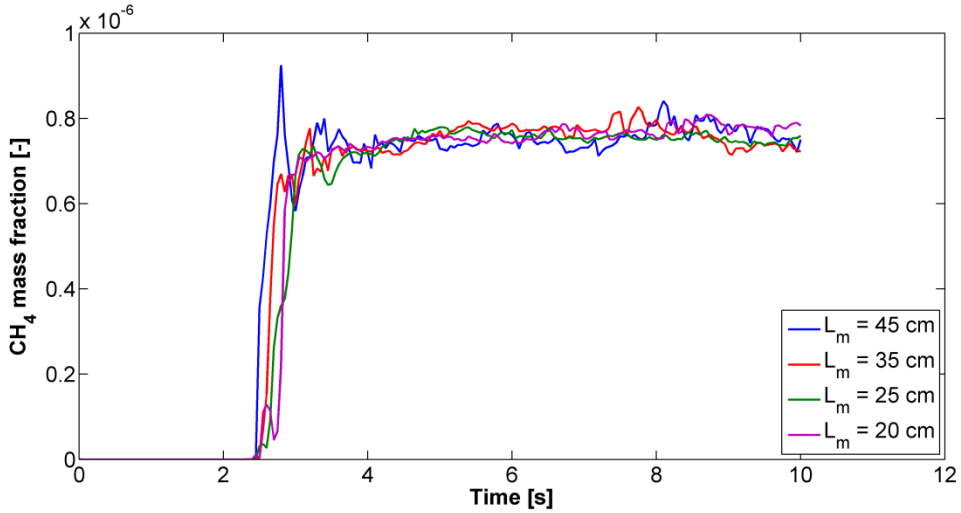

Fig. 3.3 CH_4 mass fraction averaged on X axis at the bed exit vs. time at U_o = 36 cm/s (high kinetics case)

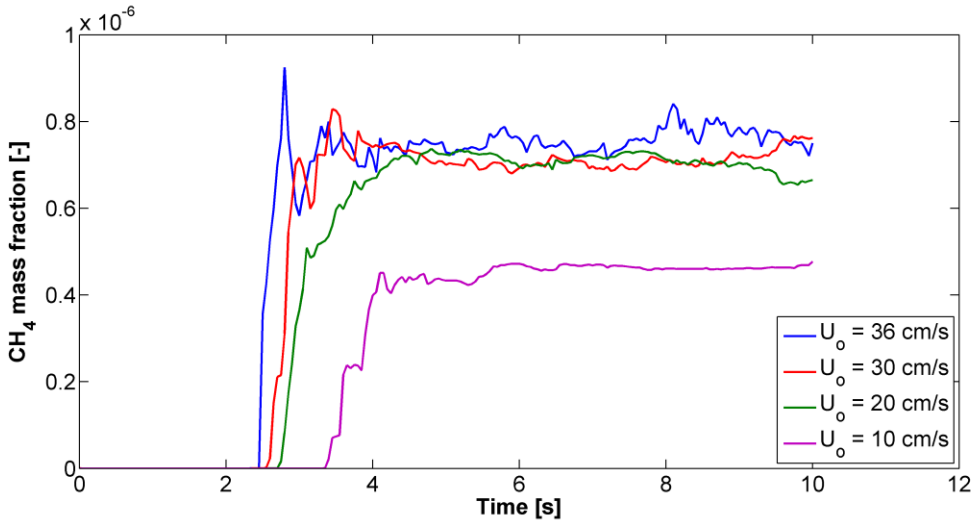

Fig. 3.4 CH_4 mass fraction averaged on X axis at the bed exit vs. time at L_m = 45 cm (high kinetics case)

Figs. 3.5 - 3.6 show, for the low kinetics case, the void fraction and the solid volume fraction respectively in the dense phase versus X axis averaged over Y axis between 12.95 and 16.45 cm; the solid inventory is changed while keeping U_o constant at 36 cm/s. The low kinetics case is averaged over time between 13 and 15 seconds. Figs. 3.5 - 3.6 exhibit lower void fraction and thus higher solid volume fraction close to the walls and the opposite trend at the centre of the bed. This feature can be explained with the bubbles flow pattern: bubbles formation occurs at the bottom of the fluidised bed and they rise and coalesce along the bed height mostly far from the walls leaving a "layer" of solids close to the walls flowing downwards due to recirculation effects.

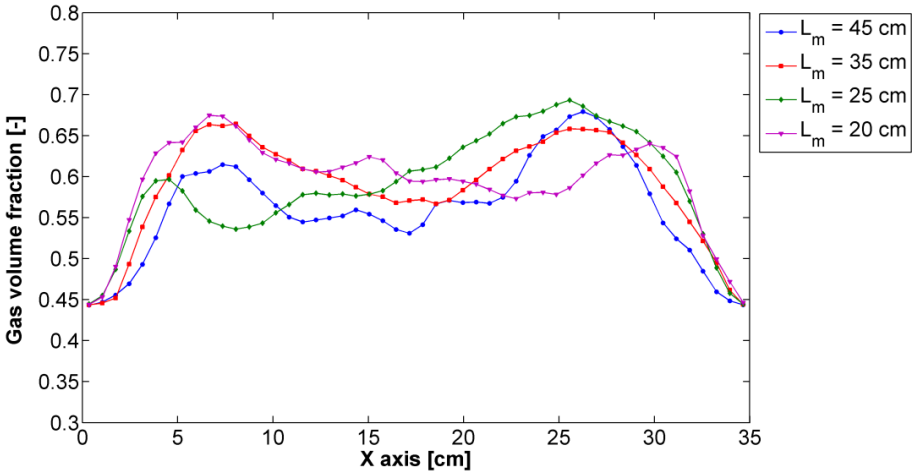

Fig. 3.5 Gas volume fraction vs. X axis for low kinetics at U_o = 36 cm/s

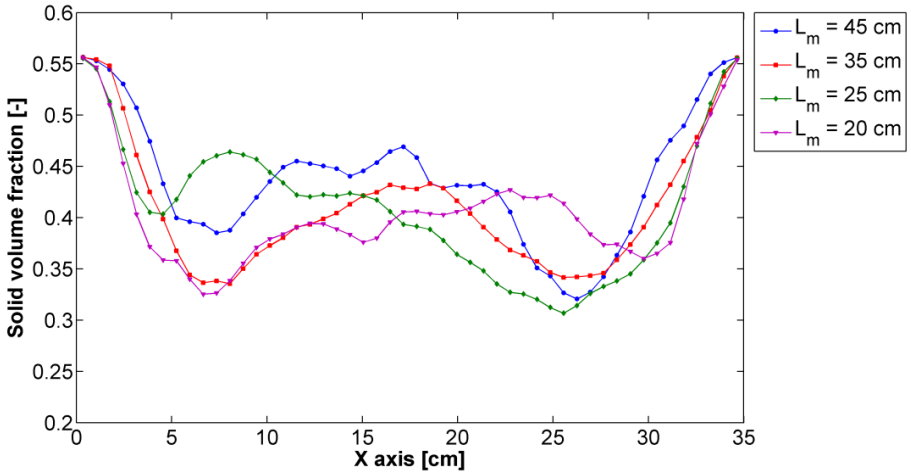

Fig. 3.6 Solid volume fraction vs. X axis for low kinetics at U_o = 36 cm/s

Fig. 3.7 shows the axial component of the gas velocity, V_g, for the low kinetics case varying L_m while keeping U_o constant at 36 cm/s. Two main features can be noticed: the applied no slip condition for the gas phase (with V_g equal to zero at the walls) and higher values of V_g in the centre of the bed due to the bubble tendency to rise mostly towards the centre. The rising of the bubbles creates recirculation of the solid phase in the so called "emulsion phase" that leads to negative value of V_g close to the walls.

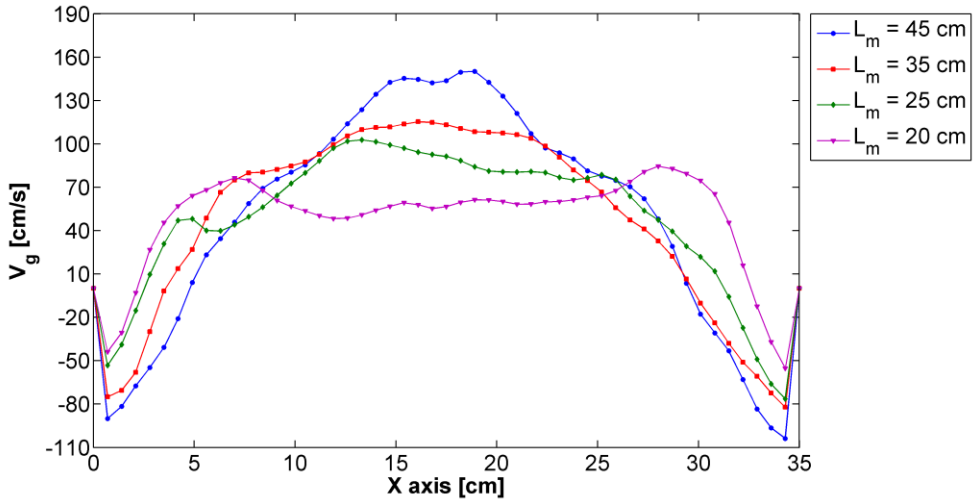

Fig. 3.7 Axial gas velocity V_g vs. X axis for low kinetics at U_o = 36 cm/s

Fig. 3.8 shows the axial component of the solid velocity, V_s, for the low kinetics case. The solid free slip condition is verified (with $V_s \neq 0$) at the walls. The bubbles' rising pushes the solid particles upward in the centre of the bed and subsequently they fall down following the recirculation motions. The change in the solid inventory inside the system affects the solid recirculation motions; indeed, for low solid inventory (i.e. L_m =

20 cm) the velocity profiles, V_g and V_s, are flatter meaning that the upward gas motion is more uniform with less preferential patterns for the bubbles towards the centre of the bed.

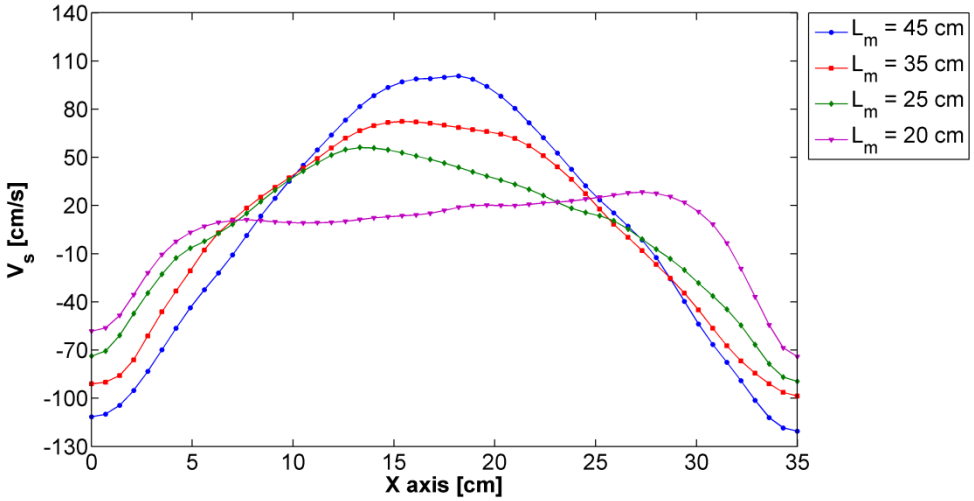

Fig. 3.8 Axial solid velocity V_s vs. X axis for low kinetics at U_o = 36 cm/s

Fig. 3.9 shows the gas pressure profile averaged over time and X axis varying L_m. The outlet boundary condition, setting P_g equal to the atmospheric pressure, is verified. Furthermore, the inlet values of the gas pressure reflect the hydrostatic pressure distribution being higher at higher solid inventories.

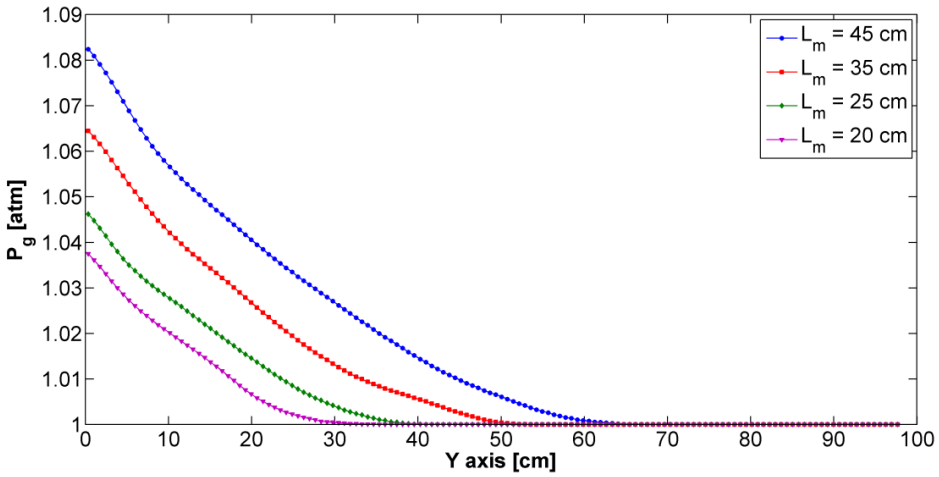

Fig. 3.9 Gas pressure vs. Y axis for low kinetics at U_o = 36 cm/s

Figs. 3.10 – 3.14 exhibit, in sequence, the void and the solid volume fraction, the axial gas and solid velocity as well as the gas pressure averaged under the conditions of Figs. 3.5 – 3.9 but varying the inlet superficial gas velocity at L_m = 45 cm.

Figs. 3.10 – 3.14 exhibit all the typical features of a bubbling bed as discussed previously: bubbles flow pattern far from the walls, solids recirculation with downward flow close to the walls, higher axial gas velocity as well as higher axial solid velocity at the centre of the bed due to solid particles pushed upwards by fast bubbles. In each graph, the only trend that is considerable different from the other refers to the case at U_o = 10 cm/s. Indeed, while approaching the minimum fluidisation conditions, less bubbles are present in the system and the upwards gas motion tends to be uniform on the radial direction leading to flatter profile of void fraction and axial gas and solid velocity.

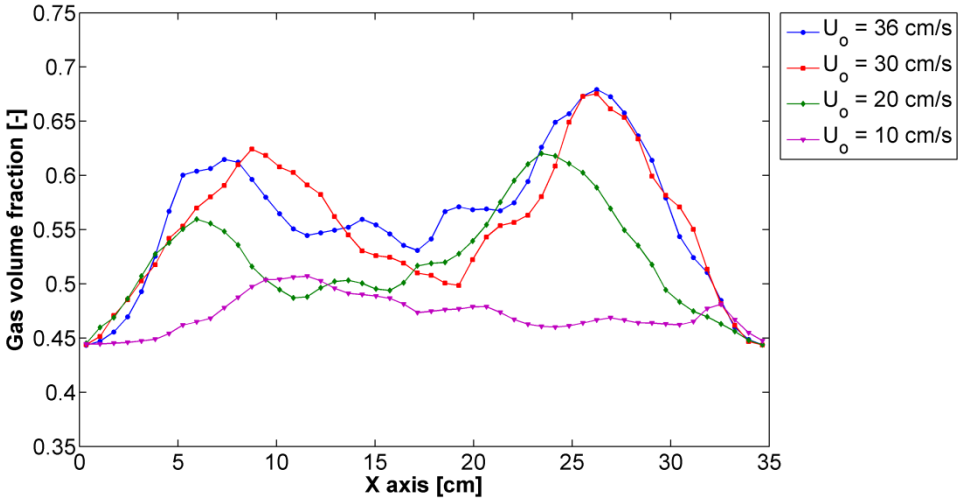

Fig. 3.10 Gas volume fraction vs. X axis for low kinetics at L_m = 45 cm

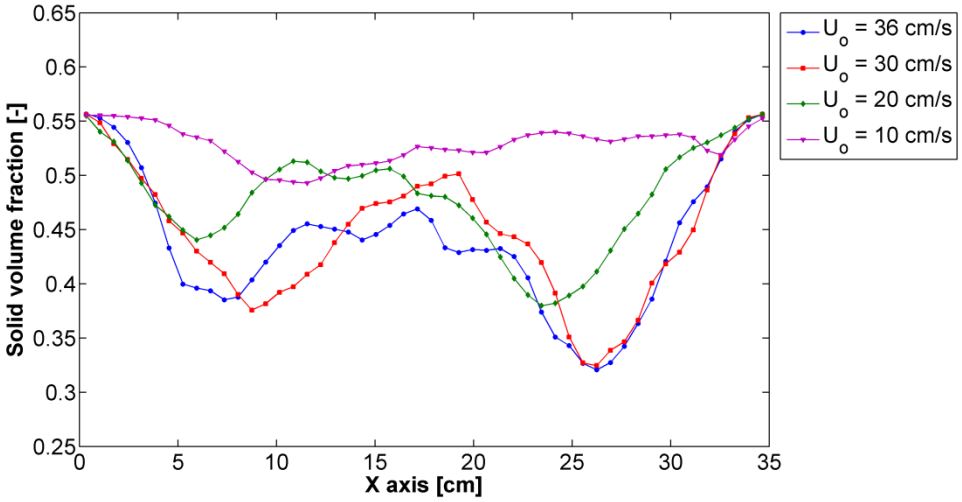

Fig. 3.11 Solid volume fraction vs. X axis for low kinetics at L_m = 45 cm

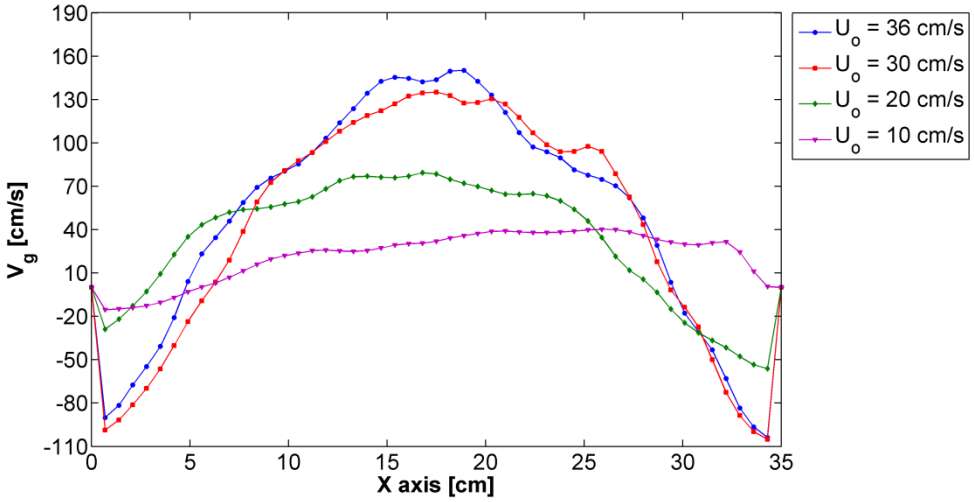

Fig. 3.12 Axial gas velocity V_g vs. X axis for low kinetics at L_m = 45 cm

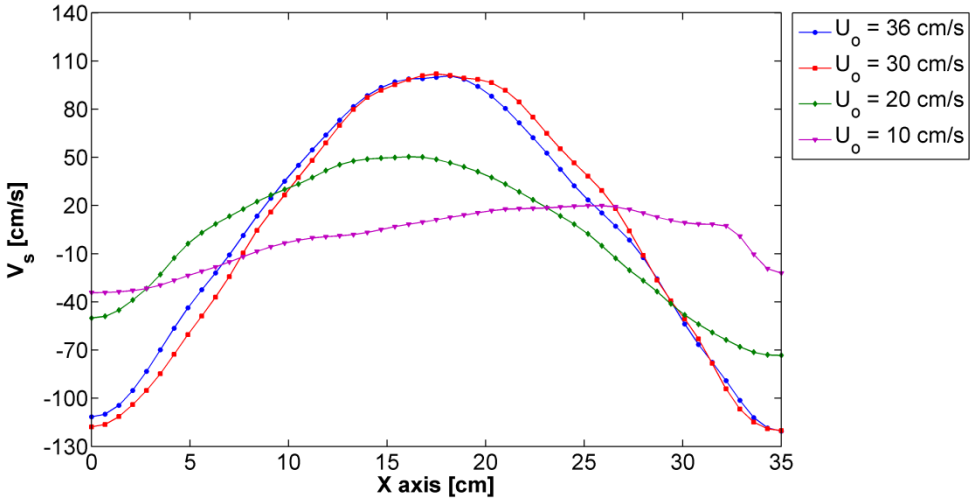

Fig. 3.13 Axial solid velocity V_s vs. X axis for low kinetics at L_m = 45 cm

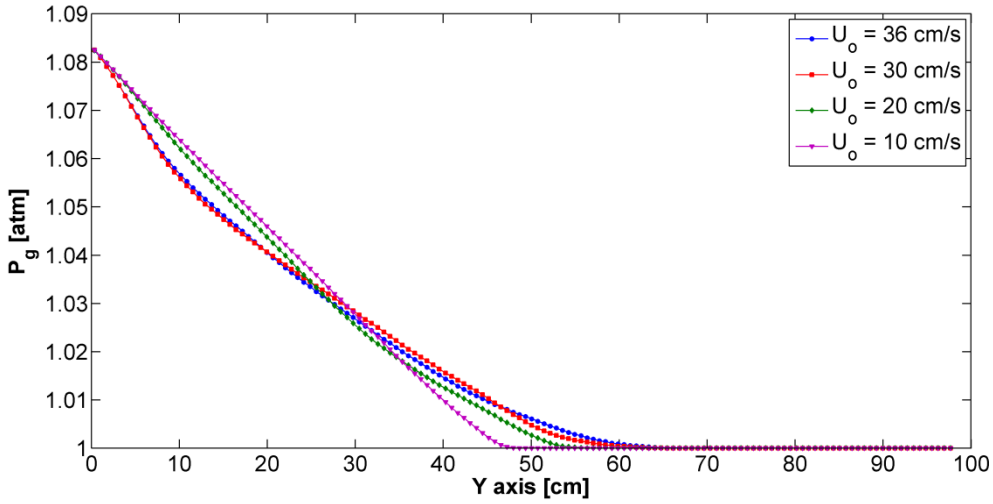

Fig. 3.14 Gas pressure vs. Y axis for low kinetics at L_m = 45 cm

The same hydrodynamic analysis was carried out for the case at high kinetics. The variables under investigation were averaged over times between 8 and 10 seconds. All the radial profiles are averaged over Y axis between 12.95 and 16.45 cm as previously reported for the low kinetic case. All the main features discussed for the low kinetics case are valid also for the high kinetics case (Figs. 3.15 – 3.24).

It is worth noting that in Fig. 3.24 the inlet gas pressure is influenced by the change in the inlet superficial gas velocity. At the inlet P_g decreases while increasing U_o. This phenomenon does not occur at the low kinetics case (Fig. 3.14). A possible explanation is related to the large increase in the void fraction due to two simultaneous effects: high inlet gas velocity and high kinetics. The latter leads to a considerable change in the number of moles and so in the gas volume fraction, ε_g, affecting the inlet gas pressure as described by Eq. 3.34 (Kunii and Levenspiel, 1991):

$$\Delta P = (\rho_s - \rho_g)(1 - \varepsilon_g) g L_m \tag{3.34}$$

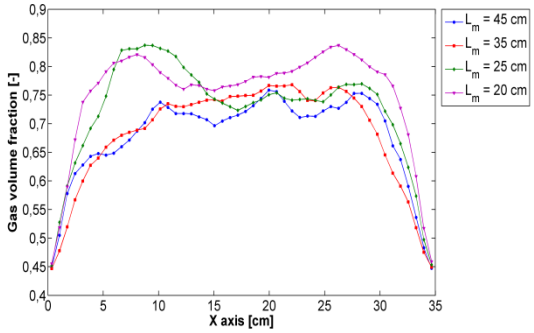

Fig. 3.15 Gas volume fraction vs. X axis for high kinetics at U_o = 36 cm/s

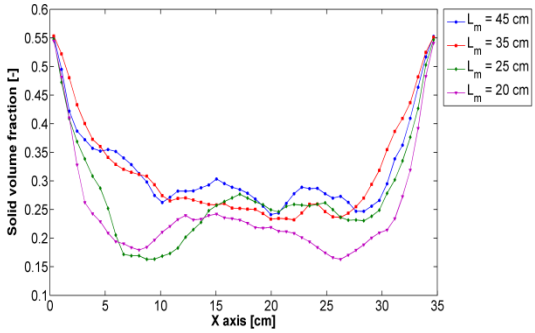

Fig. 3.16 Solid volume fraction vs. X axis for high kinetics at U_o = 36 cm/s

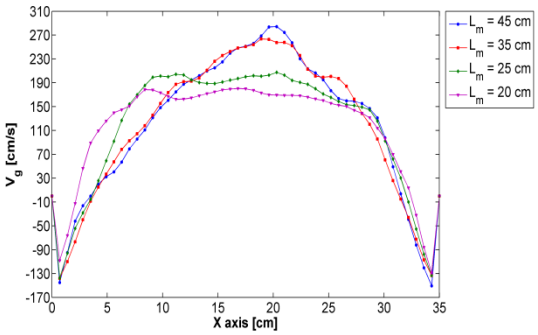

Fig. 3.17 Axial gas velocity V_g vs. X axis for high kinetics at U_o = 36 cm/s

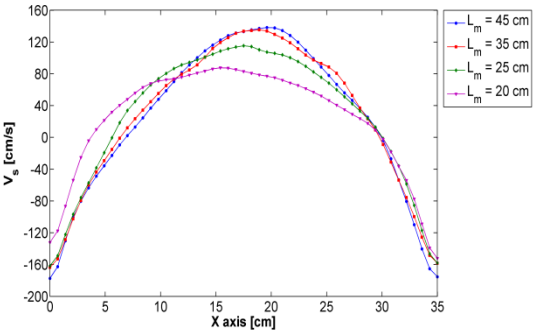

Fig. 3.18 Axial solid velocity V_s vs. X axis for high kinetics at U_o = 36 cm/s

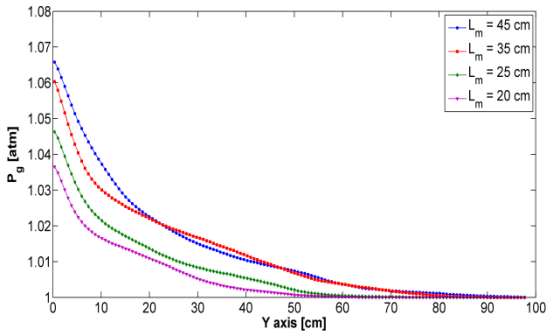

Fig. 3.19 Gas pressure vs. Y axis for high kinetics at U_o = 36 cm/s

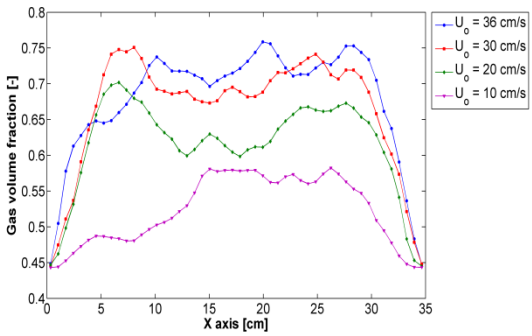

Fig. 3.20 Gas volume fraction vs. X axis for high kinetics at L_m = 45 cm

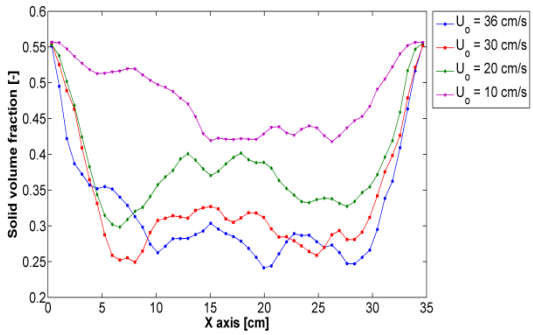

Fig. 3.21 Solid volume fraction vs. X axis for high kinetics at L_m = 45 cm

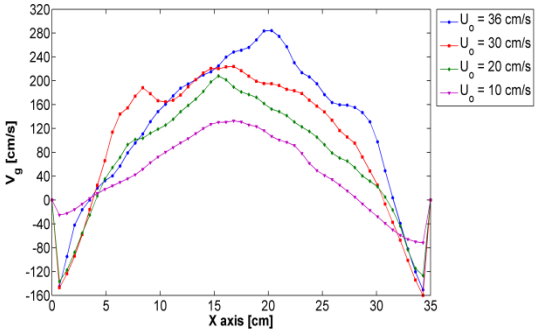

Fig. 3.22 Axial gas velocity V_g vs. X axis for high kinetics at L_m = 45 cm

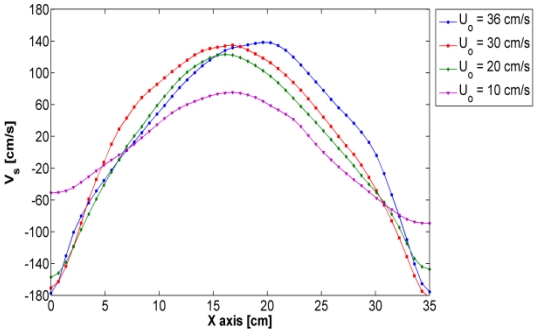

Fig. 3.23 Axial solid velocity V_s vs. X axis for high kinetics at L_m = 45 cm

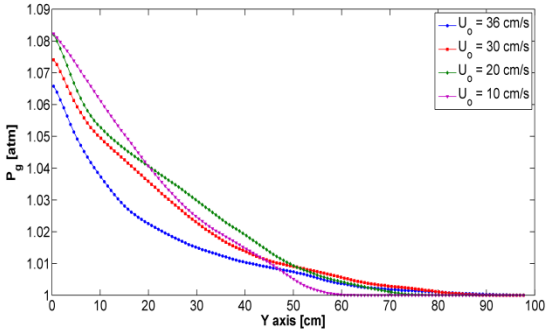

Fig. 3.24 Gas pressure vs. Y axis for high kinetics at L_m = 45 cm

Comparisons between the low and the high kinetics case are shown in Figs. 3.25 - 3.29 keeping constant U_o at 36 cm/s and L_m at 45 cm.

The reaction of methane with NiO is characterised by an increase of the number of moles in the gas phase (with an expansion factor ξ equal to 2). Thus, rapid kinetics, which leads to high methane conversion, produced an increase in the gas volume fraction (Fig. 3.25). Conversely, the solid volume fraction showed higher values in the low kinetics case (Fig. 3.26). High methane conversion produced a remarkable increase in the gas volumetric flow-rate and thus in the axial gas velocity (Fig. 3.27). The same effect was noticeable for the axial solid velocity profiles (Fig. 3.28).

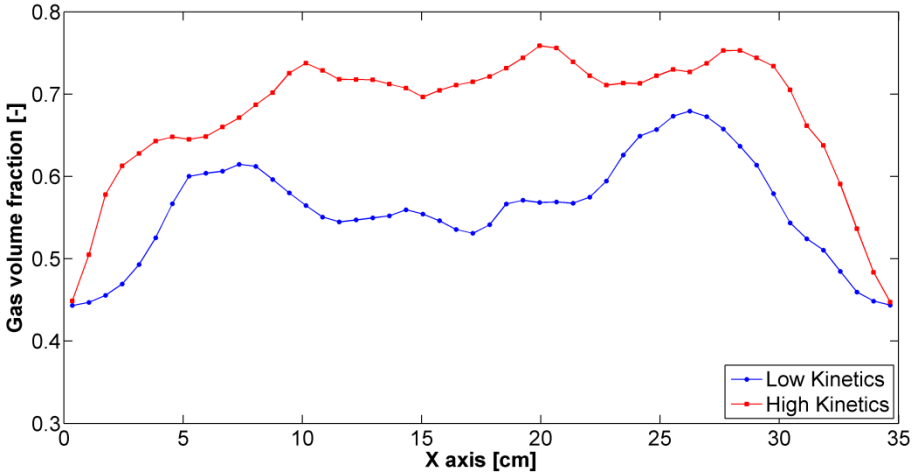

Fig. 3.25 Gas volume fraction vs. X axis at low and high kinetics

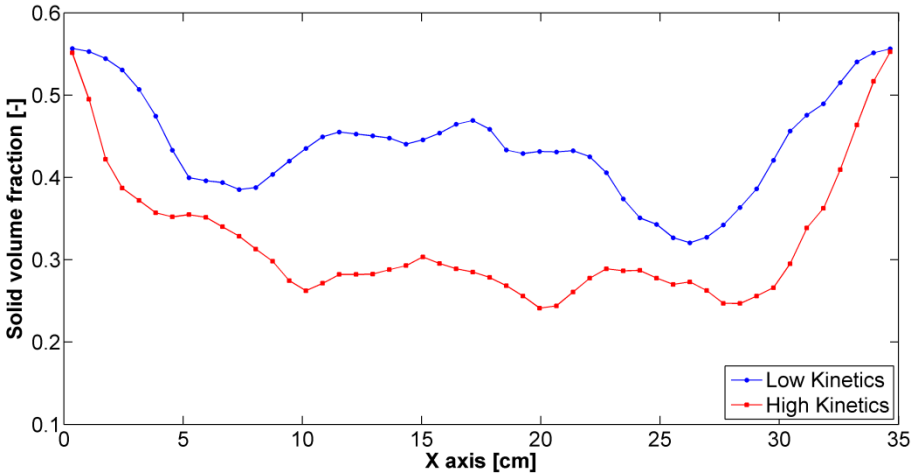

Fig. 3.26 Solid volume fraction vs. X axis at low and high kinetics

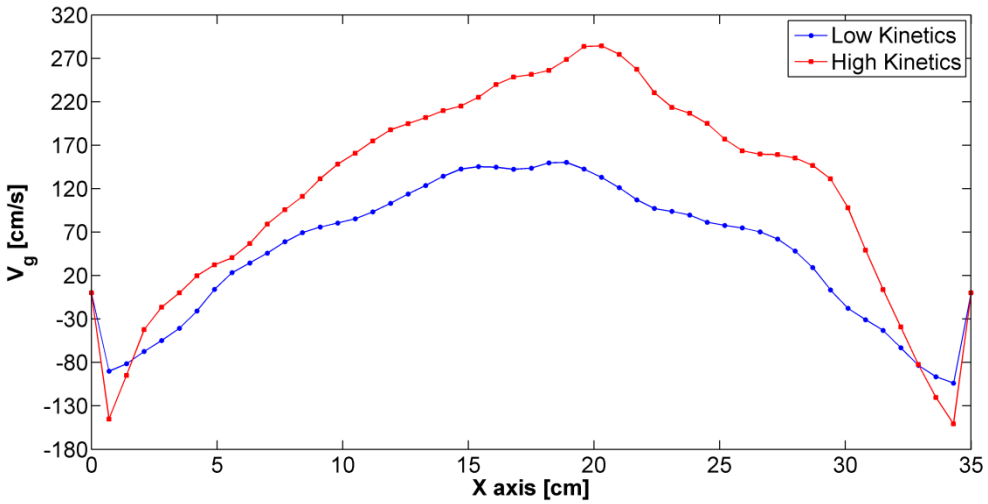

Fig. 3.27 Axial gas velocity V_g vs. X axis at low and high kinetics

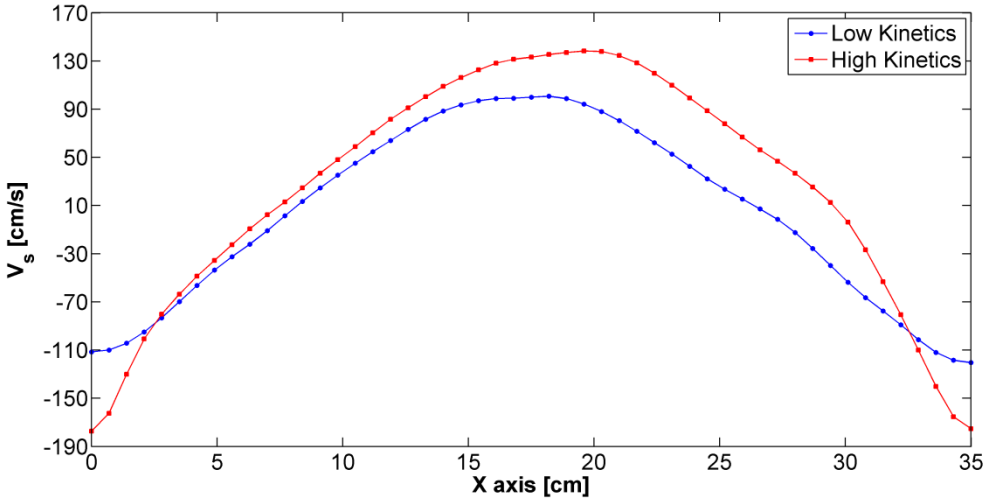

Fig. 3.28 Axial solid velocity V_s vs. X axis at low and high kinetics

Fig. 3.29 shows the change in the axial component of the gas velocity, V_g, versus Y axis averaged over time and X axis. The double effect of the heterogeneous reaction and the reduction of the void space ($\varepsilon_g < 1$), which is due to the presence of the solid particles at the bottom of the bed, produced an initial abrupt increase in V_g in the dense phase particularly pronounced for high kinetics. The value of V_g at the bed exit followed the increase in the number of moles due to the methane conversion. The outlet value of V_g verified Eq. 3.35:

$$V_{g\ outlet} = V_{g\ inlet}(1 + \xi X_{CH4}) \tag{3.35}$$

where ξ is the expansion factor for the gas species and X_{CH4} is the methane conversion.

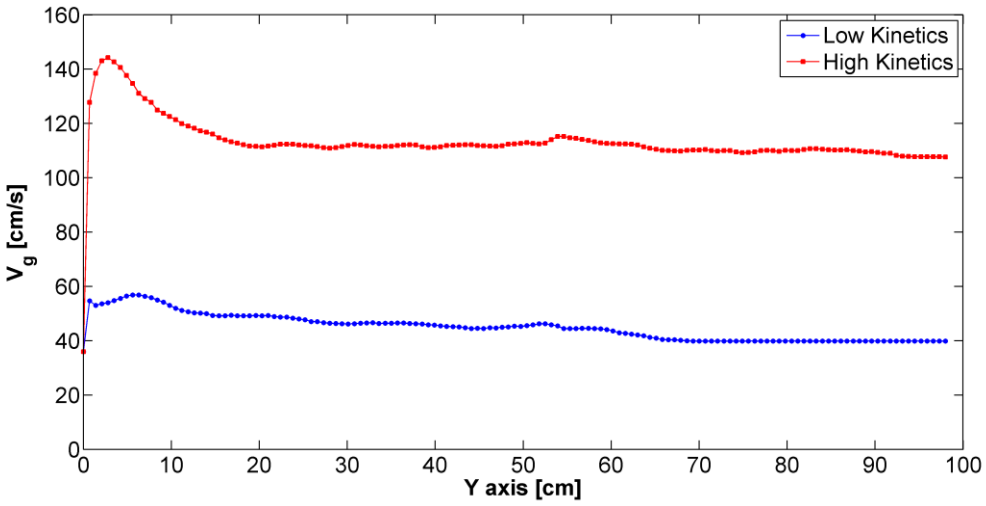

Fig. 3.29 V_g vs Y axis averaged over time and X axis at low and high kinetics

Figs. 3.30 - 3.31 show the gas volume fraction and the mass fraction of the gas species along the bed at low and high kinetics respectively.

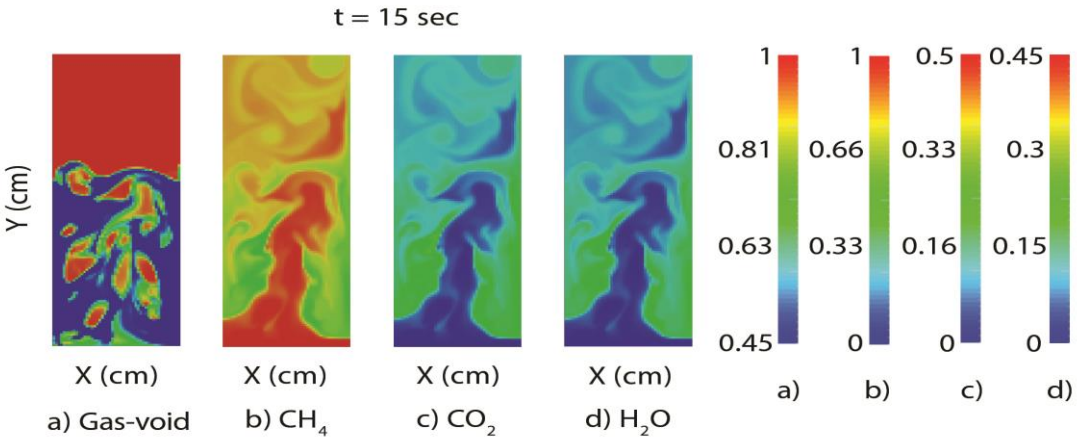

Fig. 3.30 Gas volume fraction and mass fractions of gas species at t = 15 s and low kinetics

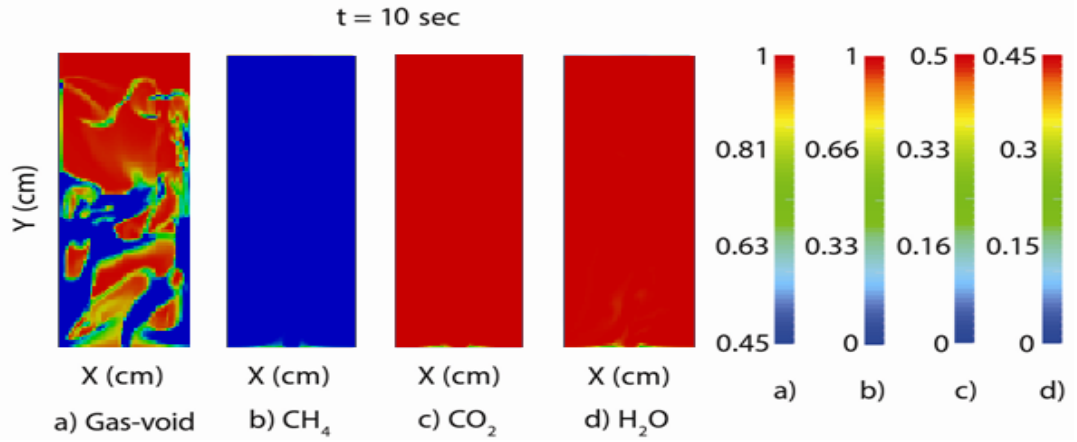

Fig. 3.31 Gas volume fraction and mass fractions of gas species at t = 10 s and high kinetics

It can be noticed the main features charactering the bubbling regime: the bubbles' formation takes place few centimetres above the gas inlet; bubbles rise mostly at the centre of the bed increasing in volume and coalescing along the bed height.

At high kinetics, bubbles are bigger and the motion approaches the turbulent regime (Fig. 3.31) due to the high methane conversion that leads to high increase in number of moles in the gas phase. This phenomenon can be ideally explained with the transfer of the gas exceeding the minimum fluidisation velocity U_{mf} from the emulsion phase at high solid content to the bubble phase at high gas content (Kunii and Levenspiel, 1990). Due to bigger and faster bubbles and their burst at the interface dense phase – freeboard, at high kinetic conditions higher bed expansion is detected.

At low kinetics (Fig. 3.30), high values of un-reacted methane mass fraction are observed, mainly in the centre of the bed where most of the bubble phase takes place. The reaction occurs mainly in the bottom section of the bed characterised by an average high solid volume fraction, high methane mass fraction and no well-defined bubble phase. Far from the bottom region, bubble phase formation determines gas by-pass along the bed, which is subtracted from the high reacting regions (Fig. 3.32); thus poor gas conversion is expected to occur.

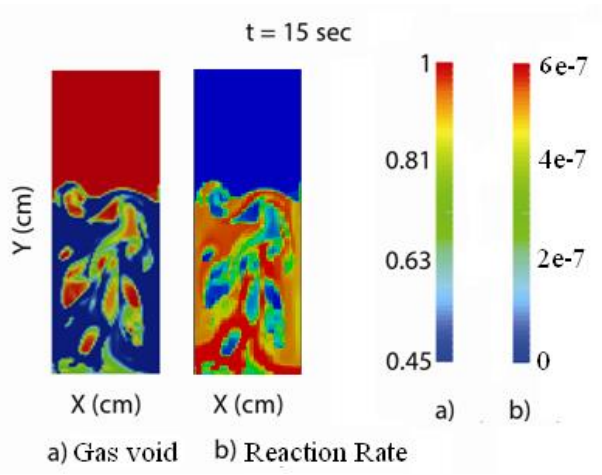

Fig. 3.32 Void fraction and reaction rate ([=] g/(cm^{3}s)) at t = 15 s and low kinetics

At high kinetics, the reaction occurs mainly in the bottom phase and gas by-pass does not seem to have any effect in lowering the gas conversion in the upper bed region. Indeed, in the bottom region, where the gas is not yet developed into bubbles, the mass

transfer has been found to be much higher than that in the upper bed region (see also Fig. 3.33). The latter is supported by experimental values that show mass transfer values more than one order of magnitude higher than those measured in the upper bed region (Scala, 2013).

However, the outcome is affected by the assumed condition of inlet uniform gas flow-rate. Modelling of the gas distributor (preferably in a 3D simulation) is expected to show bubble formation after few millimetres above the distributor reinforcing the negative effect of gas by-pass on the gas conversion.

Being aware that the gas distributor (not modelled in our work) can affect the development of the bubbles and thus the gas conversion, the simulations carried out at two different kinetics conditions show that high reacting solid materials are important to achieve full gas conversion in a fluidised bed operating under bubbling regime.

No freeboard effect in the kinetic reaction is detected (Deng et al., 2008; Jung and Gamwo, 2008; Wang et al., 2011). The influence of the freeboard region characterised by low solid content on the gas conversion was experimentally demonstrated (De Lasa and Grace, 1979; Furusaki et al., 1976; Kunii and Levenspiel, 1990). As reported by Wang et al. (2011), the zero solid – gas contact efficiency in the freeboard might be related to the failure of the Eulerian – Eulerian approach to describe the gas/solid mechanisms in regions at very low solid particles concentrations. An Eulerian – Lagrangian approach might help to estimate the reduction of the reaction in the freeboard region.

3.3 Improvement of the macro-model in Aspen Plus

Several authors have applied the concept of dividing axially the bubbling bed into stages and considering a number of stages of the same length (Hashemi Sohi et al., 2012; Jafari et al., 2004; Porrazzo et al., 2014; Sarvar-Amini et al., 2007). Previous CFD simulations showed how most of the heterogeneous reaction occurs at the bottom of the fluidised bed, in particular at high kinetics. Indeed, at the bottom of the bed the reacting gas concentration is higher and the bubbles' diameter is at its minimum; furthermore, the incoming gas, which encounters the solid particles, creates turbulent

motions that enhance the gas-solid contact efficiency promoting an increase in the gas conversion.

The mass transfer between the bubble and the emulsion phase decreases significantly along the bed due to the increase in the bubble diameter that reduces the mass transfer coefficient K_{be} between the bubble and the emulsion phase (see Eqs. 2.34 - 2.36). Moreover, the increase in the bubble volumetric fraction, σ, along the bed, due to the gas expansion, reduces the emulsion volume fraction and thus the portion of the bed where most of the reaction takes place. Consequently, two adjustments to the macro scale model reported in Chapter 2 are introduced:

1) Implementing of the change in the bubble diameter, d_b, along the bed height, according to the Darton correlation (Eq. 2.37); indeed, the bubble growth along the bed height leads to an increase in d_b that cannot be neglected since it affects greatly the gas conversion, especially at high kinetics;
2) New concept of stages.

In the preliminary multi stages model, the whole bed was divided into 5 stages of the same length (see Chapter 2). The new concept of stages refers to a different split of the bed length according to the following strategy: 4 stages were used to model the bottom of the bed whereas the last (fifth) stage was used to model the rest of the fluidised bed length.

Based on the increment in the bubble diameter per unit bed height (Fig. 3.33), as an indicator of the mass transfer effectiveness between the two phases, 4 stages were employed to model the first 10 centimetres of the bed above the inlet and the last stage was employed to model the rest of the bed length. The trend of the mass transfer coefficient K_{be} follows the same trend of the incremental bubble diameter per height unit. In this way, it is assured a good utilisation of the limited number of stages employed since we mainly focus on the modelling of the bed zone where the most of the phenomena of interest occur.

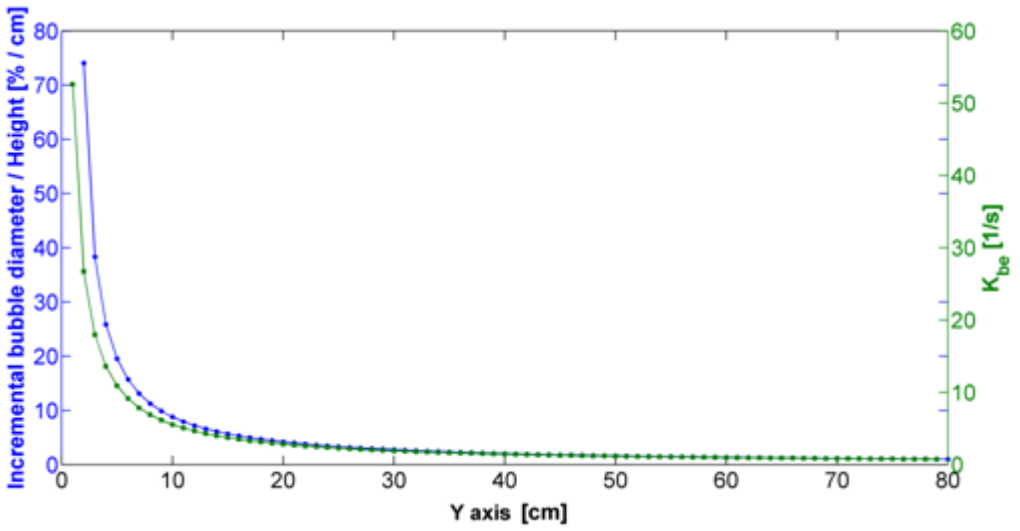

Fig. 3.33 Incremental bubble diameter per height unit vs. bed length

3.3.1 Comparative results CFD – Aspen Plus

The two fuel reactor models (MFIX and Aspen Plus) were tested under different operating conditions: various superficial gas velocity, solid inventory and kinetics of reaction.

Fig. 3.34 shows the variation of the methane mass fraction along the bed height for different superficial gas velocities at constant solid inventory L_m equal to 45 cm and low kinetics. The values of the CH_4 mass fraction in the Aspen Plus model are detected at the end of each reaction stage. The CH_4 mass fraction in the CFD model is averaged over X axis and over time between 13 and 15 seconds.

In both models, a reduction in the superficial gas velocity U_o determines a decrease in the methane mass fraction and thus an increase in the gas conversion; indeed, values of U_o closer to the minimum fluidisation velocity lead to a reduction of the gas by-pass through the bubble phase promoting the reaction in the emulsion phase. The increase in methane conversion is amplified from the fact that keeping constant the area of the reactor, a decrease in U_o leads to a decrease in the fuel power and thus the same amount of solid inventory reacts with less methane flow-rate driving the gas conversion to higher values.

As mentioned previously, most of the reaction occurs in the bottom of the bed where gas and solid show high contact efficiency. The Aspen Plus model assumes an initial

split of the superficial gas flow-rate between the two phases based on the amount of gas exceeding the minimum fluidisation conditions (see Chapter 2); thus, part of the gas flow-rate is initially subtracted to react with the solid particles leading to lower values of gas conversion compared to the CFD model. In the CFD model, we assume uniform inlet gas flow-rate and the modelling of the gas distributor is not taken into account.

The gas distributor affects the bubble phase in terms of bubble diameter and distance of initial formation from the bottom of the bed (Geldart and Baeyens, 1985; Kunii and Levenspiel, 1990). For this reason, it is believed that the modelling of a gas distributor in a 3D CFD simulation could give a better match between the macro-scale and micro-scale models.

The mass transfer term appears as playing a negligible role far from the inlet, determining almost flat profiles of methane mass fraction above 10 cm from the inlet. This aspect justifies the implementation of just one stage to model the rest of the bed height in Aspen Plus.

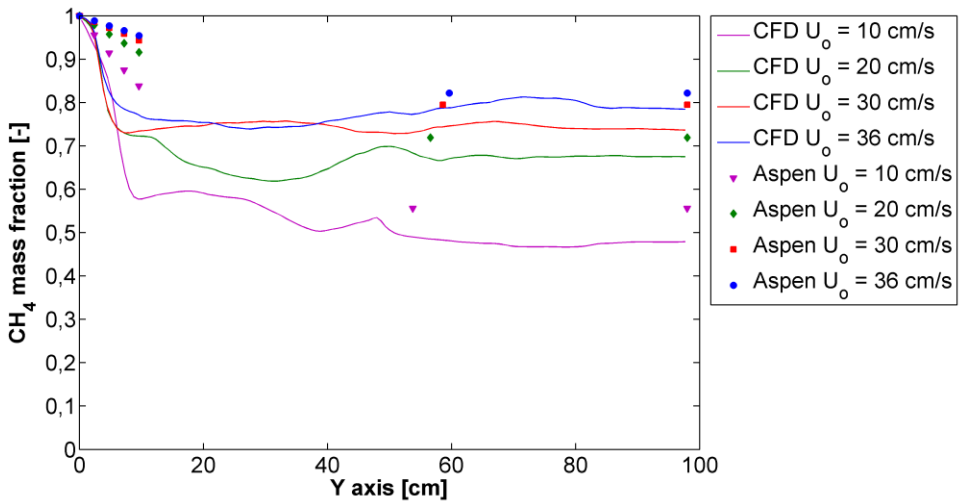

Fig. 3.34 Methane mass fraction along the bed under different superficial gas velocities (low kinetics)

Fig. 3.35 and 3.36 show the rate of reaction and the solid volume fraction respectively along the bed height for different superficial gas velocities at constant solid inventory and low kinetics. A lower superficial gas velocity leads to higher solid volume fraction near to the bottom of the bed (Fig. 3.36); thus, the reaction rate, which is a function of ε_s (see Eq. 3.32), is higher (Fig. 3.35) and the overall effect is a larger decrease in the

methane mass fraction. It is worth to point out that the abrupt change in the solid volume fraction in Fig. 3.36 occurring at any gas velocity is due to the transition from the bubbling region to the freeboard region characterised by a low solid content.

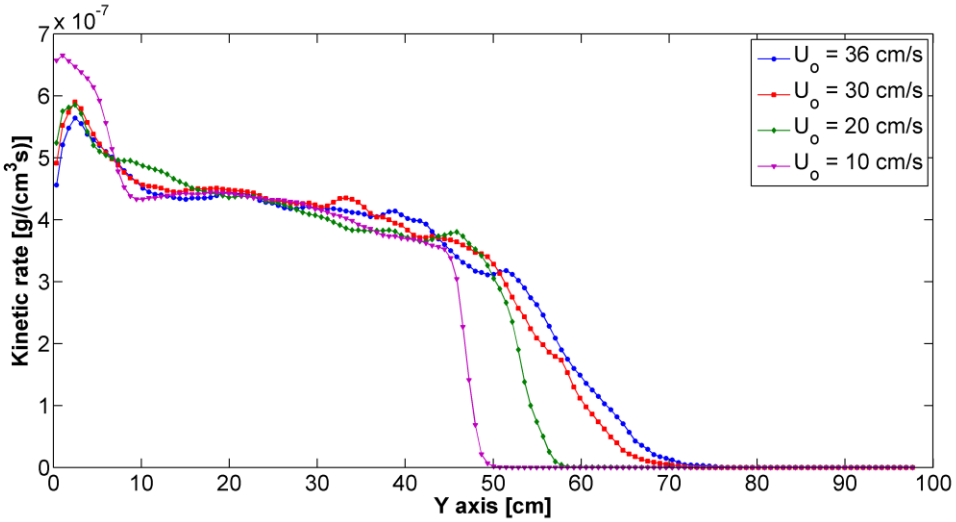

Fig. 3.35 Reaction rate along the bed under different superficial gas velocities (low kinetics)

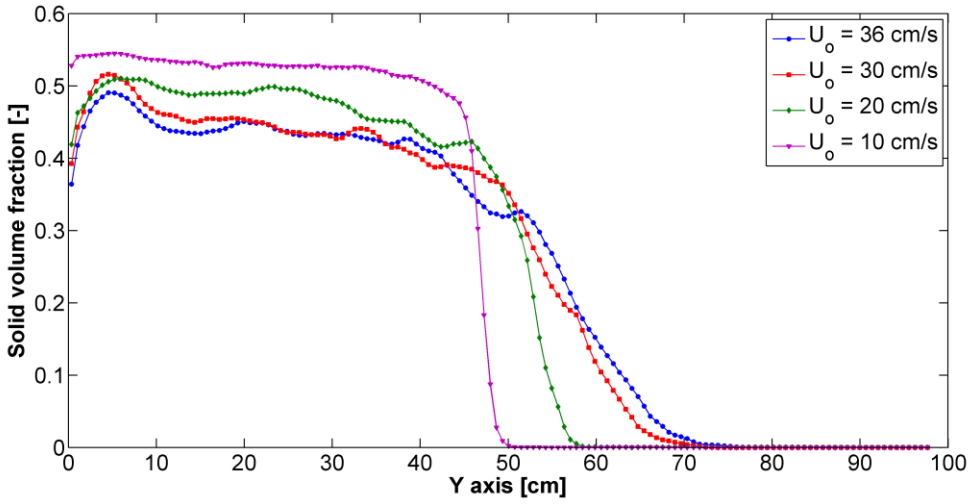

Fig. 3.36 Solid volume fraction along the bed under different superficial gas velocities (low kinetics)

Fig. 3.37 shows the methane conversion at the bed exit for the two models at different initial superficial gas velocities. As previously mentioned, the Aspen model gives lower methane conversion compared to the CFD model due to the initial split of the gas flow-rate at the bed inlet. The CFD trend is slightly affected by fluctuations in the axial velocity component (pseudo stationary condition). The difference in the outlet gas conversion between the two models ranges from 1 to 6%.

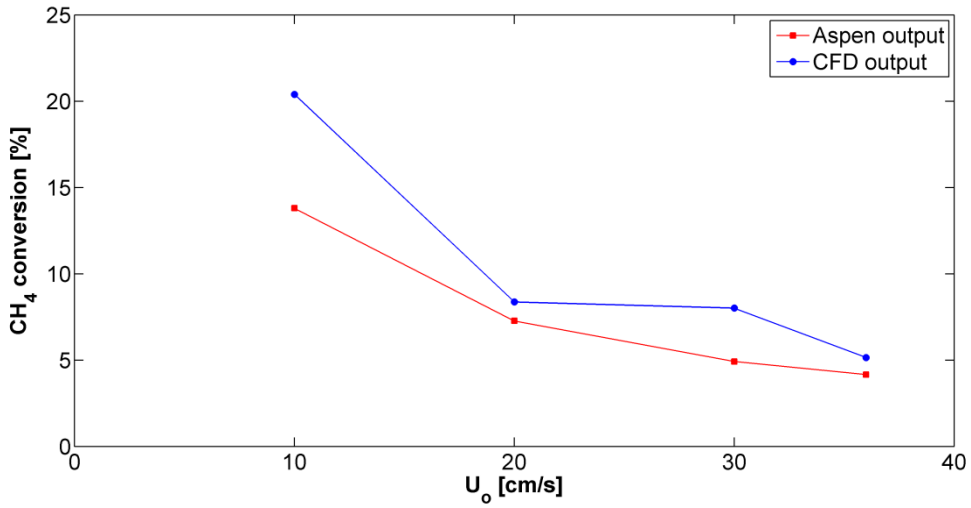

Fig. 3.37 Gas conversions vs. U_o at low kinetics

Fig. 3.38 shows the variation of the methane mass fraction along the bed for different solid inventories at constant initial superficial gas velocity, equal to 36 cm/s, and slow kinetics.

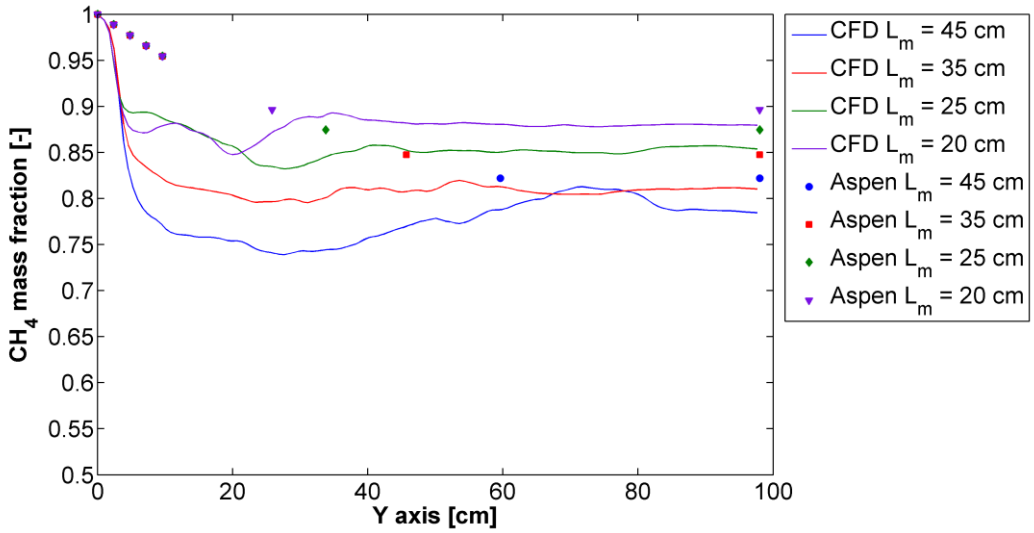

Fig. 3.38 Methane mass fraction along the bed under different solid inventories (low kinetics)

The reduction in the solid inventory, expressed as height of fixed bed L_m, determines lower gas residence time into the bed driving to lower gas conversion. The Aspen model captures this feature in the last stage of reaction that is smaller in terms of volume of reaction at lower solid inventories.

In the CFD simulations, the change in solid inventory affects the solid volume fraction distribution in the bottom of the bed (Fig. 3.40) and thus the kinetic rates (Fig. 3.39).

Higher solid inventories lead to higher average solid volume fraction in the bottom zone because statistically more solid particles participate to the recirculation motions into the bed; consequently, higher solid volume fractions lead to higher kinetic rates (see Eq. 3.32 and Fig. 3.39) and thus lower methane mass fractions.

The comparison in gas conversion at the bed exit between the two models is good (Fig. 3.41). The difference in the outlet gas conversion between the two models is below 3%.

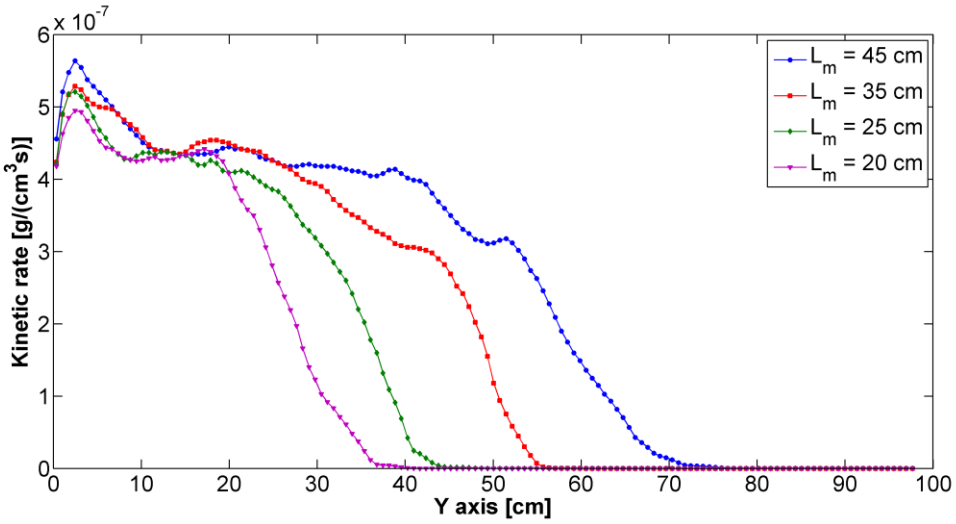

Fig. 3.39 Reaction rate along the bed under different solid inventories (low kinetics)

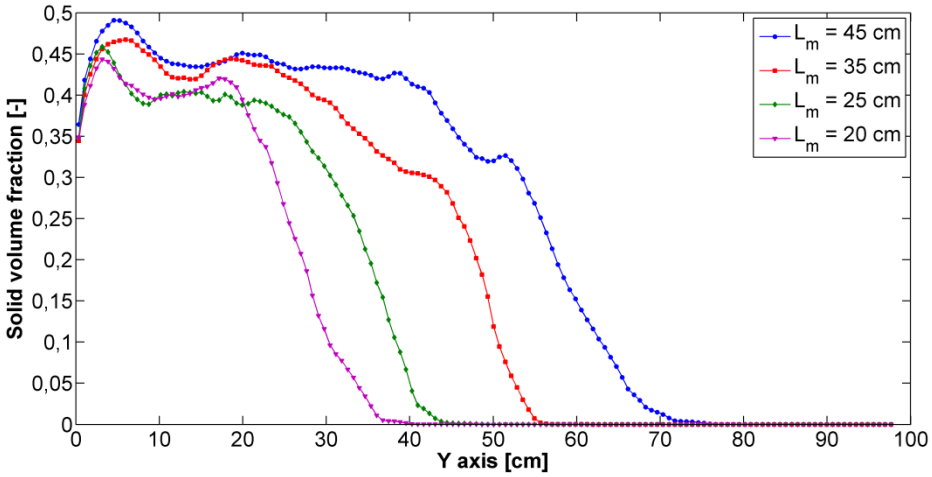

Fig. 3.40 Solid volume fraction along the bed under different solid inventories (low kinetics)

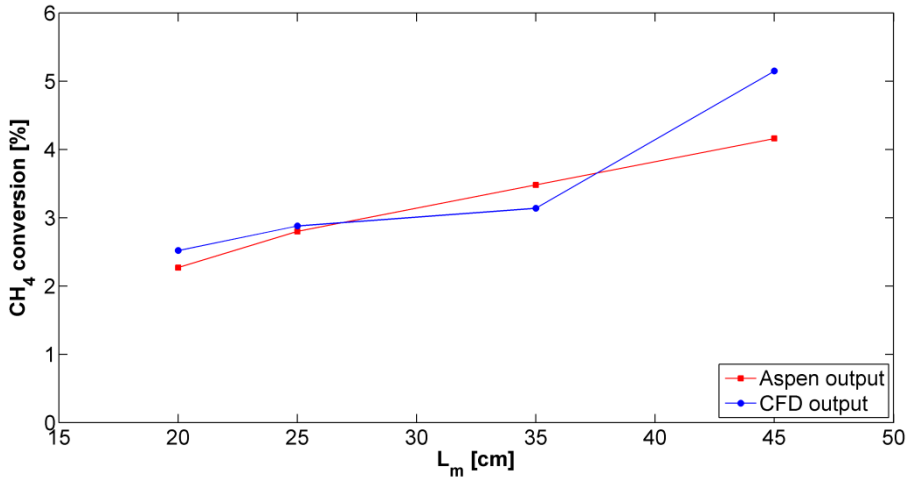

Fig. 3.41 Gas conversions vs. L_m at low kinetics

The same analysis on the methane mass fraction under different superficial gas velocities and solid loading is carried out for the case at high kinetics. Fig. 3.42 shows the change in methane mass fraction along the bed for different superficial gas velocities keeping L_m equal to 45 cm.

The effect of the kinetics in reducing steeply the methane mass fraction at the bottom of the bed is more evident for high kinetics. The effect of changing the superficial gas velocity on the gas conversion is much more appreciable from the Aspen model calculations. Also in this case, lower values of U_o determine higher gas conversion.

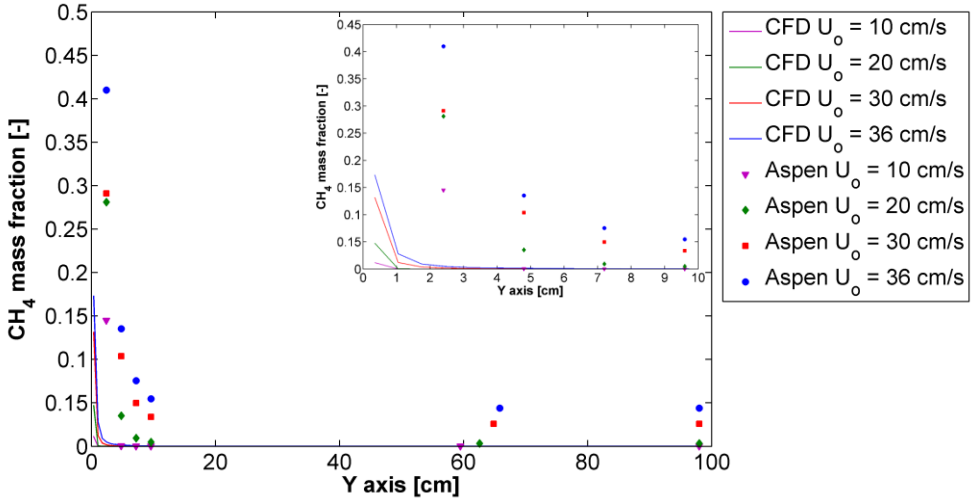

Fig. 3.42 Methane mass fraction along the bed under different superficial gas velocities (high kinetics)

From Fig. 3.43 it is noticeable how the difference in the gas conversion between the two models decreases at lower U_o. Indeed, at lower U_o values, less gas flow-rate goes to the bubble phase and the effect of the initial gas splitting in the Aspen model is reduced: decreasing U_o, the gas conversion values coming from the two models tend to converge. In Aspen Plus, the initial split of the superficial gas flow-rate between the two phases based on the amount of gas exceeding the minimum fluidisation conditions determines that part of the gas flow-rate is initially subtracted to react with the solid particles leading to lower values of gas conversion compared to the CFD model.

The difference in the outlet gas conversion between the two models ranges from 0.05% to 15%. Once again, the modelling of the gas distributor in a 3D CFD simulation is believed to reduce the difference in the detected gas conversion between the two models. Indeed the effect of the distributor in the CFD simulations would determine bubble formation and gas by-pass before that all the methane reacts, lowering, in this way, the gas conversion.

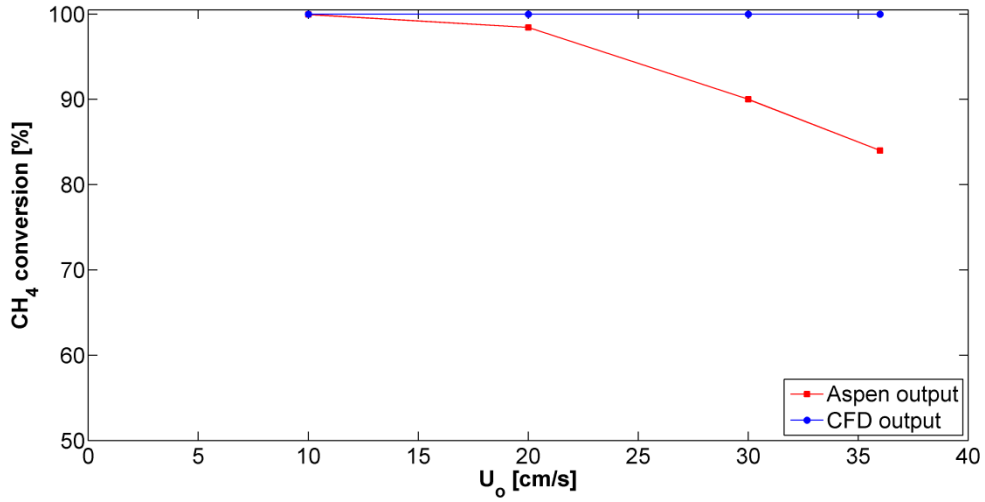

Fig. 3.43 Gas conversions vs. U_o at high kinetics

Finally, at high kinetics, a change in solid inventory in a range 20 – 45 cm of height of fixed bed does not influence appreciably the methane gas conversion in both models.

3.3.2 Additional comparisons CFD – Aspen Plus at low kinetics

Additional tests to compare the macro and the micro model were carried out. Since the CFD simulations running at high kinetics cover the effect of changing the operating

variables on the gas conversion (mainly due to the absence of a gas distributor), the following tests were carried out for the low kinetics case.

Fig. 3.44 shows the change in methane mass fraction along the bed for different superficial gas velocities keeping L_m equal to 45 cm at pressurised conditions (P = 10 atm). Since the area of the reactor is kept constant, the increase in the operating pressure determines an increase in the inlet methane mass flow-rate and thus in the fuel power (i.e. 100 MW for the reactor in Aspen and 100 kW for the reactor in MFIX at U_o = 36 cm/s). In Aspen, the circulating solid mass flow-rate increases up to 750 kg/s to keep the same ratio fuel/metal oxide as in the case at atmospheric conditions.

Fig. 3.45 shows the comparison in terms of gas conversion between the two models. The results, similar to those reported at atmospheric pressure (see Fig. 3.37), are characterised by an increase in the gas conversion while decreasing U_o and a good match between the two models (the difference in gas conversion ranges from 1 to 6%).

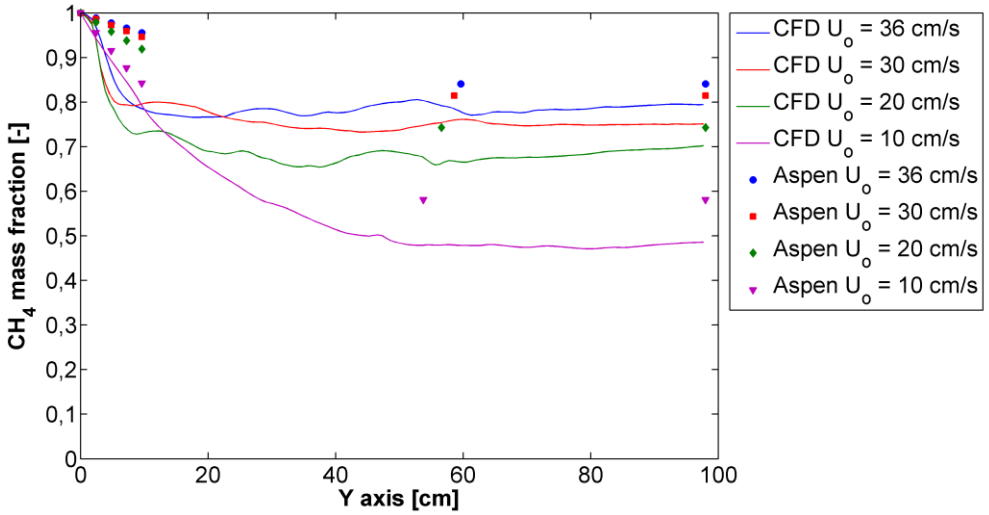

Fig. 3.44 Methane mass fraction along the bed under different superficial gas velocities at P = 10 atm

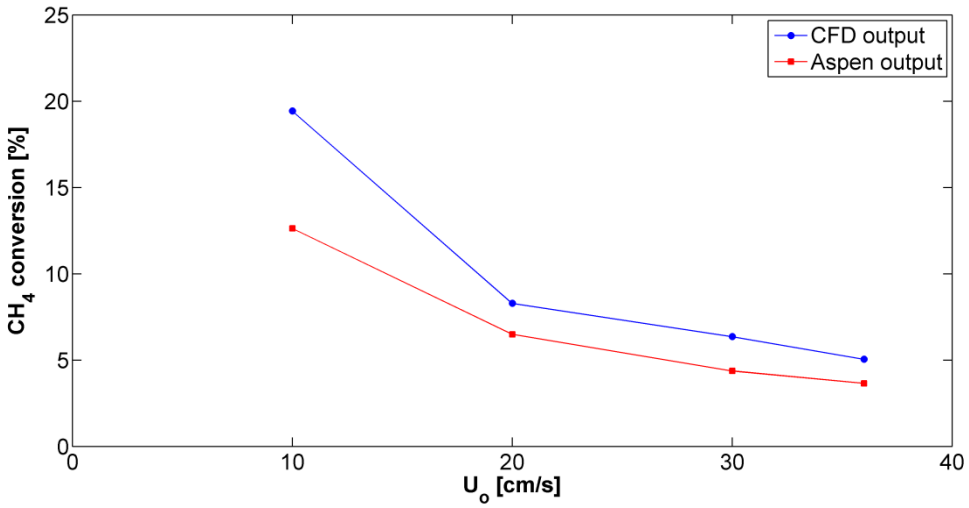

Fig. 3.45 Gas conversions vs. U_o at P = 10 atm

In all the previous simulations, the change in the inlet superficial gas velocity at constant area determines a change in the fuel power, P_{fuel}, which is equal to 10 MW in Aspen and 10 kW in MFIX at atmospheric conditions just for U_o = 36 cm/s. If we want to keep constant the fuel power, the area of the reactor A_{FR} must be change while varying U_o (Table 3.2).

Fig. 3.46 shows the change in methane mass fraction along the bed for different superficial gas velocities keeping L_m equal to 45 cm while also varying A_{FR}. In this case, L_m equal to 45 cm refers to different values of solid inventory W_{bedFR} due to the change in A_{FR}.

Table 3.2 Changing the reactor area to keep constant P_{fuel}

P_{fuel}: MW (Aspen) / kW (MFIX)	U_o: m/s	A_{FR}: m^2 (Aspen) / cm^2x10^{-1} (MFIX)	W_{bedFR} at L_m = 45 cm: kg (Aspen) / g (MFIX)
10	0.36	3.48	3000
10	0.3	4.18	3600
10	0.25	5.02	4300
10	0.2	6.27	5400

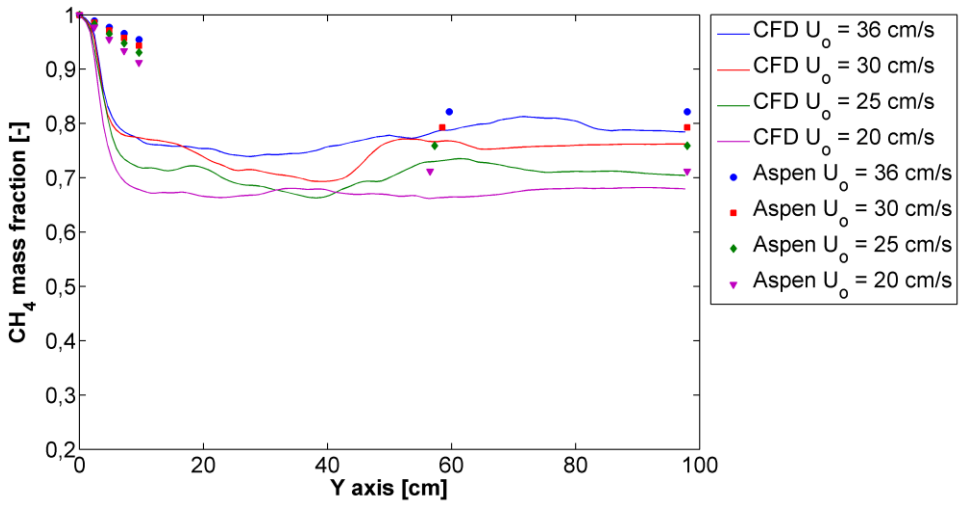

Fig. 3.46 Methane mass fraction along the bed under different superficial gas velocities at constant P_{fuel}

Fig. 3.47 shows the comparison in terms of gas conversion between the two models. A good match between the two models is detected under the aforementioned conditions.

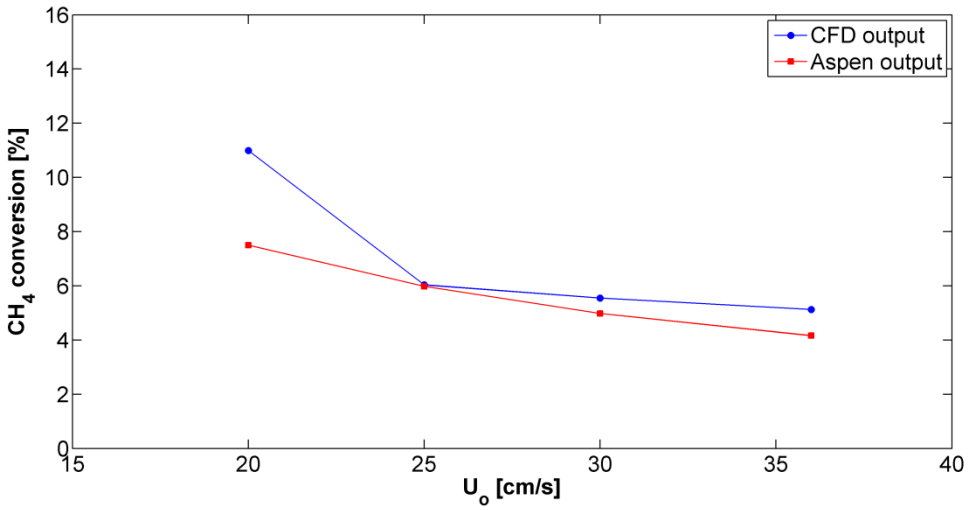

Fig. 3.47 Gas conversions vs. U_o at constant P_{fuel}

Keeping the fuel power constant at 10 MW in Aspen and 10 kW in MFIX, the system is pressurised at P = 2 atm. It is chosen U_o equal to 0.2 m/s changing the area of the reactor accordingly (Table 3.3). Fig. 3.48 shows the methane mass fraction along the bed for different solid inventories at constant U_o.

Table 3.3 Changing the reactor area to keep constant P_{fuel} at P = 2 atm

P_{fuel}: MW (Aspen) / kW (MFIX)	U_o: m/s	A_{FR}: m^2 (Aspen) / cm^2x10^{-1} (MFIX)	L_m cm	W_{bedFR}: kg (Aspen) / g (MFIX)
10	0.2	3.136	45	2700
10	0.2	3.136	60	3600
10	0.2	3.136	70	4200

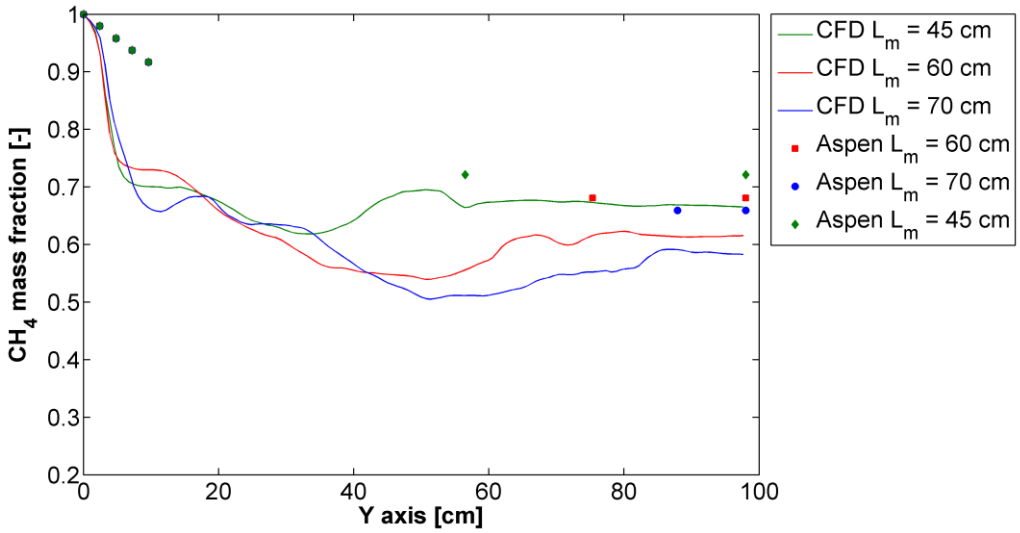

Fig. 3.48 CH_4 mass fraction along the bed under different L_m at constant P_{fuel} and 2 atm

Under pressurised conditions and constant fuel power, the increase in the ratio height/diameter of the reactor leads to a decrease in methane mass fraction also far from the bottom of the bed (Fig. 3.48). Indeed the fluid motion tends to a plug flow and an increase in gas conversion occurs along the bed height far from the bottom. This phenomenon is mainly due to a double effect: low kinetics under plug flow motion and mass transfer from the bubble phase to the emulsion phase.

Fig. 3.49 shows the comparison in terms of gas conversion between the two models. At higher L_m (meaning high ratio height/diameter of the reactor), the two models seem to diverge. Indeed, since the system tends to plug flow and the kinetics is slow, just one stage of reaction to model the bed in Aspen Plus far from the bottom might not be enough.

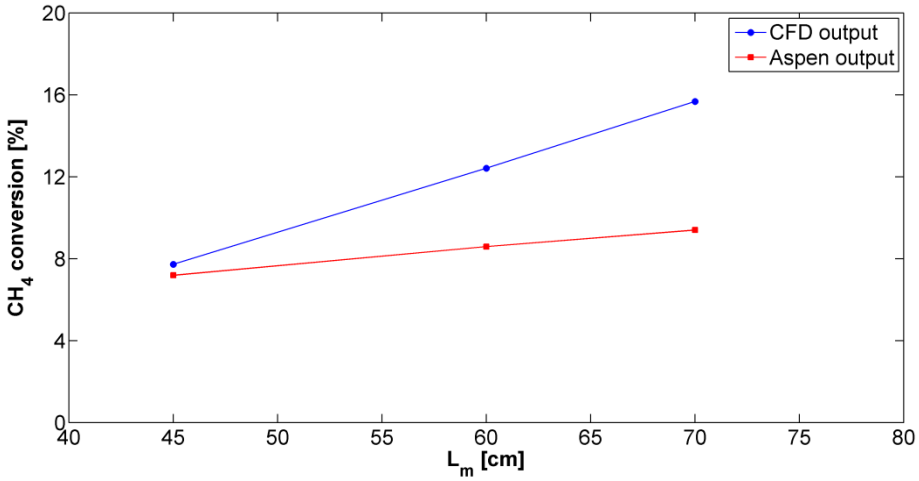

Fig. 3.49 Gas conversions vs. L_m at constant P_{fuel} and 2 atm (low kinetics)

Being aware of the latter, 5 stages to model the fuel reactor in Aspen Plus, in the fashion explained in Section 3.4, are kept to carry on our study (see Chapter 4), since in CLC systems the kinetics are fast and thus the most of the reaction occurs at the bottom of the bed.

All the tests performed in Sections 3.4.1 - 3.4.2 show that at different kinetics (low and high), solid inventories, inlet superficial gas velocities and pressures the comparison between the macro model implemented in Aspen and the micro model implemented in MFIX are in good agreement.
The CFD simulations exhibit that the most of the reaction occurs at the bottom of the bed and thus a new concept of stages in the Aspen model together with the implementation of a variable bubble diameter is introduced to capture this feature.

Overall, both models follow the same trends while changing the operating conditions; furthermore, the numerical differences in the main outcome of interest, which is the methane conversion, are considered acceptable for engineering purposes. Indeed, for low kinetics the difference in gas conversion between the two models under various operating conditions is always within 6%; in the high kinetics case, which represents the actual kinetics to implement in the CLC system, the maximum difference in gas conversion is 15% (Fig. 3.43). In the latter case, we strongly believe that the modelling of a gas distributor in MFIX environment would lead to a reduction in the gas conversion detected in the CFD simulations, lowering the methane conversion difference between the two models.

The degree of approximation in designing the unit operations for cost analysis purposes is in a range 0-30% (Branan, 2002). Thus, bearing in mind that the main objective of the present work is to calculate the total solid inventory of the CLC unit, to estimate its impact on the cost of electricity, we evaluate as reasonable the results achieved. Therefore, in the next chapter we carry on with the completion of the macro model in Aspen Plus and its integration in different CLC power plant configurations.

Chapter 4

Integration of the CLC unit in NGCC power plants

In Chapter 2, a preliminary macro model implemented in Aspen Plus was proposed to model the fuel reactor working in the bubbling bed regime. In Chapter 3, such a model was improved through comparisons with a CFD model under various operating conditions. In both chapters, only the bubbling phase characterising the fuel reactor was taken into account. Indeed, another region defining the bubbling bed is also present; the latter is called the "freeboard" or lean phase and it is characterised by an exponential decrease in solid distribution, which may affect greatly the gas conversion. Kunii and Levenspiel (1990) reported that the gas conversion might rise by up to 30% under specific conditions in the freeboard region.

The effect of the freeboard region was experimentally demonstrated (De Lasa and Grace, 1979; Furusaki et al., 1976; Kunii and Levenspiel, 1990) and therefore it has to be modelled.

As explained in Chapter 3, CFD simulations based on the Eulerian – Eulerian approach fail in modelling appropriately the freeboard due to the very low solid particles concentrations (Wang et al., 2011) and thus no attempt at comparisons between the macro and the micro model was undertaken in relation to this lean region.

Overall, in the present chapter, the fuel reactor implementation in Aspen Plus was completed by adding a model for the freeboard to the multi stage model; moreover, since the CLC unit is composed of fuel and air reactor with solid flow-rate circulating between them, the modelling of the air reactor (riser) at fast fluidisation conditions is also accomplished.

Finally, the CLC unit was embedded into three different power plant configurations working with both atmospheric and pressurised conditions; for each configuration, the analysis of the optimum operating conditions to minimise the total solid inventory of the CLC unit is carried out, specifically optimising the circulating solid flow-rate, F_s, and the average solid conversion at the riser exit, $X_{MO\ exit}$. For each configuration, mass and energy balances are solved simultaneously at the conditions specified by each plant

arrangement and a thermal efficiency estimation of the whole power plants was carried out. The outcomes coming from this analysis were used in Chapter 5 to carry out an economic analysis of a CLC power plant.

4.1 Fuel reactor: freeboard model

As explained by Kunii and Levenspiel (1990), the bubbles, breaking at the surface of the bubbling dense region, throw solids into the freeboard through three different mechanisms: spraying solids from the bubble roofs into the freeboard, throwing clumps of solids from their wakes, ejecting wake solids after coalescence with other bubbles and later breakage. As reported by Kunii and Levenspiel (1990), Adanez et al. (2003) and Abad et al. (2010), the freeboard region influences largely the final gas conversion. This zone of the bed, which starts at the end of the bubble-emulsion region (Fig. 4.1), is characterised by an exponential decrease in the solid volume fraction (Kunii and Levenspiel, 1990) according to Eq. 4.1:

$$\frac{\varepsilon_s{}^* - \varepsilon_s(z)}{\varepsilon_s{}^* - \varepsilon_{sd}} = e^{-az} \tag{4.1}$$

where $\varepsilon_s{}^*$ is the solid volume fraction at the exit of the fluidised bed that can be assumed equal to zero, ε_{sd} is the solid volume fraction of the bubble-emulsion region at the interface bubbling region – freeboard, *a* is the decay index, which is a function of U_o, and z is the height of the freeboard. The decay factor *a* was calculated from the formula reported by Johnsson and Leckner (1995):

$$a = 4\frac{U_t}{U_o} \tag{4.2}$$

In the freeboard, gas and solid are mixed and the gas – solid contact efficiency ζ increases with the height of the bed. ζ was calculated applying the equation proposed by Furusaki et al. (1976):

$$\zeta = 1 - 0.75\left(\frac{\varepsilon_s}{\varepsilon_{sd}}\right)^{0.4} \tag{4.3}$$

The rate of the gas-solid reaction is affected by the solid volume fraction (Eq. 2.9) and the contact efficiency, meaning that it changes along the bed height. To take into

account this change, the freeboard was split into three parts modelled with three CSTRs in series characterised by different kinetics (Fig. 4.1). In each CSTR, different mean solid volume fractions were present, assumed to be calculated as follows:

$$\varepsilon_{si} = \varepsilon_s{}^* - \frac{(\varepsilon_{sd} - \varepsilon_s{}^*)}{a(z_i - z_{i-1})}\left(e^{-az_i} - e^{-az_{i-1}}\right) \tag{4.4}$$

with i =2,3,4. z_1 is the height of the bubbling dense phase which, summed with all the other zones, up to z_4, gives the height of the whole fuel reactor. The previous system of three equations (Eq. 4.4) was solved with the following constraint:

$$z_2 - z_1 = z_3 - z_2 = z_4 - z_3 \tag{4.5}$$

and the constraint of the solid mass balance:

$$L_m(1 - \varepsilon_m) = z_1\varepsilon_{sd} + \Delta z \sum_{i=2}^{4} \varepsilon_{si} \tag{4.6}$$

where $L_m(1 - \varepsilon_m)$ is the height of the packed solid loading equal to $W_{bedFR}/(\rho_s\, A_{FR})$. Fig. 4.1 is a general sketch of the complete bubbling bed model run in Aspen Plus (not all the calculator blocks are shown).

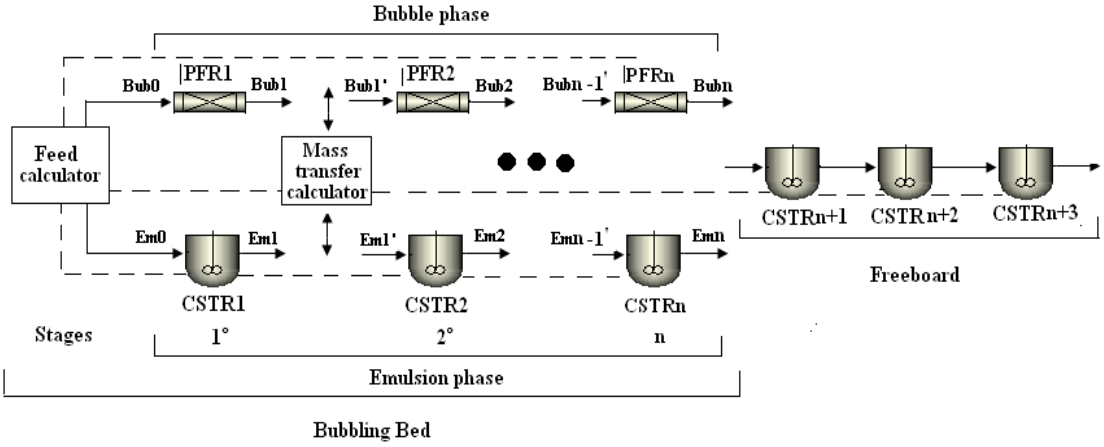

Fig. 4.1 Full fuel reactor model in Aspen Plus

The streams coming from the bubble phase and the emulsion phase, at the exit of the bubbling region, were combined using a mixer block (not shown in Fig. 4.1). A calculator block written in Excel was used to define the operating conditions of the freeboard region. Specifically, in this Excel spreadsheet, the imported value from Aspen

of the gas volumetric flow-rate at the exit of the bubbling region was used to calculate U_o and thus the decay constant a (Eq. 4.2). Then, the final value of the bubble volumetric fraction, σ, was calculated to solve Eq. 2.24 and find out ε_{sd} to apply in Eq. 4.4.

By solving Eqs. 4.4 - 4.6, three different mean solid volume fractions were calculated as well as the heights of the three CSTRs. The volumes of the CSTRs were derived (i.e. the volumes occupied by the gas phase) and then, exported into Aspen to solve the mass balances in the freeboard region.

The three different mean solid volume fractions influence the kinetic constant, which changes for each sub-reactor. Thus, three additional calculator blocks were implemented to take into account the latter as well as the change in the gas – solid contact efficiency. A FORTRAN code was written into the calculator blocks (Kin Ci) to modify in each CSTR the kinetic rate. Specifically, each Kin Ci block contains a k value in the form of Eq. 2.28. The latter is a tear variable since its value depends on the solid outlet stream (see Chapter 2) and for this reason an internal loop in each sub-reactor needs to be run to solve the mass balances and get the convergence of the system, as in the case of the sub-reactors in the bubbling region. The Broyden convergence solver (Gupta, 1995) was used for solving the mass balances in each CSTR composing the freeboard.

4.2 Riser model

The reduced metal oxide particles exiting the fuel reactor, against gravity, need to be regenerated. Thus, they enter the air reactor where the oxidation reaction occurs according to the Eq. 4.7:

$$O_2 + 2Ni \longrightarrow 2NiO \qquad (4.7)$$

The outlet solid flow-rate in the riser (air reactor) must match the inlet rate circulating in the bubbling bed fuel reactor. Usually a system of cyclones between the two beds allows for the separation between gas and solid products from the air reactor.

The kinetic parameters for the oxidation of the metal oxide are taken from the work of Abad et al. (2007) as reported in Table 2.1 (see Chapter 2). As in the case of the

reduction reaction, the Shrinking Core Model (SCM) for spherical grain size geometry is applied to derive the kinetic parameters. The kinetic constant k for the oxidation reaction follows the Arrhenius law and the kinetic expression to employ in Aspen Plus is in the same form of the reduction rate (see Eqs. 2.9 and 2.10). Additionally, a negative effect of the total pressure on the oxidation reaction rate was found (Garcia-Labiano et al., 2006); thus an apparent pre-exponential factor $k_{o,p}$ was determined by Abad et al. (2007) as follows:

$$k_{o,p} = \frac{k_o}{P^q} \tag{4.8}$$

where k_o is the pre-exponential factor, P is the total pressure and q is the pressure effect exponent (see Table 2.1). In Section 2.1, some considerations were made about other potential mechanisms of reaction for the oxidation of nickel. From the literature (Ruy et al., 2001), it appears that the oxidation reaction is likely governed by internal mass transfer diffusion; the latter explains why the kinetic rate is negatively affected by an increase in the total pressure. It is likely that Abad et al. (2007) introduced an apparent pre-exponential factor, pressure-dependent, to keep the same kinetic model applied to the reduction reaction. For the modelling of the fluidised bed reactors, the investigation of the actual kinetic mechanism was not of essential interest and thus, the kinetic parameters reported by Abad et al. (2007) were still applied.

The air reactor works in the fast fluidisation regime to convey the solid particles to the fuel reactor. Fast fluidisation is assumed when the superficial velocity of the inlet gas, U_{air}, is greater than the terminal velocity of an isolated particle, U_t (Kunii and Levenspiel, 1990). In fast fluidisation, perfect mixing of the gas and the solid is assumed. The solid volume fraction is assumed to remain constant in the bed radial direction, while two zones along the bed height are identified: the dense and the lean phases; the latter is divided into lower acceleration region, upper acceleration region and completely fluidised region (Sotudeh-Gharebaagh et al., 1998; Liu et al., 2012; Kunii and Levenspiel, 1990) (Fig. 4.2). The relative height of those regions varies with the inlet superficial gas velocity. The solid volume fraction of the dense phase is assumed constant whereas the solid volume fraction of the lean phase decreases along the bed height.

An exponential change in the solids loading is assumed to describe the variation of solid volume fraction, ε_s, along the lean phase in the same form of Eq. 4.1. In this case, ε_s^* is the solid volume fraction at the exit of riser, ε_{sd} is the solid volume fraction of the dense phase, a is the decay index and z is the height of the riser.

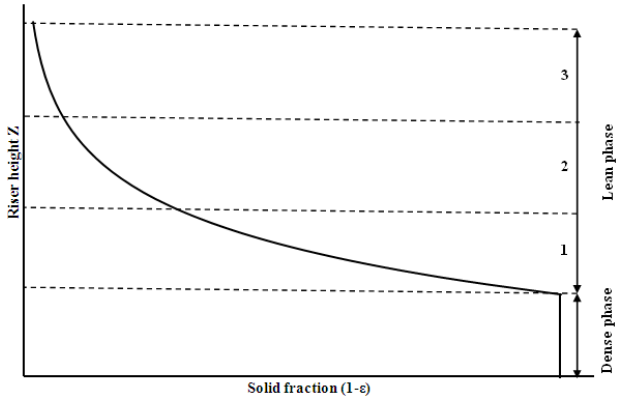

Fig. 4.2 Trend of the solid volume fraction ($1-\varepsilon_g$) in the riser

a and ε_{sd} are both functions of the inlet air superficial gas velocity, U_{air}. In particular, ε_{sd} ranges from 0.22 at very low U_{air} to 0.16 at high U_{air} (Kunii and Levenspiel, 1990). With regard to the decay factor a, the product aU_{air} is a constant ranging from 4 to 12 s^{-1} for particles with mean diameter higher than 88 μm meaning that higher gas velocities lead to lower decay factor (Kunii and Levenspiel, 1990). In our simulations we assumed a value of 9 s^{-1}.

The modelling of the riser can be developed under similar considerations as those applied for the freeboard model of the fuel reactor. Thus, the different amount of solid in the different regions of the riser affects the reaction. Since the kinetic rate changes depending on the solid volume fraction (Eq. 2.10), the riser is split into a number of CSTRs in series (Sotudeh-Gharebaagh et al., 1998; Liu et al., 2012). In the case under exam, the system is split into four CSTRs in series following the division of the zone characterising the riser: one CSTR is assumed to represent the dense phase and three CSTRs are assumed to mimic the lean phase characterised by three different mean volume fractions calculated according to the Eqs. 4.4 - 4.6. In this case, $L_m(1-\varepsilon_m)$ is the height of the packed solid loading equal to $W_{bedAR}/(\rho_s A_{AR})$, where W_{bedAR} and A_{AR} refer to the solid inventory and the superficial area in the riser, respectively.

Fig. 4.3 is a general sketch of the riser model run in Aspen Plus.

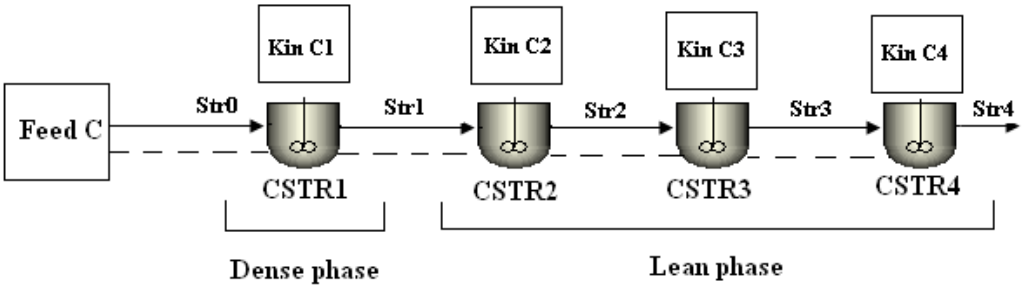

Fig. 4.3 Riser model in Aspen Plus

Most of the reaction occurs in the dense zone because of the large quantity of reactant solid present. A calculator block (Feed C) written in Excel is used to define the operating conditions of the feed and the volume of each sub-reactor. The calculator block, by solving the Eqs 4.4 - 4.6, determines the heights of the four CSTRs, the different mean solid volume fractions and thus the volume of each CSTR for an assumed value of the solid inventory and U_{air}.

The air volumetric flow-rate is linked to the power of the plant through the air to fuel ratio (see Table 4.1). At fixed air volumetric flow-rate, the chosen value for U_{air} must guarantee the fast fluidisation conditions, meaning $U_{air} > U_t$.

The calculated volumes of the CSTRs (i.e. the volumes occupied by the gas phase) are exported into Aspen to solve the mass balances (Table 4.2). Additionally, a FORTRAN code is written into four calculator blocks (Kin Ci) to modify in each CSTR the kinetic rate, following the same concept explained in the case of the freeboard model (see Section 4.1). Broyden convergence solver is used for solving the mass balances in each CSTR.

Table 4.1 Initial conditions implemented in the riser model

$F_{O_2} = \frac{MW_{O_2}}{MW_{CH4}} F_{fuel} st$	stoichiometric inlet mass oxygen flow-rate
$F_{air} = \frac{F_{O_2}}{0.233}$	stoichiometric inlet mass air flow-rate
$Q_{air} = \frac{F_{air}}{\rho_{air}}$	inlet volumetric air flow-rate
$U_{air} = \frac{Q_{air}}{A_{AR}}$	inlet superficial air velocity

Table 4.2 List of mass balances for each component in each CSTR of the riser model

$M_{O2(i-1)} - M_{O2i} - r_{O2i} V_{CSTRi} = 0$
$M_{Ni(i-1)} - M_{Nii} - 2\, r_{O2i} V_{CSTRi} = 0$
$M_{NiO(i-1)} - M_{NiOi} + 2\, r_{O2i}\, V_{CSTRi} = 0$

4.3 Understanding the CLC system

The models of the fuel and air reactor are ready to be integrated in different CLC power plant configurations and a sensitivity analysis of the main variables that might affect the process needs to be carried out with particular attention on the total solid inventory inside the system. Indeed, one of the issues for the feasibility of the CLC process for electricity generation concerns the cost of the total solid inventory in the fluidised beds that must be minimised.

Many variables play an important role in the CLC process and understanding how they affect the operation is essential to optimise it. The main variables and the relationships among them that must be analysed are:

- Solid circulating mass flow-rate between the fluidised beds, F_s;
- Total solid inventory into the beds, W_{bedTOT};
- Difference in solid conversion between riser and fuel reactor, ΔX_{solid};
- Solid average conversion rate in the riser and fuel reactor, dX/dt;
- Metal oxide conversion at the riser outlet, X_{MO_exit}.

All those variables affect largely the average gas conversion in the fuel reactor and an optimal combination of these variables must be found to achieve full gas conversion with minimal metal oxide cost. The experiments conducted by Mattisson et al. (2001) on α-Fe_2O_3 metal oxide at 950 °C, exposed to reduction and oxidation cycles with methane and oxygen respectively, show the following main features:

- The average solid conversion rate *dX/dt* decreases as the variation in the average solid conversion ΔX_{solid} increases;
- The efficiency of the metal oxide in converting completely the gas reactant decreases as the gas-solid reaction progresses;
- At fixed exposure time of the metal oxide to the reducing agent, an increase of the sample mass determines an increase of the average yield of methane to CO_2, although the average solid conversion rate decreases;
- At fixed weight of solid, the decrease of the exposure time of the metal oxide to the gas reactant determines a lower average solid conversion ΔX_{solid}, which is inversely proportional to the average solid conversion rate *dX/dt*.

The relationships between the exposure time of the solid sample to methane, the average solid conversion, ΔX_{solid}, the average solid conversion rate, *dX/dt*, and the weight of the metal oxide, lead to the conclusion that a larger amount of solid material and lower exposure time of the solid sample to the reducing agent, (which means lower average solid conversion ΔX_{solid}) produce higher average gas yield. The experiments conducted in fixed beds (Iliuta et al., 2010; Mattisson et al., 2001; Ryu et al., 2003) as well as TGA experiments (Ishida et al., 2002; Mattisson et al., 2003; Ryu et al., 2001) are essential for the design of a CLC system with two interconnected fluidised beds, as pointed out by Lyngfelt et al. (2001), since they provide good indications on the optimal operating conditions involved in the red-ox reactions. Indeed, as reported by Mattisson et al. (2001):

- Slow reduction and oxidation kinetic rates mean an increase in the total solid inventory to achieve full gas conversion in a CLC unit;
- The exposure time of the solid to the gas reactant in a fixed bed or TGA experiments corresponds to the solid residence time W_{bed}/F_s in a CLC setup; thus, a high solid mass flow-rate, meaning low exposure time, is needed to keep high the solid average conversion rate *dX/dt* and consequently to work with less

amount of solid material in the beds at the desired gas conversion in the fuel reactor.

All the relationships among the variables aforementioned can be summarised in the following equations:

$$bF_{fuel}\Delta X_{fuel} = F_s\Delta X_{solid} \tag{4.9}$$

$$F_s\Delta X_{solid} = W_{bedFR}\frac{dXred}{dt} \tag{4.10}$$

Eq. 4.9 states that the gas reaction rate is equal to the solid reaction rate according to the stoichiometry of the reaction. b is the ratio between the gas and solid stoichiometric coefficients and molecular weights; F_{fuel} and F_s represent the mass flow-rate in the fuel reactor for the gas and the solid, respectively; ΔX_{fuel} and ΔX_{solid} represent the variation in conversion in the fuel reactor for gas and solid, respectively.

Eq. 4.10 represents the mass balance for the oxygen carrier in the fuel reactor. W_{bedFR} is the solid inventory in the fuel reactor and dX_{red}/dt is the solid reduction rate. Since the target is the full gas conversion in the fuel reactor, ΔX_{fuel} is assumed usually to be 1. Furthermore, for a fixed fuel power, F_{fuel} is a constant and thus all the identities above must be constants. From Eq. 4.10:

- higher reduction rate requires lower inventory of solid material in the bed to achieve full gas conversion;
- higher solid circulation rates give lower average solid conversion and thus higher reduction rate and requiring lower solid inventory for full gas conversion.

From Eq. 4.9, if $\Delta X_{solid} = 1$, F_s is equal to the stoichiometric mass flow-rate for full fuel conversion ($\Delta X_{fuel} = 1$). This condition is not feasible in an interconnected fluidised bed CLC system since the reduction rate is also a function of the solid conversion (see Eq. 2.10) leading to low values of dX_{red}/dt and thus to extremely high values of W_{bedFR}.

As explained by Abad et al. (2007), the actual solid flow-rate that can be circulated between the two reactors presents two limits:

- The upper limit depends on the capability of the riser to convey solid particles to the fuel reactor; from experimental data available in the literature, values of mass solid flow-rate per area of the riser, G_s, are in the range of 20-100 kg/(m^{2}s);
- The lower limit depends on the heat balance between the two reactors if the reduction reaction is endothermic; in the case under study the solid circulating flow-rate presents a minimum value required to convey the heat (generated by the exothermic oxidation reaction in the riser) and thus maintain a high reduction rate in the fuel reactor.

4.4 CLC power plant configurations

The reactor models, previously discussed, were embedded in a full NGCC power plant with CO_2 capture section, replacing the traditional combustion chamber. Mass and energy balances were solved simultaneously under different operating conditions depending on the plant arrangements. In all the simulations some parameters are kept constant as summarised in Table 4.3.

Table 4.3 Parameters employed in each CLC power plant configurations

P_{fuel}	10	MW	Min ΔT across heat exchangers	20	ºC
Fuel reactor inlet gas velocity U_o	$\approx 10U_{mf}$	m/s	Gas turbines isentropic efficiency	0.9	
CH_4 conversion target	99.9	%	Steam turbines isentropic efficiency	0.92	
Inlet plant air pressure	1	atm	Compressors isentropic efficiency	0.9	
Inlet plant air temperature	25	ºC	Pumps efficiency	0.8	
Inlet plant CH_4 temperature	25	ºC	Vapour fraction steam turbines exit	0.91	
Inlet plant cooling H_2O temperature	15	ºC	Overall mechanical efficiency	0.98	
Outlet plant cooling H_2O temperature	50	ºC	CO_2 final compression	110	atm
Air reactor temperature exit	1200	ºC			

4.4.1 Power plant at atmospheric conditions

The NGCC power plant configuration used to demonstrate the effectiveness of CLC model integration is shown in Fig. 4.4.

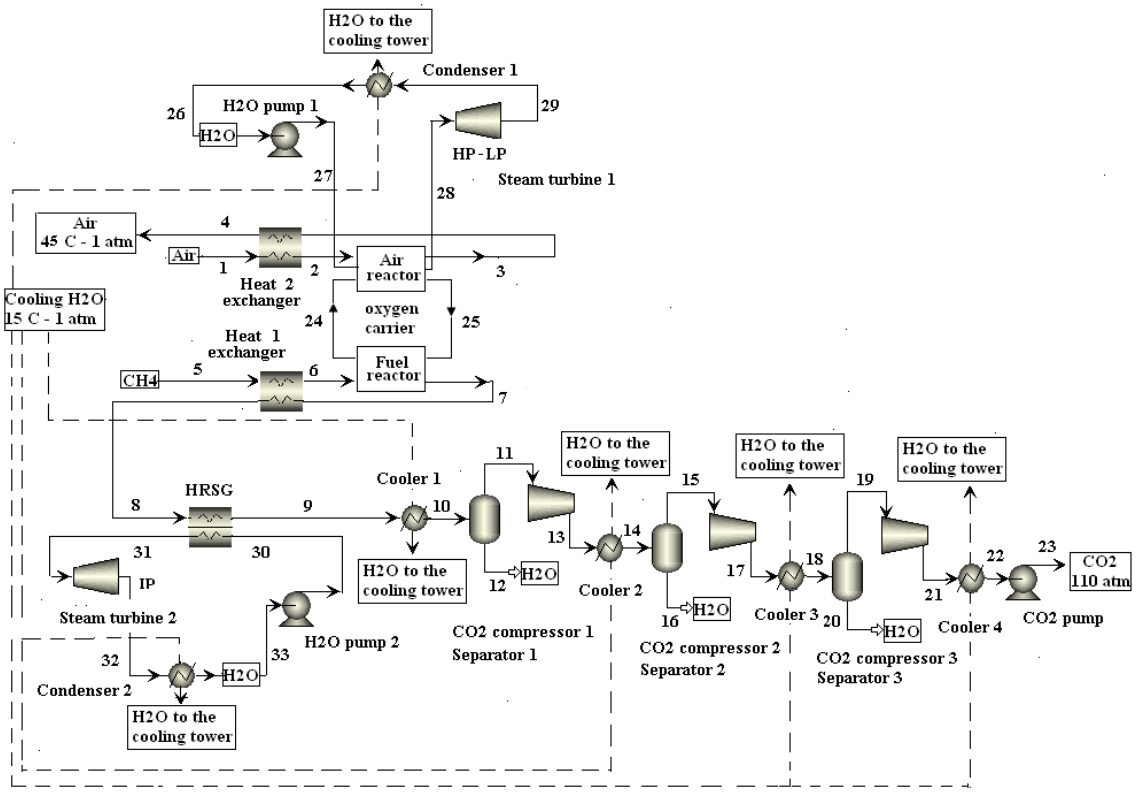

Fig. 4.4 Power plant scheme at atmospheric pressure conditions

At atmospheric pressure, methane enters in the system at 25°C. The feed is pre-heated exchanging heat with the products (CO_2 and H_2O) of the reduction reaction before entering the fuel reactor. The fuel reactor is adiabatic and the endothermic reduction reaction is sustained with the heat conveyed by the solid particles. Air enters the system at 25°C and after being pre-heated with the depleted air from the oxidation reaction, reacts in the air reactor with the solid particles to regenerate the metal oxide. The oxidation reaction is exothermic and some heat has to be removed from the riser to fulfil the heat balance of the whole system (air reactor + fuel reactor). Water at high pressure is used to remove the excess of heat produced in the air reactor. Consequently, the produced steam feeds two steam turbines working at 160 atm and 30 atm with two superheating at 560°C. The final steam turbine discharge pressure is 0.04 atm. In the same way, the heat associated with the products of the reduction reaction is recovered in a Hirn cycle working at 60 atm with the inlet steam turbine temperature depending on

the solid flow-rate circulating in the CLC unit. The final stages of the plant are three stages of intercooled compression and separation (at compression ratio equal to 4) and final pumping allow for capturing CO_2 at 110 atm. In this way, it is captured the power needed for typical CO_2 export. More information about each stream of the power plant under investigation are given in Appendix B.

Given the above conditions, the minimum total solid inventory required in the CLC unit to get 99.9% of methane conversion is estimated. Fig. 4.5 shows how the methane conversion changes with varying the solid inventory at different solid circulating mass flow-rates, F_s. In this case, it is assumed that the oxygen carrier flows into the fuel reactor in its fully oxidised state (X_{MO_exit} = 1).

As shown in Fig. 4.5, at fixed F_s the gas conversion increases as the solid inventory, W_{bedfFR}, increases. At fixed W_{bedfFR}, the gas conversion increases as F_s increases. The latter is due to a decrease in the average solid conversion in the fuel reactor and an increase in its operating temperature since at higher F_s more heat is conveyed from the riser. Both phenomena lead to faster kinetics (see Eqs. 2.9 and 2.10). Since mass and energy balances are solved simultaneously, each value in Fig. 4.5 refers to a different fuel reactor outlet temperature and methane temperature condition at the reactor inlet.

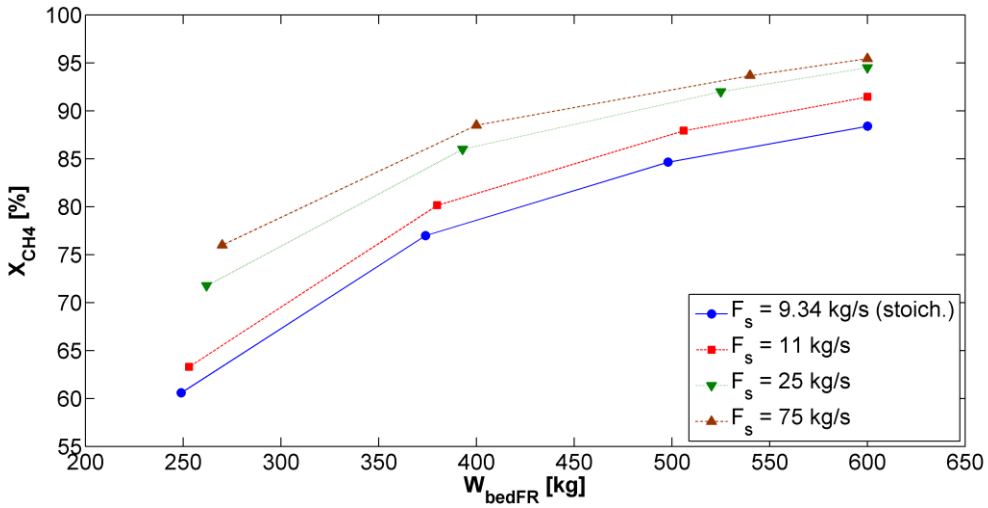

Fig. 4.5 CH_4 conversion vs. W_{bedFR} at X_{MO_exit} = 1 for different values of F_s

Fig. 4.6 exhibits the change in gas and average solid conversion while varying F_s at fixed W_{bedFR} equal to 600 kg. The increase in F_s leads to a decrease in the average solid

conversion as well as an increase in gas conversion due to a faster kinetic rate; for F_s higher than 3 times the stoichiometric quantity, this effect is reduced.

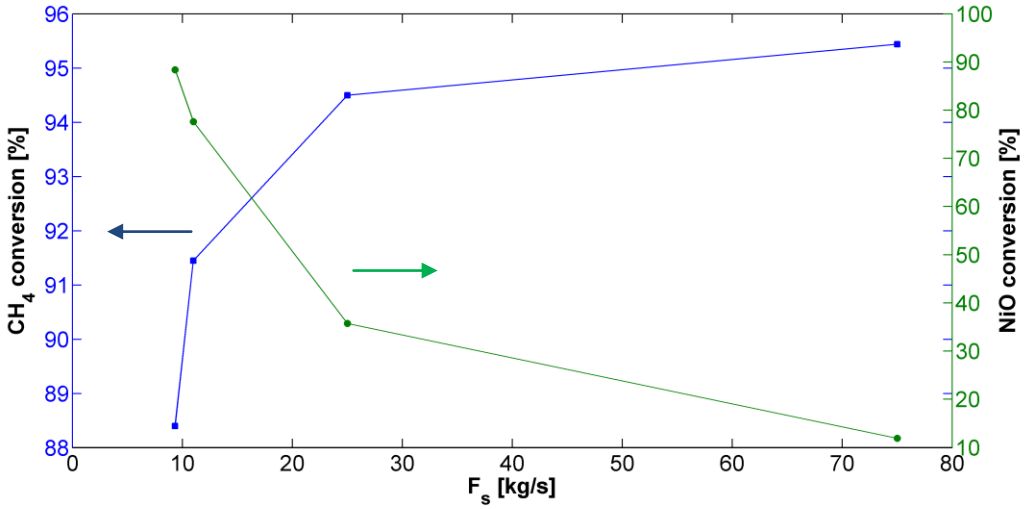

Fig. 4.6 CH_4 and NiO conversion vs. F_s at W_{bedFR} = 600 kg and X_{MO_exit} = 1

Fig. 4.7 shows the solid inventory variation in the fuel reactor when F_s is changed to achieve 99.9% methane conversion at X_{MO_exit} = 1. At fixed gas conversion, an increase in F_s determines a decrease in the average solid conversion in the fuel reactor. Furthermore, at fixed outlet riser temperature, equal to 1200°C, a higher F_s leads to a decrease in the temperature drop between the two reactors (Fig. 4.7) since more heat is transferred from the air reactor. Both effects increase the reduction rate leading to a lowering at the solid inventory required.

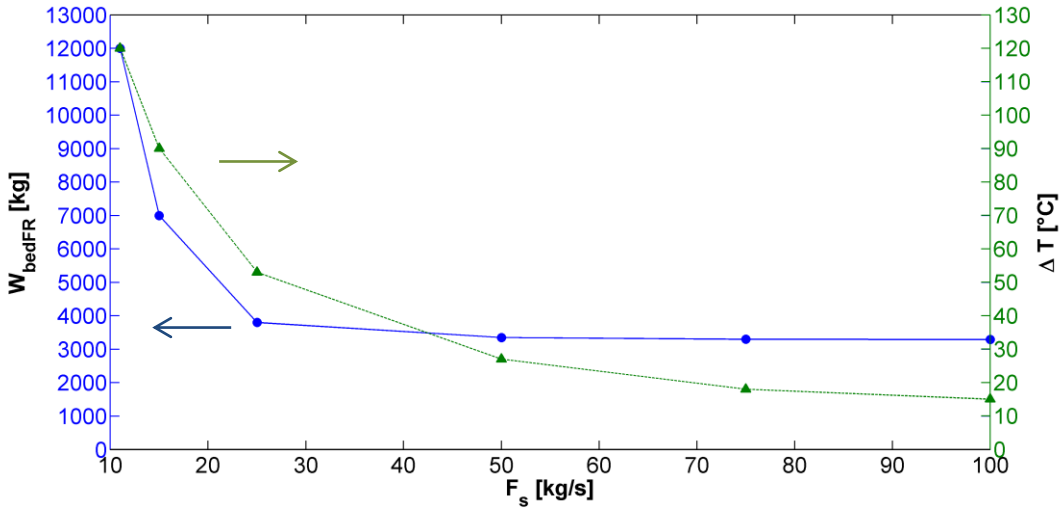

Fig. 4.7 W_{bedFR}/temperature drop vs. F_s at X_{MO_exit} = 1 and X_{CH4} = 99.9%

Since the methane temperature at the reactor inlet changes with varying F_s (to keep a ΔT equal to 20°C at the heat exchanger), A_{FR} changes (Fig. 4.8) to keep, at fixed fuel power, the same inlet hydrodynamic conditions in the reactor (inlet U_o is constant).

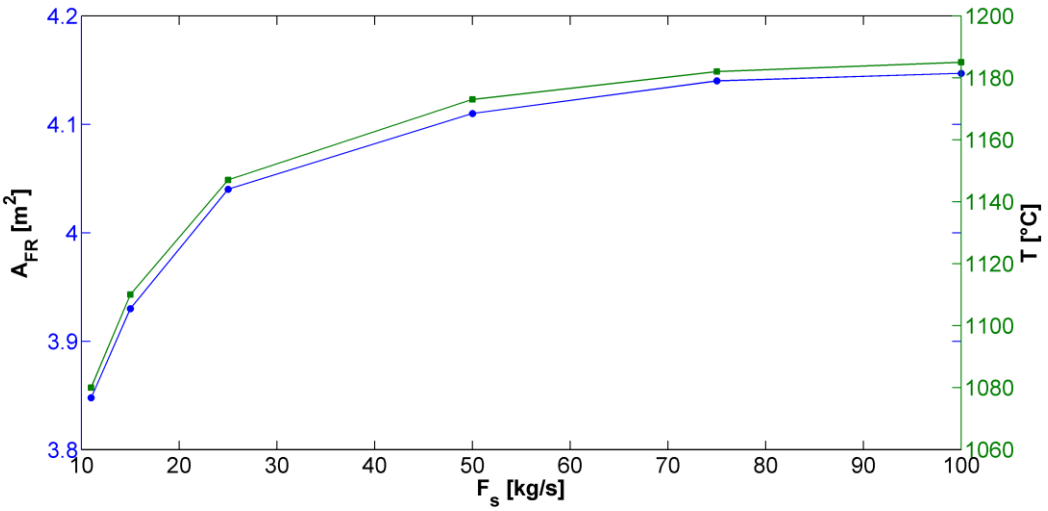

Fig. 4.8 A_{FR}/temperature vs. F_s at X_{MO_exit} = 1 and X_{CH4} = 99.9%

The solid mass flow-rate applied to minimise the solid inventory has to be as high as possible for the reasons explained in Section 4.3. The maximum mass flow-rate value applicable depends on the capacity of the riser to convey the solid particles. Lyngfelt et al. (2001) suggest a value for G_s to approximately 50 kg/(m^{2}s). In this analysis, G_s is kept in a range of 40 to 60 kg/(m^{2}s). The riser design has to meet the following requirements:

- superficial gas velocity must be higher than U_t to guarantee the fast fluidization regime and convey the solid metal oxide to the fuel reactor;
- employed superficial area in conjunction with F_s has to lead to G_s values in the range 40 – 60 kg/(m^{2}s);
- riser height must be higher than the fuel reactor one to allow the cyclones to be allocated;
- metal oxide content at the riser exit has to match the metal oxide composition at the fuel reactor inlet.

Assuming 10% of air excess at the riser inlet, we can apply a value for F_s as high as 75 kg/s having a riser superficial gas velocity and a superficial area about 8.33 m/s and 1.9 m^2, respectively.

All the previous simulations were carried out for a fully oxidised oxygen carrier flowing in the fuel reactor (X_{MO_exit} = 1). Since X_{MO_exit} is an important variable in the optimisation of the system, additional simulations were carried out changing the amount of NiO in the inlet solid mass flow-rate to the fuel reactor. Fig. 4.9 shows the effect of changing X_{MO_exit} on the solid inventory for each reactor as well as for the whole system at F_s equal to 75 kg/s.

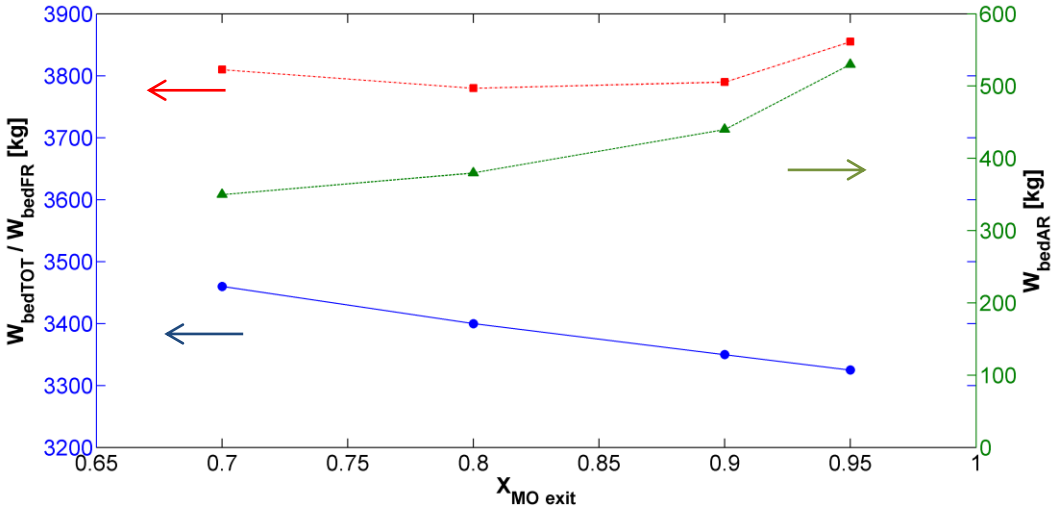

Fig. 4.9 Solid inventories vs. X_{MO_exit} at F_s = 75 kg/s and X_{CH4} = 99.9%

Lower values of X_{MO_exit} decrease the amount of oxygen transferred by the solid particles from the air to the fuel reactor able to react with methane; this phenomenon leads to higher values of W_{bedFR} required. On the other hand, a decrease in X_{MO_exit} results in a lower value of W_{bedAR} required since a lower amount of NiO has to be regenerated. The optimal value of X_{MO_exit} to minimise the overall solid inventory is 0.8. A total minimal solid inventory equal to 3780 kg is required to achieve 99.9% fuel conversion.

Fig. 4.10 shows the change in the methane conversion along the fuel reactor height under the given conditions. About 85% of the gas conversion occurs in the bubbling region and progressively the conversion target is accomplished in the freeboard. Table 4.4 summarises the final conditions for the CLC unit embedded in a power plant working at atmospheric pressure conditions.

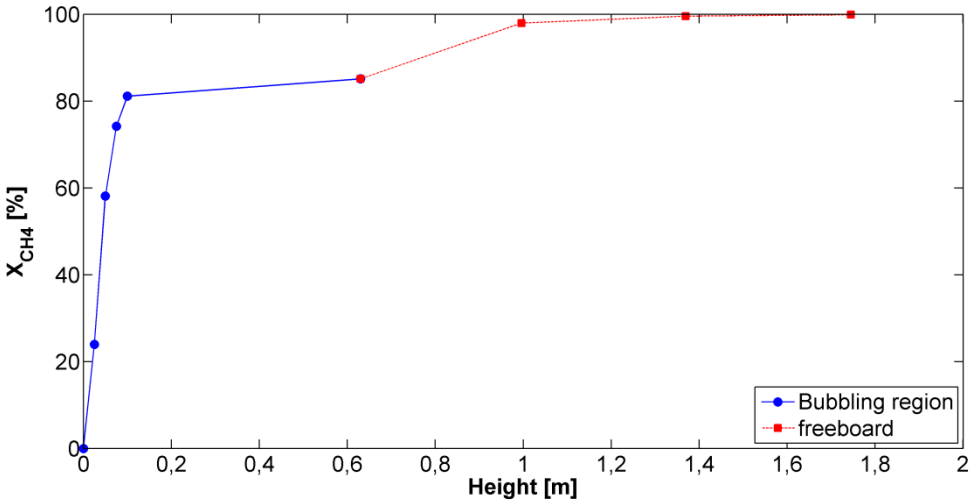

Fig. 4.10 Trend of the methane conversion along the fuel reactor height

Table 4.4 CLC unit main parameters at atmospheric conditions

Adiabatic fuel reactor			**Riser at heat extraction**		
U_o	0.36	m/s	U_{air}	8.33	m/s
A_{FR}	4.14	m^2	A_{AR}	1.9	m^2
Height FR	1.745	m	Height AR	3	m
Inlet solid Temperature	1200	°C	Inlet air temperature	968	°C
Inlet CH_4 temperature	1162	°C	air excess	10	%
Outlet products temperature	1182	°C	Inlet solid mass flowrate F_s	74.2	kg/s
Inlet solid mass flowrate F_s	75	kg/s	G_s	40	kg/(m^2s)
CH_4 conversion	99.9	%	X_{MO_exit}	0.8	
Solid inventory W_{bedFR}	3400	kg	Solid inventory W_{bedAR}	380	kg
Solid inventory W_{bedFR} per MW	340	kg/MW	Solid inventory W_{bedAR} per MW	38	kg/MW

The inlet methane temperature is equal to 1162 °C (see Table 4.4) to keep a ΔT at the heat exchanger equal to 20 °C. This temperature can lead to thermal methane decomposition. Indeed, as reported by Abadanes et al. (2011), temperatures higher than 700-800 °C can decompose methane into carbon and hydrogen under adequate residence times. The low residence times in the heat exchanger (few seconds), should prevent this phenomenon but the technical feasibility of the applied methane temperature at the reactor inlet has to be investigated carefully.

The net thermal efficiency of the power plant is defined as follows:

$$\eta_{th} = \frac{W_{turbines} - W_{compressors} - W_{pumps}}{m_{fuel} LHV} 100 \quad (4.11)$$

A value of the net thermal efficiency equal to 41.71% was found for the plant at atmospheric pressure. The outcome was in agreement with the findings from Naqvi et al. (2004) who reported a thermal efficiency equal to 40.1% for a system at atmospheric conditions and 850 °C at the riser exit.

The CO_2 capture efficiency of the plant, defined as:

$$\eta_{CO2} = \frac{CO_2\ captured}{CO_2\ generated} 100 \quad (4.12)$$

was 97%, making this technology very attractive. *CO_2 captured* refers to the kmol/h stored at 110 atm whereas *CO_2 generated* refers to the kmol/h at the fuel reactor exit. The CO_2 emission rate to the atmosphere is zero.

4.4.2 Power plant at 10 atm with riser at heat extraction

Fig. 4.11 shows the NGCC power plant under pressurised conditions and riser with heat extracted to keep 1200 °C at the riser exit. The use of pressurised conditions leads to higher plant efficiencies than systems working at atmospheric pressure. In this simulation here, an operating pressure equal to 10 atm is applied since, as reported by Wolf et al. (2001) and Naqvi et al. (2004), the pressure has no significant impact on the plant efficiency in the range 10 – 18 atm.

After depressurisation through a valve (not shown in Fig. 4.11), methane at 10 atm is pre-heated exchanging heat with the exhausted products from the CO_2/H_2O gas turbine. The reduction reaction occurs at 10 atm in the fuel reactor under adiabatic conditions. Extra heat from the products stream is recovered in a heat recovery steam generator (HRSG) to drive a steam turbine working at 60 atm and inlet temperature depending on the solid flow-rate circulating in the CLC unit. At a later stage, the CO_2/H_2O stream enters the CO_2 capture section as explained in Section 4.4.1. Air is compressed at 10 atm and pre-heated with the depleted air coming from the air gas turbine before entering the oxidation reactor. The spent air is cooled further to pre-heat the pressurised water stream of the Hirn cycle. The latter stream removes the excess of heat produced by the

exothermic reaction occurring in the riser to fulfil the heat balance in the whole CLC system. Two steam turbines working at 160 atm and 30 atm with two superheating to 560°C are employed to generate extra electricity. More information about each stream of the power plant under investigation are given in Appendix B.

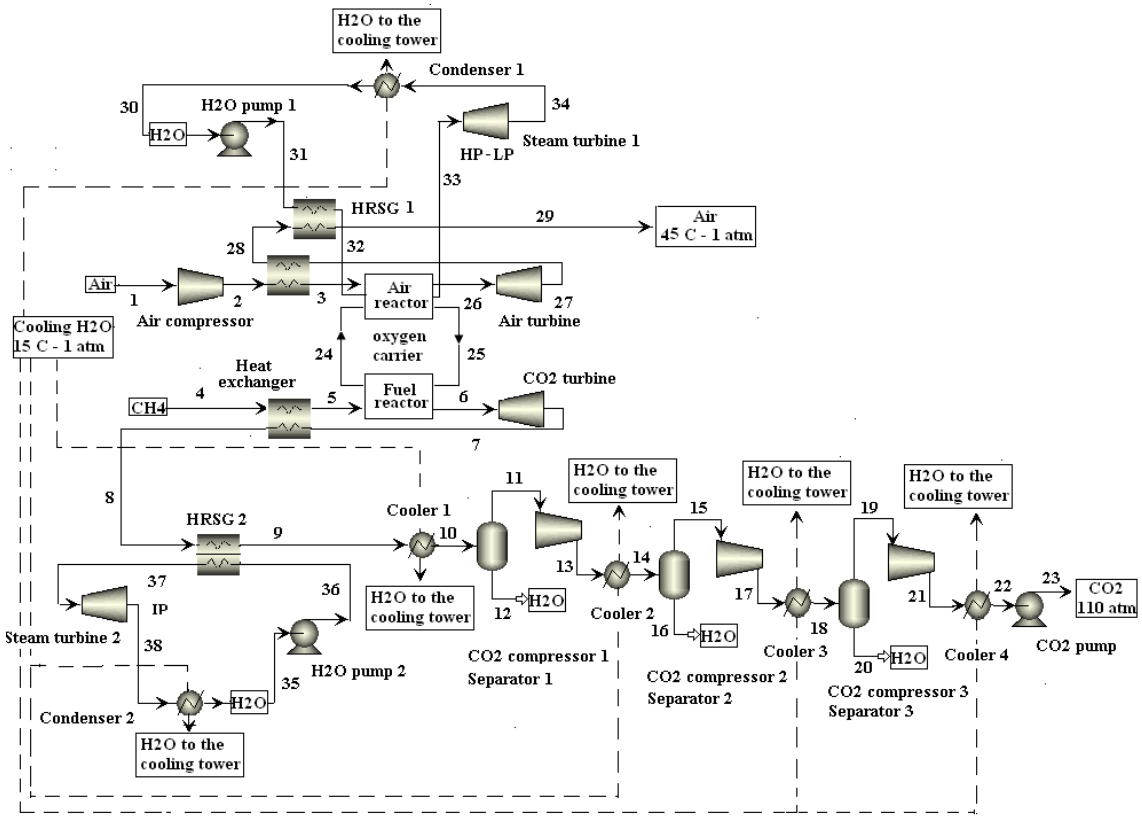

Fig. 4.11 Power plant scheme at pressurised conditions with riser at heat extraction

Given the aforementioned conditions, the total solid inventory of the fluidised beds was estimated.

Fig. 4.12 shows the solid inventory variation in the fuel reactor on changing F_s at X_{MO_exit} = 1 to get 99.9% in methane conversion.

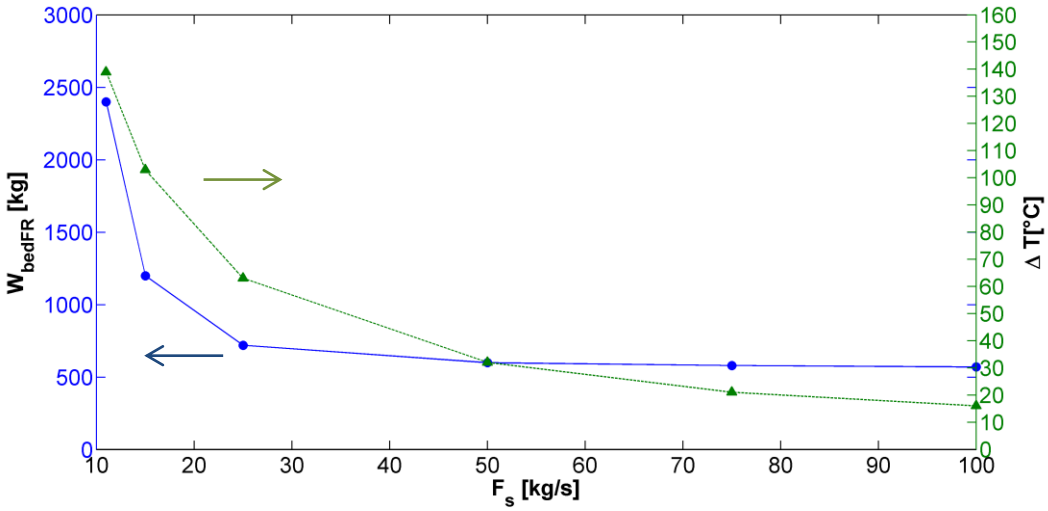

Fig. 4.12 W_{bedFR}/temperature drop vs. F_s at X_{MO_exit} = 1 and P = 10 atm

For the reasons explained in Section 4.4.1, the solid inventory decreases at higher F_s as well as the temperature drop between air and fuel reactor. Since the pressure changes from 1 to 10 atm, different effects take place:

- At higher pressure the gas concentration increases and thus the kinetic rate becomes faster under the hypothesis that the reaction is still under kinetic control (Abad et al., 2007);
- At higher pressure, the gas concentration is higher in the bubble phase increasing the driving force for the mass transfer from the bubble to the emulsion phase;
- The coefficient of diffusivity is inversely proportional to the total pressure leading to a decrease in the mass transfer coefficient K_{be} while increasing the pressure (Eqs. 2.34 – 2.36); the latter influences negatively the mass transfer between the bubble and the emulsion phase;
- The bubble size is not affected by an increase in pressure for Geldart B particles (Kunii and Levenspiel, 1991).

The overall result from our simulations is less solid inventory required at fixed F_s changing the pressure from 1 to 10 atm.

The temperature drop between the two reactors at 10 atm is slightly higher than the case at atmospheric pressure since the inlet methane temperature at the fuel reactor is lower.

The maximum solid mass flow-rate depends on the riser capacity to convey solids, as explained previously. Fluidised beds working under pressurised conditions tend to be slimmer and taller than those working at atmospheric pressure; thus, the decrease of the cross sectional area of the riser leads to a reduction in the maximum F_s applicable.

Assuming 10% of air excess, F_s as high as 25 kg/s is applied, having a riser superficial gas velocity and a superficial area about 4 m/s and 0.4 m^2 respectively. A value of G_s equal to 60 kg/(m^2s) is obtained.

Fig. 4.13 shows that X_{MO_exit} equal to 0.7 minimises the total solid inventory of the CLC unit. At pressurised conditions, the solid inventory in the riser is higher than the atmospheric case since a negative effect of the pressure on the kinetic oxidation rate was found (see Eq. 4.8). A total solid inventory equal to 1830 kg is required to get 99.9% in fuel conversion.

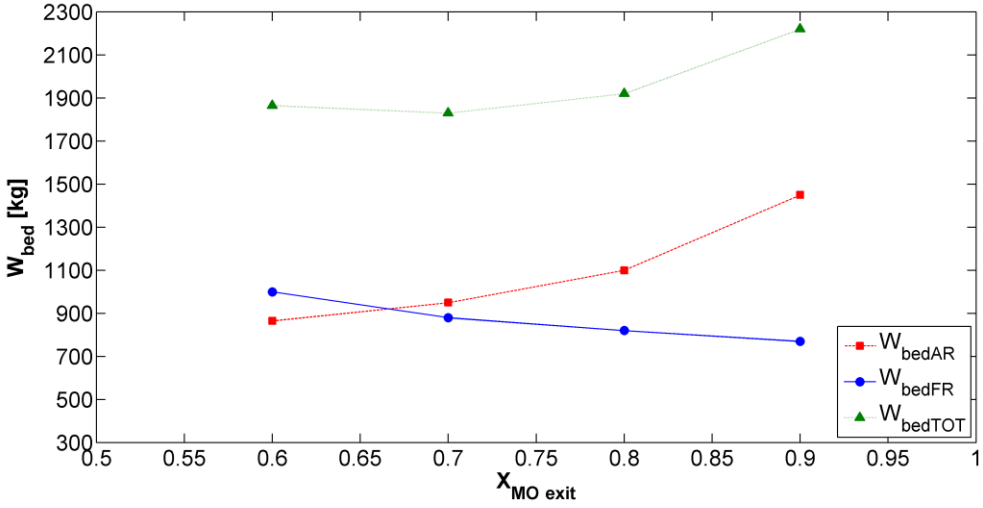

Fig. 4.13 Solid inventories vs. X_{MO_exit} at F_s = 25 kg/sec and X_{CH4} = 99.9%

Fig. 4.14 shows the change in the methane conversion along the fuel reactor height under the given conditions. 89% of the gas conversion occurs in the bubbling region and 99.9% gas conversion target is achieved in the freeboard.

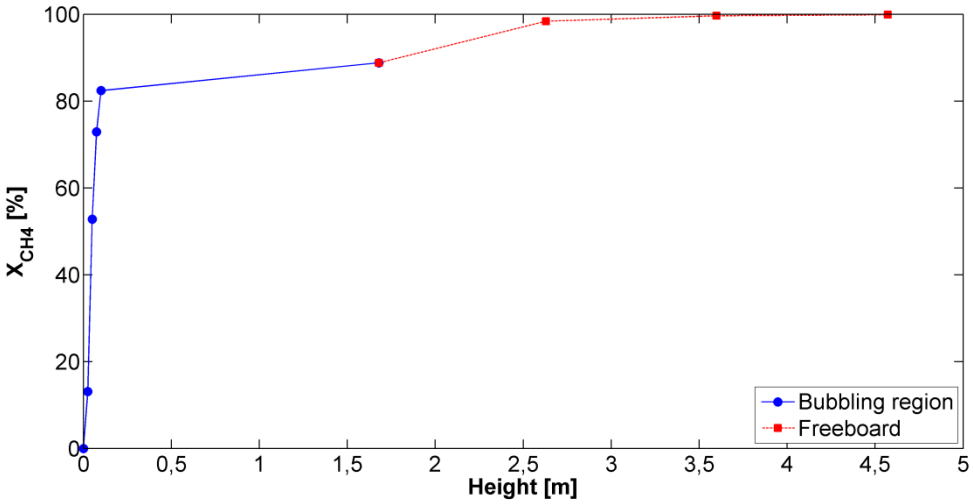

Fig. 4.14 Trend of the methane conversion along the fuel reactor height at 10 atm

Table 4.5 summarises the final conditions for the CLC unit working at 10 atm and heat extracted from the riser.

Table 4.5 CLC unit main parameters under P = 10 atm and riser at heat extraction

Adiabatic fuel reactor			**Riser at heat extraction**		
U_o	0.36	m/s	U_{air}	4	m/s
A_{FR}	0.4	m^2	A_{AR}	0.4	m^2
Height FR	4.572	m	Height AR	13.78	m
Inlet solid Temperature	1200	ºC	Inlet air temperature	550	ºC
Inlet CH_4 temperature	698	ºC	air excess	10	%
Outlet products temperature	1137	ºC	Inlet solid mass flowrate F_s	24.2	kg/s
Inlet solid mass flowrate F_s	25	kg/s	G_s	60	kg/(m^2s)
CH_4 conversion	99.9	%	X_{MO_exit}	0.7	
Solid inventory W_{bedFR}	880	kg	Solid inventory W_{bedAR}	950	kg
Solid inventory W_{bedFR} per MW	88	kg/MW	Solid inventory W_{bedAR} per MW	95	kg/MW

The net thermal efficiency of the power plant is equal to 47.16%. This agrees with results reported by Garcia-Labiano et al. (2005), Naqvi et al. (2004) and Wolf et al. (2001) that state how η_{th} increases under pressurised conditions. As in the case at atmospheric pressure (see Section 4.4.1), the CO_2 capture efficiency is equal to 97%. with no CO_2 emission rate to the atmosphere. The relative small increase in the thermal efficiency after the plant pressurisation (from 41.71% to 47.16%) was likely due to the

inefficient heat extraction at the riser via steam cycle. A different plant configuration will lead to better performances as described below.

4.4.3 Power plant at 10 atm with riser at adiabatic conditions

Fig. 4.15 shows the NGCC power plant under pressurised conditions working with both reactors under adiabatic conditions. Although the heat produced from the exothermic reaction is higher than the one from the endothermic reaction, it is possible to work with both reactors at adiabatic conditions processing a large excess of air flow-rate. In this way, the amount of air, which does not participate to the reactive process, mitigates the temperature rise in the riser fulfilling the energy balance.

Spent airflow exiting from the air turbine is used in a heat recovery steam generator (HRSG) to produce energy from a steam turbine working at 60 atm and 530°C of inlet temperature. More information about each stream of the power plant under investigation are given in Appendix B.

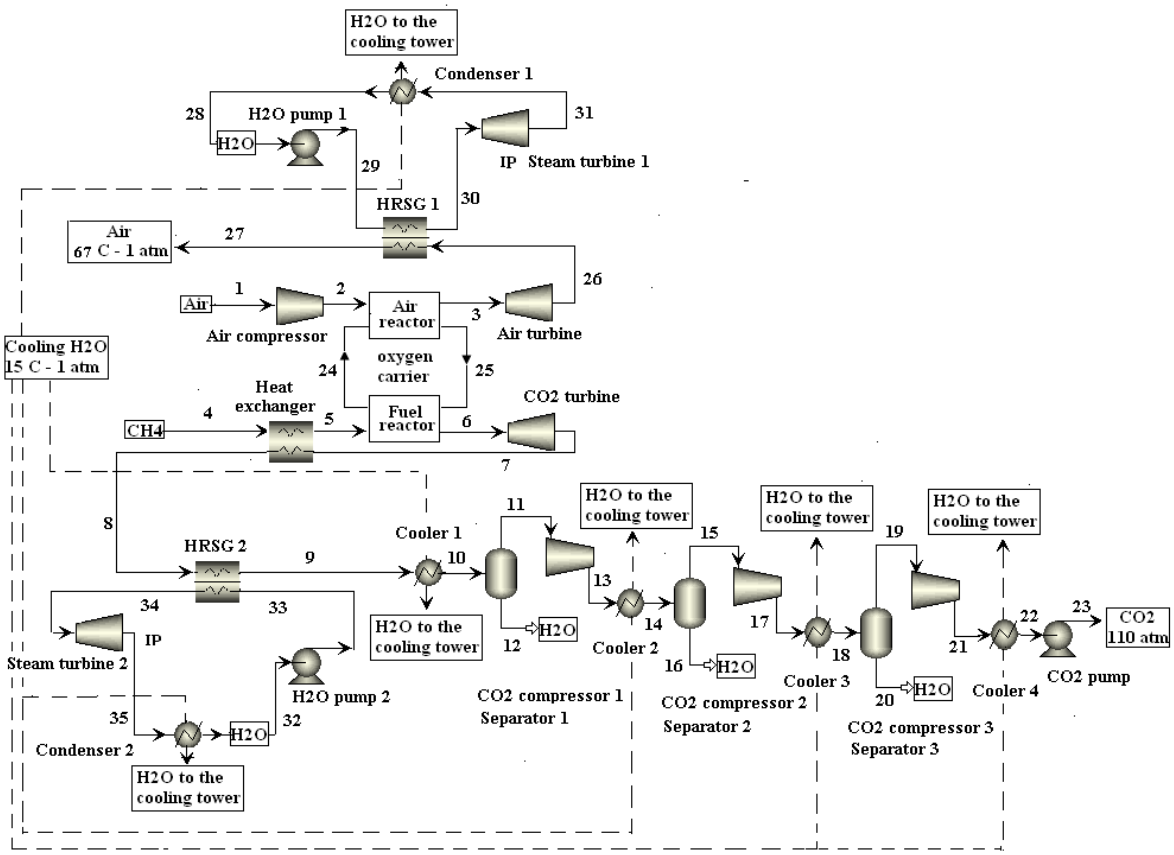

Fig. 4.15 Power plant scheme at pressurised conditions with riser at adiabatic conditions

The fuel reactor conditions are not affected by this change in the plant configuration (see Fig. 4.12, 4.14). On the other hand, the increase in the amount of air processed, compared to the previous cases, reduces slightly the solid inventory required in the riser since the kinetic oxidation rate shows a low dependence from the oxygen concentration (see Table 2.1).

The maximum feasible solid mass flow-rate F_s circulating between the two reactors is still 25 kg/s, having a riser superficial gas velocity and a superficial area about 7.7 m/s and 0.5 m^2 respectively. A value of G_s equal to 50 kg/(m^2s) is obtained. X_{MO_exit} = 0.7 leads to a minimum total solid inventory equal to 1555 kg (Fig. 4.16).

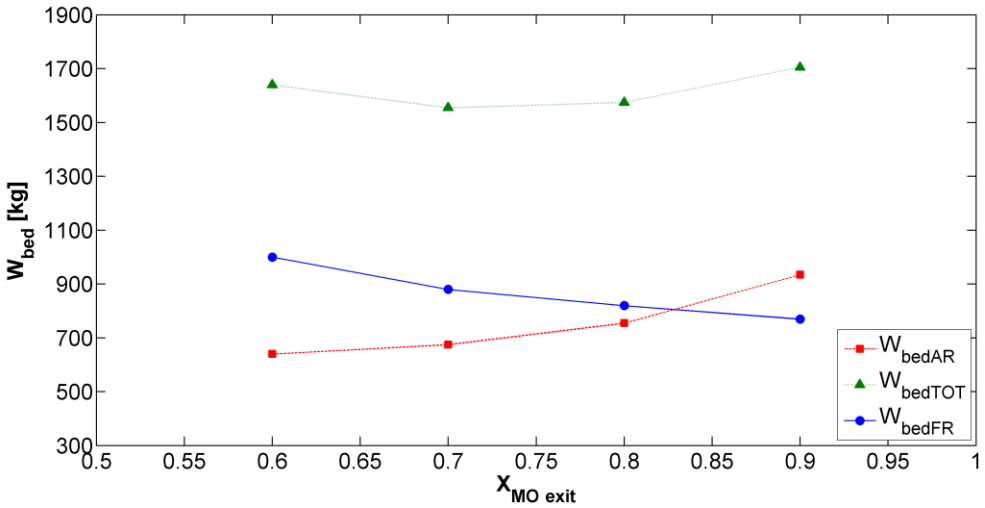

Fig. 4.16 Solid inventories vs. X_{MO_exit} at F_s = 25 kg/s and large air excess

Table 4.6 summarises the final conditions for the CLC unit working at 10 atm with adiabatic reactors.

Table 4.6 CLC unit main parameters under P = 10 atm and adiabatic conditions

Adiabatic fuel reactor			**Adiabatic air reactor**		
U_o	0.36	m/s	U_{air}	7.7	m/s
A_{FR}	0.4	m^2	A_{AR}	0.5	m^2
Height FR	4.572	m	Height AR	15.67	m
Inlet solid Temperature	1200	ºC	Inlet air temperature	326	ºC
Inlet CH_4 temperature	698	ºC	air flowrate	9.6	kg/s
Outlet products temperature	1137	ºC	Inlet solid mass flowrate F_s	24.2	kg/s
Inlet solid mass flowrate F_s	25	kg/s	G_s	50	kg/(m^2s)
CH_4 conversion	99.9	%	X_{MO_exit}	0.7	
Solid inventory W_{bedFR}	880	kg	Solid inventory W_{bedAR}	675	kg
Solid inventory W_{bedFR} per MW	88	kg/MW	Solid inventory W_{bedAR} per MW	67.5	kg/MW

The comparison between Table 4.6 and 4.5 shows how the riser at adiabatic conditions is taller than the case at heat extraction although the solid inventory is less. Indeed, at adiabatic conditions the higher superficial gas velocity leads to a solid volume fraction profile that extends more along the bed height. It is worthy to point out, once again, that the combination of U_{air} and riser cross sectional area is selected to guarantee a riser height that allows for allocating the cyclones, which are presented in Chapter 5, between the fuel and the air reactor.

The net thermal efficiency of the power plant is equal to 52.04% with 97% of CO_2 capture efficiency and no CO_2 atmospheric emissions. This value is in good agreement with data from the literature derived under similar operating conditions (e.g., both reactors are adiabatic). Indeed, Wolf et al. (2001) reported a net power efficiency as high as 52-53% for a riser operating at 1200 °C and 13 atm whereas Naqvi et al. (2007) reported a net power efficiency of 52.2% for a plant working at 18 atm and an air turbine inlet temperature of 1140 °C.

Table 4.7 shows the comparison between the two different plant configurations considered at 10 atm in terms of MW consumed and generated.

Table 4.7 MW consumed and generated for the CLC systems of Fig. 4.11 and 4.15

	Riser at heat extraction	**Adiabatic riser**
Air compressor (MW)	-1.17	-2.86
Air turbine (MW)	2.06	5.72
Steam turbine 1 (MW)	3.32	1.82
CO_2 turbine (MW)	0.75	0.75
Steam turbine 2 (MW)	0.15	0.15
CO_2 capture energy penalties (MW)	-0.25	-0.25
Pump energy penalties (MW)	-0.04	-0.01
Tot (MW) (at overall mech. efficiency = 0.98)	**4.72**	**5.20**

Processing a large excess of air, needed to work with both reactors adiabatic, leads to a higher power consumed by the air compressor; nevertheless, more work is also extracted from the air turbine and thus more net power is extracted from the air flow. The overall outcome is a thermal efficiency higher for the system working with both reactors adiabatic.

The CO_2 energy penalties linked with the CO_2 capture are calculated comparing the CLC power plant with an NGCC power plant without CO_2 capture (Fig. 4.17).

The NGCC power plant runs under the same conditions applied for the CLC configuration with both reactors adiabatic. Air is pressurised at 10 atm before entering the combustion chamber to react with methane. An adiabatic stoichiometric reactor implements the combustion chamber. The latter runs under the following conditions: 10 atm, 1200 °C at the reactor exit, 99.9% in methane conversion. 9 kg/s of inlet air guarantee adiabatic conditions inside the reactor and 1200 °C of air turbine inlet temperature. Spent airflow exiting from the air turbine is used in a heat recovery steam generator (HRSG) to produce energy from a steam turbine working at 60 atm and 530°C of inlet temperature.

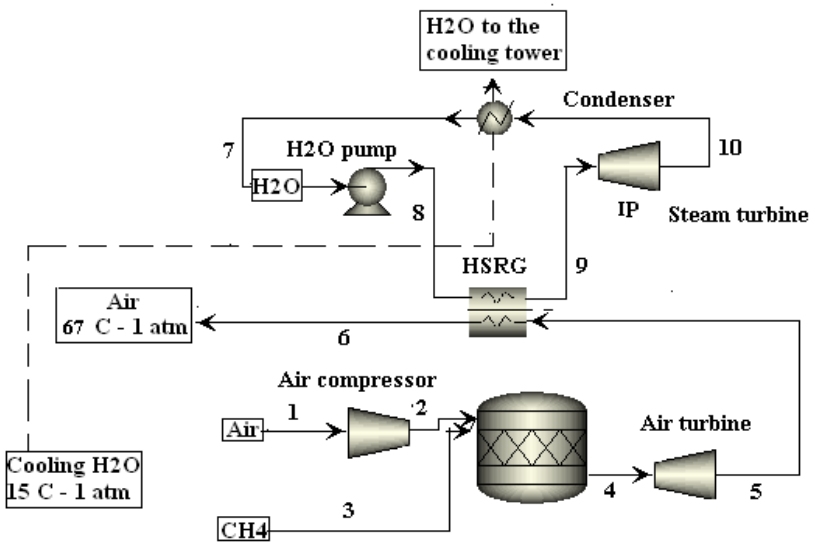

Fig. 4.17 NGCC without CO_2 capture

The net thermal efficiency of the power plant is equal to 55% with 358 kg/MWh of CO_2 produced.

The CO_2 energy penalties drop the thermal efficiency of the plant by 3% points (55% against 52.04%). A thermal efficiency reduction equal to 3% is perfectly in agreement with data from the literature that report energy penalties for a CLC power plant in a range of 2-3% compared to a similar system without CO_2 capture (Naqvi et al., 2004, 2007; Wolf et al., 2001, 2005).

Table 4.8 summarises the thermal efficiency for the three CLC plant configurations and for the NGCC without CO_2 capture.

Table 4.8 Summary of the net power efficiencies for the different cases analysed

Net power efficiency %			
P = 1atm	**Riser at heat extraction (P = 10 atm)**	**Adiabatic Riser (P = 10 atm)**	**Ref. Plant (P = 10 atm)**
41.71	47.16	52.04	55

Concerning the plant configuration working with both reactors adiabatic, Fig. 4.18 shows the change in the air mass flow-rate, to keep adiabatic conditions in the riser, as well as the outlet temperature of the fuel reactor while changing F_s.

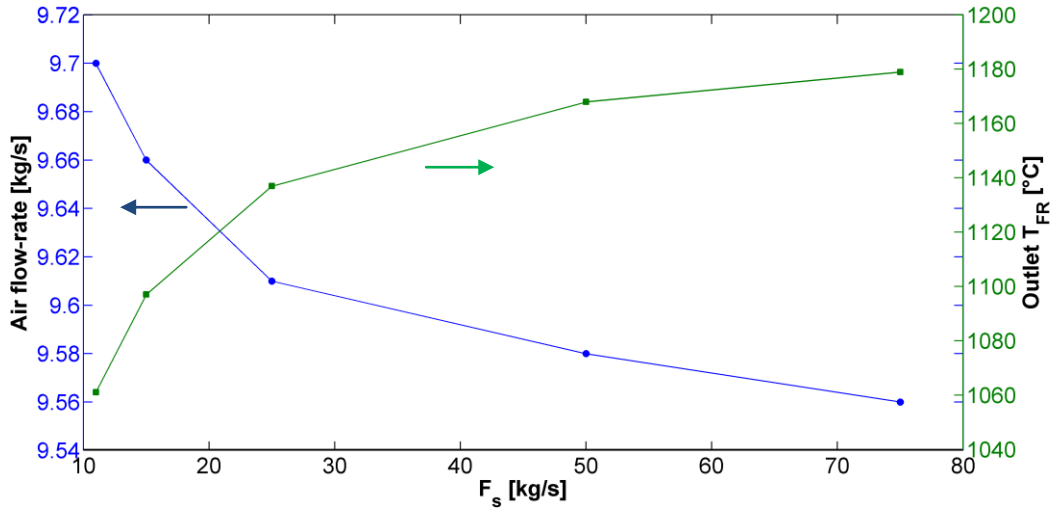

Fig. 4.18 Mass air flow-rate/outlet fuel reactor temperature vs. F_s

When F_s increases the amount of air to keep adiabatic conditions in the riser decreases since the solid thermal inertia is higher and thus the change in the riser outlet temperature, due to the exothermic reaction, is reduced. On the other hand, the increase in F_s determines higher values in the fuel reactor outlet temperature since more heat is conveyed from the riser to the fuel reactor to sustain the methane endothermic reaction.

If the plant was split in two sections, called air and fuel reactor loop, Fig. 4.19 shows how a change in F_s affects the net power extracted in both loops. The air loop comprises the air compressor, the air turbine and the HRSG connected with the spent air leaving the air turbine; conversely, the fuel loop comprises the CO_2/H_2O turbine, the HRSG connected to it and the CO_2 capture section.

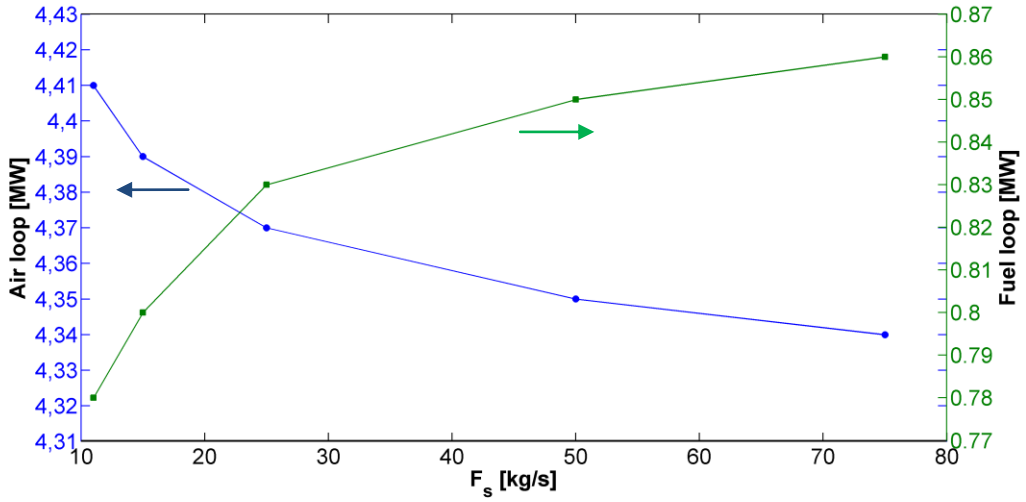

Fig. 4.19 Air/fuel loop vs. F_s

When F_s increases less air is processed (Fig. 4.18) and thus the net power extracted in the air loop is less (Fig. 4.19); conversely, the fuel reactor outlet temperature is higher and thus more power is extracted from the fuel loop. The overall net power extracted from the plant is constant and equal to about 5.20 MW (i.e. about 52% of net thermal efficiency) while changing F_s.

The latter result comes from the assumption that the compressor and all the turbines in the plant have the same isentropic efficiency equal to 0.9. If in a CLC power plant the latter units present different isentropic efficiencies, it is interesting to notice how changing F_s can improve the overall thermal efficiency of the process just extracting more power from the section that comprises the units at higher isentropic efficiency.

Keeping a value for F_s equal to 25 kg/s (i.e. the value that minimises the total solid inventory inside the CLC unit), the plant configuration with both reactor adiabatic, which presents the highest thermal efficiency, is subject at a cost analysis in the next chapter to evaluate the Levelised Cost Of the Electricity generated (LCOE).

Overall, the system composed of the two fluidised bed reactors was connected to the NGCC power plant: the overall net thermal efficiency of the plant was estimated for atmospheric and pressurised conditions. It was found that working with adiabatic reactors at pressurised conditions leads to 52.04% of thermal efficiency with about 3% in CO_2 capture energy penalties and no CO_2 emissions in the atmosphere.

Moreover, the variables involved in the optimisation of the operating conditions of the two interconnected fluidised beds were investigated, mainly the degree of oxidation of the solid particles at the riser exit and the solid circulating flow-rate between the two reactors. Finally, since the solid material represents an important cost for the CLC technology, an analysis of the minimum total solid inventory in the reactors to achieve almost full methane conversion was carried out.

Chapter 5

Economic analysis of the CLC power plant

In Chapter 4, three different CLC power plant configurations are proposed. The case with both reactors working at adiabatic conditions exhibits a highly competitive thermal efficiency equal to 52.04%; moreover, the reported energy penalty for CO_2 capture lowers the plant thermal efficiency by just 3%.

The energy penalties for CO_2 capture using traditional technologies such as MEA absorption or air separation units lower the thermal efficiency of the process of 8-10% (Audus, 2000; Gottlicher and Pruschek, 1997; Wolf et al., 2005; Mores et al., 2014). This aspect makes the CLC technology, including the CO_2 capture section, able to reach a thermal efficiency higher than about 5% compared to conventional technologies for CO_2 capture (Wolf et al., 2001); however, this advantage is not sufficient to claim that the CLC technology is more profitable than the conventional ones.

Indeed, the main issue for the feasibility of the CLC technology might concern the amount of the solid material needed to get full fuel conversion, which was accurately minimised applying optimal operating conditions in Chapter 4 (see Table 4.6), and the associated costs (Abad et al., 2007). The total solid inventory affects the sizes of the fluidised beds and thus the capital cost of the CLC power plant. Furthermore, the price of the metal oxide particles, together with their lifetime would be partly responsible for the extra operating cost due to the solid make-up. The latter aspects have to be taken into account in making comparisons between CLC and traditional carbon capture technologies such as chemical absorption with MEA since they largely influence the *LCOE* generated.

For the aforementioned reasons, an adequate comparison among carbon capture technologies has to be based on a full economic analysis of the processes. In the present chapter, an economic analysis is applied to the CLC power plant working with adiabatic reactors since it shows the highest thermal efficiency. The effect of the lifetime of the solid particles on the *LCOE* is highlighted and an approach to compare the CLC technology with state-of-art technologies for CO_2 capture is suggested.

5.1 Sizing the equipment

The CLC power plant with both reactors at adiabatic conditions (Fig. 4.15) was scaled up to 500 MW thermal, which means a power plant of medium capacity (the power plant generates about 260 MW of power at 52.04% of thermal efficiency), and all the facilities were sized to estimate the purchased equipment costs. Table 5.1 summarises the final conditions for the CLC unit working at 10 atm with adiabatic reactors scaled up to 500 MW. The air and fuel reactor have a volume of 392 and 91 m^3 respectively (Table 5.1) and those values were used to estimate the cost of both reactors in Section 5.2.

Table 5.1 CLC unit main parameters under P = 10 atm, P_{fuel} = 500 MW and adiabatic conditions

Adiabatic fuel reactor			**Adiabatic air reactor**		
U_o	0.36	m/s	U_{air}	7.7	m/s
A_{FR}	20	m^2	A_{AR}	25	m^2
Height FR	4.572	m	Height AR	15.67	m
Inlet solid Temperature	1200	ºC	Inlet air temperature	326	ºC
Inlet CH_4 temperature	698	ºC	air flowrate	480	kg/s
Outlet products temperature	1137	ºC	Inlet solid mass flowrate F_s	1210	kg/s
Inlet solid mass flowrate F_s	1250	kg/s	G_s	50	kg/(m^2s)
CH_4 conversion	99.9	%	X_{MO_exit}	0.7	
Solid inventory W_{bedFR}	44000	kg	Solid inventory W_{bedAR}	33750	kg
Solid inventory W_{bedFR} per MW	88	kg/MW	Solid inventory W_{bedAR} per MW	67.5	kg/MW

5.1.1 Cyclones

In a circulating fluidised beds system, a cyclone allows the separation between the solid and gas outlet products from the riser. Cyclones are the principal type of gas-solid separator employing centrifugal force. They are suitable to separate particles with average diameter above 5 μm. There are two basic types of gas cyclones depending on how the clean gas leaves the cyclone: the uni-flow and the reverse flow. In the uni-flow cyclone, the gas enters at one end of the cylindrical body and it leaves at the other end; this type of cyclone has limited use in industry. The reverse flow cyclone is by far the most commonly used in industry. The body of the reverse flow cyclone consists of a cylindrical section joined to a conical section. The clean gas outlet is through a central

pipe at the same end of the cyclone as the tangential inlet. The gas outlet pipe extends some distance axially into the body, through the top lid. The discharge of the separated dust is through a central orifice in the apex of the conical section. There are four different types of inlet used in gas cyclones: axial, tangential, spiral or helical. Each inlet type has its advantages and applications.

In this work, a reverse flow cyclone with tangential inlet gas is applied. Fig. 5.1 shows the cyclone geometry employed in Aspen Plus:

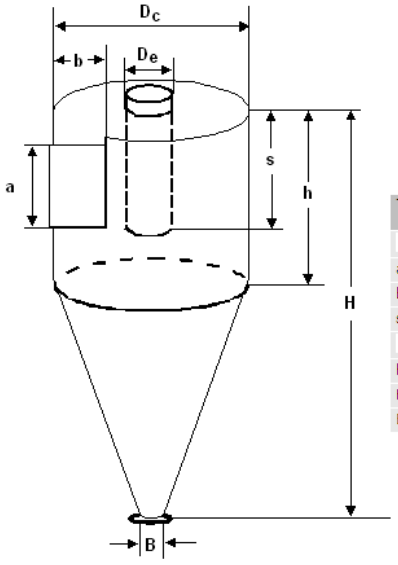

Term	Description	High efficiency
D	Body diameter	1.0
a	Inlet height	0.5
b	Inlet width	0.2
s	Outlet length	0.5
D_e	Outlet diameter	0.5
h	Cylinder height	1.5
H	Overall height	4.0
B	Dust outlet diameter	0.375

Fig. 5.1 Cyclone geometry employed in Aspen Plus

The diameter of the body of the cyclone D_c was calculated as follows:

$$D_c = 0.0502\left(\frac{Q_{oc}\rho_g{}^2}{\mu_g(\rho_s-\rho_g)}\frac{\left(1-\frac{b}{D_c}\right)}{\left(\frac{a}{D_c}\right)\left(\frac{b}{D_c}\right)^{2.2}}\right)^{0.454} \quad (5.1)$$

where Q_{oc} is the overflow volumetric gas flow-rate, ρ_g is the density of the gas, μ_g is the viscosity of the gas and ρ_s is the density of the particles. The overall separation efficiency, η_c, as a ratio between the flow rate of solids removed from the inlet and the total inlet flow rate of solids is calculated as follows:

$$\eta_c = 1 - \frac{E_c}{Q_{oc}C_c} \quad (5.2)$$

where C_c is the concentration of solids in the inlet gas and E_c is the outlet emission rate of solids in the cleaned gas. The Leith and Licht efficiency correlation, accurate for inlet velocities approximately from 15 up to 30 m/s, is applied. The overall gas–solid separation efficiency is chosen equal to 99.9%. When the efficiency of a single cyclone is less than the required efficiency, Aspen Plus calculates the number of cyclones to be located in parallel to achieve the desired gas-solid separation. The cyclone design results are shown in Table 5.2.

Table 5.2 Cyclone design results

O_2 inlet	68	kg/s
N_2 inlet	352.6	kg/s
Ni inlet	148	kg/s
NiO inlet	349	kg/s
Al_2O_3 inlet	753	kg/s
Number of cyclones	8	
Diameter of cylinder	1.4	m
Efficiency	99.9	%
Length of vortex	3.69	m
Length of cylinder	2.1	m
Length of cone	3.5	m
Diameter of gas outlet	1.05	m
Length of gas outlet	1.23	m
Width of gas inlet	0.53	m
Height of gas inlet	1.05	m
Diameter of solid outlet	0.53	m
Number of gas turns	4	

The height of each cyclone is 5.6 m (see Table 5.2). The difference in height between the riser and the fuel reactor (see Table 5.1) is adequate to locate the cyclone system.

5.1.2 Gas – liquid separators

The gas – liquid separators as part of the CO_2 capture section allow the separation of CO_2 and H_2O after cooling (i.e. H_2O condensation) at 30 °C. Separators are usually designed for continuous operation; they employ cylindrical shapes arranged in both vertical and horizontal configurations depending on the inlet flow-rate to the process. The separator diameter has to be large enough to guarantee a gas velocity across the unit equal to or lower than the settling velocity of the liquid droplets. The vessel diameter and its length are not independent variables; their combination has to lead to a gas

residence time inside the separator that allows for the settling of the liquid droplets. Typical length/diameter ratios of the vessel range from 3 to 5 depending on the operating pressure. The standard procedure for the gas – liquid separator design comes from Branan (2002). The settling velocity of the liquid droplets, U_L, is calculated as follows:

$$U_L = K_{drum}\sqrt{\frac{(\rho_L - \rho_V)}{\rho_V}} \tag{5.3}$$

$$K_{drum} = \exp[A + blnF_{lv} + C(lnF_{lv})^2 + D(lnF_{lv})^3 + E(lnF_{lv})^4] \tag{5.4}$$

$$F_{lv} = \frac{W_L}{W_V}\sqrt{\frac{\rho_V}{\rho_L}} \tag{5.5}$$

where W_V and W_L are the gas and liquid mass flow-rates, respectively. The gas velocity, U_V, is calculated as follows:

$$U_V = \frac{Q_V}{A_V} \tag{5.6}$$

where Q_v represents the volumetric gas flow-rate and A_V represents the fraction of the total cross sectional area crossed by the gas flow-rate. The diameter and the length of the vessel have to guarantee that the effective residence time, τ_{eff}, expressed by Eq. 5.7, is equal to the required residence time, τ_{req}, expressed by Eq. 5.8:

$$\tau_{eff} = \frac{L_{vessel}}{U_v} \tag{5.7}$$

$$\tau_{req} = \frac{(1 - f_V)D_{vessel}}{U_L} \tag{5.8}$$

where f_V represents the transversal fraction of the vessel crossed by the gas phase. The latter value depends on the liquid hold up inside the vessel that has to guarantee a liquid residence time (see Eq. 5.9) of about 10 minutes.

$$\tau_{hold-up} = \frac{V_L}{Q_L} \tag{5.9}$$

where V_L and Q_L are the volume of the vessel occupied by the liquid and the volumetric liquid flow-rate, respectively. Both vertical and horizontal separators were designed but only the horizontal separators matched our requirements. Table 5.3 shows the horizontal separators design results.

Table 5.3 Separators design results

	Separator 1		**Separator 2**		**Separator 3**	
Pressure	1	atm	4	atm	16	atm
Temperature	30	°C	30	°C	30	°C
Vessel diameter	2.28	m	1.15	m	0.712	m
Vessel length	6.85	m	3.44	m	2.14	m
Total volume	28	m^3	3.54	m^3	0.85	m^3
Liquid hold up	11.3	min	10.8	min	10.9	min

5.1.3 Heat transfer units

The CLC power plant is composed of four coolers, two condensers, one heat exchanger and two HRSGs designed as heat exchangers (see Fig. 4.15). All the aforementioned heat transfer units are designed applying the Eq. 5.10:

$$Q_{hex} = U_{hex} A_{hex} \Delta T_{mln} \tag{5.10}$$

where Q_{hex} is the heat duty, U_{hex} is the overall heat transfer coefficient, A_{hex} is the total heat transfer area and ΔT_{mln} is the logarithmic mean temperature difference. To calculate the total heat transfer area, A_{hex}, a simple approach is applied; thus, given Q_{hex} and ΔT_{mln}, A_{hex} is derived assuming a constant value for U_{hex} depending on the characteristics of the streams involved as reported by Coulson and Richardson (2003). This approach gives a rough estimation of the total area of the heat exchangers without the need to design all the geometry of each heat exchanger.

All the coolers were designed under the specifications of cooling water inlet temperature equal to 15 °C and outlet temperature of the process stream equal to 30 °C. The inlet cooling water flow-rate is chosen to guarantee a maximum cooling water outlet temperature equal to 50 °C. All the condensers were designed under the specification of cooling water inlet temperature equal to 15 °C and maximum cooling

water outlet temperature equal to 50 °C; furthermore, the inlet cooling water flow-rate chosen has to guarantee a minimum difference in temperature across the condensers equal to 10 °C. The heat exchanger to pre-heat the methane stream before entering the fuel reactor is designed under the specification of minimum difference in temperature between the two process streams equal to 20 °C. The two HRSGs are simply designed as heat exchangers splitting the heat transfer in two sections, sub-cooling and vaporisation, and keeping a minimum difference in temperature across the heat exchangers equal to 10 °C. Table 5.4 shows the heat transfer units design results.

Table 5.4 Heat transfer units design results

	Q_{hex} (kW)	U_{hex} (kW/(m^2°C))	A_{hex} (m^2)
Cooler 1	58492	0.85	2105
Cooler 2	4151	0.25	350
Cooler 3	3366	0.3	219
Cooler 4	8742	0.3	508
Condenser 1	161000	4	2275
Condenser 2	17161	4	81
Heat exchanger	22670	0.15	1126
HRSG 1	240000	0.3	18312
HRSG 2	23700	0.3	2865

5.1.4 Compressors, pumps and turbines

The design of compressors, pumps and turbines was confined to the calculation of the installed electrical power. The power consumed at the compressors, P_{eff}, is expressed by Eq. 5.11:

$$P_{eff} = \frac{m_{in}T_{in}}{\eta_{is}} \frac{R'}{Mw} \frac{c_p/c_v}{c_p/c_v - 1} \left[\beta_c^{\frac{c_p/c_v - 1}{c_p/c_v}} - 1 \right] \tag{5.11}$$

where m_{in} is the inlet gas mass flow-rate, T_{in} is the gas inlet temperature, $R^{'}$ is the universal gas constant, M_w is the molecular weight of the inlet gas, c_p and c_v are the specific heat at constant pressure and constant volume respectively, β_c is the compression ratio and η_{is} is the isentropic efficiency of the compressor. In the same way, the power extracted at the gas turbines is expressed as follows:

$$P_{eff} = \eta_{is} m_{in} T_{in} \frac{R'}{Mw} \frac{c_p/c_v}{c_p/c_v - 1} \left[1 - \beta_c^{\frac{1-c_p/c_v}{c_p/c_v}} \right] \quad (5.12)$$

The power consumed at the pumps is derived from Eq. 5.13:

$$P_{eff} = \frac{Q_{p,in} \Delta P}{\eta_{eff}} \quad (5.13)$$

where $Q_{p,in}$ is the inlet volumetric flow-rate, ΔP is the difference in pressure between the inlet and the outlet of the pump and η_{eff} is the pump efficiency. Finally, the power extracted at the steam turbines is calculated as follows:

$$P_{eff} = -\eta_{is} m_{in} (h_1 - h_{2s}) \quad (5.14)$$

where h_1 is the inlet enthalpy, h_{2s} is the isentropic outlet enthalpy, m_{in} is the inlet mass flow-rate and η_{is} is the turbine isentropic efficiency. Table 5.5 shows the power consumed by pumps and compressors and generated from the turbines.

Table 5.5 Power consumed/generated

	P_{eff} (kW)
Air compressor	142800
CO_2 compressor 1	3200
CO_2 compressor 2	3100
CO_2 compressor 3	3400
Air turbine	-286000
CO_2 turbine	-37500
Steam turbine 1	-90750
Steam turbine 2	-7250
H_2O pump 1	600
H_2O pump 2	65
CO_2 pump	2800

5.2 Cost of the equipment

The reference costs for all the facilities (see Fig. 4.15) were taken from Peters et al. (2004) apart from the cost of the riser and the fuel reactor that come from Klara (2007). Usually the cost of the equipment refers to a specific year. Since the prices can change

considerably with time due to changes in economic conditions, some methods were developed for updating the equipment costs. One of those methods is the cost index. As reported by Peters et al. (2004), the present cost of a unit is equal to the original cost multiplied by the ratio between the cost index at present and the cost index at time original cost was obtained:

$$Present\ cost = original\ cost\left(\frac{cost\ index\ at\ present}{cost\ index\ at\ time\ original\ cost\ was\ obtained}\right) \quad (5.15)$$

Many different types of cost indexes are published regularly such as: *Marshall and Swift all-Industry, process industry equipment indexes, Engineering news Record construction index, Nelson-Ferrar refinery construction index* and the *Chemical Engineering Plant Cost Index* (CEPCI). The *Marshall and Swift* and the CEPCI indexes are recommended for process equipment and chemical plant investment estimates (Peters et al., 2004). In this work, a CEPCI index, updated to January 2015 and equal to 577, is applied. The reference CEPCI index is calculated for January 2002 and it is equal to 390.4.

As aforementioned, the cost of the equipment was calculated using tables, graphs and formulas provided by Peters et al. (2004). When the cost data of a piece of equipment was not available because its size was out of range, two options were usable. The first option refers to the application of multi stage machines/units to locate in a parallel configuration to reduce the size of each component. The second option refers to the application of the *six-tenths factor rule* (Peters et al., 2004). According to the latter, the cost of a unit for a particular size *a* is equal to the cost of the same unit of size *b* times the ratio between the two different capacities powered at 0.6, as expressed by Eq. 5.16:

$$cost\ of\ a = cost\ of\ b\left(\frac{capacity\ of\ a}{capacity\ of\ b}\right)^{0.6} \quad (5.16)$$

In this work, we decided to apply the *six-tenths factor rule* when needed. Applying the CEPCI index updated to January 2015 and assuming carbon steel for all the equipment, Table 5.6 exhibits all the costs of the units of the CLC power plant (see Fig. 4.15) highlighting for each unit the main parameter that determines its cost.

The volumes of the reactors are strictly dependent on the amount of solid inventory and their cost counts for the 64% of the cost of the whole plant. Once again, the minimisation of the total solid inventory in reducing the plant capital costs was very important. The delivery of the equipment was assumed to cost 10% of the purchased equipment (Peters et al., 2004). Based on the purchased equipment (delivered) (DPE), the Fixed Capital Investment (FCI) and the Total Capital Investment (TCI) were estimated in the next section.

Table 5.6 List of the costing of the equipment

	P_{eff} (kW)	Cost		Area (m^2)	Cost
Air compressor	142800	$ 9,899,475	**Heat exchanger**	1126	$ 126,964
CO_2 compressor 1	3200	$ 1,049,360	**HRSG 1**	18312	$ 790,829
CO_2 compressor 2	3100	$ 1,034,580	**HRSG 2**	2865	$ 259,615
CO_2 compressor 3	3400	$ 1,093,699	**Cooler 1**	2105	$ 184,802
Air turbine	-286000	$ 7,737,197	**Cooler 2**	350	$ 44,339
CO_2 turbine	-37500	$ 2,286,561	**Cooler 3**	219	$ 29,559
Steam turbine 1	-90750	$ 1,665,311	**Cooler 4**	508	$ 66,509
Steam turbine 2	-7250	$ 369,493	**Condenser 1**	2275	$ 193,618
H_2O pump 1	600	$ 99,313	**Condenser 2**	81	$ 14,780
H_2O pump 2	65	$ 26,603			**Sub TOT cost**
CO_2 pump	2800	$ 58,326			$ 1,711,014
		Sub TOT cost		L_v (m) / D_v (m)	**Cost**
		$ 25,319,917	**Separator 1**	6.85 / 2.28	$ 17,736
	Volume (m^3)	**Cost**	**Separator 2**	3.44 / 1.15	$ 5,173
Air reactor	392	$ 34,292,681	**Separator 3**	2.14 / 0.71	$ 4,730
Fuel reactor	91	$ 14,318,962			**Sub TOT cost**
		Sub TOT cost			$ 27,638
		$ 48,611,643			**TOT cost**
	D_c (m) / H_c (m)	**Cost**			
Cyclones	1.4 / 5.6	$ 108,991			
		Sub TOT cost			**$ 75,779,204**
		$ 108,991			

5.3 Plant cost analysis

The plant cost analysis was carried out using Excel spreadsheets. Through the link between Aspen Plus and Excel, the main parameters of the units that determine their cost (see Table 5.6) are exported from Aspen Plus to Excel; thus, the equipment cost (or DPE) is automatically calculated making use of appropriate cost formulas. Based on the latter, all the economic evaluation of the plant is automatically developed in cascade as

explained from now on. In this way, it was possible to estimate very quickly the influence that every change in the plant operating conditions has on the cost of the electricity generated.

In the economic evaluation of a project the main costs to take into account are: Total Capital Investment (TCI) and operating Cost (C_o). The TCI includes all the expenses to purchase the equipment, to install it and all the entries of cost to physically build the plant. TCI can be split in Fixed Capital Investment (FCI), which represents the capital needed to supply the required manufacturing and plant facilities, and Working Capital (WC), which represents the initial capital to start the operations. The FCI can be further split in direct and indirect costs. The direct costs comprise: purchased equipment and installation, instrumentation and control, piping, electrical system, buildings, yard improvement, service facilities and land. The indirect cost refer to all the capital required for construction overhead and for all the plant components not directly related to the process operation. They include: engineering and supervision, legal expenses, construction expenses, contractor's fee and contingency. On the other hand, the WC refers to the total amount of money invested in raw material and supplies carried in stock, finished products in stock, cash kept on hand for monthly payment of operating expenses (Peters et al., 2004).

Different methods can be applied to evaluate the TCI depending on the accuracy required as listed by Peters et al. (2004):

- *Detailed-Item Estimate*: detailed estimation of each individual item based on completed drawings and specifications, accurate estimates of engineering, field supervision and complete site surveys. This method gives an accuracy of 5%:
- *Percentage of Delivered-Equipment Cost*: the TCI estimation is based on the purchased equipment (delivered) (DPE); the items of the TCI are calculated as percentages of the DPE. This method gives an accuracy of 10-20%;
- *Lang Factor for Approximation of Capital Investment*: this technique is based on multiplying the equipment cost for a factor, called Lang factor, to obtain the TCI; the Lang factor depends on the type of plant, i.e. solid, solid-fluid or fluid plant. This method gives an accuracy of 30%.

In the present work the *Percentage of Delivered-Equipment Cost* method was applied. Peters et al. (2004) defines for each item of the FCI a range of percentages of DPE

associated. The average percentage values for each items of FCI are assumed. The WC usually amounts to 10 to 20% of the TCI. It was assumed a WC equal to 15% of the TCI, meaning 17% of the FCI as displayed in Table 5.7. In the first year of operation, the start-up expenses have to be also considered. A range between 8-10% of the FCI is suggested by Peters et al. (2004); thus, in this work the start-up expenses were assumed equal to 9% of FCI.

Table 5.7 FCI and TCI estimation (Peters et al., 2004)

	Direct cost (DC)		**Indirect cost (IC)**
Purchased equipment installation	30%DPE	Engineering and supervision	30%DPE
Instrumentation and control	20%DPE	Legal Expenses	4%DPE
Piping	55%DPE	Construction Expenses	37%DPE
Electrical system	20%DPE	Contractor's Fee	20%DPE
Buildings	12%DPE	Contingencies	40%DPE
Yard improvements	15%DPE	**SubTOT indirect cost**	**$ 110,448,189**
Service facilities	40%DPE	**FCI = DC + IC**	**$ 358,435,633**
Land	6%DPE	**Working Capital (WC) = 17%*FCI**	**$ 60,934,058**
SubTOT direct cost	**$ 247,987,444**	**TCI = FCI + WC**	**$ 419,369,691**

A widely used parameter to compare power plants is the overnight capital cost. The overnight capital cost of the CLC power plant under investigation, defined as the ratio between the FCI and the net electricity generated, is equal to 1363 $/kW. This value is in agreement with the estimated range of overnight capital cost from different NGCC power plants including those with carbon capture technologies as reported by IPCC (2005), Rubin et al. (2007) and Davison (2007) updated to the end of 2014. Furthermore, Petrakopoulou et al. (2011) reported a value of overnight capital cost for a NGCC power plant with CLC technology equal to 980 €/kW (2011 prices). The latter value, updated to the end of 2014, is close to the value estimated in our work. We conclude that our financial model can be applied to a number of different scenarios with some degree of confidence in the final costing.

As TCI defines the initial cost of a plant, another entry of cost called annual operating Cost (C_o) accounts for the annual costs directly related to the production. Among them, the most relevant entries are the cost of the raw materials and utilities. The C_o can be

divided in: Variable Production Cost (VPC), Fixed Charge (FC), Plant Overhead Cost (POC) and General Expenses (GE). The VPC are directly associated with the production and they includes expenditures for: raw materials, utilities, solvents, catalysts, operating labour, operating supervision, maintenance and repairs, operating supplies, laboratory charges, patents and royalties. The FC are costs that do not change with the amount of production; they are a direct function of TCI and comprise financing, local taxes and property insurance. The POC refers to costs not related to the production and they account mainly for payroll overhead, packaging, medical services, safety, protection and storage facilities. Finally, the GE accounts for administrative costs, distribution and marketing expenses, research and development costs. Peters et al. (2004) suggest how to calculate the annual operating costs as displayed in Table 5.8. The percentages shown in Table 5.8 are the average percentages over a range suggested. The methodology suggested by Peters et al. (2004) to calculate the TCI (see Table 5.7) and the C_o (see Table 5.8) is in agreement with the report published by the Global CCS Institute in March 2013 on *"Towards a common method of cost estimation for CO_2 capture and storage at fossil fuel power plants"*.

Table 5.8 Annual operating cost (C_o) (Peters et al., 2004)

Variable production cost (VPC)	
Raw materials and utilities	
Operating labour (OL)	
Operating supervision (OS)	15%OL
Maintenance and Repairs (MR)	2%DPE
Operating Supplies	15%MR
Laboratories Charges	15%OL
Patents and Royalties	0.5%Sales
Fixed charges (FC)	
Financing	5%TCI
Local Taxes	2%FCI
Property Insurance	1%FCI
Plant Overhead costs (POC)	
60%(OS+OL+MR)	
General Expenses (GE)	
Administrative costs	20%OL
Distribution and marketing costs	2%Sales
Research and development costs	2%Sales
TOT annual operating cost (C_o)	**VPC + FC + POC + GE**

The annual operating labour was calculated assuming an annual average salary equal to 40000 $, as an average between common and skilled labour, multiplied for the number of employees, equal to 40 in this scenario. The latter value comes from a graph (Peters et al., 2004) that expresses the number of employees as a function of the plant capacity assuming 8 hour – shift system.

The cost of the raw materials refers to the cost of the natural gas. Its price is subjected to high fluctuations depending on the location and the type of the contracts stipulated. For this reason in our analysis the fuel price was varied from 3.8 $/GJ to 8.8 $/GJ.

The utilities costs are related mainly to the cost of the cooling water and the solid metal oxide make-up. A reasonable price of 0.05 $/m^3 was assumed for the cooling water (Peters et al., 2004). For NiO solid particles supported with Al_2O_3 a cost of 15.3 $/kg was assumed. This cost comprises raw material and manufacture cost as reported by Abad et al. (2007) and Lyngfelt and Thunman (2005). In our analysis the NiO make-up varies depending on the metal oxide lifetime as explained later. Furthermore, the cost of the initial total solid inventory is taken into account as an extra cost in the annual variable production costs spreading its cost over the lifetime of the power plant. Table 5.9 summarises the annual raw material and utilities expenditures assuming 24 h and 330 days of operation (i.e. 90% of capacity factor). The cost related to the disposal of the spent nickel carrier was not included in the economic analysis.

Table 5.9 Annual cost of raw material and utilities

	Gas Natural		Cooling Water		NiO make up
Cost ($/kg)	variable	Cost ($/m^3)	0.05	Cost ($/kg)	15.3
Flow-rate (kg/h)	36000	Flow-rate (m^3/s)	2.2675	Flow-rate (kg/h)	variable
Cost ($/year)	variable	Cost ($/year)	**$ 3,232,548**	Cost ($/year)	variable

Another important item to consider in the cost analysis is the depreciation. Depreciation refers to two concepts: decrease in value of a facilities and their amortisation. All physical facilities deteriorate and lower in effectiveness with time; thus, the value of a facility decreases. Wear and tear, corrosion and deterioration are all causes of depreciation (Peters et al., 2004). The equipment and other material objects including a

manufacturing plant require an initial investment that must be paid back. For this reason, depreciation is claimed as a manufacturing expense. The total cost due to depreciation is equal to the initial value of the property minus its final value at the end of the period at which depreciation is calculated, which usually corresponds to the lifetime of the plant. In other terms, the total cost due to depreciation corresponds to the FCI minus the cost of the purchased land; the latter as well as the WC are recovered at the end of the lifetime of the plant since they can be sold to other investors.

Depreciation is considered as an annual operating cost and it is an important entry of cost since it results in a reduction in income tax payable in the period in which it is charged (Peters et al., 2004). The total depreciation has a fixed value at fixed FCI and lifetime of the plant but the way how it is distributed in the years can change. From the investor's point of view, it is preferable to receive benefits such as tax savings sooner rather than later; from the federal government's point of view, it is preferable to receive tax revenues sooner rather than later. For the aforementioned reasons, there are different ways to apply depreciation depending on the government policy in every specific country.

The two main methods to apply depreciation are: the *straight-line method* and the *Modified Accelerated Cost Recovery System* (MACRS). In the first method the annual depreciation, *dj*, is equal to the FCI divided by the lifetime of the plant; thus, its value is constant year by year. In the second method, used for most economic evaluations, the annual depreciation changes every year and different recovery period can be selected (up to 20 years); specifically, it is calculated every year as twice the average rate of recovery on the remaining un-depreciated balance for the full recovery period (Peters et al., 2004). More details on how the MACRS depreciation is calculated are reported by Peters et al. (2004). In the present work, we apply the MACRS method over a period of 16 years.

Along with the annual operating costs, annual revenues (S_j) form a part of the cost analysis of a project. The annual revenues of the CLC power plant come from the annual sales of the net electricity generated (≈ 260 MW for the plant under study) and their amount depends on the price at which the electricity is sold expressed in \$/kWh. This aspect will be explained in detail in Section 5.4. Total capital investment, annual

operating cost, depreciation and incomes define the cash flow of a project as shown in Fig. 5.2.

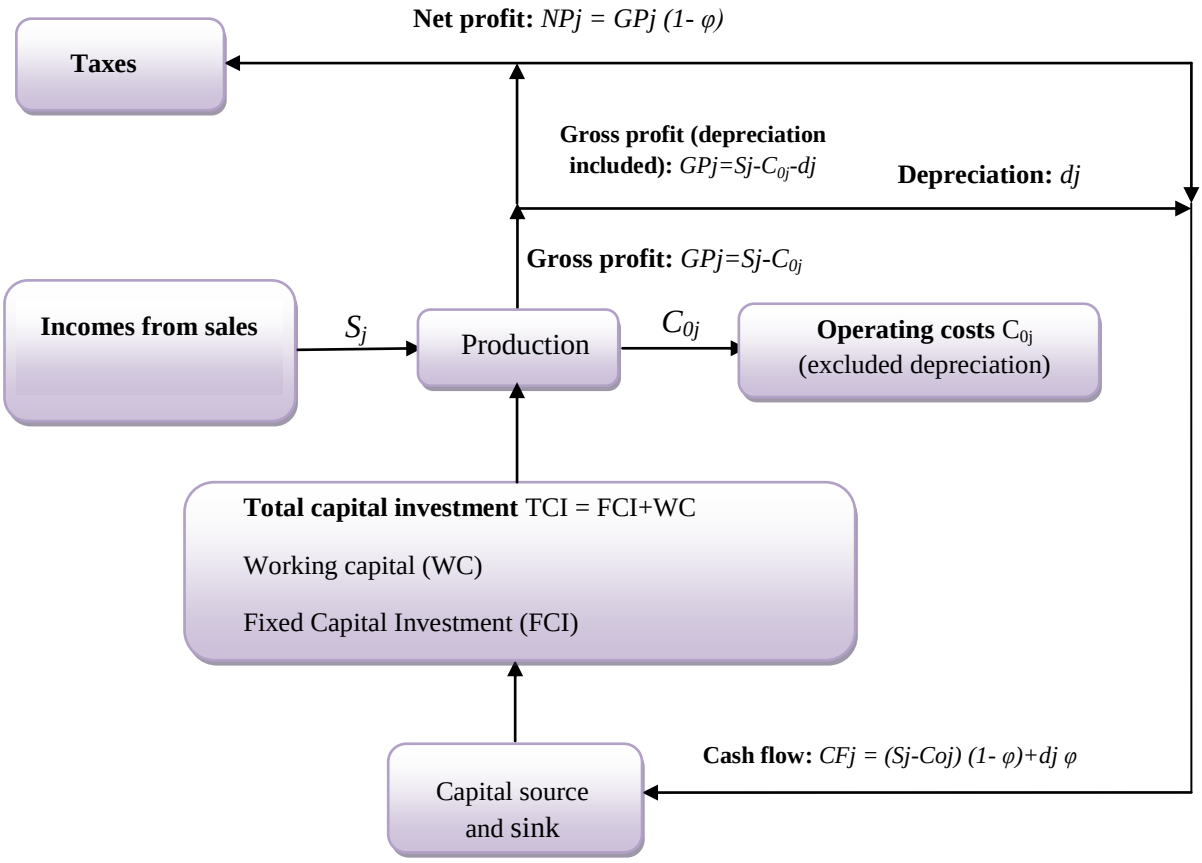

Fig. 5.2 Cash flow sketch

The annual gross profit with depreciation included, GP_j, is defined as follows:

$$GP_j = S_j - C_{0j} - d_j \tag{5.17}$$

where j is the generic year. The net profit, NP_j, is the amount retained of the profit after income taxes have been paid, expressed as follows:

$$NP_j = GP_j(1 - \varphi) \tag{5.18}$$

where φ is the fractional income tax rate. The income tax rate depends on the taxable income but it is common in preliminary cost analysis to use a fixed value equal to 35% (Peters et al., 2004). The annual cash flow, CF_j, resulting from process operations, is expressed as follows:

$$CF_j = NP_j + d_j \quad (5.19)$$

It is worthy noticing from Eqs. 5.17 - 5.19 how depreciation results in tax savings for the investor.

The sum of all the annual cash flows over the life cycle of a project defines the cumulative cash flow, which represents the starting point to make a profitability analysis of a project.

5.3.1 Inflation

Inflation is an increase in prices of goods and services over time and affects the amount of money required to purchase goods and services. The effect of inflation on the price of a service or product is reported by Peters et al. (2004) as follows:

$$Price\ at\ j\ years = (price\ at\ 0\ years)(1 + i')^j \quad (5.20)$$

where *i'* is the annual rate of inflation and *j* is the generic year. The inflation has an impact on all the entries of cost excluding depreciation. For this reason, we apply an inflation rate on the TCI, the annual operating costs (depreciation excluded) and the revenues. Although inflation changes year by year, we assume a constant inflation rate equal to 1.2%, which represents the UK inflation rate updated to the end of 2014.

5.3.2 Time value of money

The *time value of money* refers to the capability of the money to make other money through investments, for example, in saving accounts, stocks, bonds or projects. The effect of the aforementioned process is that an amount of money at the present is worth a greater amount of money in the future as expressed by the following relation:

$$Present\ amount\ of\ money = \frac{Future\ amount\ of\ money}{(1+i)^j} \quad (5.21)$$

where *i* is the interest rate. The time value of money is an important factor to be considered while comparing investments that require different amount of funds at

different time since the timing of the expenses and incomes could largely influence the present worth of such funds. For the abovementioned reason, Eq. 5.21, called discrete discounting interest formula, is applied in our work to derive the so-called *current cumulative cash flow* as shown in Section 5.4.

5.4 Profitability analysis and the Levelised Cost Of the Electricity (*LCOE*)

The cumulative cash flow is a tool that has to be used together with methods that calculate the profitability of a project. Different methods for calculating profitability of a project exist and among them two main categories can be defined: simple methods and accurate methods. The simple methods refer to those methods that do not consider the time value of money; among them the most applied are the *Return On Investment* (*ROI*), the *PayBack Period* (*PBP*) and the *Net Return* (*NR*). More details on how to apply the aforementioned methods are reported by Peters et al. (2004). On the other hand, the accurate methods refer to those methods that consider the time value of money and among them the most applied are the *Net Present Worth* (*NPW*) and the *Discount Cash Flow Rate of Return* (*DCFR*). The latter two methods are applied in our analysis since they include the largest number of factors influencing profitability.

The application of the profitability methods requires the introduction of a new concept called *Minimum Acceptable Rate of Return* (m_{ar}). The m_{ar}, expressed in percentage per year, is a rate of earning that must be targeted by an investment to be acceptable to the investor (Peters et al., 2004). Since any investor can earn money safely just investing in corporate bonds, government bonds and loans, a new project must guarantee a rate of earning that at least is equal to the highest rate of interest that the aforementioned safe investments can guarantee. Usually the value of m_{ar} is chosen as high as the project is risky and a typical range goes from 4% to 32% per year moving from safe investments to highly risky investments. Given a definition for m_{ar}, we express the first accurate method of profitability as follows:

$$NPW = \sum_{j=1}^{N} \frac{CF_j}{(1+m_{ar})^j} - \sum_{j=-b}^{N} \frac{TCI_j}{(1+m_{ar})^j} \tag{5.22}$$

The *Net Present Worth* (*NPW*) is the total of the present worth of all cash flows minus the present worth of all capital investments (Peters et al., 2004). The *NPW* is the amount of money earned over the repayment of all the investments and the earnings on the

investments at the earning rate equal to the m_{ar}. In Eq. 5.22, CF_j is the annual cash flow, TCI_j is the annual fraction of the TCI and N is the lifetime of the project. If the *NPW* is positive, then the project predicts a return at a rate greater than the m_{ar} selected; if the *NPW* is zero, then the project predicts a return at a rate that matches the earning rate chosen; if the NPW is negative, then the project predicts a return at a rate lower than the m_{ar} selected. The higher the value of *NPW* is, the more favourable the project is.

The *NPW* is helpful to introduce the most applied profitability method that is the *Discount Cash Flow Rate of Return* (*DCFR*). The *DCFR* refers to the value of the earning rate that sets the *NPW* equal to zero:

$$0 = \sum_{j=1}^{N} \frac{CF_j}{(1+DCFR)^j} - \sum_{j=-b}^{N} \frac{TCI_j}{(1+DCFR)^j} \tag{5.23}$$

The *DCRF* represents the highest earning rate at which the return of the investments is guaranteed. The higher the *DCRF* is, the more favourable the project is. Eq. 5.23 leads to the definition of *LCOE* generated.

Indeed, we can manipulate the CF_j term as follows:

$$0 = \sum_{j=1}^{N} \left[\frac{(S_j - C_{oj} - d_j)}{(1+DCFR)^j} (1-\varphi) \right] + \sum_{j=1}^{N} \frac{d_j}{(1+DCFR)^j} - \sum_{j=-b}^{N} \frac{TCI_j}{(1+DCFR)^j} \tag{5.24}$$

The annual revenue S_j is equal to the cost of the electricity sold multiplied by the net electricity generated; following the latter definition, after some manipulations of Eq. 5.24, the *LCOE* is finally derived:

$$LCOE = \frac{\sum_{j=-b}^{N} TCI_j (1+DCFR)^{-j} + \sum_{j=1}^{N} [(C_{oj} + d_j)(1+DCFR)^{-j}(1-\varphi)] - \sum_{j=1}^{N} [d_j (1+DCFR)^{-j}]}{\sum_{j=1}^{N} [P_{rj}(1+DCFR)^{-j}(1-\varphi)]} \tag{5.25}$$

where P_{rj} is the annual product rate expressed in kWh/year. The *LCOE*, expressed in \$/kWh, represents the price at which electricity must be generated from a specific source to break even over the lifetime of the project (see also Section 1.5). It represents the most important parameter to look at while comparing different power plant configurations either in terms of the type of fuel to burn or in terms of the best separation technologies for carbon capture to implement.

Given the TCI and C_o of the CLC power plant under study (see Table 5.7 – 5.8), the *LCOE* is calculated under the following conditions:

- Plant construction period equal to 3 years with FCI split over the 3 years as in 15%, 35% and 50%;
- Inflation rate, equal to 1.2% (UK value updated to the end of 2014), applied on annual operating costs (see Table 5.8), annual revenues and TCI (see Table 5.7);
- Income tax rate applied equal to 35%;
- Plant capacity factor applied equal to 90% (i.e. 24 h and 330 days);
- *DCFR* applied equal to 10%;
- Plant lifetime equal to 30 years;
- Depreciation based on MACRS method over 16 years;
- Plant operating rate applied: 50% the first year of production, 90% the second year and 100% from the third year;
- Cost of natural gas applied: from 3.8 $/GJ to 8.8 $/GJ;
- Solid particles make-up applied: dependent on the solid particles lifetime.

The annual metal oxide make-up cost ($/year) is defined as follows:

$$Make\ up\ cost = Metal\ oxide\ cost\ \frac{Total\ solid\ inventory}{particles\ lifetime} \tag{5.26}$$

The lifetime of the solid particles (LT_{MO}) is defined as the average time that a particle is under reaction, reduction or oxidation, in the system without any reactivity loss. Lyngfelt and Thunman (2005) reported a LT_{MO} for their NiO particles supported with Al_2O_3 equal to 4000 h. Fig. 5.3 shows the change in *LCOE* varying the fuel price from 3.8 $/GJ to 8.8 $/GJ (LHV basis) under two different conditions: 4000 h of metal oxide LT_{MO} and no solid make-up (ideal case).

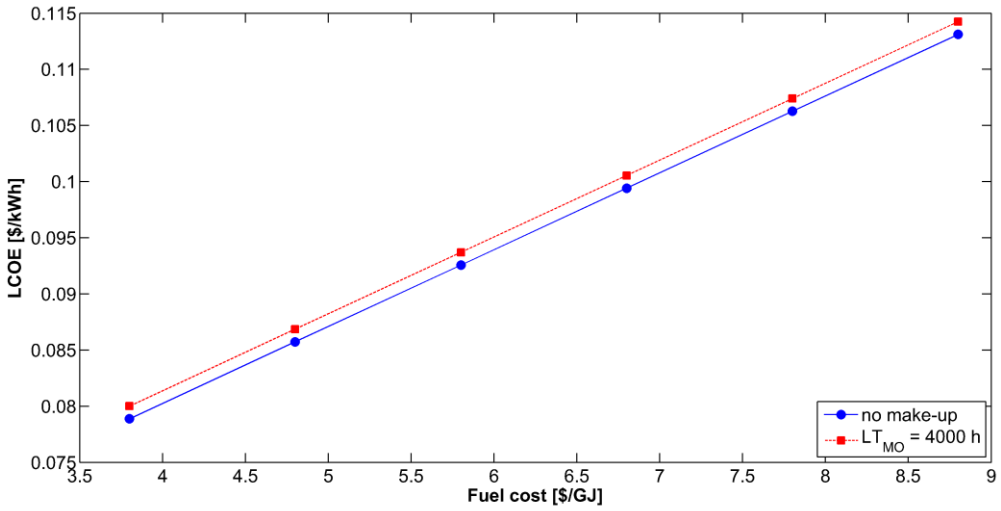

Fig. 5.3 *LCOE* vs. Fuel cost

Depending on the fuel price, the increase in *LCOE* due to a finite LT_{MO} of the solid particles ranges from 1 to 1.43%. Therefore, if a metal oxide can reach a LT_{MO} of thousands of hours, its cost does not seem to represent a limitation to the development of the CLC technology.

Fig. 5.4 shows the current cumulative cash flow with applied *DCFR* for the CLC power plant. Its trend is the same regardless the fuel and solid make-up cost selected since the *LCOE* is adjusted while varying the latter entries of cost to break even over the plant lifetime. Table C.1 (see Appendix C) displays all the entries of costs year by year to derive the cash flow shown in Fig. 5.4.

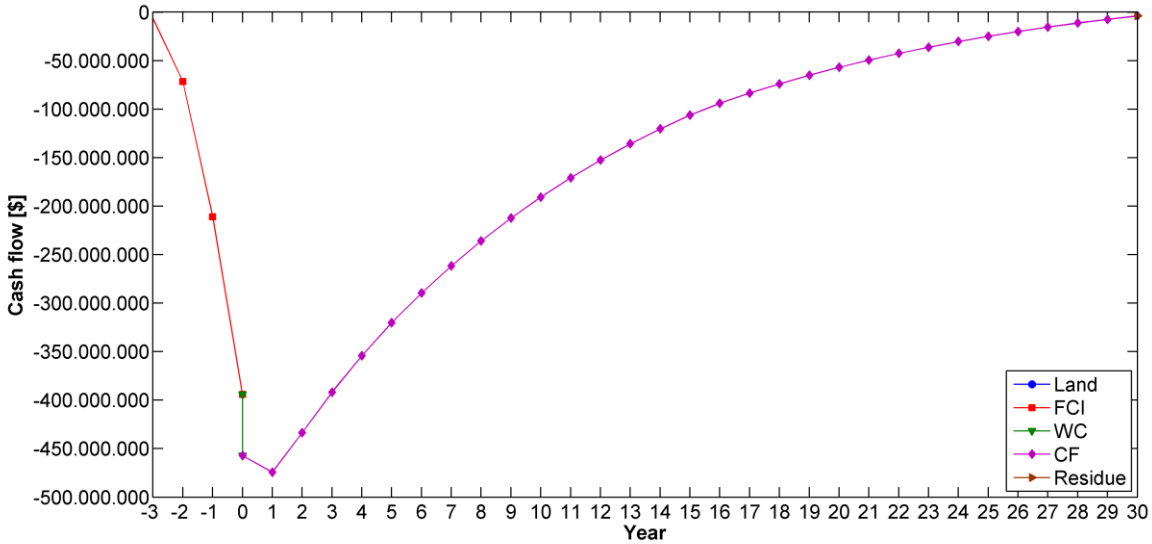

Fig. 5.4 Current cumulative cash flow with *DCFR*

In the literature, the *LCOE* is usually expressed according to the following relation:

$$LCOE = \frac{\frac{CAPEX}{CRF} + OPEX}{W_{net} POT} \quad (5.27)$$

with *CRF* defined as below:

$$CRF = \frac{(DCFR+1)^N - 1}{DCFR(DCFR+1)^N} \quad (5.28)$$

In Eq. 5.27, *CAPEX* refers to the TCI, expressed in $, *OPEX* refers to the mean annually operating costs, expressed in $/year, W_{net} is the net electricity produced, expressed in kW, *POT* is the capacity factor or plant operating time, expressed in h/year, *CRF* is the recovery factor (also called continuous discounting factor) over a plant lifetime of *N* years, expressed in year.

Eq. 5.27 is a simplified formula to calculate *LCOE* that does not take into account depreciation, inflation and income tax rate. Eq. 5.27 avoids the need to calculate the current cumulative cash flow to have an initial rough estimation of the *LCOE*. Eq. 5.27 is also applied in our calculation to quantify the difference with the more accurate Eq. 5.25. Depending on the fuel price, the *LCOE* calculated with Eq. 5.27 is from 7 to 11% lower than the one derived from Eq. 5.25. When inflation, depreciation and income tax rate are nullified, the two formulas (i.e. Eq. 5.25 and Eq. 5.27) lead to the same results.

5.4.1 Effect of the LT_{MO} on LCOE

A solid particles lifetime equal to 4000 h, as reported by Lyngfelt and Thunman (2005), is a prevision based on the loss of fines during their tests (0.0023% per hour). None of the CLC pilot plant was run for 4000 h and not all the metal oxide materials present the same durability, reactivity and mechanical strength. For the latter reasons, an economic sensitivity analysis has to be carried out.

Fig. 5.5 shows how the *LCOE* is affected by the LT_{MO} of the metal oxide at different fuel prices.

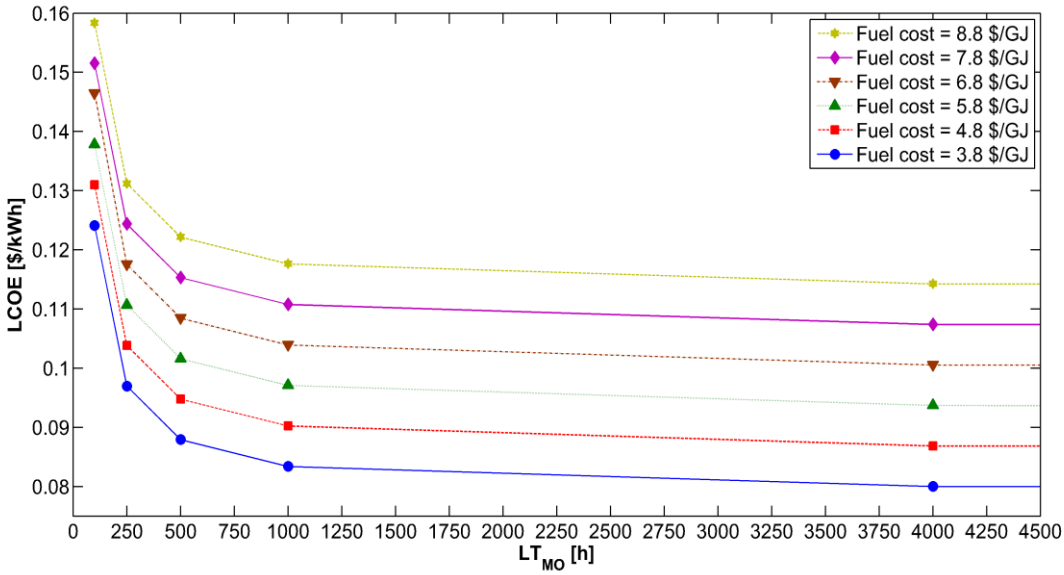

Fig. 5.5 *LCOE* vs. LT_{MO} at different fuel prices

The lifetime of the solid material influences greatly the *LCOE*; indeed, the reduction of the LT_{MO} down to 100 h causes an increase in the LCOE from 40 to 57% depending on the fuel price.

The trends shown in Fig. 5.5 can be used to make an actual comparison between CLC and other carbon capture technologies based on the main parameter that matters: the cost of the electricity generated. Indeed, Fig. 5.5 is the result of all the parameters affecting the economics of the plant: from the kinetics and hydrodynamics inside the reactors to the entries of costs of the plant and its cost factors.

For instance, Mores et al. (2014) reported a *LCOE* for a NGCC power plant working with MEA absorption post combustion technology equal to 77.5 $/MWh. In Mores et al.'s (2014) work, the *LCOE* was calculated under the following conditions:

- Fuel price equal to 3.318 $/GJ;
- DCFR equal to 8%;
- Capacity factor equal to 90%;
- Plant lifetime equal to 25 years;
- No income tax rate, depreciation and inflation applied.

Applying the same conditions to this work, it was found that 500 h of metal oxide lifetime are needed to get the same *LCOE*. Higher particles lifetime would make the

CLC technology more favourable than MEA absorption post combustion based power plants. Therefore, assuming 4000 h as LT_{MO} of the solid metal oxide particles involved, we can state that the NGCC power plant with the CLC technology employed exhibits a real advantage compared to a post combustion configuration with MEA.

The trends of Fig. 5.5 can be derived for different solid materials to compare them and understand which one leads to lower *LCOE*. Different metal oxides will produce different trends of *LCOE* vs. particles LT_{MO} since they influence differently the plant capital costs, the operating costs and the revenues as explained below:

- Different solid materials have different kinetic rates that lead to different solid inventories required to get full gas conversion; this aspect influences greatly the reaction volumes and so the total capital investment;
- Different solid materials have different oxygen carrier capacities; since there is a maximum flow-rate that can be circulated between the riser and the fuel reactor, the maximum allowed ratio solid flow-rate/solid stoichiometric flow-rate changes with the oxygen carrier; this aspect leads to different percentages of solid conversion inside the reactors and so to different kinetic rates and solid inventories, eventually affecting the capital costs;
- Different solid materials have different enthalpies of reaction that influence the operating conditions of the whole plant and so the production rate in terms of electricity generated at the turbines;
- Not all the metal oxides can handle the same riser operating temperature (e.g. 1200 °C); this aspect influences largely the amount of electricity generated since the air Turbine Inlet Temperature (TIT) has one of the most important impact on the thermal efficiency of the process; Wolf et al. (2005) reported a drop in thermal efficiency equal to 4% due to a decrease in the TIT of 200 °C (i.e. from 1200 °C to 1000 °C);
- Different solid materials have different prices leading to a different impact of the solid make-up expenditures on the annual operating costs.

For example, when we consider Fe_2O_3 as oxygen carrier, it is expected from the literature a kinetic rate much lower, even 5-6 times depending on the inert support applied (Mattisson et al., 2003; Abad et al., 2007; Galinsky et al., 2013), than the case applying NiO as oxygen carrier under similar operating conditions. In addition, the

oxygen carrier capacity of the Fe_2O_3 is lower (about 6 times) compared to the NiO oxygen capacity. Thus, since there is also a limitation in the maximum value of G_s to be applied to guarantee the feasibility of the operations, the maximum allowed solid circulating flow-rate for the Fe_2O_3 carrier leads to a ratio solid circulating flow-rate/solid stoichiometric flow-rate lower than the case under NiO as oxygen carrier.

The latter aspect affects largely the average solid conversion inside the reactors, which is higher than the NiO scenario, and thus negatively the kinetic rates and, in cascade, the minimum solid inventory required (see Section 4.3).

All the previous factors drive to the conclusion that the application of Fe_2O_3 as oxygen carrier leads to a required minimum total solid inventory much higher than the NiO scenario (roughly from 10 to 60 times higher depending on the inert support applied and the hydrodynamic conditions). Thus, the total capital investments, which are mostly affected by the cost of the CLC unit, are expected to be much higher than the case studied in our work.

On the other hand, the cost of Fe_2O_3 is lower on average than the NiO cost, even 100 times (Abad et al., 2007), so reducing drastically the annual expenditures for the solid make-up. Thus, an economic analysis, producing a graph similar to Fig. 5.5, is needed to evaluate if and under which conditions of LT_{MO} the use of Fe_2O_3 would lead to advantageous values of *LCOE* compared to the NiO scenario.

The same approximate analysis can be carried out for CuO oxygen carrier. Compared to the NiO case, the application of CuO is expected to give total solid inventories and thus TCI of the same order of magnitude since both kinetic rate and oxygen carrier capacity are comparable with those associated with NiO.

The drawback of employing CuO is related to a limitation in the maximum reaction temperature that this material can handle (see Section 1.6.1.3) leading to a lower air turbine inlet temperature than the NiO case; the latter aspect affects widely and negatively the efficiency of the process (Wolf et al., 2005), so decreasing the annual revenues.

On the other hand, the cost of CuO is lower on average than the NiO cost, about 10 times (Abad et al., 2007), so reducing the annual operating costs due to the solid make-up. Once again, a full economic evaluation would give the answer if and under which conditions of LT_{MO} the use of CuO would be beneficial in terms of *LCOE* compared to the NiO scenario.

5.4.2 Sensitivity analysis on the TCI, operating costs and thermal efficiency

The *TCI* and the operating costs of the CLC power plant were estimated assuming, for each entry of cost, average percentages suggested by Peters et al. (2004) (see Tables 5.7 – 5.8). Based on the latter assumptions, Fig. 5.5 was obtained consequently. However, different uncertainties might be present in the system: from the actual size and cost of the equipment to the percentages applied to calculate the entries of cost. To account for all these potential uncertainties, +/- 20% of variation was applied on the *TCI* and the operating costs. The impact of the applied change on the *LCOE* was calculated consequently. Fig. 5.6 shows the change in the *LCOE* while varying the lifetime of the solid particles for different fuel prices and *TCI*.

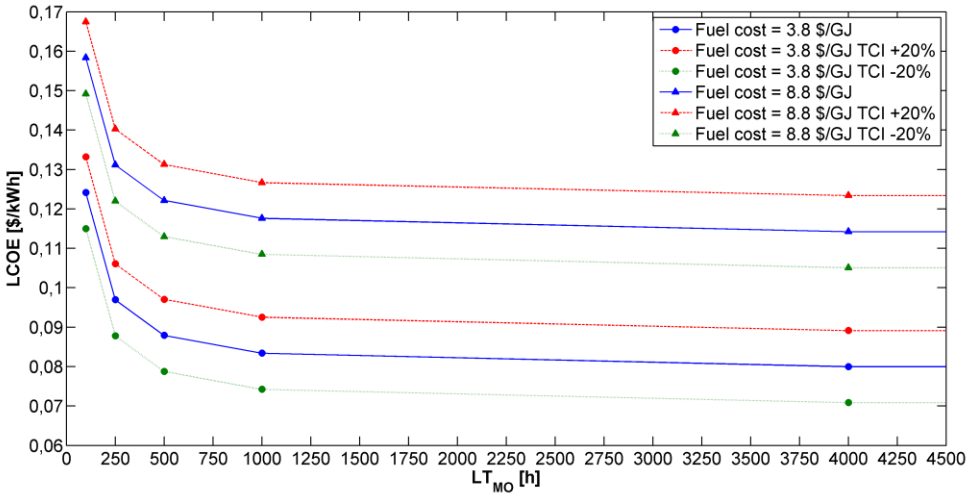

Fig. 5.6 *LCOE* vs. LT_{MO} at different fuel prices and *TCI*

Compared to the base-case, an increase of 20% in the *TCI* determines an increase in the *LCOE* ranging from 7.3 to 11.6% at a fuel price of 3.8 $/GJ and from 5.8 to 8.1% at a fuel price of 8.8 $/GJ depending on the LT_{MO}. The opposite effect occurs when *TCI* is reduced by 20%. Fig. 5.7 shows the change in the *LCOE* while varying the lifetime of the solid particles for different fuel prices and operating costs (C_o).

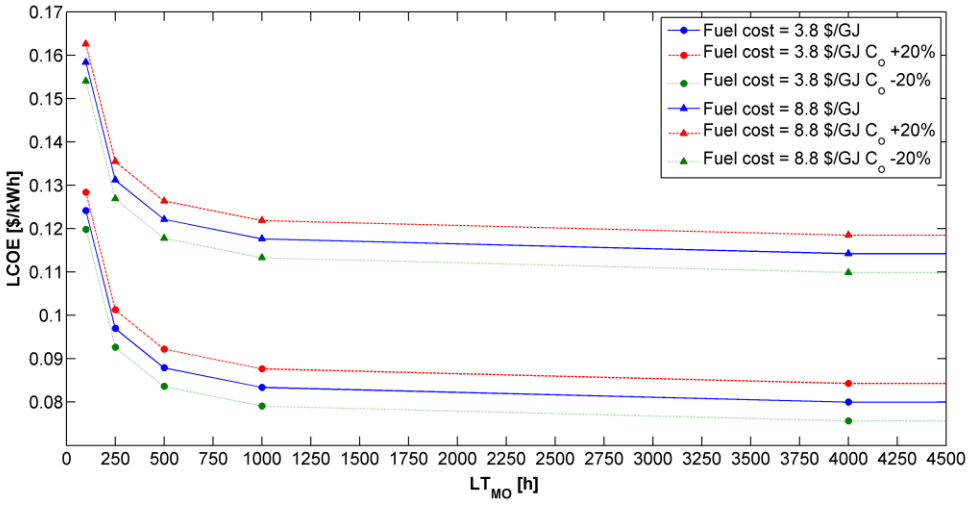

Fig. 5.7 *LCOE* vs. LT_{MO} at different fuel prices and C_o

Compared to the base-case, an increase of 20% in C_o determines an increase in the *LCOE* ranging from 3.4 to 5.5% at a fuel price of 3.8 $/GJ and from 2.7 to 3.8% at a fuel price of 8.8 $/GJ depending on the LT_{MO}. The opposite effect occurs when C_o is reduced by 20%.

Another uncertainty concerns the thermal efficiency of the power plant. Indeed, during the operations, a change in the mechanical and/or isentropic efficiency of the machineries, as well as heat losses can lead to a reduction in the thermal efficiency of the process.

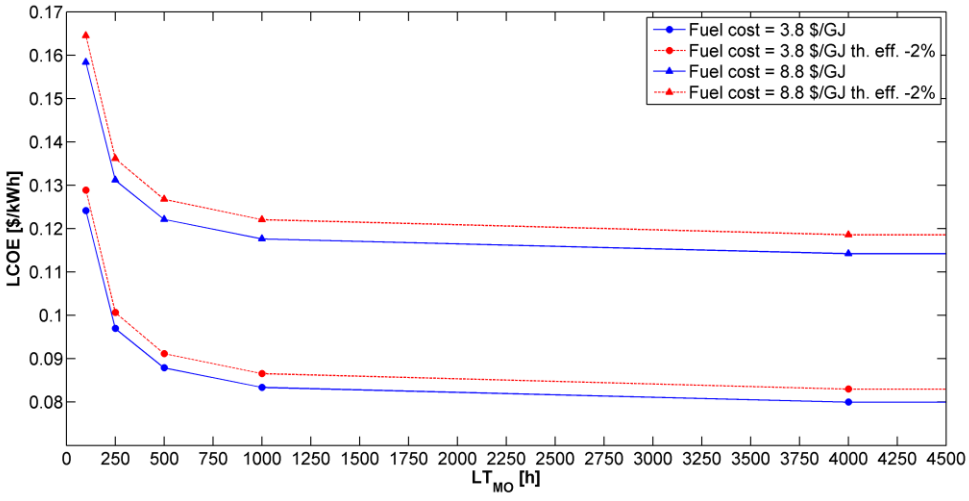

Fig. 5.8 *LCOE* vs. LT_{MO} at different fuel prices and thermal efficiency

Fig. 5.8 shows the change in the *LCOE* while varying the lifetime of the solid particles for different fuel prices and thermal efficiency. Compared to the base-case, a decrease

of 2% in the thermal efficiency determines an increase in the *LCOE* around 3.8% under all different fuel prices and LT_{MO}.

The outcomes from Figs. 5.6 - 5.8 highlight the dominant role of the LT_{MO} in affecting the *LCOE* over all the potential inaccuracies in all the entries of cost and energy losses. Indeed, a decrease in the LT_{MO} causes an increase in the *LCOE* ranging from 40 to 57% depending on the fuel price, which is higher than that resulting from different *TCI*, C_o and thermal efficiency applied (Figs. 5.6 - 5.8).

In Section 5.4.1, the CLC power plant was compared to a MEA carbon capture solution (Mores et al., 2014) and a value of 500 h of metal oxide lifetime was found to get the same *LCOE*. Thus, we concluded that higher particles lifetime would make the CLC technology more favourable than the MEA solution since they would lead to a reduction in the *LCOE*. Table 5.10 exhibits the lifetime of the metal oxide needed to get the same *LCOE* reported by Mores et al. (2014) when uncertainties on *TCI* and C_o are taken into account.

Table 5.10 LT_{MO} under different uncertainties on the entries of cost applied

	LT_{MO} [h]
Base case (see Section 5.4.1)	500
***TCI* +20%**	3000
***TCI* -20%**	270
C_o +20%	900
C_o -20%	320

Assuming that the metal oxide particles can reach a lifetime of 4000 h (Lyngfelt and Thunman, 2005), it was concluded that the CLC solution resulted more favourable than the MEA solution also in the case of additional costs considered for *TCI* and C_o (Table 5.10).

Chapter 6

Conclusions and future work

This chapter presents the conclusions achieved by our study summarising the main findings of each chapter and addressing the future work.

6.1 Summary of conclusions

Chapter 1 set the motivations of our research such as responding to the increase in the electricity demand while reducing the CO_2 emissions in the atmosphere and it addresses to the CLC technology. This chapter described how the CLC technology applied to fossil fuel power plants represents a viable solution to capture CO_2, given its potential advantages compared to the well-known state of the art technologies in reducing the number of separation units and the utilities need while increasing the plant thermal efficiency. Several past works on CLC are revised highlighting the main features of each aspect of the CLC process: solid oxygen carriers, experimental findings from CLC pilot plants, kinetic and hydrodynamic models of the CLC reactors, power plant configurations and thermal efficiency estimations. Given that, the gap in the literature is pointed out and the novelty of our work presented: linking the kinetic and hydrodynamic phenomena of CLC to the cost of the electricity generated. The latter is carried out employing Aspen Plus software, properly linked with FORTRAN subroutines for the kinetics implementation and Excel subroutines for the hydrodynamics and cost model implementation. An NGCC power plant with CLC technology integrated represented our case study.

Chapter 2 described a macro scale fuel reactor model implemented in Aspen Plus. The model has a multi stage structure composed of several sub-reactors (PFRs and CSTRs); a FORTRAN subroutine is introduced to implement the kinetics while different Excel spreadsheets are linked to Aspen Plus to mimic the hydrodynamics of the reactor. The first step in the development of the model concerned the determination of the right number of stages to apply. A suitable number of stages, equal to 5, was chosen and a sensitivity analysis based on different kinetic rates and solid inventories was carried out to evaluate the rightness of the relations employed and considerations made. The model responded as expected to the change in the operating variables and it was considered qualitatively suitable to mimic the behaviour of a bubbling bed despite the assumptions

made. The second step in the development of the model concerned the determination of the correct amount of solid inventory needed to achieve a desired gas conversion. For this reason, the model was further investigated in Chapter 3 to address to quantitative improvements.

Chapter 3 focused on the improvement of the bubbling bed model to target the main outcome of interest: the gas conversion inside the fuel reactor. This work was undertaken making use of a CFD analysis. A micro scale model based on Eulerian – Eulerian approach was developed in MFIX environment. Two models for CLC bubbling bed, one at macro-scale (Aspen Plus) and one at micro-scale level (CFD) were compared. Based on CFD simulations, a new division of the number of stages in Aspen Plus was introduced together with a variable bubble diameter to capture the phenomena occurring at the bottom of the bed. The methane mass fraction trends along the bed and the outlet gas conversions were evaluated at different kinetic rates, inlet superficial gas velocities and solid inventories. Despite the construction of the multi-stage macro-scale model is based on idealised hydrodynamic and kinetic phenomena, the trends and the overall results from the two models were comparable. The multi-stage model implemented in Aspen Plus could capture the influence of the kinetics, superficial gas velocity and solid inventory on the gas conversion. A new division of the stages that models better the bottom of the fuel reactor reduced the gap between the macro-scale and micro-scale model. The initial split of the bubble and the emulsion phase in Aspen Plus model together with the absence of gas distributor modelling were considered responsible for the residual gap between the two models. It was believed that a 3D modelling of a gas distributor at micro-scale level might enhance the match between the two models since bubbles' formation and diameter are affected by the distributor design. However, the difference in the outlet gas conversion between the two models was evaluated with good confidence for engineering purposes. Consequently, the improved fuel reactor macro-scale model was considered satisfactory to be embedded into a fuel power plant simulation.

Chapter 4 presented the completion of the CLC unit. A freeboard model is added to complete the fuel reactor and a model for the riser is developed. Different CLC power plant configurations for energy production were implemented in Aspen Plus under both atmospheric and pressurised conditions. The variables involved in the optimisation of

the operating conditions of the two interconnected fluidised beds were investigated. The amount of solid inventory in the two reactors, the average solid conversion, the degree of oxidation of the solid particles at the riser exit and the solid circulating flow-rate greatly affect the gas conversion and thus they were optimised. Since the solid material represents an important cost for the CLC technology, an analysis of the minimum total solid inventory in the reactors to achieve almost full methane conversion was carried out. The system composed of the two fluidised bed reactors was embedded in a NGCC power plant: the overall net thermal efficiency of the plant was estimated for atmospheric and pressurised conditions. It was found that working with adiabatic reactors at pressurised conditions led to the highest thermal efficiency, equal to 52.04%, with about 3% in CO_2 capture energy penalties, compared to an NGCC plant without CO_2 capture, and 97% of CO_2 capture efficiency with zero atmospheric CO_2 emissions.

Chapter 5 presented a full economic analysis of the NGCC-CLC power plant exhibiting the highest thermal efficiency. A cost model was developed in Excel and properly linked with Aspen Plus. The plant equipment cost was evaluated and consequently the Total Capital Investment calculated. All the entries of cost were defined and a cash flow was generated under specific assumptions. The *LCOE* was calculated and the impact of the metal oxide lifetime on the *LCOE* was discussed. A comparison between the CLC technology and a post-combustion technology with MEA was presented. The final finding was that the CLC power plant under study with solid particles lifetime higher than 500 h led to a lower cost of the electricity compared to the MEA solution. Moreover, a sensitivity analysis was carried out to evaluate the impact of a change in *TCI*, operating costs and thermal efficiency on the *LCOE*. Under the operating conditions applied and the metal oxygen carrier employed, we could state that CLC technology was more favourable than MEA absorption post combustion based power plant.

Overall, the goal of this work was successfully achieved. All the aspects of the CLC process were combined together to obtain a better understanding of the advantages and disadvantages of this technology, useful to address the future work as described below.

6.2 Future work

The logical sequence conducted in our work is recommended to be followed to make actual valuable comparisons among different CO_2 capture technologies and, with reference to CLC, also among different solid metal oxides. For this reason, the future work has to be addressed in improving each section of the research carried out.

The kinetics can be improved accounting for all the secondary reactions occurring in the reduction step: methane reforming catalysed by nickel, CO and H_2 formation and recombination. If the kinetic parameters for both reduction and oxidation of a metal oxygen carrier are available, they can be easily implemented in Aspen Plus leading to a more accurate kinetic model. For example, Iliuta et al. (2010) and Ortiz et al. (2011) reported a highly accurate kinetics of reduction of methane when NiO is employed; unfortunately, they did not present kinetic results for the oxidation reaction and for the latter reason their kinetic parameters could not be incorporated in our simulation.

The hydrodynamic model can be improved at each level: micro and macro scale. At micro scale (CFD), a 3D modelling of the gas distributor could enhance the accuracy of the results since the bubble's formation at the bottom of the fluidised bed can be captured more precisely and thus its effect on the gas conversion detected. Furthermore, the application of the Eulerian – Langragian approach in the freeboard region of the bubbling bed could give more information about the degree of gas conversion that occurs in that zone, helping also to choose more accurately the solid fraction decay constant in the macro scale model. At macro scale level several improvements could be made. Information on gas distributor would allow using different hydrodynamic models (see Sections 2.2 - 2.4) and comparing them either with CFD models or with experimental data, when available. The multi stage model structure could be also codified entirely e.g. in FORTRAN language to overcome the limited number of stages employed in our work driving to more precise outcomes. In the latter, a way to link Aspen Plus with a hydrodynamic model entirely developed in a different code would need to be found.

The considerations expressed for the fuel reactor are applicable also to the riser. In the latter, both experimental findings and micro scale models could help in calculating e.g. the gas–solid contact efficiency that affects largely the solid inventory (in our case we

assumed gas–solid contact efficiency equal to the unity lacking of additional information).

The CLC unit composed of an air reactor in fast fluidisation condition and a fuel reactor in bubbling conditions might be replaced with a different CLC configuration to study the impact of this change on the total solid inventory. For instance, Kolbitsh et al. (2009a, 2009b, 2010) proposed a different design for the two interconnected fluidised bed reactors. Specifically, in their work the riser was in the fast fluidisation regime whereas the fuel reactor was in the turbulent regime. The general concept concerns with the minimisation of the by-pass effect of the gas through the bubbles phase making use of a different hydrodynamics and reactor design.

In terms of power plant configurations, the CLC process could be improved carrying out a deep analysis of the HRSG; indeed in our work we used one level pressure but the operation can be conducted with two or three levels of pressure determining a slight increase in the thermal efficiency of the process.

Overall, all the variables of the process could be further optimised and refined. Different oxygen carriers could be employed, once their kinetic rates are known, to find out the best option in terms of *LCOE* to make the CLC technology stood out among all the other CO_2 capture technologies, traditional and not.

Appendix A

The CFD code employed is called MFIX (Multiphase Flow with Interphase eXchanges, (Syamlal et al., 1993)). MFIX is an open source multiphase flow solver designed to describe chemical reactions and heat transfer in dense or dilute fluid-solids flows. MFIX is written in FORTRAN and it is primarily designed to run on Linux operating system; its calculations provide time-dependent information on composition, temperature, pressure and velocity distributions in the reactors.

MFIX is composed of two main subdirectories: *model* and *post_mfix*. The subdirectory *model* contains the MFIX source files whereas the subdirectory *post_mfix* contains files for the post-processing programs. A third subdirectory, called *user subdirectory*, has to be created by the user to compile the MFIX code through a FORTRAN compiler and eventually generate an executable file *.exe*. This file can be executed either in serial or in parallel mode although the latter is preferred to speed up the calculations (in the latter case a number of processors to run must be selected). In the same user subdirectory, a file called *mfix.dat* has to be dragged from the *model* subdirectory. *Mfix.dat* file contains the simulation setup. In this file, the user defines the geometry of the computational domain, the number of computational cells, the parameters and all the initial and boundary conditions of interest. Furthermore, the user launches the set of PDEs of interest to be solved and additionally he can recall user-defined files to customise the simulation; in this respect, the list of subroutines that are most commonly modified by the user are described below:

- *calc_physprop.f* : in this file the fluid viscosity, wall heat transfer coefficient as well as the fluid and solids specific heat and thermal conductivity can be modified;
- *usr_rate.f* : in this file a user-defined kinetic rate and heat of reaction can be added;
- *body_force.inc* : in this file the gravitational force can be modified;
- *eosg.f* : in this file a different equation of state for the gas can be defined (by default the ideal gas law is applied);
- *tolerance.inc* : this file contains the tolerance used for judging the convergence and it can also be modified.

The file *.exe* is executed to run the simulation under the conditions specified in the *mfix.dat* file and in all the other files linked to it. As result of the simulation, different output files are created as listed below:

- *.LOG*: this file contains error messages, information on convergence and number of iterations about the output files being written; e.g. this file shows for every interval of time in which the PDEs are solved the total solid inventory in the reactor; if the latter is not preserved, the run diverges and time step size is reduced to obtain the convergence; if other errors occur, the simulation is aborted and the *.LOG* file exhibits the information useful to fix it;
- *.OUT*: this file contains a summary of the input specified by *mfix.dat* and it ensures that initial conditions, boundary conditions and internal surfaces, if present, are at the correct locations. Indeed, this file contains a map of all the computational cells and for each of them the initial and boundary conditions applied are highlighted;
- *.RES*: this file contains all the data required to restart a run but it is not directly accessible by the user;
- *.SPx*: these files contain the data for different field variables calculated during the run such as void fraction, ε_g, gas pressure, P_g, gas velocity vectors, U_g, V_g and W_g, solid velocity vectors, U_s, V_s and W_s, bulk solid density, ρ_s, gas temperature, T_g, solid temperature, T_s, gas mass fractions, Y_{gn}, solid mass fractions, Y_{sn}, granular temperature, Θ, reaction rates and turbulence quantities. These files are not directly accessible by the user.

All the results contained in the *.SPx* files can be analysed in three different ways. The first two ways are graphical; indeed, it is possible to run a graphical representation of the MFIX results executing either a program called “animate_mfix” or a program called “Paraview”. In this way, the user can visualise how the field variables change over the time and space while the simulation runs. The third mode to analyse the results refers to the post-processing program called “post_mfix”. This program extracts data, contained in the *.SPx* files, at any particular location in the flow field. It is possible to know values of the flow variables at a specific time or space as well as time average values over a specific time interval, space average values over a specific space interval or both averages simultaneously. The third approach was the most applied in our work since all the values of the variables of interest at any time and location can be exported in excel spreadsheets to be analysed. The post_mfix program allows also for calculating gas and

solid mass flow-rates as well as gas and solid species flow-rates in any direction. Examples of *mfix.dat*, *.OUT* and user defined *usr_rate.f* files are shown below.

A.1 Example of mfix.dat file

```
!
!  Bubbling Fluidized Bed Simulation fuel reactor
!
!  bub02 - uniform fluidization

!  CPU time on R10000 Octane - 2494 s, Storage = 1.34 Mb

! Run-control section

  RUN_NAME              = 'BUBfuelreactorkinetic'
  DESCRIPTION           = 'uniform fluidization'
  RUN_TYPE              = 'restart_1'
  UNITS                 = 'cgs'
  TIME                  = 2.0000                        !start time
  TSTOP                 = 10.0
  DT                    = 1.0E-4                        !time step
  DT_MAX                = 5.0E-4
  DT_MIN                = 1E-9
  Max_Inlet_vel_Fac     = 3
  MAX_NIT               = 1000
  NORM_G                = 0
  NORM_S                = 0

  MOMENTUM_Z_EQ(0)      = .FALSE.
  MOMENTUM_Z_EQ(1)      = .FALSE.
  ENERGY_EQ             = .FALSE.           !do not solve   energy eq
  SPECIES_EQ(0)         = .TRUE.               !do solve species eq
  SPECIES_EQ(1)         = .TRUE.                !do solve species eq
  CALL_USR              = .FALSE.

! Under relaxation factors
  UR_FAC(1) = 0.7  ! gas pressure
  UR_FAC(3) = 0.3  ! gas and solids u-momentum
  UR_FAC(4) = 0.3  ! gas and solids v-momentum

! Geometry Section

  COORDINATES           = 'cartesian'
  XLENGTH               =   35                             !diameter
  IMAX                  =   50                    cells in i direction
  YLENGTH               =   98                          !height
  JMAX                  =   140                 !cells in j direction
  NO_K                  = .TRUE.                 !2D, no k direction


! Gas-phase Section

  MU_g0                 = 2.27E-4             !constant gas viscosity

  MW_g(1) = 16.04246
  MW_g(2) = 18.01528
  MW_g(3) = 44.00980
  MW_g(4) = 28.01340

  NMAX_g = 4
```

```
  SPECIES_g(1) = "CH4"                SPECIES_ALIAS_g(1) = "CH4"
  SPECIES_g(2) = "H2O"                SPECIES_ALIAS_g(2) = "H2O"

  SPECIES_g(3) = "CO2"                SPECIES_ALIAS_g(3) = "CO2"
  SPECIES_g(4) = "N2"                 SPECIES_ALIAS_g(4) = "N2"

! Solids-phase Section

  RO_s                  = 3.446                      !solids density
  D_p0                  = 0.02                     !particle diameter
  e                     = 0.92           !restitution coefficient
  e_w                   = 0.99         !restitution coefficient wall
  Phi                   = 30.0           !angle of internal friction
  EP_star               = 0.45             !packed bed void fraction


  MW_s(1,1)= 74.69280
  MW_s(1,2)= 58.69340
  MW_s(1,3)= 101.96128

  MMAX = 1


  NMAX_s(1)      = 3

  SPECIES_s(1,1) = "NiO(cr)C"          SPECIES_ALIAS_s(1,1) = "NiO"
  SPECIES_s(1,2) = "Ni(cr)"            SPECIES_ALIAS_s(1,2) = "Ni"
  SPECIES_s(1,3) = "AL2O3(a)"         SPECIES_ALIAS_s(1,3) = "inert"


! Initial Conditions Section

    ! 1. bed
  IC_X_w(1)             =  0.0                   !lower of the domain
  IC_X_e(1)             =  35                ! 0 < x < 35, 0 < y < 45
  IC_Y_s(1)             =  0.0
  IC_Y_n(1)             =  45
                                          !initial values in the region
  IC_EP_g(1)            =  0.45                    !void fraction
  IC_U_g(1)             =  0.0                  !radial gas velocity
  IC_V_g(1)             =  @(36/0.45)           !axial gas velocity
  IC_U_s(1,1)           =  0.0                !radial solids velocity
  IC_V_s(1,1)           =  0.0                 !axial solids velocity

  IC_T_g(1)   = 1223.0 ! (K)
  IC_T_s(1,1) = 1223.0 ! (K)

  IC_X_g(1,1) = 0.0   ! CH4
  IC_X_g(1,2) = 0.0   ! H2O
  IC_X_g(1,3) = 0.0   ! CO2
  IC_X_g(1,4) = 1.0   ! N2

  IC_X_s(1,1,1) = 0.36 ! NiO
  IC_X_s(1,1,2) = 0.04 ! Ni
  IC_X_s(1,1,3) = 0.6  ! AL2O3

    !  2. Freeboard
  IC_X_w(2)             =   0.0                 !upper of the domain
  IC_X_e(2)             =   35             ! 0 < x < 35, 45 < y < 98
  IC_Y_s(2)             =   45
  IC_Y_n(2)             =   98

  IC_EP_g(2)            =   1.0
```

```
  IC_U_g(2)              =   0.0
  IC_V_g(2)              =   36
  IC_U_s(2,1)            =   0.0
  IC_V_s(2,1)            =   0.0

  IC_T_g(2)   = 1223.0 ! (K)
  IC_T_s(2,1) = 1223.0 ! (K)

  IC_X_g(2,1) = 0.0   ! CH4
  IC_X_g(2,2) = 0.0   ! H2O
  IC_X_g(2,3) = 0.0   ! CO2
  IC_X_g(2,4) = 1.0   ! N2

  IC_X_s(2,1,1) = 0.0  ! NiO
  IC_X_s(2,1,2) = 0.0  ! Ni
  IC_X_s(2,1,3) = 0.0  ! AL2O3


!  Boundary Conditions Section

      ! 1. Distributor flow
  BC_X_w(1)              =  0.0                 !gas distributor plate
  BC_X_e(1)              =  35                    ! 0 < x < 35, y = 0
  BC_Y_s(1)              =  0.0
  BC_Y_n(1)              =  0.0

  BC_TYPE(1)             = 'MI'                 !specified mass inflow

  BC_EP_g(1)             =  1.0
  BC_U_g(1)              =  0.0
  BC_V_g(1)              =  36
  BC_U_s(1,1)            =  0.0               !radial solids velocity
  BC_V_s(1,1)            =  0.0                !axial solids velocity
  BC_P_g(1)              =  1.0E6

  BC_T_g(1)          = 1223      ! (K)
  BC_T_s(1,1)        = 1223      ! (K)

  BC_X_g(1,1)        = 1.0          ! CH4
  BC_X_g(1,2)        = 0.0          ! H2O
  BC_X_g(1,3)        = 0.0          ! CO2
  BC_X_g(1,4)        = 0.0          ! N2

  BC_X_s(1,1,1)      = 0.0          ! NiO
  BC_X_s(1,1,2)      = 0.0          ! Ni
  BC_X_s(1,1,3)      = 0.0          ! AL2O3


      ! 2. Exit
  BC_X_w(2)              =   0.0                       !top exit
  BC_X_e(2)              =   35                  ! 0 < x < 35, y = 98
  BC_Y_s(2)              =   98
  BC_Y_n(2)              =   98

  BC_TYPE(2)             =  'PO'            !specified pressure outflow
  BC_P_g(2)              =  1.0E6


       ! 3. walls
  BC_TYPE(3)             = 'PSW'
  BC_X_w(3)              =  0.0
  BC_X_e(3)              =  0.0
  BC_Y_s(3)              =  0.0
```

```
  BC_Y_n(3)              =  98
  BC_Uw_g(3)             =  0.0
  BC_Vw_g(3)             =  0.0
  BC_hw_s(3,1)           =  0.0
  BC_Uw_s(3,1)           =  0.0
  BC_Vw_s(3,1)           =  0.0

  BC_Tw_g(3)   = 1223.0  ! (K)
  BC_Tw_s(3,1) = 1223.0  ! (K)

  BC_Hw_X_g(3,1) = 0.0       BC_C_X_g(3,1) = 0.0
  BC_Hw_X_g(3,2) = 0.0       BC_C_X_g(3,2) = 0.0
  BC_Hw_X_g(3,3) = 0.0       BC_C_X_g(3,3) = 0.0
  BC_Hw_X_g(3,4) = 0.0       BC_C_X_g(3,4) = 0.0

  BC_Hw_X_s(3,1,1) = 0.0     BC_C_X_s(3,1,1) = 0.0
  BC_Hw_X_s(3,1,2) = 0.0     BC_C_X_s(3,1,2) = 0.0
  BC_Hw_X_s(3,1,3) = 0.0     BC_C_X_s(3,1,3) = 0.0


  ! 4. walls
  BC_TYPE(4)             = 'PSW'
  BC_X_w(4)              =  35
  BC_X_e(4)              =  35
  BC_Y_s(4)              =  0.0
  BC_Y_n(4)              =  98
  BC_Uw_g(4)             =  0.0
  BC_Vw_g(4)             =  0.0
  BC_hw_s(4,1)           =  0.0
  BC_Uw_s(4,1)           =  0.0
  BC_Vw_s(4,1)           =  0.0

  BC_Tw_g(4)   = 1223  ! (K)
  BC_Tw_s(4,1) = 1223  ! (K)

  BC_Hw_X_g(4,1) = 0.0       BC_C_X_g(4,1) = 0.0
  BC_Hw_X_g(4,2) = 0.0       BC_C_X_g(4,2) = 0.0
  BC_Hw_X_g(4,3) = 0.0       BC_C_X_g(4,3) = 0.0
  BC_Hw_X_g(4,4) = 0.0       BC_C_X_g(4,4) = 0.0

  BC_Hw_X_s(4,1,1) = 0.0     BC_C_X_s(4,1,1) = 0.0
  BC_Hw_X_s(4,1,2) = 0.0     BC_C_X_s(4,1,2) = 0.0
  BC_Hw_X_s(4,1,3) = 0.0     BC_C_X_s(4,1,3) = 0.0

! CHEMICAL REACTION SECTION

  @(RXNS)

   Methane_Combustion { chem_eq = "CH4 + 4.0NiO --> 4.0Ni + 2.0H2O +
CO2"}


  @(END)

!
!  Output Control
!
  OUT_DT                 = 10.              !write text file BUB04.OUT
                                                !  every 10 s

  RES_DT                 = 0.1              !write binary restart file
                                             !  BUB03.RES every 0.1 s
```

```
  NLOG                  = 25                  !write logfile BUB04.LOG
                                                  !every 25 time steps

  FULL_LOG              = .TRUE.          !display residuals on screen


!SPX_DT values determine how often SPx files are written.  Here
BUB04.SP1, which
!contains void fraction (EP_g), is written every 0.01 s, BUB03.SP2,
which contains
! gas and solids pressure (P_g, P_star), is written every 0.1 s, and
so forth.
!
  SPX_DT(1)  = 0.05   ! EP_g
  SPX_DT(2)  = 0.05   ! P_g, P_star
  SPX_DT(3)  = 0.05   ! U_g, V_g, W_g
  SPX_DT(4)  = 0.05   ! U_s, V_s, W_s
  SPX_DT(5)  = 0.05   ! ROP_s
  SPX_DT(6)  = 0.05   ! T_g, T_s
  SPX_DT(7)  = 0.05   ! X_g, X_s
  SPX_DT(8)  = 0.05   ! theta
  SPX_DT(9)  = 100.   ! Scalar
  SPX_DT(10) = 0.05   ! Reaction Rates

  nRR = 1 ! Number of reaction rates to write to .SPA

!  The decomposition in I, J, and K directions for a Distributed
Memory Parallel machine

  NODESI = 2   NODESJ = 4   NODESK = 1

!  Sweep Direction

LEQ_SWEEP(1) = 'ISIS'
LEQ_SWEEP(2) = 'ISIS'
LEQ_SWEEP(3) = 'ISIS'
LEQ_SWEEP(4) = 'ISIS'
LEQ_SWEEP(5) = 'ISIS'
LEQ_SWEEP(6) = 'ISIS'
LEQ_SWEEP(7) = 'ISIS'
LEQ_SWEEP(8) = 'ISIS'
LEQ_SWEEP(9) = 'ISIS'
LEQ_IT(1) = 100
LEQ_IT(2) = 100
LEQ_TOL(1) = 1.0D-4
LEQ_TOL(2) = 1.0D-4
LEQ_TOL(3) = 1.0D-4
LEQ_TOL(4) = 1.0D-4
LEQ_TOL(5) = 1.0D-4
LEQ_TOL(6) = 1.0D-4
LEQ_TOL(7) = 1.0D-4
LEQ_TOL(8) = 1.0D-4
LEQ_TOL(9) = 1.0D-4
UR_FAC(2) = 0.4
DISCRETIZE(1) = 2
DISCRETIZE(2) = 2
DISCRETIZE(3) = 2
DISCRETIZE(4) = 2
DISCRETIZE(5) = 2
DISCRETIZE(6) = 2
DISCRETIZE(7) = 2
DISCRETIZE(8) = 2
DISCRETIZE(9) = 2
```

```
DEF_COR = .TRUE.

#_____________________________________________________________________________
__
THERMO DATA

CH4             g 8/99C  1.H  4.   0.   0.G   200.000  6000.000  B  16.04246 1
 1.91178600E+00 9.60267960E-03-3.38387841E-06 5.38797240E-10-3.19306807E-14 2
-1.00992136E+04 8.48241861E+00 5.14825732E+00-1.37002410E-02 4.93749414E-05 3
-4.91952339E-08 1.70097299E-11-1.02453222E+04-4.63322726E+00-8.97226656E+03 4
CO2             L 7/88C   1O   2    0    0G   200.000  6000.000  A  44.00980 1
 0.46365111E+01 0.27414569E-02-0.99589759E-06 0.16038666E-09-0.91619857E-14 2
-0.49024904E+05-0.19348955E+01 0.23568130E+01 0.89841299E-02-0.71220632E-05 3
 0.24573008E-08-0.14288548E-12-0.48371971E+05 0.99009035E+01-0.47328105E+05 4
H2O          L 5/89H   2O   1    0    0G 200.000  6000.000  A  18.01528      1
 0.26770389E+01 0.29731816E-02-0.77376889E-06 0.94433514E-10-0.42689991E-14 2
-0.29885894E+05 0.68825500E+01 0.41986352E+01-0.20364017E-02 0.65203416E-05 3
-0.54879269E-08 0.17719680E-11-0.30293726E+05-0.84900901E+00-0.29084817E+05 4
N2 REF ELEMENT G 8/02N  2.   0.   0.   0.G   200.000  6000.000  A  28.01340 1
 2.95257637E+00 1.39690040E-03-4.92631603E-07 7.86010195E-11-4.60755204E-15 2
-9.23948688E+02 5.87188762E+00 3.53100528E+00-1.23660988E-04-5.02999433E-07 3
 2.43530612E-09-1.40881235E-12-1.04697628E+03 2.96747038E+00 0.00000000E+00 4
NiO(cr)C        B   89NI 1.O  1.   0.   0.C   200.000  2228.000  C  74.69280 1
 7.14189288E+02-1.82136013E+00 1.69476820E-03-6.82322488E-07 1.00866137E-10 2
-2.42828596E+05-3.74557181E+03 6.39887637E+02-3.32219822E+00 6.45073892E-03 3
-5.50899949E-06 1.74671215E-09-1.25931429E+05-2.91203063E+03-2.88291192E+04 4
Ni(cr)          j12/76NI 1.   0.   0.   0.S   200.000  1728.000  B  58.69340 1
 4.74937907E+01-1.27190456E-01 1.36757995E-04-6.43326525E-08 1.12738627E-11 2
-1.30199931E+04-2.42569730E+02 2.16764993E+01-4.22985698E-02 2.46246101E-05 3
 0.00000000E+00 0.00000000E+00-6.09924048E+03-1.11681145E+02 0.00000000E+00 4
AL2O3(a)        coda89AL 2.O  3.   0.   0.S   200.000  1200.000  B 101.96128 1
 2.60994032E+00 3.76023553E-02-4.63474789E-05 2.73301680E-08-6.21672705E-12 2
-2.03702845E+05-1.83258490E+01-8.37648940E+00 1.09323686E-01-2.25731157E-04 3
 2.29482917E-07-9.22595951E-11-2.02316511E+05 2.94431298E+01-2.01539237E+05 4
```

A.2 Example of mfix.out file

```
1. RUN CONTROL

Run name(RUN_NAME): BUBFUELREACTORKINETIC
Brief description of the run (DESCRIPTION:UNIFORM FLUIDIZATION
Units (UNITS) : CGS
Start-time (TIME) =   2.0000
Stop_time (TSTOP) =   10.000
Time step (DT) =  0.10000E-03
Max time step (DT_MAX) =  0.50000E-03
Min time step (DT_MIN) =  0.10000E-08
Time step adjustment factor (DT_FAC) =  0.90000
Type of run (RUN_TYPE) : RESTART_1
(Initial conditions from the restart (.RES) file)

* Gas momentum equation-X is solved.

* Gas momentum equation-Y is solved.
* Gas momentum equation-Z is NOT solved.

* Solids-1 momentum equation-X is solved.

* Solids-1 momentum equation-Y is solved.

* Solids-1 momentum equation-Z is NOT solved.

* Energy equations are NOT solved.
```

```
* Gas Species equations are solved.

* Solids-1 Species equations are solved.

* User-defined subroutines are NOT called.

* Schaeffer frictional model is solved


2. PHYSICAL AND NUMERICAL PARAMETERS

Coefficient of restitution (C_e) =  0.92000
Angle of internal friction (Phi) =   30.000
Default turbulence length scale (L_scale0) =   0.0000
Maximum turbulent viscosity (MU_gmax) =  0.98765E+32
Reference pressure (P_ref) =   0.0000
Pressure scale-factor (P_scale) =   1.0000
Gravitational acceleration (GRAVITY) =   980.66
Under relaxation (UR_FAC) and Iterations in Leq solver (LEQ_IT):

                     UR_FAC  LEQ_IT  LEQ_METHOD  LEQ_SWEEP  LEQ_TOL    DISCRETIZE

  Fluid cont. and P_g  = 0.700   100        2         ISIS     0.1000E-03  Superbee
  Solids cont. and P_s = 0.400   100        2         ISIS     0.1000E-03  Superbee
  U velocity           = 0.300     5        2         ISIS     0.1000E-03  Superbee
  V velocity           = 0.300     5        2         ISIS     0.1000E-03  Superbee
  W velocity           = 0.500     5        2         ISIS     0.1000E-03  Superbee
  Energy               = 1.000    15        2         ISIS     0.1000E-03  Superbee
  Species              = 1.000    15        2         ISIS     0.1000E-03  Superbee
  Granular Energy      = 0.500    15        2         ISIS     0.1000E-03  Superbee
  User scalar          = 0.800    15        2         ISIS     0.1000E-03  Superbee

3. GEOMETRY AND DISCRETIZATION

Coordinates: CARTESIAN

X-direction cell sizes (DX) and East face locations:
I        1            2            3            4            5
DX   0.70000      0.70000      0.70000      0.70000      0.70000
X_E    0.0000       0.70000       1.4000       2.1000       2.8000

I        6            7            8            9           10
DX   0.70000      0.70000      0.70000      0.70000      0.70000
X_E    3.5000       4.2000       4.9000       5.6000       6.3000

I       11           12           13           14           15
DX   0.70000      0.70000      0.70000      0.70000      0.70000
X_E    7.0000       7.7000       8.4000       9.1000       9.8000

I       16           17           18           19           20
DX   0.70000      0.70000      0.70000      0.70000      0.70000
X_E    10.500       11.200       11.900       12.600       13.300

I       21           22           23           24           25
DX   0.70000      0.70000      0.70000      0.70000      0.70000
X_E    14.000       14.700       15.400       16.100       16.800

I       26           27           28           29           30
DX   0.70000      0.70000      0.70000      0.70000      0.70000
X_E    17.500       18.200       18.900       19.600       20.300

I       31           32           33           34           35
DX   0.70000      0.70000      0.70000      0.70000      0.70000
X_E    21.000       21.700       22.400       23.100       23.800
```

I	36	37	38	39	40
DX	0.70000	0.70000	0.70000	0.70000	0.70000
X_E	24.500	25.200	25.900	26.600	27.300

I	41	42	43	44	45
DX	0.70000	0.70000	0.70000	0.70000	0.70000
X_E	28.000	28.700	29.400	30.100	30.800

I	46	47	48	49	50
DX	0.70000	0.70000	0.70000	0.70000	0.70000
X_E	31.500	32.200	32.900	33.600	34.300

I	51	52
DX	0.70000	0.70000
X_E	35.000	35.700

Number of cells in X, or R, direction (IMAX) = 50
Reactor length in X, or R, direction (XLENGTH) = 35.000

Y-direction cell sizes (DY) and North face locations:

J	1	2	3	4	5
DY	0.70000	0.70000	0.70000	0.70000	0.70000
Y_N	0.0000	0.70000	1.4000	2.1000	2.8000

J	6	7	8	9	10
DY	0.70000	0.70000	0.70000	0.70000	0.70000
Y_N	3.5000	4.2000	4.9000	5.6000	6.3000

J	11	12	13	14	15
DY	0.70000	0.70000	0.70000	0.70000	0.70000
Y_N	7.0000	7.7000	8.4000	9.1000	9.8000

J	16	17	18	19	20
DY	0.70000	0.70000	0.70000	0.70000	0.70000
Y_N	10.500	11.200	11.900	12.600	13.300

J	21	22	23	24	25
DY	0.70000	0.70000	0.70000	0.70000	0.70000
Y_N	14.000	14.700	15.400	16.100	16.800

J	26	27	28	29	30
DY	0.70000	0.70000	0.70000	0.70000	0.70000
Y_N	17.500	18.200	18.900	19.600	20.300

J	31	32	33	34	35
DY	0.70000	0.70000	0.70000	0.70000	0.70000
Y_N	21.000	21.700	22.400	23.100	23.800

J	36	37	38	39	40
DY	0.70000	0.70000	0.70000	0.70000	0.70000
Y_N	24.500	25.200	25.900	26.600	27.300

J	41	42	43	44	45
DY	0.70000	0.70000	0.70000	0.70000	0.70000
Y_N	28.000	28.700	29.400	30.100	30.800

J	46	47	48	49	50
DY	0.70000	0.70000	0.70000	0.70000	0.70000
Y_N	31.500	32.200	32.900	33.600	34.300

J	51	52	53	54	55

DY	0.70000	0.70000	0.70000	0.70000	0.70000
Y_N	35.000	35.700	36.400	37.100	37.800
J	56	57	58	59	60
DY	0.70000	0.70000	0.70000	0.70000	0.70000
Y_N	38.500	39.200	39.900	40.600	41.300
J	61	62	63	64	65
DY	0.70000	0.70000	0.70000	0.70000	0.70000
Y_N	42.000	42.700	43.400	44.100	44.800
J	66	67	68	69	70
DY	0.70000	0.70000	0.70000	0.70000	0.70000
Y_N	45.500	46.200	46.900	47.600	48.300
J	71	72	73	74	75
DY	0.70000	0.70000	0.70000	0.70000	0.70000
Y_N	49.000	49.700	50.400	51.100	51.800
J	76	77	78	79	80
DY	0.70000	0.70000	0.70000	0.70000	0.70000
Y_N	52.500	53.200	53.900	54.600	55.300
J	81	82	83	84	85
DY	0.70000	0.70000	0.70000	0.70000	0.70000
Y_N	56.000	56.700	57.400	58.100	58.800
J	86	87	88	89	90
DY	0.70000	0.70000	0.70000	0.70000	0.70000
Y_N	59.500	60.200	60.900	61.600	62.300
J	91	92	93	94	95
DY	0.70000	0.70000	0.70000	0.70000	0.70000
Y_N	63.000	63.700	64.400	65.100	65.800
J	96	97	98	99	100
DY	0.70000	0.70000	0.70000	0.70000	0.70000
Y_N	66.500	67.200	67.900	68.600	69.300
J	101	102	103	104	105
DY	0.70000	0.70000	0.70000	0.70000	0.70000
Y_N	70.000	70.700	71.400	72.100	72.800
J	106	107	108	109	110
DY	0.70000	0.70000	0.70000	0.70000	0.70000
Y_N	73.500	74.200	74.900	75.600	76.300
J	111	112	113	114	115
DY	0.70000	0.70000	0.70000	0.70000	0.70000
Y_N	77.000	77.700	78.400	79.100	79.800
J	116	117	118	119	120
DY	0.70000	0.70000	0.70000	0.70000	0.70000
Y_N	80.500	81.200	81.900	82.600	83.300
J	121	122	123	124	125
DY	0.70000	0.70000	0.70000	0.70000	0.70000
Y_N	84.000	84.700	85.400	86.100	86.800
J	126	127	128	129	130
DY	0.70000	0.70000	0.70000	0.70000	0.70000
Y_N	87.500	88.200	88.900	89.600	90.300

```
J      131          132          133          134          135
DY   0.70000      0.70000      0.70000      0.70000      0.70000
Y_N    91.000       91.700       92.400       93.100       93.800

J      136          137          138          139          140
DY   0.70000      0.70000      0.70000      0.70000      0.70000
Y_N    94.500       95.200       95.900       96.600       97.300

J      141          142
DY   0.70000      0.70000
Y_N    98.000       98.700

Number of cells in Y direction (JMAX) =  140
Reactor length in Y direction (YLENGTH) =  98.000


Z-direction cell sizes (DZ) and Top face locations:

         K        1
        DZ    1.0000
       Z_T    0.0000

Number of cells in Z, or theta, direction (KMAX) =    1
Reactor length in Z, or theta, direction (ZLENGTH) =  1.0000
4. GAS PHASE

Viscosity (MU_g0) =  0.22700E-03  (A constant value is used
everywhere)

Number of gas species (NMAX(0)) =   4
      Gas species     Molecular weight (MW_g)
            1                 16.042
            2                 18.015
            3                 44.010
            4                 28.013


5. SOLIDS PHASE

Number of particulate phases (MMAX) =  1

M     Diameter (D_p0)      Density (RO_s0) Close_Packed
1      0.20000E-01           3.4460            T
Number of solids-1 species (NMAX(1)) =   3
       Solids species     Molecular weight (MW_s)
            1                    74.693
            2                    58.693
            3                    101.96
       Solids species     Species density (RO_ss)
            1                  0.98765E+32
            2                  0.98765E+32
            3                  0.98765E+32

       Void fraction at maximum packing (EP_star) =  0.45000


6. INITIAL CONDITIONS

7. BOUNDARY CONDITIONS

       Boundary condition no :    1
       Type of boundary condition : MASS_INFLOW
       (Inlet with specified gas and solids mass flux)
```

```
                                        Specified        Simulated
X coordinate of west face   (BC_X_w) =   0.0000          0.0000
X coordinate of east face   (BC_X_e) =   35.000          35.000
Y coordinate of south face  (BC_Y_s) =   0.0000         -0.70000
Y coordinate of north face  (BC_Y_n) =   0.0000          0.0000
Z coordinate of bottom face (BC_Z_b) =   0.0000         -1.0000
Z coordinate of top face    (BC_Z_t) =   1.0000          0.0000
I index of cell at west   (BC_I_w) =    2
I index of cell at east   (BC_I_e) =   51
J index of cell at south  (BC_J_s) =    1
J index of cell at north  (BC_J_n) =    1
K index of cell at bottom (BC_K_b) =    1
K index of cell at top    (BC_K_t) =    1
Boundary area =   35.000
Void fraction (BC_EP_g) =   1.0000
Gas pressure (BC_P_g) =  0.10000E+07
Gas temperature (BC_T_g) =   1223.0
Gas species     Mass fraction (BC_X_g)
     1                1.0000
     2                0.0000
     3                0.0000
     4                0.0000
X-component of gas velocity (BC_U_g) =   0.0000
Y-component of gas velocity (BC_V_g) =   36.000
Z-component of gas velocity (BC_W_g) =   0.0000
Solids phase-1 Density x Volume fr. (BC_ROP_s) =   0.0000
Solids phase-1 temperature (BC_T_s) =   1223.0
Solids-1 species     Mass fraction (BC_X_s)
       1                     1.0000
       2                     0.0000
       3                     0.0000
X-component of solids phase-1 velocity (BC_U_s) =  0.0000
Y-component of solids phase-1 velocity (BC_V_s) =  0.0000
Z-component of solids phase-1 velocity (BC_W_s) =  0.0000

   Boundary condition no :    2
   Type of boundary condition : P_OUTFLOW
   (Outlet with specified gas pressure)
                                        Specified        Simulated
X coordinate of west face   (BC_X_w) =   0.0000          0.0000
X coordinate of east face   (BC_X_e) =   35.000          35.000
Y coordinate of south face  (BC_Y_s) =   98.000          98.000
Y coordinate of north face  (BC_Y_n) =   98.000          98.700
Z coordinate of bottom face (BC_Z_b) =   0.0000         -1.0000
Z coordinate of top face    (BC_Z_t) =   1.0000          0.0000
I index of cell at west   (BC_I_w) =    2
I index of cell at east   (BC_I_e) =   51
J index of cell at south  (BC_J_s) =  142
J index of cell at north  (BC_J_n) =  142
K index of cell at bottom (BC_K_b) =    1
K index of cell at top    (BC_K_t) =    1
Boundary area =   35.000
Gas pressure (BC_P_g) =  0.10000E+07

   Boundary condition no :    3
   Type of boundary condition : PAR_SLIP_WALL
   (Partial slip condition at wall)
                                        Specified        Simulated
X coordinate of west face   (BC_X_w) =   0.0000         -0.70000
X coordinate of east face   (BC_X_e) =   0.0000          0.0000
Y coordinate of south face  (BC_Y_s) =   0.0000          0.0000
Y coordinate of north face  (BC_Y_n) =   98.000          98.000
Z coordinate of bottom face (BC_Z_b) =   0.0000         -1.0000
```

```
    Z coordinate of top face    (BC_Z_t) =   1.0000           0.0000
    I index of cell at west   (BC_I_w) =    1
    I index of cell at east   (BC_I_e) =    1
    J index of cell at south  (BC_J_s) =    2
    J index of cell at north  (BC_J_n) =  141
     K index of cell at bottom (BC_K_b) =    1
     K index of cell at top    (BC_K_t) =    1
     Boundary area =   0.0000
     Partial slip coefficient   (BC_hw_g) =  0.98765E+32
     Slip velociity U at wall   (BC_Uw_g) =   0.0000
     Slip velociity V at wall   (BC_Vw_g) =   0.0000
     Slip velociity W at wall   (BC_Ww_g) =   0.0000
     Solids phase: 1
     Partial slip coefficient   (BC_hw_s) =   0.0000
     Slip velociity U at wall   (BC_Uw_s) =   0.0000
     Slip velociity V at wall   (BC_Vw_s) =   0.0000
     Slip velociity W at wall   (BC_Ww_s) =   0.0000

       Boundary condition no :    4
       Type of boundary condition : PAR_SLIP_WALL
       (Partial slip condition at wall)
                                          Specified        Simulated
     X coordinate of west face   (BC_X_w) =   35.000          35.000
     X coordinate of east face   (BC_X_e) =   35.000          35.700
     Y coordinate of south face  (BC_Y_s) =   0.0000          0.0000
     Y coordinate of north face  (BC_Y_n) =   98.000          98.000
     Z coordinate of bottom face (BC_Z_b) =   0.0000         -1.0000
     Z coordinate of top face    (BC_Z_t) =   1.0000          0.0000
     I index of cell at west   (BC_I_w) =   52
     I index of cell at east   (BC_I_e) =   52
     J index of cell at south  (BC_J_s) =    2
     J index of cell at north  (BC_J_n) =  141
     K index of cell at bottom (BC_K_b) =    1
     K index of cell at top    (BC_K_t) =    1
     Boundary area =   0.0000
     Partial slip coefficient   (BC_hw_g) =  0.98765E+32
     Slip velociity U at wall   (BC_Uw_g) =   0.0000
     Slip velociity V at wall   (BC_Vw_g) =   0.0000
     Slip velociity W at wall   (BC_Ww_g) =   0.0000
     Solids phase: 1
     Partial slip coefficient   (BC_hw_s) =   0.0000
     Slip velociity U at wall   (BC_Uw_s) =   0.0000
     Slip velociity V at wall   (BC_Vw_s) =   0.0000
     Slip velociity W at wall   (BC_Ww_s) =   0.0000


8. INTERNAL SURFACES


9. OUTPUT DATA FILES:

    Extension Description                          Interval for writing
       .OUT      This file (ASCII)                          10.000
       .LOG      Log file containing messages (ASCII)
       .RES      Restart file (Binary)                     0.10000
       .SP1      EP_g (Binary, single precision)         0.50000E-01
       .SP2      P_g, P_star (Binary, single precision)  0.50000E-01
       .SP3      U_g, V_g, W_g (Binary, single precision)0.50000E-01
       .SP4      U_s, V_s, W_s (Binary, single precision)0.50000E-01
       .SP5      ROP_s (Binary, single precision)        0.50000E-01
       .SP6      T_g, T_s (Binary, single precision)     0.50000E-01
       .SP7      X_g, X_s (Binary, single precision)     0.50000E-01
       .SP8      Theta_m (Binary, single precision)      0.50000E-01
```

```
       .SP9      User Scalar (Binary, single precision)       100.00


9. OUTPUT DATA FILES:
    Extension Description                         Interval for writing
       .OUT      This file (ASCII)                         0.50000E-01
       .LOG      Log file containing messages (ASCII)
       .RES      Restart file (Binary)                     0.10000E+33
       .SP1      EP_g (Binary, single precision)


10. TOLERANCES
     The following values are specified in the file TOLERANCE.INC.

     Minimum value of EP_s tracked (ZERO_EP_s) =  0.10000E-07
     Maximum average residual (TOL_RESID) =  0.10000E-02
     Maximum average residual (TOL_RESID_T) =  0.10000E-03
     Maximum average residual (TOL_RESID_X) =  0.10000E-03
     Minimum residual at divergence (TOL_DIVERGE) =   10000.
     Tolerance for species and energy balances (TOL_COM) = 0.10000E-03
```

A.3 Example of usr_rate.f file

```
!vvvvvvvvvvvvvvvvvvvvvvvvvvvvvvvvvvvvvvvvvvvvvvvvvvvvvvvvvvvvvvvvvvv!
!                                                                   !
!  Module name: USR_RATES                                           !
!                                                                   !
!  Purpose: Hook for user defined reaction rates.                   !
!                                                                   !
!  Author: J.Musser                                 Date: 10-Oct-12 !
!                                                                   !
!  Comments: Write reaction rates in units of moles/sec.cm^3 (cgs) or!
!  kmoles/sec.m^3 (SI). Units should match those specified in the   !
!  data file.                                                       !
!  Example reaction: Methane combustion                             !
!                                                                   !
!  mfix.dat input:                                                  !
!````````````````````````````````````````````````````````````````````
!  @(RXNS)                                                          !
!      CH4_Comb { chem_eq = "CH4 + 2.0*O2 --> CO2 + 2.0*H2O" }      !
!                                                                   !
!    @(END)                                                         !
!````````````````````````````````````````````````````````````````````
!                                                                   !
!  usr_rates.f input:                                               !
!````````````````````````````````````````````````````````````````````
!    c_O2  = (RO_g(IJK)*X_g(IJK,O2)/MW_g(O2))                       !
!    c_CH4 = (RO_g(IJK)*X_g(IJK,CH4)/MW_g(CH4))                     !
!    RATES(CH4_Comb) = 2.0d5 * EP_g(IJK) * c_O2 * c_CH4             !
!````````````````````````````````````````````````````````````````````
!  * Species alias and reaction names given in the data file can be !
!    used in reference to the reaction index in RATES and a species !
!    index in gas/solids phase variables.                           !
!  * Additional information is provided in section 5.11 of the code !
!    Readme.                                                        !
!                                                                   !
!^^^^^^^^^^^^^^^^^^^^^^^^^^^^^^^^^^^^^^^^^^^^^^^^^^^^^^^^^^^^^^^^^^^!
      SUBROUTINE USR_RATES(IJK, RATES)

      USE param
```

```
      USE param1
      USE parallel
      USE fldvar
      USE rxns
      USE energy
      USE geometry
      USE run
      USE indices
      USE physprop
      USE constant
      USE funits
      USE compar
      USE sendrecv
      USE toleranc
      USE usr

      IMPLICIT NONE

      INTEGER, INTENT(IN) :: IJK

      DOUBLE PRECISION, DIMENSION(NO_OF_RXNS), INTENT(OUT) :: RATES

      INCLUDE 'species.inc'

      INCLUDE 'ep_s1.inc'
      INCLUDE 'fun_avg1.inc'

      INCLUDE 'function.inc'

      INCLUDE 'ep_s2.inc'
      INCLUDE 'fun_avg2.inc'

      INCLUDE 'usrnlst.inc'

! Reaction specific variables:
!``````````````````````````````````````````````````````````````````````//
  DOUBLE PRECISION c_CH4        ! Species CH4 concentration mol/cm^3
  DOUBLE PRECISION solidconv    ! solid conversion
  LOGICAL , EXTERNAL :: COMPARE

! Methane_Combustion:  CH4 + 4.0NiO --> 4.0Ni + 2.0H2O + CO2

(mol/cm^3.s)

! Reaction rates:
!``````````````````````````````````````````````````````````````````````
//
! Include reaction rates here. Reaction rates should be stored in the
! variable RATES. The reaction name given in the data file can be used
! to store the rate in the appropriate array location. Additional
! input format parameters are given in Section 4.11 of the code
Readme.

IF(.NOT.COMPARE(EP_g(IJK), ONE)) THEN

c_CH4 = RO_g(IJK) * X_g(IJK,CH4)/MW_g(CH4)
solidconv =
(X_s(IJK,1,NiO)/(X_s(IJK,1,NiO)+X_s(IJK,1,Ni)*6.670/8.908))**0.6666

RATES(Methane_Combustion) = 90.56*EP_s(IJK,1)*(c_CH4)**0.8*solidconv

ELSE
```

```
RATES(Methane_Combustion) = ZERO

ENDIF
IF(Methane_Combustion <= nRR ) &
ReactionRates(IJK,Methane_Combustion) = RATES(Methane_Combustion)

END SUBROUTINE USR_RATES
```

Appendix B

B.1 Streams details for each power plant configuration

In Table B.1, details about the streams characterising the power plant at atmospheric conditions and 10 MW (Fig. 4.4) are given.

Table B.1 Streams power plant at 1 atm and 10 MW

	1	2	3	4	5	6	7	8	9	10
Mole flow [kmol/s]										
CH4	0	0	0	0	0,0125	0,0125	1,2E-05	1,2E-05	1,2E-05	1,2E-05
CO2	0	0	0	0	0	0	0,0125	0,0125	0,0125	0,0125
H2O	0	0	0	0	0	0	0,025	0,025	0,025	0,025
O2	0,0275	0,0275	0,0025	0,0025	0	0	0	0	0	0
N2	0,1034	0,1034	0,1034	0,1034	0	0	0	0	0	0
NiO	0	0	0	0	0	0	0	0	0	0
Ni	0	0	0	0	0	0	0	0	0	0
Al2O3	0	0	0	0	0	0	0	0	0	0
Total flow [kmol/s]	0,1309	0,1309	0,1059	0,1059	0,0125	0,0125	0,0374	0,0374	0,0374	0,0374
Temperature [°C]	25	969	1200	45	25	1162	1182	669	80	30
Pressure [atm]	1	1	1	1	1	1	1	1	1	1

	11	12	13	14	15	16	17	18	19	20	21	22
Mole flow [kmol/s]												
CH4	1,2E-05	0	1,2E-05	1,2E-05	1,2E-05	0	1,2E-05	1,2E-05	1,2E-05	0	1,2E-05	1,2E-05
CO2	0,0121	3,30E-04	0,0121	0,0121	0,0121	2,36E-05	0,0121	0,0121	0,0121	2,78E-05	0,0121	0,0121
H2O	5,20E-04	0,024	5,20E-04	5,20E-04	1,21E-04	4,00E-04	1,21E-04	1,21E-04	2,5E-05	9,64E-05	2,5E-05	2,5E-05
O2	0	0	0	0	0	0	0	0	0	0	0	0
N2	0	0	0	0	0	0	0	0	0	0	0	0
NiO	0	0	0	0	0	0	0	0	0	0	0	0
Ni	0	0	0	0	0	0	0	0	0	0	0	0
Al2O3	0	0	0	0	0	0	0	0	0	0	0	0
Total flow [kmol/s]	0,0126	0,025	0,0126	0,0126	0,0122	4,24E-04	0,0122	0,0122	0,0121	1,24E-04	0,0121	0,0121
Temperature [ºC]	30	30	157	30	30	30	156	30	30	30	169	30
Pressure [atm]	1	1	4	4	4	4	16	16	16	16	73	73

	23	24	25	26	27	28	29	30	31	32	33
Mole flow [kmol/s]											
CH4	1,2E-05	0	0	0	0	0	0	0	0	0	0
CO2	0,0121	0	0	0	0	0	0	0	0	0	0
H2O	2,5E-05	0	0	0,125	0,125	0,125	0,125	0,025	0,025	0,025	0,025
O2	0	0	0	0	0	0	0	0	0	0	0
N2	0	0	0	0	0	0	0	0	0	0	0
NiO	0	0,2713	0,3213	0	0	0	0	0	0	0	0
Ni	0	0,1522	0,1022	0	0	0	0	0	0	0	0
Al2O3	0	0,4414	0,4414	0	0	0	0	0	0	0	0
Total flow [kmol/s]	0,0121	0,8649	0,8649	0,125	0,125	0,125	0,125	0,025	0,025	0,025	0,025
Temperature [°C]	39	1182	1200	29	34	560	29	56	514	54	54
Pressure [atm]	110	1	1	0,04	160	160/30	0,04	60	60	0,15	0,15

In Table B.2, details about the streams characterising the power plant at 10 atm and 10 MW with the riser at heat extraction (Fig. 4.11) are given.

Table B.2 Streams power plant at 10 atm and 10 MW with riser at heat extraction

	1	2	3	4	5	6	7	8	9	10	11	12	13
Mole flow [kmol/s]													
CH4	0	0	0	0,0125	0,0125	1,2E-05	1,2E-05	1,2E-05	1,2E-05	1,2E-05	1,2E-05	0	1,2E-05
CO2	0	0	0	0	0	0,0125	0,0125	0,0125	0,0125	0,0125	0,0121	0,00033	0,0121
H2O	0	0	0	0	0	0,025	0,025	0,025	0,025	0,025	0,0005	0,0245	0,00052
O2	0,0275	0,0275	0,0275	0	0	0	0	0	0	0	0	0	0
N2	0,1034	0,1034	0,1034	0	0	0	0	0	0	0	0	0	0
NiO	0	0	0	0	0	0	0	0	0	0	0	0	0
Ni	0	0	0	0	0	0	0	0	0	0	0	0	0
Al2O3	0	0	0	0	0	0	0	0	0	0	0	0	0
Total flow [kmol/s]	0,1309	0,1309	0,1309	0,0125	0,0125	0,0374	0,0374	0,0374	0,0374	0,0374	0,0126	0,0248	0,0126
Temperature [°C]	25	326	550	25	698	1137	718	441	108	30	30	30	157
Pressure [atm]	1	10	10	10	10	10	1	1	1	1	1	1	4

	14	15	16	17	18	19	20	21	22	23	24	25	26
Mole flow [kmol/s]													
CH4	1,2E-05	1,2E-05	0	1,2E-05	1,2E-05	1,2E-05	0	1,2E-05	1,2E-05	1,2E-05	0	0	0
CO2	0,0121	0,0121	2,4E-05	0,0121	0,0121	0,0121	2,8E-05	0,0121	0,0121	0,0121	0	0	0
H2O	0,00052	0,00012	0,0004	0,00012	0,00012	2,5E-05	9,6E-05	2,5E-05	2,5E-05	2,5E-05	0	0	0
O2	0	0	0	0	0	0	0	0	0	0	0	0	0,0025
N2	0	0	0	0	0	0	0	0	0	0	0	0	0,1034
NiO	0	0	0	0	0	0	0	0	0	0	0,0439	0,0937	0
Ni	0	0	0	0	0	0	0	0	0	0	0,1009	0,0511	0
Al2O3	0	0	0	0	0	0	0	0	0	0	0,1471	0,1471	0
Total flow [kmol/s]	0,0126	0,0122	0,0004	0,0122	0,0122	0,0121	0,0001	0,0121	0,0121	0,0121	0,2920	0,2920	0,1059
Temperature [°C]	30	30	30	156	30	30	30	169	30	39	1137	1200	1200
Pressure [atm]	4	4	4	16	16	16	16	73	73	110	10	10	10

	27	28	29	30	31	32	33	34	35	36	37	38
Mole flow [kmol/s]												
CH4	0	0	0	0	0	0	0	0	0	0	0	0
CO2	0	0	0	0	0	0	0	0	0	0	0	0
H2O	0	0	0	0,1033	0,103	0,103	0,103	0,103	0,0092	0,0092	0,0092	0,0092
O2	0,0025	0,0025	0,0025	0	0	0	0	0	0	0	0	0
N2	0,1034	0,1034	0,1034	0	0	0	0	0	0	0	0	0
NiO	0	0	0	0	0	0	0	0	0	0	0	0
Ni	0	0	0	0	0	0	0	0	0	0	0	0
Al2O3	0	0	0	0	0	0	0	0	0	0	0	0
Total flow [kmol/s]	0,1059	0,1059	0,1059	0,1033	0,103	0,103	0,103	0,103	0,0092	0,0092	0,0092	0,0092
Temperature [°C]	623	346	45	29	34	146	560	29	86	87	421	86
Pressure [atm]	1	1	1	0,04	160	160	160/30	0,04	0,6	60	60	0,6

In Table B.3, details about the streams characterising the power plant at 10 atm and 10 MW with the riser at adiabatic conditions (Fig. 4.15) are given.

Table B.3 Streams power plant at 10 atm and 10 MW with riser at adiabatic conditions

	1	2	3	4	5	6	7	8	9	10	11	12	13
Mole flow [kmol/s]													
CH4	0	0	0	0,0125	0,0125	1,2E-05	1,2E-05	1,2E-05	1,2E-05	1,2E-05	1,2E-05	0	1,2E-05
CO2	0	0	0	0	0	0,0125	0,0125	0,0125	0,0125	0,0125	0,0121	0,00033	0,0121
H2O	0	0	0	0	0	0,025	0,025	0,025	0,025	0,025	0,0005	0,0245	0,0005
O2	0,0699	0,0699	0,0450	0	0	0	0	0	0	0	0	0	0
N2	0,263	0,263	0,263	0	0	0	0	0	0	0	0	0	0
NiO	0	0	0	0	0	0	0	0	0	0	0	0	0
Ni	0	0	0	0	0	0	0	0	0	0	0	0	0
Al2O3	0	0	0	0	0	0	0	0	0	0	0	0	0
Total flow [kmol/s]	0,3329	0,3329	0,3080	0,0125	0,0125	0,0374	0,0374	0,0374	0,0374	0,0374	0,0126	0,0248	0,0126
Temperature [°C]	25	326	1200	25	698	1137	718	441	108	30	30	30	157
Pressure [atm]	1	10	10	10	10	10	1	1	1	1	1	1	4

	14	15	16	17	18	19	20	21	22	23	24	25	26
Mole flow [kmol/s]													
CH4	1,2E-05	1,2E-05	0	1,2E-05	1,2E-05	1,2E-05	0	1,2E-05	1,2E-05	1,2E-05	0	0	0
CO2	0,0121	0,01209	2,4E-05	0,01209	0,01209	0,01207	2,8E-05	0,01207	0,01207	0,01207	0	0	0
H2O	0,00052	0,00012	0,0004	0,00012	0,00012	2,5E-05	9,6E-05	2,5E-05	2,5E-05	2,5E-05	0	0	0
O2	0	0	0	0	0	0	0	0	0	0	0	0	0,0450
N2	0	0	0	0	0	0	0	0	0	0	0	0	0,263
NiO	0	0	0	0	0	0	0	0	0	0	0,0439	0,0937	0
Ni	0	0	0	0	0	0	0	0	0	0	0,1009	0,0511	0
Al2O3	0	0	0	0	0	0	0	0	0	0	0,1471	0,1471	0
Total flow [kmol/s]	0,0126	0,0122	0,0004	0,0122	0,0122	0,0121	0,0001	0,0121	0,0121	0,0121	0,2920	0,2920	0,3080
Temperature [°C]	30	30	30	156	30	30	30	169	30	39	1137	1200	623
Pressure [atm]	4	4	4	16	16	16	16	73	73	110	10	10	1

	27	28	29	30	31	32	33	34	35
Mole flow [kmol/s]									
CH4	0	0	0	0	0	0	0	0	0
CO2	0	0	0	0	0	0	0	0	0
H2O	0	0,083	0,083	0,083	0,083	0,0092	0,0092	0,0092	0,0092
O2	0,0450	0	0	0	0	0	0	0	0
N2	0,263	0	0	0	0	0	0	0	0
NiO	0	0	0	0	0	0	0	0	0
Ni	0	0	0	0	0	0	0	0	0
Al2O3	0	0	0	0	0	0	0	0	0
Total flow [kmol/s]	0,3080	0,083	0,083	0,083	0,083	0,0092	0,0092	0,0092	0,0092
Temperature [°C]	67	47	48	530	47	86	87	421	86
Pressure [atm]	1	0,11	60	60	0,11	0,6	60	60	0,6

In Table B.4, details about the streams characterising the power plant at 10 atm and 500 MW with the riser at adiabatic conditions (Fig. 4.15) are given.

Table B.4 Streams power plant at 10 atm and 500 MW with riser at adiabatic conditions

	1	2	3	4	5	6	7	8	9	10	11	12	13
Mole flow [kmol/s]													
CH4	0	0	0	0,625	0,625	0,00062	0,00062	0,00062	0,00062	0,00062	0,00062	0	0,00062
CO2	0	0	0	0	0	0,625	0,625	0,625	0,625	0,625	0,605	0,0165	0,605
H2O	0	0	0	0	0	1,25	1,25	1,25	1,25	1,25	0,026	1,224	0,026
O2	3,497	3,497	2,24825	0	0	0	0	0	0	0	0	0	0
N2	13,15	13,15	13,15	0	0	0	0	0	0	0	0	0	0
NiO	0	0	0	0	0	0	0	0	0	0	0	0	0
Ni	0	0	0	0	0	0	0	0	0	0	0	0	0
Al2O3	0	0	0	0	0	0	0	0	0	0	0	0	0
Total flow [kmol/s]	16,647	16,647	15,3983	0,625	0,625	1,87562	1,87562	1,87562	1,87562	1,87562	0,63162	1,2405	0,63162
Temperature [°C]	25	326	1200	25	698	1137	718	441	108	30	30	30	157
Pressure [atm]	1	10	10	10	10	10	1	1	1	1	1	1	4

	14	15	16	17	18	19	20	21	22	23	24	25	26
Mole flow [kmol/s]													
CH4	0,00062	0,00062	0	0,00062	0,00062	0,00062	0	0,00062	0,00062	0,00062	0	0	0
CO2	0,605	0,6045	0,00118	0,6045	0,6045	0,6035	0,00139	0,6035	0,6035	0,6035	0	0	0
H2O	0,026	0,00605	0,02	0,00605	0,00605	0,00123	0,00482	0,00123	0,00123	0,00123	0	0	0
O2	0	0	0	0	0	0	0	0	0	0	0	0	2,24825
N2	0	0	0	0	0	0	0	0	0	0	0	0	13,15
NiO	0	0	0	0	0	0	0	0	0	0	2,19525	4,68604	0
Ni	0	0	0	0	0	0	0	0	0	0	5,0465	2,5558	0
Al2O3	0	0	0	0	0	0	0	0	0	0	7,35583	7,35583	0
Total flow [kmol/s]	0,63162	0,61117	0,02118	0,61117	0,61117	0,60535	0,00621	0,60535	0,60535	0,60535	14,5976	14,5977	15,3983
Temperature [°C]	30	30	30	156	30	30	30	169	30	39	1137	1200	623
Pressure [atm]	4	4	4	16	16	16	16	73	73	110	10	10	1

	27	28	29	30	31	32	33	34	35
Mole flow [kmol/s]									
CH4	0	0	0	0	0	0	0	0	0
CO2	0	0	0	0	0	0	0	0	0
H2O	0	4,15	4,15	4,15	4,15	0,458	0,458	0,458	0,458
O2	2,24825	0	0	0	0	0	0	0	0
N2	13,15	0	0	0	0	0	0	0	0
NiO	0	0	0	0	0	0	0	0	0
Ni	0	0	0	0	0	0	0	0	0
Al2O3	0	0	0	0	0	0	0	0	0
Total flow [kmol/s]	15,3983	4,15	4,15	4,15	4,15	0,458	0,458	0,458	0,458
Temperature [°C]	67	47	48	530	47	86	87	421	86
Pressure [atm]	1	0,11	60	60	0,11	0,6	60	60	0,6

In Table B.5, details about the streams characterising the power plant at 10 atm and 10 MW with no carbon capture section (Fig. 4.17) are given.

Table B.5 Streams power plant at 10 atm and 10 MW with no carbon capture section

	1	2	3	4	5	6	7	8	9	10
Mole flow [kmol/s]										
CH4	0	0	0,0125	1,2E-05	1,2E-05	1,2E-05	0	0	0	0
CO2	0	0	0	0,0125	0,0125	0,0125	0	0	0	0
H2O	0	0	0	0,025	0,025	0,025	0,099	0,099	0,099	0,099
O2	0,065	0,065	0	0,04	0,04	0,04	0	0	0	0
N2	0,247	0,247	0	0,247	0,247	0,247	0	0	0	0
NiO	0	0	0	0	0	0	0	0	0	0
Ni	0	0	0	0	0	0	0	0	0	0
Al2O3	0	0	0	0	0	0	0	0	0	0
Total flow [kmol/s]	0,312	0,312	0,0125	0,325	0,325	0,325	0,099	0,099	0,099	0,099
Temperature [°C]	25	326	25	1200	646	67	47	48	530	47
Pressure [atm]	1	10	10	10	1	1	0,11	60	60	0,11

Appendix C

C.1 Cash flow

In Table C.1 the current cumulative cash flow with DCFR for the CLC power plant is shown under a fuel price of 5.8 $/GJ and no solid make-up.

Table C.1 Cash flow CLC power plant

Parameter/Year	-3	-2	-1	0	1	2	3	4	5
Purchased land	$5.001.427								
FCI		$53.651.312	$126.688.632	$183.155.566					
WC				$63.154.113					
Start up expenses					$33.835.745				
Operating rate					0,5	0,9	1	1	1
Revenues					$101.084.650	$184.135.799	$207.050.476	$209.535.082	$212.049.503
Annual TOT operating costs					$87.765.184	$126.995.381	$138.178.111	$139.836.248	$141.514.283
Depreciation factor					5%	9,50%	8,55%	7,70%	6,93%
Annual depreciation					$18.174.776	$34.532.073	$31.078.866	$27.989.154	$25.190.239
Gross profit					$13.319.466	$57.140.418	$68.872.366	$69.698.834	$70.535.220
Gross profit minus depreciation					-$4.855.309	$22.608.344	$37.793.499	$41.709.680	$45.344.981
Net profit					-$3.155.951	$14.695.424	$24.565.775	$27.111.292	$29.474.238
Annual CF	-$5.001.427	-$53.651.312	-$126.688.632	-$246.309.678	-$18.816.920	$49.227.497	$55.644.641	$55.100.446	$54.664.477
Residual value of the plant									
Current factor	1,331	1,210	1,100	1,000	0,909	0,826	0,751	0,683	0,621
Annual CF with DCFR	-$6.656.900	-$64.918.088	-$139.357.496	-$246.309.678	-$17.106.291	$40.683.882	$41.806.642	$37.634.346	$33.942.339
Cumulative CF with DCFR	-$6.656.900	-$71.574.988	-$210.932.484	-$457.242.162	-$474.348.453	-$433.664.571	-$391.857.928	-$354.223.582	-$320.281.243

Parameter/Year	6	7	8	9	10	11	12	13	14
Purchased land									
FCI									
WC									
Start up expenses									
Operating rate	1	1	1	1	1	1	1	1	1
Revenues	$214.594.097	$217.169.226	$219.775.257	$222.412.560	$225.081.511	$227.782.489	$230.515.879	$233.282.069	$236.081.454
Annual TOT operating costs	$143.212.454	$144.931.004	$146.670.176	$148.430.218	$150.211.381	$152.013.917	$153.838.084	$155.684.141	$157.552.351
Depreciation factor	6,23%	5,90%	5,90%	5,91%	5,90%	5,91%	5,90%	5,91%	5,90%
Annual depreciation	$22.645.770	$21.446.235	$21.446.235	$21.482.585	$21.446.235	$21.482.585	$21.446.235	$21.482.585	$21.446.235
Gross profit	$71.381.643	$72.238.222	$73.105.081	$73.982.342	$74.870.130	$75.768.572	$76.677.795	$77.597.928	$78.529.103
Gross profit minus depreciation	$48.735.872	$50.791.987	$51.658.846	$52.499.757	$53.423.895	$54.285.987	$55.231.559	$56.115.343	$57.082.868
Net profit	$31.678.317	$33.014.792	$33.578.250	$34.124.842	$34.725.532	$35.285.892	$35.900.514	$36.474.973	$37.103.864
Annual CF	$54.324.087	$54.461.027	$55.024.485	$55.607.427	$56.171.767	$56.768.476	$57.346.749	$57.957.538	$58.550.099
Residual value of the plant									
Current factor	0,564	0,513	0,467	0,424	0,386	0,350	0,319	0,290	0,263
Annual CF with DCFR	$30.664.531	$27.947.118	$25.669.328	$23.582.977	$21.656.648	$19.897.005	$18.272.441	$16.788.240	$15.418.071
Cumulative CF with DCFR	-$289.616.712	-$261.669.594	-$236.000.266	-$212.417.288	-$190.760.641	-$170.863.636	-$152.591.195	-$135.802.955	-$120.384.883

Parameter/Year	15	16	17	18	19	20	21	22	23
Purchased land									
FCI									
WC									
Start up expenses									
Operating rate	1	1	1	1	1	1	1	1	1
Revenues	$238.914.431	$241.781.405	$244.682.782	$247.618.975	$250.590.403	$253.597.487	$256.640.657	$259.720.345	$262.836.989
Annual TOT operating costs	$159.442.979	$161.356.295	$163.292.570	$165.252.081	$167.235.106	$169.241.927	$171.272.831	$173.328.104	$175.408.042
Depreciation factor	5,91%	2,95%							
Annual depreciation	$21.482.585	$10.723.118	$0	$0	$0	$0	$0	$0	$0
Gross profit	$79.471.452	$80.425.110	$81.390.211	$82.366.894	$83.355.296	$84.355.560	$85.367.827	$86.392.241	$87.428.948
Gross profit minus depreciation	$57.988.868	$69.701.992	$81.390.211	$82.366.894	$83.355.296	$84.355.560	$85.367.827	$86.392.241	$87.428.948
Net profit	$37.692.764	$45.306.295	$52.903.637	$53.538.481	$54.180.943	$54.831.114	$55.489.087	$56.154.956	$56.828.816
Annual cash flow	$59.175.349	$56.029.413	$52.903.637	$53.538.481	$54.180.943	$54.831.114	$55.489.087	$56.154.956	$56.828.816
Residual value of the plant									
Current factor	0,239	0,218	0,198	0,180	0,164	0,149	0,135	0,123	0,112
Annual CF with DCFR	$14.166.108	$12.193.633	$10.466.703	$9.629.366	$8.859.017	$8.150.296	$7.498.272	$6.898.410	$6.346.537
Cumulative CF with DCFR	-$106.218.775	-$94.025.143	-$83.558.440	-$73.929.074	-$65.070.057	-$56.919.761	-$49.421.489	-$42.523.079	-$36.176.541

Parameter/Year	24	25	26	27	28	29	30
Purchased land							
FCI							
WC							
Start up expenses							
Operating rate	1	1	1	1	1	1	1
Revenues	$265.991.033	$269.182.926	$272.413.121	$275.682.078	$278.990.263	$282.338.146	$285.726.204
Annual TOT operating costs	$177.512.938	$179.643.094	$181.798.811	$183.980.396	$186.188.161	$188.422.419	$190.683.488
Depreciation factor							
Annual depreciation	$0	$0	$0	$0	$0	$0	$0
Gross profit	$88.478.095	$89.539.832	$90.614.310	$91.701.682	$92.802.102	$93.915.727	$95.042.716
Gross profit minus depreciation	$88.478.095	$89.539.832	$90.614.310	$91.701.682	$92.802.102	$93.915.727	$95.042.716
Net profit	$57.510.762	$58.200.891	$58.899.302	$59.606.093	$60.321.366	$61.045.223	$61.777.765
Annual CF	$57.510.762	$58.200.891	$58.899.302	$59.606.093	$60.321.366	$61.045.223	$61.777.765
Residual value of the plant							$68.155.540
Current factor	0,102	0,092	0,084	0,076	0,069	0,063	0,057
Annual CF with DCFR	$5.838.814	$5.371.709	$4.941.973	$4.546.615	$4.182.886	$3.848.255	$7.446.290
Cumulative CF with DCFR	-$30.337.727	-$24.966.017	-$20.024.045	-$15.477.430	-$11.294.544	-$7.446.290	$0

References

Abad A., J. Adánez, F. García-Labiano, L.F. de Diego, P. Gayán (2010). Modeling of the chemical-looping combustion of methane using a Cu-based oxygen-carrier. Combustion and flame 157, 602-615.

Abad A., J. Adánez, F. García-Labiano, L.F. de Diego, P. Gayán, J. Celaya (2007). Mapping of the range of operational conditions for Cu-, Fe-, and Ni-based oxygen carriers in chemical-looping combustion. Chemical Engineering Science 62, 533-549.

Abanades A., E. Ruiz, E.M. Ferruelo, F. Hernandez, A. Cabanillas, J.M. Martinez-Val, J.A. Rubio, C. Lopez, R. Gavela, G. Barrera, C. Rubbia, D. Salmieri, E. Rodilla, D. Gutierrez (2011). Experimental analysis of direct thermal methane cracking. International Journal of Hydrogen Energy 36, 12877-12886.

Abu-Zhara M.R.M., L.H.J. Schneiders, J.P.M. Niederer, P.H.M. Feron, G.F. Versteeg (2007). CO_2 Capture from Power Plants: Part I. A Parametric Study of the Technical Performance Based on Mono-Ethanolamine. International J. Greenhouse Gas Control 1 (1), 37-46.

Abu-Zhara M.R.M., L.H.J. Schneiders, J.P.M. Niederer, P.H.M. Feron, G.F. Versteeg (2007). CO_2 Capture from Power Plants: Part II. A Parametric Study of the Technical Performance Based on Mono-Ethanolamine. International J. Greenhouse Gas Control 1 (1), 135-142.

Adánez J., F. García-Labiano, L.F. de Diego, A. Plata, J. Celaya, P. Gayán, A. Abad (2003). Optimizing the fuel reactor for chemical looping combustion, 17th International Conference on Fluidized Bed Combustion. American Society of Mechanical Engineers, 173-182.

Adanez J., L.F. de Diego, F. Garcia-Labiano, P. Gayan, A. Abad (2004). Selection of oxygen carriers for chemical-looping combustion. Energy & Fuels 18, 371–377.

Adánez J., P. Gayán, J. Celaya, L.F. de Diego, F. García-Labiano, A. Abad (2006). Chemical looping combustion in a 10 kWth prototype using a CuO/Al_2O_3 oxygen

carrier: Effect of operating conditions on methane combustion. Industrial & engineering chemistry research 45, 6075-6080.

Ahn H., M. Luberti, Z. Liu, S. Brandani (2013). Process configuration studies of the amine capture process for coal-fired power plants. Int. J. Greenhouse Gas Con. 16, 29-40.

Astarita G., D.W. Savage, A. Bisio (1983). Gas treating with chemical solvents. Chapter 9: Removal of carbon dioxide, New York.

Audus H. (2000). Leading options for the capture of CO_2 at power stations. Proceedings of the Fifth International Conference on Greenhouse Gas Control Technologies, Cairns, Australia. Citeseer, 13-16.

Berguerand N., A. Lyngfelt (2008). Design and operation of a 10 kWth chemical-looping combustor for solid fuels – testing with South African coal. Fuel 87, 2713–26.

Berguerand N., A. Lyngfelt (2009). Chemical Looping Combustion of Petroleum Coke using Ilmenite in a 10 kWth unit – High Temperature Operation, Energy & Fuels 23, 5257-5268.

Bolland O., H.M. Kvamsdal, J.C. Boden (2005). A comparison of the efficiencies of the oxy-fuel power cycles water-cycle, Graz-cycle, and Matiant-cycle. I: Carbon dioxide capture for storage in deep geologic formations—results from the CO_2 capture project. Elsevier Science Ltd, 499–512.

Branan C. (2002). Rules of thumb for chemical engineers, Third Edition. Gulf Publishing Company.

Busciglio A., G. Micale, L. Rizzuti, G. Vella (2007). Numerical Simulations of Bubbling Fluidised Beds. Chemical Engineering Transactions 11, 303-308.

Cao Y., W.P. Pan (2006). Investigation of chemical looping combustion by solid fuels. 1. Process analysis. Energy Fuels 20, 1836–44.

Carnahan N.F., K.E. Starling (1969). Equation of state for nonattracting rigid spheres. The Journal of Chemical Physics 51, 635-636.

Chakma A (1995). An energy efficient mixed solvent for the separation of CO_2. Energy Conversion and Management 36, 427-430.

Chepurniy N. (1984). Kinetic theories for granular flow: inelastic particles in Couette flow and slightly inelastic particles in a general flow field. Journal of fluid mechanics 140, 256.

Cho P., T. Mattisson, A. Lyngfelt (2004). Comparison of iron-, nickel-, copper-, and manganese-based oxygen carriers for chemical-looping combustion. Fuel 83, 1225–1245.

Committee on Climate Change (2014). Meeting Carbon Budgets – 2014 Progress Report to Parliament.

Copeland R.J., G. Alptekin, M. Cesario, Y. Gershanovich (2002). Sorbent energy transfer system (SETS) for CO_2 separation with high efficiency. Proceedings of 27th international technical conference on coal utilization & fuel systems, Clearwater, FL, USA.

Copeland R.J., G. Alptekin, M. Cessario, Y. Gerhanovich (2001). A novel CO_2 separation System. Proceedings of the First National Conference on Carbon Sequestration, DOE/NETL, Washington, DC. LA-UR-00-1850.

Constantineau J.P., J.R. Grace, C.J. Lim, G.G. Richards (2007). Generalized bubbling-slugging fluidised bed reactor model. Chemical Engineering Science 62, 70-81.

Coulson J.M., J.F. Richardson (2003). Chemical Engineering, Volume 6, Third Edition, Chemical Engineering Design. Butterworth-Heinemann.

Courant R., K. Friedrichs, H. Lewy (1967). On the partial difference equations of mathematical physics. IBM Journal, 215-234.

Darton R.C., R.D. La Nauze, F.F. Davidson, D. Harrison (1977). Bubble growth due to coalescence in fluidised beds. Trans IChemE, 55, 274.

Davidson J., D. Harrison, R. Jackson (1963). Fluidized particles. Cambridge University Press, New York, USA.

Davison J. (2007). Performance and cost of power plants with capture and storage of CO_2. Energy 32, 1163-1176.

Dean C.C., J. Blamey, N.H. Florin, M.J. Al-Jeboory, P.S. Fennell (2011). The calcium looping cycle for CO_2 capture from power generation, cement manufacture and hydrogen production. CHERD, 89, 836-855.

De Diego L.F., F. Garcia-Labiano, J. Adanez, P. Gayan, A. Abad, B.M. Corbella, J.M. Palacios (2004). Development of Cu-based oxygen carriers for chemical looping combustion. Fuel 83, 1749–1757.

De Diego L.F., F. Garcia-Labiano, P. Gayan, J. Cylaya, J.M. Palacios, J. Adanez (2007). Operation of a 10 kWth chemical-looping combustor during 200 h with a CuO–Al2O3 oxygen carrier. Fuel 86, 1036–1045.

De Lasa H.I., J.R. Grace (1979). The influence of the freeboard region in a fluidized bed catalytic cracking regenerator. AIChE Journal 25, 984-991.

Deng Z., R. Xiao, B. Jin, Q. Song (2009). Numerical simulation of chemical looping combustion process with CaSO4 oxygen carrier. International J. of Greenhouse Gas Control 3, 368-375.

Deng Z., R. Xiao, B. Jin, Q. Song, H. Huang (2008). Multiphase CFD modeling for a chemical looping combustion process (fuel reactor). Chemical engineering & technology 31, 1754-1766.

Dennis J.S. (2009). Chemical Looping Combustion: One Answer to Sequestering Carbon Dioxide. Proceedings of the European Combustion Meeting.

Dennis J.S., S. Scott (2010). In situ gasification of a lignite coal and CO_2 separation using chemical looping with a Cu-based oxygen carrier. Fuel 89, 1623–1640.

Deza M., N. Franka, T. Heindel, F. Battaglia (2009). CFD Modeling and X-Ray Imaging of Biomass in a Fluidized Bed. Journal of Fluids Engineering 131(11).

DOE/NETL (2007). Cost and performance baseline for fossil energy plants.

DOE/NETL (2010). Carbon dioxide capture and storage RD&D Roadmap.

EIA (2008). International Energy Outlook 2008. Energy information Administration (EIA), US Department of Energy (DOE), Washington, DC.

EIA (2014). Annual Energy Outlook 2014. Energy information Administration (EIA), US Department of Energy (DOE), Washington, DC.

EPAV (2008). Environment Protection Authority Victoria. Climate change glossary.

Emun F, M. Gadalla, T. Majozi, D. Boer (2010). Integrated gasification combined cycle (IGCC) process simulation and optimization. Computers and Chemical Engineering, 34, 331-338.

Eslami A., H. Sohi, A. Sheikhi, R. Sotudeh-Gharebagh (2012). Sequential modeling of coal volatile combustion in fluidized bed reactors. Energy & Fuels 26, 5199-5209.

Fan L.S., C.J. Easton (2010). Chemical Looping Systems for Fossil Energy Conversions, WILEY.

Fan L.S., F. Li (2010). Chemical Looping Technology and Its Fossil Energy Conversion Applications. Ind. Eng. Chem. Res. 49, 10200–10211.

Feron P.H.M. (1994). Membranes for carbon dioxide recovery from power plants. In Carbon Dioxide Chemistry: Environmental Issues, 236-249.

Fueki K., B. Wagner Jr. (1965). Studies of the oxidation of nickel in the temperature range of 900-1400 °C. J. Electrochem. Soc. 112, 4, 384-388.

Furusaki S., T. Kikuchi, T. Miyauchi (1976). Axial distribution of reactivity inside a fluid-bed contactor. AIChE Journal 22, 354-361.

Galinsky N., Y. Huang, A. Shafiefarhood, F. Li (2013). Iron Oxide with Facilitated O_2− Transport for Facile Fuel Oxidation and CO_2 Capture in a Chemical Looping Scheme. ACS Sustainable Chem. Eng. 1, 364−373.

Garcia-Labiano F., J. Adanez, L.F. de Diego, P. Gayan, A. Abad (2006). Effect of pressure on the behaviour of copper-, iron-, and nickel-based oxygen carrier for chemical-looping combustion. Energy & Fuel 20, 26–33.

García-Labiano F., L.F. de Diego, J. Adánez, A. Abad, P. Gayán (2005). Temperature variations in the oxygen carrier particles during their reduction and oxidation in a chemical-looping combustion system. Chemical Engineering Science 60, 851-862.

Geldart D., J. Baeyens (1985). The design of distributors for gas-fluidized beds. Powder Technology 42, 67-78.

Gidaspow D. (1994). Multiphase flow and fluidization: continuum and kinetic theory descriptions. Academic press.

Gidaspow D., L. Huilin (1998). Equation of State and Radial Distribution Function of FCC Particles in a CFB. AIChE Journal 44(2), 279.

Global CCS institute (2013). Towards a common method of cost estimation for CO_2 capture and storage at fossil fuel power plants.

Göttlicher G., R. Pruschek (1997). Comparison of CO_2 removal systems for fossil-fuelled power plant processes. Energy Conversion and Management 38, S173-S178.

Griffin T., D. Winkler, M. Wolf, C. Appel, J. Mantzaras (2004). Staged catalytic combustion method for the advanced zero emissions gas turbine power plant. In: Proceedings of the ASME turbo expo, Vienna, Austria.

Gupta S.K. (1995). Numerical method for Engineers, New Age International.

Hashemi Sohi A., A. Eslami, A. Sheikhi, R. Sotudeh-Gharebagh (2012). Sequential-based process modeling of natural gas combustion in a fluidized bed reactor. Energy & Fuels 26, 2058-2067.

Hassan B., T. Shamim (2012). Parametric and Exergetic Analysis of a Power Plant with CO_2 Capture using Chemical Looping Combustion. International Conference on Clean and Green Energy, Singapore.

Hatanaka T., S. Matsuda, H. Hatano (1997). A new-concept gas–solid combustion system "MERIT" for high combustion efficiency and low emissions. Proceedings of Intersociety energy conversion engineering conference, 30, 944–948.

Hendriks C.S. (1994). Carbon dioxide removal from coal-fired power plants. Dissertation, Utrecht University, Utrecht.

Herzog H., D. Golomb, S. Zemba (1991). Feasibility, modeling and economics of sequestering power plant CO_2 emissions in the deep ocean. Environmental Progress 10, 64-74.

Herzog H.J. (1999). The economics of CO_2 capture. Proceedings of the 4th International Conference on Greenhouse Gas Control Technologies, 101-106.

Hoffmann B.S., A. Szklo (2011). Integrated gasification combined cycle and carbon capture: A risky option to mitigate CO_2 emissions of coal-fired power plants. Applied Energy 88, 3917-3929.

Hossain M.M., H.I. de Lasa (2008). Chemical-looping Combustion (CLC) for Inherent CO_2 Separations-A Review. Chemical Engineering Science 63, 4433–4451.

IEA (2003). CO_2 emissions from fuel combustion, OECD/IEA, Paris.

Iliuta I., R. Tahoces, G.S. Patience, S. Rifflart, F. Luck (2010). Chemical-looping combustion process: Kinetics and mathematical modeling. AIChE journal 56, 1063-1079.

International Society of Beverage Technologists (ISBT) (2006). Carbon dioxide quality guidelines and analytical procedure bibliography, US.

IPCC (2005). Special report on carbon dioxide capture and storage.

IPCC (2007). Special report on mitigation of climate change.

IPCC (2008). Annex B: Glossary of terms.

IPCC (2014). Special report on mitigation of climate change.

Ishibashi M., K. Otake, S. Kanamori, A. Yasutake (1999). Study on CO_2 removal technology from flue gas of thermal power plant by physical adsorption method. Greenhouse Gas Control Technologies, 95-100.

Ishida M., D. Zheng, T. Akehata (1987). Evaluation of a chemical-looping combustion power-generation system by graphic exergy analysis. Energy 12, 147–154.

Ishida M., H. Jin (1996). A novel chemical-looping combustor without NO_x formation. Industrial & Engineering Chemistry Research 35, 2469-2472.

Ishida M., H. Jin (1997). CO_2 recovery in a power plant with chemical looping combustion. Energy Conversion & Management 38, 187–192.

Ishida M., H. Jin, T. Okamoto (1996). A fundamental study of a new kind of medium material for chemical-looping combustion. Energy & Fuels 10, 958–963.

Ishida M., H. Jin, T. Okamoto (1998). Kinetic behavior of solid particles in chemical looping combustion: suppressing carbon deposition in reduction. Energy & Fuels 12, 223–229.

Ishida M., M. Yamamoto, T. Ohba (2002). Experimental results of chemical-looping combustion with $NiO/NiAl_2O_4$ particle circulation at 1200° C. Energy Conversion and Management 43, 1469-1478.

Jacob D. (1999). Introduction to atmospheric chemistry. Princeton University Press, Princeton.

Jafari R., R. Sotudeh-Gharebagh, N. Mostoufi (2004). Modular simulation of fluidized bed reactors. Chemical engineering & technology 27, 123-129.

Jenkins J.T., S.C. Cowin, (1979). Theories for Flowing Granular Materials. Mech. Applied to Transport of Bulk Materials, Ap. Mech. Div. of ASME, 31, 79-89.

Jericha H., E. Gottlich, W. Sanz, F. Heitmeir (2003). Design optimisation of the Graz prototype plant. In: Proceedings of the ASME turbo expo conference, Atlanta, USA.

Jerndal E., T. Mattisson, A. Lyngfelt (2006). Thermal analysis of chemical-looping combustion. Chemical Engineering Research and Design 84, 795–806.

Jin H., T. Okamoto, M. Ishida (1999). Development of novel chemical-looping combustion: synthesis of solid looping material of $Ni/NiAl_2O_4$. Industrial & Engineering Chemistry Research 38, 126–132.

Johnson F., S. Andersson, B. Leckner (1991). Expansion of a freely bubbling fluidised bed. Powder Technology 68, 117-123.

Johnsson F., B. Leckner (1995). Vertical distribution of solids in a CFB furnace. Proceedings of the 13th International Conference on Fluidized Bed Combustion, 671–679.

Jordal K., R. Bredesen, H.M. Kvamsdal, O. Bolland (2004). Integration of H_2-separating technology in gas gurbine processes for CO_2 sequestration. In: Proceedings of the sixth international conference on greenhouse gas control technologies—GHGT-6, Kyoto, Japan.

Jung J., I.K. Gamwo (2008). Multiphase CFD-based models for chemical looping combustion process: fuel reactor modeling. Powder Technology 183, 401-409.

Kang K.S., C.H. Kim, K.K. Bae, W.C. Cho, S.H. Kim, C.S. Park (2010). Oxygen-carrier selection and thermal analysis of the chemical looping process for hydrogen production. Int. J. Hydrogen Energy 35, 12246−12254.

Kanniche M., R. Gros-Bonnivard, P. Jaud, J. Valle-Marcos, J. Amann, C. Bouallou (2010). Pre-combustion, post-combustion and oxy-combustion in thermal power plant for CO_2 capture. Applied Thermal Engineering 30 (1), 53-62.

Karmhag R., G.A. Niklasson (1999). Oxidation kinetics of small nickel particles. Journal of Applied Physics 85, 1186.

Kerr H.R. (2005). Capture and separation technologies gaps and priority research needs. In: Thomas, D., Benson, S. (Eds.), Carbon Dioxide Capture for Storage in Deep Geologic Formations—Results from the CO_2 Capture Project, vol. 1. Elsevier Ltd., Oxford, UK, Chapter 38.

Klara J.M. (2007). Chemical-Looping Process in a Coal-to-Liquids, Independent Assessment of the Potential of the OSU Chemical Looping Concept. U.S. Department of Energy, National Energy Technology Laboratory (DOE/NETL-2008/1307).

Kofstad P. (1957). Oxidation of Metals: Determination of Activation Energies. Nature 179, 1362-1363.

Kolbitsch P., J. Bolhar-Nordenkampf, T. Proll, H. Hofbauer (2009b). Design of a Chemical Looping Combustor using a Dual Circulating Fluidized Bed Reactor System. Chem. Eng. Technol. 32(3), 398–403.

Kolbitsch P., J. Bolhar-Nordenkampf, T. Proll, H. Hofbauer (2010). Operating experience with chemical looping combustion in a 120 kW dual circulating fluidized bed (DCFB) unit. International J. of Greenhouse Gas Control 4, 180–185.

Kolbitsch P., T. Proll, H. Hofbauer (2009a). Modelling of a 120kW chemical looping combustion reactor system using a Ni-based oxygen carrier. Chemical Engineering Science 64, 99 – 108.

Kovvali A.S., K.K. Sirkar (2001). Dendrimer liquid membranes: CO_2 separation from gas mixtures. Ind. Eng. Chem. 40, 2502-2511.

Kronberger B., A. Lyngfelt, G. Loffler, H. Hofbauer (2005a). Design and fluid dynamic analysis of a bench-scale combustion system with CO_2 separation chemical-looping combustion. Industrial & Engineering Chemistry Research 44, 546–556.

Kronberger B., G. Löffler, H. Hofbauer (2005b). Simulation of mass and energy balances of a chemical-looping combustion system. Clean Air 6, 1–14.

Kruggel-Emden H., . Stepanek, A. Munjiza (2011). A Study on the Role of Reaction Modeling in Multi-phase CFD-based Simulations of Chemical Looping Combustion. Oil Gas Sci. Technol. – Rev. IFP Energies nouvelles 66, 313-331.

Kruggel-Emden H., S. Rickelt, F. Stepanek, A. Munjiza (2010). Development and testing of an interconnected multiphase CFD-model for chemical looping combustion. Chemical Engineering Science 65, 4732-4745.

Kunii D., O. Levenspiel (1990). Fluidized reactor models. 1. For bubbling beds of fine, intermediate, and large particles. 2. For the lean phase: freeboard and fast fluidization. Industrial & engineering chemistry research 29, 1226-1234.

Kunii D., O. Levenspiel (1991). Fluidization Engineering, 2nd edn. Butterworth-Heinemann Series in Ch. Eng.

Kvamsdal H.M., I.S. Ertesvag, O. Bolland, T. Tolstad (2002). Exergy analysis of gas turbine combined cycle with CO_2 capture using pre-combustion of natural gas. In: Proceedings of ASME turbo expo, Amsterdam, The Netherlands.

Kvamsdal H.M., K. Jordal, O. Bolland (2007). A quantitative comparison of gas turbine cycles with CO_2 capture. Energy 32, 10-24.

Lackner K.S. (2003). Climate change: a guide to CO_2 sequestration. Science 300, 1677-1678.

Landau L.D., E.M. Lifshitz (1959). Fluid Mechanics (Volume 6 of A Course of Theoretical Physics), Pergamon Press.

Launder B.E., D.B. Spalding (1974). The numerical computation in turbulent flow. Computer methods in applied mechanics and engineering, Elsevier.

Lazarus M., S. Kartha (2009). Linking technology development with emissions commitments Exploring metrics for effort and outcome. Stockholm Environment Institute Working paper WP-US-0909.

Leion H., T. Mattisson, A. Lyngfelt (2007). The use of petroleum coke as fuel in chemical looping combustion. Fuel 86, 1947–58.

Leites I.L., D.A. Sama, N. Lior (2003). The theory and practice of energy saving in the chemical industry: some methods for reducing thermodynamic irreversibility in chemical technology processes. Energy, 28, 55-97.

Levenspiel O. (1972). Chemical reaction engineering. Wiley New York etc.

Li F., H.R. Kim, D. Sridhar, F. Wang, L. Zeng, J. Chen, L.S. Fan (2009). Syngas Chemical Looping Gasification Process: Oxygen Carrier Particle Selection and Performance. Energy & Fuels 23, 4182–4189.

Linderholm C., A. Abad, T. Mattisson, A. Lyngfelt (2008). 160 h of chemical looping combustion in a 10 kW reactor system with a NiO-based oxygen carrier. International J. of Greenhouse Gas Control 2(4), 520–530.

Liu B., X. Yang, W. Song, W. Lin (2012). Process simulation of formation and emission of NO and N_2O during coal decoupling combustion in a circulating fluidized bed combustor using Aspen Plus. Chemical Engineering Science 71, 375-391..

Luberti M., D. Friedrich, D. Can Oczan, S. Brandani, H. Ahn (2014). A novel strategy to produce ultrapure hydrogen from coal with pre-combustion carbon capture. Energy Procedia 63, 2023–2030.

Lyngfelt A. (2011). Oxygen carriers for chemical looping combustion-4 000 h of operational experience. Oil & Gas Science and Technology–Revue d'IFP Energies nouvelles 66, 161-172.

Lyngfelt A., B. Leckner, T. Mattisson (2001). A fluidized-bed combustion process with inherent CO_2 separation; application of chemical-looping combustion. Chemical Engineering Science 56, 3101-3113.

Lyngfelt A., H. Thunman (2005). Construction and 100 h of operational experience of a 10-kW chemical-looping combustor. Carbon Dioxide Capture for Storage in Deep Geologic Formations-Results from the CO_2 Capture Project 1, 625-645.

Lyngfelt A., M. Johansson, T. Mattisson (2008). Chemical-Looping Combustion − Status of Development. In Proceedings of the 9th International Conference on Circulating Fluidized Beds, Hamburg, Germany.

Mahalatkar K., J. Kuhlman, E.D. Huckaby, T. O'Brien (2011). Computational fluid dynamic simulations of chemical looping fuel reactors utilizing gaseous fuels. Chemical Engineering Science 66, 469-479.

Makkawi Y., R. Ocone (2009). Mass Transfer in Fluidized Bed Drying of Moist Particulate. Chemical Engineering & Technology, 1-10.

Mattisson T., A. Järdnäs, A. Lyngfelt (2003). Reactivity of some metal oxides supported on alumina with alternating methane and oxygen application for chemical-looping combustion. Energy & Fuels 17, 643-651.

Mattisson T., A. Lyngfelt (2001a). Capture of CO_2 using chemical-looping combustion. Proceedings of First Biennial Meeting of the Scandinavian-Nordic Section of the Combustion Institute, Göteborg, Sweden.

Mattisson T., A. Lyngfelt (2001b). Applications of chemical-looping combustion with capture of CO_2. Second Nordic Minisymposium on CO_2 Capture and Storage, Göteborg, Sweden.

Mattisson T., A. Lyngfelt, P. Cho (2001). The use of iron oxide as an oxygen carrier in chemical-looping combustion of methane with inherent separation of CO_2. Fuel 80, 1953–1962.

Mattisson T., E. Jerndal, C. Linderholm, A. Lyngfelt (2011). Reactivity of a spray-dried $NiO/NiAl_2O_4$ oxygen carrier for chemical-looping combustion. Chemical Engineering Science 66, 4636–4644.

Mattisson T., M. Johansson, A. Lyngfelt (2003). Reactivity of some metal oxides supported on alumina with alternating and oxygen–Application of chemical looping combustion. Energy & Fuel 17, 643–651.

Mattisson T., M. Johansson, A. Lyngfelt (2004). Multicycle reduction and oxidation of different types of iron oxide particles–Application to chemical-looping combustion. Energy & Fuel 18, 628–637.

Mattisson T., M. Johansson, A. Lyngfelt (2006). The use of NiO as an oxygen carrier in chemical looping combustion. Fuel 85, 736–747.

Mattisson, T., E. Jerndal, C. Linderholm, A. Lyngfelt (2011). Reactivity of a spray-dried $NiO/NiAl_2O_4$ oxygen carrier for chemical-looping combustion. Chemical Engineering Science 66, 4636-4644.

Maurstad O., R. Bredesen, H.M. Kvamsdal, M. Schell, O. Bolland (2004). SOFC and gas turbine power systems—evaluation of configurations for CO_2 capture. In: Proceedings of the seventh international conference on greenhouse gas control technologies—GHGT-7, Vancouver, Canada.

Miller F.P., A.F. Vandome, J. McBrewster (2009). Carbon credit. VDM Publishing.

Mimura T, H. Simayoshi, T. Suda, M. Iijima, S. Mitsuoka (1997). Development of energy saving technology for flue gas carbon dioxide recovery in power plant by chemical absorption method and steam system. Energy Conversion and Management 38, 57-62.

Mimura T, S. Satsumi, M. Iijima, S. Mitsuoka (1999). Development on energy saving technology for flue gas carbon dioxide recovery by the chemical absorption method and steam system in power plant. Greenhouse Gas Control Technologies, 71-76.

Mora C. (2013). The projected timing of climate departure from recent variability. Nature 502, 183–187.

Mores P.L., E. Godoy, S.F. Mussati, N.J. Scenna (2014). A NGCC power plant wit ha CO_2 post-combustion capture option. Optimal economics for different generation/capture goals. Chemical Engineering Research and Design 92, 1329-1353.

Naqvi R., J. Wolf, O. Bolland (2007). Part-load analysis of a chemical looping combustion (CLC) combined cycle with CO_2 capture. Energy 32, 360-370.

Naqvi R., O. Bolland, Ø. Brandvoll, K. Helle (2004). Chemical looping combustion-analysis of natural gas fired power cycles with inherent CO_2 capture. ASME Turbo Expo: Power for Land, Sea, and Air. American Society of Mechanical Engineers, 301-309.

NOAA/ESRL (2015). Annual Mean Carbon Dioxide Data. NOAA/ESRL.

Nsakala Y.N., J. Marion, C. Bozzuto, G. Liljedahl, M. Palkes, D. Vogel, J.C. Gupta, M. Guha, H. Johnson, S. Plasynski (2001). Engineering feasibility of CO_2 capture on an

existing US coal-fired power plant. Paper presented at First National Conference on Carbon Sequestration, Washington, DC.

Okabe K., N. Matsumija, H. Mano, M. Teramoto (2003). Development of CO_2 separation membranes facilitated transport membrane. Greenhouse Gas Control Technologies, 1555-1558.

Ozcan D.C., H. Ahn, S. Brandani (2013). Process integration of a Ca-looping carbon capture process in a cement plant. International Journal of Greenhouse Gas Control, 19, 530-540.

Ortiz M., L. F. de Diego, A. Abad, F. García-Labiano, P. Gayán, J. Adánez (2012). Catalytic Activity of Ni-Based Oxygen-Carriers for Steam Methane Reforming in Chemical-Looping Processes. Energy Fuels 26, 791−800.

Patankar S. (1980). Numerical heat transfer and fluid flow. CRC Press.

Peters M.S., K.D. Timmerhaus, R.E. West (2004). Plant Design and Economics for Chemical Engineers, Fifth Edition. McGraw Hill.

Petrakopoulou F., A. Boyano, M. Cabrera, G. Tsatsaronis (2011). Exergoeconomic and exergoenvironmental analyses of a combined cycle power plant with chemical looping technology. International Journal of Greenhouse Gas Control 5, 475-482.

Petrakopoulou F., G. Tsatsaronis, T. Morosuk (2010). Convetional Exergetic and Exergoeconomic Analyses of a Power Plant with Chemical Looping Combustion for CO_2 capture. Int. J. of Thermodynamics 13, 77-86.

Porrazzo R., G. White, R. Ocone (2014). Aspen Plus simulations of fluidised beds for chemical looping combustion. Fuel 136, 46-56.

Proll T., J. Bolhar-Nordenkampf, P. Kolbitsch, H. Hofbauer (2010). Syngas and a separate nitrogen/argon stream via chemical looping reforming – A 140 kW pilot plant study. Fuel 89 (6), 1249 –1256.

Rao A.B., E.S. Rubin (2002). A technical economic and environmental assessment of amine-based CO_2 capture technology for power plant greenhouse gas control. Environmental Science & Technology 36, 4467–4475.

REN21 (2010). Renewable Energy Policy Network for the 21st Century.

Rezvani S., Y. Huang, D. McIlveen-Wright, N. Hewitt, J.D. Mondol (2009). Comparative assessment of coal fired IGCC systems with CO_2 capture using physical absorption, membrane reactors and chemical looping. Fuel 88, 2463-2472.

Riemer P.W.F., W.G. Ormerod (1995). International perspectives and the results of carbon dioxide capture disposal and utilisation studies. Energy Conversion and Management 36, 813-818.

Ritcher H., K. Knoche (1983). Reversibility of combustion process. ACS Symposium Series 235, 71–85.

Rubin E.S., A.B. Rao (2003). Uncertainties in CO_2 capture and sequestration costs. Greenhouse Gas Control Technologies, Proceedings of the 6th International Conference on Greenhouse Gas Control Technologies.

Rubin E.S., C. Chen, A.B. Rao (2007). Cost and performance of fossil fuel power plants with CO_2 capture and storage. Energy Policy 35, 4444-4454.

Ryden M., A. Lyngfelt (2006). Using Steam Reforming to Produce Hydrogen with Carbon Dioxide Capture by Chemical-Looping Combustion. Int. J. Hydrogen Energy 31(10), 1271–1283.

Ryden M., A. Lyngfelt, T. Mattisson, D. Chen, A. Holmen, E. Bjørgum (2008). Novel oxygen-carrier materials for chemical-looping combustion and chemical-looping reforming; LaxSr1−xFeyCo1−yO3−δ perovskites and mixed-metal oxides of NiO, Fe_2O_3 and Mn_3O_4. International J. Greenhouse Gas Control 2, 21−36.

Ryu H.-J., D.H. Bae, G.T. Jin (2003). Effect of temperature on reduction reactivity of oxygen carrier particles in a fixed bed chemical-looping combustor. Korean Journal of Chemical Engineering 20, 960-966.

Ryu H.-J., D.H. Bae, K.H. Han, S.Y. Lee, G.T. Jin, J.H. Choi (2001). Oxidation and reduction characteristics of oxygen carrier particles and reaction kinetics by unreacted core model. Korean Journal of Chemical Engineering 18, 831-837.

Ryu H.-J., G.T. Jin, C.K. Yi (2004). Demonstration of inherent CO_2 separation and no NO_x emission in a 50 kW chemical-looping combustor: continuous reduction and oxidation experiment. Proceedings of the 7th International Conference on Greenhouse Gas Control Technologies, 5-9, Vancouver.

Ryu H.J., S.H. Jo, Y.C. Park, D.H. Bae, S. Kim (2010). Long-term operation experience in a 50 kWth chemical looping combustor using natural gas and syngas as fuels. 1st International Conference on Chemical Looping.

Sarvar-Amini A., R. Sotudeh-Gharebagh, H. Bashiri, N. Mostoufi, A. Haghtalab (2007). Sequential Simulation of a Fluidized Bed Membrane Reactor for the Steam Methane Reforming Using ASPEN PLUS. Energy & Fuels 21, 3593–3598.

Scala F. (2013). Fluidised Bed Technologies for near-zero emission Combustion and Gasification. Woodhead Publishing Series in Energy.

Schaeffer D.G. (1987). Instability in the evolution equations describing incompressible granular flow. Journal of Differential Equations 66, 19-50.

Schmidt G.A., R. Ruedy, R.L. Miller, A.A. Lacis (2010). The attribution of the present-day total greenhouse effect. *J. Geophys. Res.* 115, D20106 doi:101029/2010JD014287.

Scott S.A., J.S. Dennis, A.N. Hayhurst, T. Brown (2006). In Situ Gasification of a Solid Fuel and CO_2 Separation using Chemical Looping. AIChE J. 52(9), 3325–3328.

Shafiefarhood A., N. Galinsky, Y. Huang, Y. Chen, F. Li (2014). Fe2O3@LaxSr1_xFeO3 Core–Shell Redox Catalyst for Methane Partial Oxidation. ChemCatChem 6, 790–799.

Shen L., F. Johnson, B. Leckner (2004). Digital image analysis of hydrodynamics two dimensional bubbling fluidised beds. Chemical Engineering Science 59, 2607-2617.

Shimizu T., T. Hirama, H. Hosoda, K. Kitano, M. Inagaki, K. Tejima (1999). A twin fluid-bed reactor for removal of CO_2 from combustion processes. CHERD 77, 62-68.

Shuai W., L. Guodong, L. Huilin, C. Juhui, H. Yurong, W. Jiaxing (2011a). Fluid dynamic simulation in a chemical looping combustion with two interconnected fluidized beds. Fuel Processing Technology 92, 385-393.

Shuai W., Y. Yunchao, L. Huilin, W. Jiaxing, X. Pengfei, L. Guodong (2011b). Hydrodynamic simulation of fuel-reactor in chemical looping combustion process. Chemical Engineering Research and Design 89, 1501-1510.

Simbeck D.R. (1999). A portfolio selection approach for power plant CO_2 capture, separation and R&D options. Proceedings of the 4th International Conference on Greenhouse Gas Control Technologies.

Singh D., E. Croiset, P.L. Douglas, M.A. Douglas (2003). Techno-Economic Study of CO_2 Capture from an Existing Coal-Fired Power Plant: MEA Scrubbing vs. O_2/CO_2 Recycle Combustion, Energy Conversion and Management 44 (19), 3073-3091.

Sircar S. (1979). Separation of multi-component gas mixtures. US Patent No. 4171206.

Son S.R., S.D. Kim (2006). Chemical-looping combustion with NiO and Fe_2O_3 in a thermo balance and circulating fluidized bed rector with double loops. Industrial & Engineering Chemistry Research 45, 2689–2696.

Sotudeh-Gharebaagh R., R. Legros, J. Chaouki, J. Paris (1998). Simulation of circulating fluidized bed reactors using Aspen Plus. Fuel 77(4), 327-337.

Syamlal M. (1998a). “MFIX Documentation: Numerical Technique,” National Energy Technology Laboratory, Department of Energy, Technical Note DOE/MC31346–5824 and NTIS/DE98002029.

Syamlal M. (1998b). “High Order Discretization Methods for the Numerical Simulation of Fluidized Beds,” Department of Energy, Technical Note DOE/FETC/C-98/7305 and CONF-971113.

Syamlal M., W. Rogers, T.J. O’Brien (1993). MFIX documentation: Theory guide. Technical Note, DOE/METC-94/1004, NTIS/DE94000087, National Technical Information Service, Springfield, VA.

Takami KM, J. Mahmoudi, R.W. Time (2009). A simulated H_2O/CO_2 condenser design for oxy-fuel CO_2 capture process. Energy Procedia 1, 1443-1450.

Teaters L. (2012). A Computational Study of the Hydrodynamics of Gas-Solid Fluidized Beds. Thesis, Virginia Polytechnic Institute and State University, USA.

Teramoto M., K. Nakai, N. Ohnishi, Q. Huang, T. Watari, H. Matsuyama (1996). Facilitated transport of carbon dioxide through supported liquid membranes of aqueous amine solutions. Ind. Eng. Chem. 35, 538-545.

Van der Sluijs J.P., C.A. Hendriks, K. Blok (1992). Feasibility of polymer membranes for carbon dioxide recovery from flue gases. Energy Conversion Management 33, 429-436.

Versteeg H.K., W. Malalasekera (1995). An introduction to computational fluid dynamics. John Wiley.

Villa R., C. Cristiani, G. Groppi, L. Lietti, P. Forzatti, U. Cornaro, S. Rossini (2003). Ni based mixed oxide materials for CH_4 oxidation under redox cycle conditions. Journal of Molecular Catalysis 204–205, 637–646.

Wang X., B. Jin, Y. Zhang, W. Zhong, S. Yin (2011). Multiphase computational fluid dynamics (CFD) modelling of chemical looping combustion using a CuO/Al2O3

oxygen carrier: effect of operating conditions on coal gas combustion. Energy & Fuels 25, 3815-3824.

Wilkinson M.B., M. Simmonds, R.J. Allam, V. White (2003). Oxy-fuel conversion of heaters and boilers for CO_2 capture. 2nd Annual Conference on Carbon Sequestration, Virginia (USA).

Wolf J. (2004). CO_2 mitigation in advanced power cycles—Chemical looping combustion and steam-based gasification. Doctoral Thesis, Department of Chemical Engineering and Technology Energy Processes, KTH-Royal Institute of Technology, SE-100 44 Stockholm, Sweden.

Wolf J., M. Anheden, J. Yan (2001). Performance analysis of combined cycles with chemical looping combustion for CO_2 capture. Proceedings of 18th Pittsburg Coal Conference, 3-7.

Wolf J., M. Anheden, J. Yan (2005). Comparison of nickel-and iron-based oxygen carriers in chemical looping combustion for CO_2 capture in power generation. Fuel 84, 993-1006.

World Energy Outlook (WEO) (2012). International Energy Agency.

Yokoyama T. (2003). Japanese R&D on CO_2 capture. Greenhouse Gas Control Technologies, Proc. of the 6th International Conference on Greenhouse Gas Control Technologies 13-18.

Zafar Q., T. Mattisson, B. Gevert (2006). Redox investigation of some oxides of transition-state metals Ni, Cu, Fe, and Mn supported on SiO_2 and $MgAl_2O_4$. Energy & Fuels 20, 34–44.

Zheng X.Y., Y.F. Diao, B.S. He, C.H. Chen, X.C. Xu, W. Feng (2003). Carbon dioxide recovery from Flue gases by ammonia scrubbing. Greenhouse Gas Control Technologies, Proc. of the 6th International Conference on Greenhouse Gas Control Technologies, Kyoto.